METALLOENZYMES AS INSPIRATIONAL ELECTROCATALYSTS FOR ARTIFICIAL PHOTOSYNTHESIS – FROM MECHANISM TO MODEL DEVICES



Andreas S. J. L. Bachmeier
St John's College
Trinity Term 2015

A thesis submitted to the Board of the Faculty of Physical Sciences, for the degree of Doctor of Philosophy, University of Oxford

© Andreas S. J. L. Bachmeier 2015

METALLOENZYMES AS INSPIRATIONAL ELECTROCATALYSTS FOR ARTIFICIAL PHOTOSYNTHESIS – FROM MECHANISM TO MODEL DEVICES

Andreas S. J. L. Bachmeier, St. John's College, University of Oxford
A thesis submitted for the degree of D.Phil., Trinity Term 2015

Artificial photosynthesis, an important route towards future supply of renewable energy, seeks to convert sunlight into storable chemical energy such as fuels. Building upon the principles of biological solar energy conversion, artificial photosynthesis can be broken down into four essential processes: harvesting of visible light, charge (electron-hole) separation, oxidation of water to dioxygen, and fuel formation. Importantly, unlike natural photosynthesis, artificial photosynthesis is solely dedicated to efficient formation of fuels and is not restricted by the availability of arable land.

Both water oxidation and fuel formation require efficient and selective catalysts. This work utilises certain metalloenzymes, which have evolved to catalyse fuel-generating reactions such as the formation of H_2 or the reductive activation of CO_2 to carbon-based fuels with unmatched efficiencies. In contrast to most artificial catalysts, these enzymes are composed solely of abundant elements and operate efficiently at neutral pH. Thus, although not suitable for scale-up, they can be used to mimic conditions under which future devices will have to operate and provide design criteria for the components of applied technologies.

In this thesis, physico-chemical techniques are used to study the mechanism of [FeFe]-hydrogenases, the most proficient H_2 evolving catalysts that rival platinum in activity, by investigating how reversible inhibitors intercept transient enzyme states. The interaction of fuel-forming enzymes with light-absorbing semiconductor electrodes is also explored, leading to the construction of a photoelectrochemical cell for the selective, light-driven reduction of CO_2. Furthermore, this thesis demonstrates that metalloenzymes can be used to establish new directions in artificial photosynthesis research, driving endergonic organic reactions such as specific C=C hydrogenation.

ACKNOWLEDGEMENTS

First and foremost, I would like to thank Professor Fraser Armstrong, for offering me a place in his group and for providing me with all the freedom I needed to pursue my own ideas, while, at the same time, being a constant source of inspiration and intellectual challenge. I thoroughly enjoyed working under his guidance.

Thanks must also go to my collaborators, without the contributions of whom this work would not have been possible. I am particularly grateful to Dr. William Myers for all his contributions to the work on [FeFe]-hydrogenases and for teaching me (or trying to, at least) a fair bit on pulsed-EPR during the many long nights we shared sitting in front of the spectrometer. In this regard Julian Esselborn is also acknowledged, not only for supplying me with copious amounts of highly concentrated enzyme ('black gold'), but also for his helpful comments regarding mechanistic aspects of [FeFe]-hydrogenases.

To my proof-readers, Dr. Rhiannon Evans, Professor Radim Beranek, Dr. Suzannah Hexter, Dr. Thomas Esterle, and Dr. Holly Reeve: I am grateful for all the valuable and constructive feedback. Thanks to my part II students Samuel Hall and Sophie Bell for their heroic efforts; it has been great pleasure overseeing their first steps into research.

A very special thanks goes to my fellow leaders of the 'Solar Fuels' exhibit at the 2013 Royal Society Summer Science Exhibition: Non, Suzannah, and Alison. Not only has it been a very exciting (albeit stressful, at times) experience organising the exhibit and bringing it to success; I also feel it has brought us closer together as friends.

Thank you to past and present and members of the Armstrong group: Non, Suzannah, Philip, Bonnie, Thomas, Vincent, Maxie, Tom, Yatendra, Gopan, Edgar, Alison, Carina, Emily, and Bhavin, for all the help and support, for teaching me a great deal about science,

for sharing your expertise on enzymes and electrochemistry, and, of course, for all the fun we had in- and outside the lab

I am also thankful for all the help I received from the Department of Chemistry's support staff over the years, in particular from Terri Adams (glassblowing), Nenad Vranjes (electronics), Ashleigh Hewson and Jonathan Hawkins (building management), Charlie Jones (PCTL student workshop), as well as Karl Harrison, Keith Waters, and Tom Bradshaw (IT).

St John's College Oxford is gratefully acknowledged for providing my with a Graduate Scholarship that allowed me to pursue my doctoral studies in such a vibrant and stimulating environment. Furthermore, I am grateful to St John's College and also the UK Solar Fuels Network for generous financial contributions towards the attendance of several international conferences. I would like to thank the SCG innovation fund for a six months funding extension in form of a 'pump prime' grant.

Last but not least, special thanks go to my family, who have been a constant source of support, and to all my friends who have made my time at Oxford so memorable and enjoyable. I dedicate this work to both my late father, who is sorely missed, and Stephanie: I have been fortunate to meet the most wonderful person so early on in my life.

COLLABORATIONS

The following collaborators contributed to the work presented in this thesis. Enzyme samples were kindly provided by several laboratories: [FeFe]-hydrogenase enzymes were prepared by Julian Esselborn (laboratory of Professor Thomas Happe, Ruhr-Universität Bochum, Germany). Carbon monoxide dehydrogenase was provided by Dr. Mehmet Can (laboratory of Professor Stephen Ragsdale, University of Michigan, USA), and [NiFeSe]-hydrogenase was prepared by Dr. Christine Cavazza, (laboratory of Professor Juan-Carlos Fontecilla-Camps, Institute de Biologie Structurale, Grenoble). Samples of flavocytochrome c_3 were provided by Professors Graeme Reid (Institute of Cell and Molecular Biology, University of Edinburgh) and Stephen Chapman (Department of Chemistry, University of Edinburgh).

The pulsed-EPR experiments presented in chapter 3 were carried out together with Dr. William Myers (Centre for Advanced Electron Spin Resonance, University of Oxford), who developed the mathematical framework for data analysis, analysed the data, and prepared the Figures. The DFT calculations presented in chapter 3 were performed by Professor John McGrady (Inorganic Chemistry Laboratory, University of Oxford).

Some of the electrochemistry experiments presented in chapter 4 were carried out by Sophie Bell under my supervision, and some of the electrochemistry experiments shown in chapter 5 were conducted by Samuel Hall, also under my supervision. In both these cases, I devised the experiments.

The SEM images presented in chapters 4 and 5 were recorded by Professor Jamie Warner (Department of Materials, University of Oxford).

PUBLICATIONS

1. How Formaldehyde Inhibits Hydrogen Evolution by [FeFe]-Hydrogenases: Determination by ^{13}C ENDOR of Direct Fe–C Coordination and Order of Electron and Proton Transfers. Andreas Bachmeier, Julian Esselborn, Suzannah V. Hexter, Tobias Krämer, Kathrin Klein, Thomas Happe, John E. McGrady, William K. Myers, and Fraser A. Armstrong, *J. Am. Chem. Soc.* **2015**, *137*, 5381.

2. Enzymes as Exploratory Catalysts in Artificial Photosynthesis. Andreas Bachmeier, Bhavin Siritanaratkul, and Fraser A. Armstrong, in 'From Molecules to Materials – Pathways to Artificial Photosynthesis', Eds: E. A. Rozhkova, K. Ariga, Springer **2015**, 99.

3. Solar-driven proton and carbon dioxide reduction to fuels – lessons from metalloenzymes. Andreas Bachmeier and Fraser Armstrong, *Curr. Opin. Chem. Biol.* **2015**, *25*, 141.

4. Selective Visible-Light-Driven CO_2 Reduction on a p-Type Dye-Sensitized NiO Photocathode. Andreas Bachmeier, Samuel Hall, Stephen W. Ragsdale, and Fraser A. Armstrong, *J. Am. Chem. Soc.* **2014**, *136*, 13518.

5. A Multi-Heme Flavoenzyme as a Solar Conversion Catalyst. Andreas Bachmeier, Bonnie J. Murphy, and Fraser A. Armstrong, *J. Am. Chem. Soc.* **2014**, *136*, 12876 (highlighted as 'JACS-Spotlight': *J. Am. Chem. Soc.* **2014**, *136*, 13469).

6. How Light-Harvesting Semiconductors Can Alter the Bias of Reversible Electrocatalysts in Favor of H_2 Production and CO_2 Reduction. Andreas Bachmeier, Vincent C. C. Wang, Thomas W. Woolerton, Sophie Bell, Juan C. Fontecilla-Camps, Mehmet Can, Stephen W. Ragsdale, Yatendra S. Chaudhary, and Fraser A. Armstrong, *J. Am. Chem. Soc.* **2013**, *135*, 15026.

7. Visible Light-Induced Hole Injection into Rectifying Molecular Wires Anchored on Co_3O_4 and SiO_2 Nanoparticles. Han Sen Soo, Anil Agiral, Andreas Bachmeier, and Heinz Frei, *J. Am. Chem. Soc.* **2012**, *134*, 17104.

Publications 1 – 6 feature in this thesis and have been adapted with permission from the respective publisher: American Chemical Society (1, 4 – 6), Springer (2), and Elsevier (3).

NOTATION

Acronyms and Abbreviations

$[2Fe]_H$	two-iron subsite of H-cluster
[Ox]	concentration of oxidised species
[Red]	concentration of reduced species
a_i	activity of component i
a.c.	alternating current
adt	azadithiolate
aq	aqueous
A	area
	hyperfine coupling constant
Acetyl-CoA	acetyl coenzyme A
ACS	acetyl-CoA synthase
ADP	adenosine diphosphate
AM 1.5 G	air mass 1.5 global standard G173
APCE	absorbed photon-to-current efficiency
Arg	arginine
Asp	aspartic acid
ATP	adenosine triphosphate
B	magnetic field
bp	boiling point
bpy	2,2'-bipyridine
Bu	butyl
C	capacitance
c	concentration
Ca	*Clostridium acetobutylicum*
*Ca*HydA	*Clostridium acetobutylicum* hydrogenase A
CA	chronoamperometry
CB	conduction band
CE	counter electrode
Ch	*Carboxydothermus hydrogenoformans*
CIGS	copper indium gallium selenide

Co-Pi	cobalt phosphate (oxide) oxygen evolution electrocatalyst
CODH	carbon monoxide dehydrogenase I from *Carboxydothermus hydrogenoformans*
Cp	*Clostridium pasteurianum*
CPE	constant phase element
Cr	*Chlamydomonas reinhardtii*
*Cr*HydA1	*Chlamydomonas reinhardtii* hydrogenase A1
CV	cyclic voltammogram
CW	continuous-wave
Cys	cysteine
Cyt	cytochrome
D	diffusion coefficient
d	separation distance between two reactants
d_0	separation distance in encounter complex
d.c.	direct current
D1	photosynthetic protein D1
D2	photosynthetic protein D2
Dd	*Desulfovibrio desulfuricans*
DFT	density functional theory
DSSC	dye-sensitised solar cell
e^-	electron
e_0	elementary charge = 1.602×10^{-19} C
E. coli	*Escherichia coli*
E	electrode potential
E^0	standard electrode potential
E_a	acceptor level
E_{cb}	conduction band potential
E_d	donor level
E_F	Fermi level
E_{fb}	flat-band potential
E_g	band gap
E_{oc}	open-circuit photopotential
E_{on}	photocurrent onset potential
E_{vb}	valence band potential
EIS	electrical impedance spectroscopy
ENDOR	electron nuclear double resonance

EPR	electron paramagnetic resonance
EQE	external quantum efficiency
ESEEM	electron spin echo envelope modulation
EXAFS	extended X-ray absorption fine structure
f	force constant
ff	fill factor
fcc_3	flavocytochrome c_3 from *Shewanella frigidimarina* NCIMB400
F	Faraday's constant = 96,485 C mol^{-1}
FAD	flavin adenine dinucleotide
Fd	ferredoxin
FDH	formate dehydrogenase
FID	free-induction decay
FTIR	Fourier transform infrared spectroscopy
FTO	fluorine doped tin oxide
G	Gibbs free energy
GC	gas chromatography
Glu	glutamic acid
h	Planck constant = 6.626×10^{-34} J s
$\hbar$	reduced Planck constant = $h/2\pi$
H_2ase	hydrogenase
H_{el}	electronic coupling matrix element
His	histidine
HOMO	highest occupied molecular orbital
Hyd1	*E. coli* hydrogenase I
HYSCORE	hyperfine sublevel correlation spectroscopy
i	current
	imaginary number
i_{ph}	photocurrent
I	nuclear spin
	photon flux
IHP	inner Helmholtz plane
IPCE	incident photon-to-current efficiency
IQE	internal quantum efficiency
IR	infrared (spectroscopy)
ITO	indium tin oxide

j	current density
j_0	exchange current density
k	kinetic rate constant
k_B	Boltzmann constant = 1.381×10^{-23} J K^{-1}
K	equilibrium constant
KPi	0.1 M potassium phosphate buffer
L	minority carrier diffusion length
LSV	linear sweep voltammetry
LUMO	lowest unoccupied molecular orbital
Lys	lysine
M	metal
m_s	electron spin quantum number
Me	methyl
MES	2-(*N*-morpholino)ethanesulfonic acid
MMCT	metal-to-metal charge-transfer
MO	molecular orbital
MPA	3-mercaptopropionic acid
n	amount of substance
	electron density, concentration
N_A	acceptor density
N_D	donor density
NADP(H)	nicotinamide adenine dinucleotide phosphate
NHE	normal hydrogen electrode
NMR	nuclear magnetic resonance
OEC	oxygen evolving cluster
OHP	outer Helmholtz plane
Ox	oxidised species
p	hole density, concentration
P_{in}	incident illumination power density
P1	4-[Bis(4-{5-[2,2-dicyanovinyl]-thiophene-2-yl}phenyl)amino]benzoic acid
P25	TiO_2 nanopowder: primary particle size 21 nm, 80% anatase/20% rutile
PCET	proton-coupled electron transfer
PDB	protein data bank
PEC	photoelectrochemical cell
PFE	protein film electrochemistry

PFIRE	protein film infrared electrochemistry
PGE	pyrolytic graphite edge
Phe	pheophytin *a*
Pr	propyl
PSI	photosystem I
PSII	photosystem II
PV	photovoltaics
Py	pyridyl
PZC	point of zero charge
q	charge stored on capacitor
Δq	change in equilibrium bond distance
Q_A	plastoquinone A
Q_B	plastoquinone B
Q_BH_2	plastoquinol B
r	radius
rpm	revolutions per minute
R	ideal gas constant = 8.314 J K^{-1} mol^{-1}
	resistance
RE	reference electrode
Red	reduced species
RHE	reversible hydrogen electrode
RuBisCO	ribulose-1,5-biphosphate carboxylase-oxygenase
RuBP	ribulose-1,5-biphosphate
RuP	$[Ru^{II}(bpy)_2(4,4'\text{-}(PO_3H_2)_2bpy)]Br_2$
S	electron spin
S	state in Kok cycle
SCE	saturated calomel electrode
SeCys	selenocysteine
SEM	scanning electron microscopy
Ser	serine
SHE	standard hydrogen electrode
SOMO	singly occupied molecular orbital
STH	solar-to-hydrogen
STS	solar-to-succinate
t	time

T	temperature
T	dipolar component of hyperfine interaction
TEOA	triethanolamine
TOF	turnover frequency
TON	turnover number
TST	transition state theory
UV	ultraviolet
UV/vis	ultraviolet-visible absorption spectroscopy
v	scan rate
	kinematic viscosity of the solvent
v_i	stoichiometric coefficient of component i
v	volume
V	voltage
V_{oc}	open-circuit voltage
VB	valence band
wt	weight
W	depletion layer width
WE	working electrode
XAE	X-ray absorption and emission
XAS	X-ray absorption spectroscopy
z	number of electrons
Z	impedance
Z_w	Warburg impedance
α	transfer coefficient
	absorption coefficient
β	attenuation factor
ε	dielectric constant
ε_0	permittivity of free space
ε_{op}	optical dielectric constant of the solvent
ε_s	static dielectric constant
ϕ	electric potential
Φ	quantum yield
Γ	(electroactive) coverage
η	overpotential
	efficiency

η_{e^-/h^+}	absorptance
κ_{el}	electronic factor
κ_n	nuclear factor
λ	wavelength
	reorganisation energy
μ	electrochemical potential
$\tilde{\mu}$	chemical potential
μ_0	vacuum permeability
μ_B	Bohr magneton
μ_n	nuclear magnetic moment
ν	frequency
Θ	phase difference
ρ	spin density
τ	decay constant
	delay time (EPR)
ω	rotation rate
	angular frequency

Units of measure

‰	per mille
Å	Ångström
atm	atmosphere(s)
au	atomic units
bn	billion
C	Coulomb(s)
Da	Dalton(s)
eV	electron Volt(s)
F	Farad(s)
G	Gauss
h	hour(s)
Hz	Hertz
J	Joule(s)
K	Kelvin

L	litre(s)
m	metre(s)
M	mol L^{-1}
min	minute(s)
Mtoe	million tons of oil equivalent
ppm	parts per million
rad s^{-1}	radian per second
s	second(s)
scc	standard cubic centimetre(s)
S	Siemens
T	Tesla
V	Volt(s)
W	Watt(s)
Ω	Ohm(s)

Prefices

p	pico	10^{-12}
n	nano	10^{-9}
μ	micro	10^{-6}
m	milli	10^{-3}
c	centi	10^{-2}
k	kilo	10^{3}
M	mega	10^{6}
G	giga	10^{9}
T	tera	10^{12}
i	iso	
meso	mesoporous	
p	para	

Common subscripts and superscripts

*	excited state
‡	transition state
0	standard state
a	anodic
c	cathodic
cat	catalytic
ct	charge-transfer
d	differential
	distal
diff.	diffuse layer
dl	double layer
e	electron
eq	equilibrium
et	electron transfer
F	Faradaic
	Fermi
H	Helmholtz layer
i	inner-sphere
in	incident
iso	isotropic
lim	limiting
m	midpoint
	metal
o	outer-sphere
obs	observed
oc	open-circuit
ox	oxidised
p	pendant
	product
	proximal
ph	photo
r	reactant
red	reduced

ref	reference
s	solution
sc	short-circuit
	space-charge layer
w	working electrode

CONTENTS

1 Introduction 1

1.1 Rationale for artificial photosynthesis 2

1.2 Principles of photosynthetic energy conversion 6

1.2.1 Energy flow in biology and photosynthetic efficiencies 6

1.2.2 The photosynthetic reactions 8

1.2.2.1 From light-absorption to carbon dioxide fixation – a brief overview 8

1.2.2.2 Water splitting by Photosystem II 11

1.2.3 Using Photosystem II as a guide for assembling an artificial photosynthetic system 18

1.3 The individual components of artificial photosynthetic systems 21

1.3.1 Light-absorption and charge-separation 21

1.3.1.1 General considerations 21

1.3.1.2 Molecular dyes 21

1.3.1.3 Metal-to-metal-charge-transfer units 22

1.3.1.4 Semiconductors 22

1.3.1.5 Photovoltaics 24

1.3.2 Water oxidation catalysis 27

1.3.3 H_2 formation 30

1.3.3.1 Molecular catalysts 30

1.3.3.2 Solid-state catalysts 32

1.3.3.3 Hydrogenases 34

1.3.4 CO_2 reduction 35

1.3.4.1 General considerations on the reduction of carbon dioxide to fuels and chemicals 35

1.3.4.2 Heterogeneous electrocatalysts for CO_2 reduction 37

1.3.4.3 Molecular CO_2 reduction catalysts 40

1.3.4.4 CO_2 reduction in biology 41

1.4 Strategies for integrated systems 44

1.4.1 Integrating the individual components 44

1.4.2 Photochemical *vs.* photoelectrochemical water splitting 46

1.4.2.1 Photoelectrochemical cells 46

1.4.2.2 Photochemical systems 50

1.4.3 The combination of photovoltaics and electrolysis 53

1.5 The role of enzymes in artificial photosynthesis 56

1.5.1 General considerations ... 56
1.5.2 Photosystem II in artificial systems ... 57
1.5.3 Fuel-forming enzymes for artificial photosynthesis ... 58
1.5.3.1 Configurations ... 58
1.5.3.2 Photoenzymes ... 59
1.5.3.3 From photoenzymes to fusion-complexes: the limiting case of stoichiometric architectures ... 60
1.5.3.4 Enzymes on semiconductor nanoparticles ... 60
1.5.3.5 Photoelectrode assemblies for fuel-formation ... 65
1.6 The mechanisms of fuel-forming enzymes ... 66
1.6.1 Common mechanistic principles ... 66
1.6.2 [FeFe]-Hydrogenases ... 67
1.6.2.1 Structural features ... 67
1.6.2.2 Active site and redox states ... 69
1.6.2.3 Artificial maturation ... 72
1.6.2.4 Mechanism ... 75
1.6.3 [NiFe]-Hydrogenases ... 77
1.6.3.1 Structural features ... 77
1.6.3.2 Active site and redox states ... 80
1.6.3.3 Catalytic mechanism ... 82
1.6.3.4 Oxygen tolerance ... 84
1.6.4 Carbon monoxide dehydrogenase ... 86
1.6.4.1 Structural features and active site ... 86
1.6.4.2 Redox states and catalytic mechanism ... 88
1.7 Aims of this thesis ... 92
2 Theory of experimental techniques ... 95
2.1 Rate and efficiency parameters in artificial photosynthesis ... 96
2.2 Protein film electrochemistry ... 99
2.2.1 A brief introduction to protein film electrochemistry ... 99
2.2.2 The electrochemical setup ... 99
2.2.3 Non-Faradaic processes ... 102
2.2.4 Faradaic current ... 104
2.2.5 Mass transport and interfacial electron transfer ... 105
2.2.6 Catalytic voltammetry ... 111
2.2.7 Chronoamperometry ... 113

2.3 Semiconductor electrochemistry 116
2.3.1 The energy band model 116
2.3.2 The semiconductor/solution interface 119
2.3.3 The semiconductor/electrolyte junction under applied bias 122
2.3.3.1 Qualitative description of the semiconductor/liquid interface under applied bias 122
2.3.3.2 Current potential curves of semiconductor electrodes in the dark 124
2.3.3.3 Case studies: TiO_2 and NiO 126
2.3.4 Photoeffects at the semiconductor/electrolyte interface 129
2.3.5 Measurement of the flat-band potential 132
2.3.5.1 Photocurrent onset potential 132
2.3.5.2 Open-circuit photovoltage 132
2.3.5.3 The Mott-Schottky plot 133
2.4 Marcus theory and theoretical treatment of photoinduced electron transfer 140
2.4.1 The electron transfer rate constant 140
2.4.2 The free energy of activation 141
2.4.3 Reorganisation 143
2.4.4 The normal and inverted regions 144
2.4.4.1 Implications from the Marcus equation 144
2.4.4.2 Pictorial representations of electron transfer processes 145
2.4.4.3 Photoinduced electron transfer 149
2.4.5 Electronic coupling 150
2.4.5.1 Adiabatic and nonadiabatic electron transfer 150
2.4.5.2 Distance dependence of electron transfer and the semiclassical Marcus equation 153
2.4.6 Electron transfer in biological systems 154
2.5 Electron paramagnetic resonance spectroscopy 156
2.5.1 The electronic *g* value 156
2.5.2 The *g* value is anisotropic 158
2.5.3 Multiple magnetic interactions 160
2.5.4 'Advanced' EPR techniques 161
3 The mechanism of [FeFe]-hydrogenases – how aldehydes inhibit H_2 evolution 163
Abstract 164
3.1 Introduction 166
3.2 Protein film electrochemistry investigations 171
3.2.1 Inhibition by formaldehyde 172

3.2.2 Inhibition by trifluoroacetaldehyde 173
3.2.3 Inhibition by acetaldehyde 176
3.2.4 Inhibition by butyraldehyde 178
3.2.5 Inhibition by isovaleraldehyde 179
3.3 Discussion 182
3.3.1 Discussion of the different aldehyde reactivities 182
3.3.2 Implications from the investigation of formaldehyde inhibition of the H-cluster by pulsed-EPR techniques 188
3.3.2.1 Formaldehyde inhibition of the H-cluster detected by ENDOR and ESEEM 188
3.3.2.2 Implications 193
3.3.3 Insight from density functional theory 195
3.3.4 Comparative analysis and discussion 198
3.4 Conclusions and perspectives 202
4 The direct electrochemistry of fuel-forming enzymes on semiconducting electrodes: how light-harvesting semiconductors can alter the bias of reversible electrocatalysts in favour of H_2 production and CO_2 reduction 205
Abstract 206
4.1 Introduction 207
4.2 Results 210
4.2.1 Characteristics of porous CdS and TiO_2 electrodes and enzyme immobilisation 210
4.2.2 Direct electrochemistry of CODH and [NiFeSe]-hydrogenase on TiO_2 and CdS 214
4.2.3 Mott-Schottky measurements 221
4.2.3.1 The flat-band potential of TiO_2 and CdS electrodes 221
4.2.3.2 The flat-band potential of CODH-TiO_2 in the absence of substrate 224
4.2.3.3 The flat-band potential of CODH-modified TiO_2 under turnover conditions. 228
4.2.4 Photoelectrochemistry 229
4.3 Discussion 231
4.4 Conclusions and perspectives 235
5 Selective visible-light-driven CO_2 reduction on a *p*-type dye-sensitised NiO photocathode 237
Abstract 238
5.1 Introduction 239
5.2 Results and discussion 242

5.2.1 Electrocatalytic activity of carbon monoxide dehydrogenase adsorbed on a *p*-type NiO electrode 242
5.2.2 Photoelectrocatalytic CO_2 reduction 246
5.3 Conclusions and perspectives 254
6 A multi-haem flavoenzyme as a solar conversion catalyst 257
Abstract 258
6.1 Introduction 259
6.2 Results and discussion 261
6.2.1 Protein film electrochemistry 261
6.2.2 Photocatalytic fumarate formation 263
6.2.3 Closing the photosynthetic cycle 269
6.3 Conclusions and perspectives 275
7 Conclusions and perspectives 277
7.1 Conclusions 278
7.2 Perspectives 280
7.3 New directions in artificial photosynthesis – where do we go from here and how enzymes may lead the way 285
8 Experimental section 287
8.1 General considerations 288
8.2 The mechanism of [FeFe]-hydrogenases – how aldehydes inhibit H_2 evolution 289
8.2.1 General considerations 289
8.2.2 Enzyme preparation 289
8.2.3 Protein film electrochemistry 290
8.2.4 Electron paramagnetic resonance 291
8.2.5 Density functional theory 292
8.3 The direct electrochemistry of fuel-forming enzymes on semiconducting electrodes 295
8.3.1 General considerations 295
8.3.2 Semiconductor electrodes 295
8.3.2.1 Synthesis of semiconductor thin films 295
8.3.2.2 Electrode fabrication 297
8.3.3 Enzyme preparation 297
8.3.4 Protein film electrochemistry 298
8.4 Selective visible-light-driven CO_2 reduction on a *p*-type dye-sensitised NiO photocathode 300
8.4.1 General considerations 300
8.4.2 Fabrication of NiO electrodes 300

8.4.2.1 Synthesis of NiO particles 300
8.4.2.2 Fabrication of electrodes from NiO particles 301
8.4.2.3 Synthesis of P1 and sensitisation of NiO electrodes 301
8.4.3 Enzyme preparation 303
8.4.4 Protein film electrochemistry 303
8.5 A multi-haem flavoenzyme as a solar conversion catalyst 305
8.5.1 General considerations 305
8.5.1.1 Buffer solutions 305
8.5.1.2 RuP synthesis 306
8.5.2 Protein purification 306
8.5.3 Preparation of thin film electrodes 306
8.5.3.1 Cadmium sulphide and titanium dioxide 306
8.5.3.2 *meso*-Indium tin oxide 306
8.5.3.3 Tungsten-doped bismuth vanadate 307
8.5.3.4 Electrode fabrication 307
8.5.4 Protein film electrochemistry experiments 307
8.5.5 Photocatalysis experiments 307
8.5.5.1 Adsorption of fcc_3 on TiO_2 nanoparticles 307
8.5.5.2 Adsorption of RuP on TiO_2 nanoparticles 308
8.5.5.3 Photocatalysis by RuP–TiO_2–fcc_3 308
8.5.5.4 Photochemistry experiment – RuP–fcc_3 in solution 310
8.5.5.5 Photochemistry experiment – RuP–ZrO_2–fcc_3 310
8.5.6 Photoelectrochemistry experiments 315
8.5.6.1 Experimental procedures 315
8.5.6.2 Catalyst deposition on W–$BiVO_4$ electrodes 316
8.5.6.3 Photoelectrocatalysis experiments 316
Bibliography 319
Appendices 341
Appendix A 342
Appendix B 345
Appendix C 348
Appendix D 349
Appendix E 350
Appendix F 351
Appendix G 352

1 Introduction

1.1 Rationale for artificial photosynthesis

New sources of energy have to be utilised to empower us to address the world's growing energy demand, which is projected to double by 2050 and triple by the end of the century [1-3]. The global human power requirement in 2009 was approximately 16 TW; more than 10,000 nuclear power plants would be needed to satisfy this demand [4]. In 2012, fossil fuels (oil, gas, coal) comprised more than 80% of the world's primary energy supply (Figure 1:1), followed by biomass (10%, much of it simple deforestation [5]) and nuclear fission (4.8%) – all renewables combined only accounted for 3.5% [6].

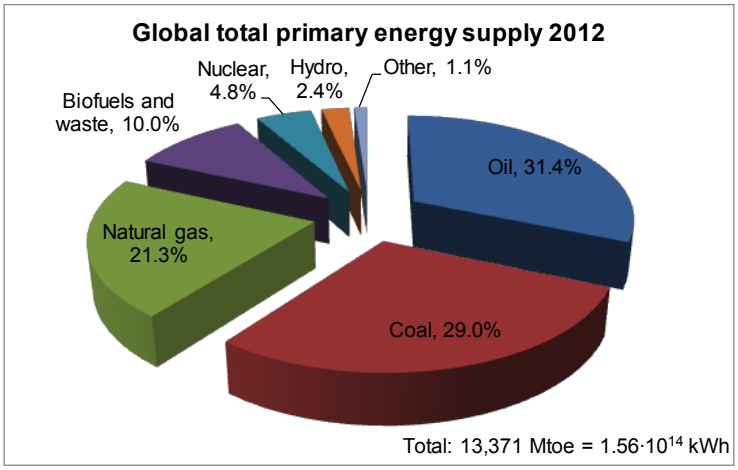


Figure 1:1 World total primary energy supply 2012, data taken from reference [6]. Peat and oil shale are aggregated with coal, 'other' includes geothermal, solar, wind, heat etc. Mtoe = million tons of oil equivalent.

Although fossil fuels sources are dwindling, problems and challenges do not arise from availability: projections estimate the global oil resources to 50 – 150 years, natural gas to 200 – 600 years, and coal to almost 200 years [4]. Rather, it is the effects caused by releasing ever more amounts of anthropogenic carbon dioxide into the atmosphere when fossil fuels are burned. The existence of climate change and global warming caused by increasing atmospheric CO_2 levels is now widely accepted among the scientific community [7,8], albeit less so in the general public. According to Thomas [4], to combat global warming, it is of vital importance, amongst other things, to decrease the liberation of CO_2 into the atmosphere

to a minimum, seek new ways to harvest and convert CO_2 into useful products, pursue existing and develop new ways of implementing the principles of green chemistry and clean technology including the development of a hydrogen economy, and evolve and extend new ways of utilising renewable sources of energy. Sunlight is by far the most abundant of all carbon-neutral energy sources and therefore constitutes the most viable option to address the latter challenge on a global scale. More energy from sunlight strikes the Earth in one hour (1.19×10^{14} kWh) than all the energy currently consumed on the planet in one year (1.14×10^{14} kWh) [1].

Solar electricity (photovoltaics, PV) is an established technology with commercialised silicon-cells obtaining solar conversion efficiencies > 20% [9]. Solar cells are familiar in society as artificial, engineered devices that utilise sunlight and convert its energy into electricity. Although variations of this approach are widely used nowadays, for example on house roofs, electricity generally cannot be easily stored: cost-effective and efficient large-scale energy storage systems that can buffer the intermittency of solar-electricity generation are not yet available. Moreover, solar energy could and should be converted directly into chemical energy, *i.e.* a portable fuel such as hydrocarbon(s) or hydrogen, that can be stored, used when needed, and is suitable for powering transport. The direct conversion of sunlight into fuels, *e.g.* using a photoelectrochemical cell, is known as artificial photosynthesis, because it mimics the action of green plants. Defined most loosely, artificial photosynthesis means using solar energy to make fuels *in vitro*, *i.e.* without a living organism.

Artificial photosynthesis research seeks to develop robust synthetic systems, inspired by Nature's design principles, for the direct conversion of CO_2 and water to fuels, *e.g.* methanol, hydrogen, or hydrocarbons ('solar fuels'), or valued organic chemicals ('solar chemicals'). Whereas solar fuels have the potential to, ultimately, 'power the planet', solar

chemicals may one day replace the myriad chemicals currently derived from petroleum (see Figure 1:2).

Products from petroleum

Tents	Toothpaste	Combs	Motorcycle helmet	Golf bags
Crayons	Gasoline	CD's & DVD's	Caulking	Life jackets
Parachutes	Heart valves	Paint brushes	Petroleum jelly	Percolators
Telephones	Candles	Detergents	Transparent tape	Rubbing alcohol
Enamel	Trash bags	Perfumes	CD player	Tennis rackets
Pillows	House paint	TV cabinets	Faucet washers	Rubber cement
Dishes	Water pipes	Shag rugs	Antiseptics	Fishing boots
Cameras	Hand lotion	Electrician's tape	Clothesline	Vaporisers
Anaesthetic	Roller skates	Tool racks	Curtains	Balloons
Artificial turf	Surf boards	Car battery cases	Food preservatives	Sun glasses
Artificial limbs	Shampoo	Epoxy	Basketballs	Solvents
Bandages	Wheels	Paint	Soap	Diesel fuel
Dentures	Paint rollers	Mops	Vitamin capsules	Motor oil
Model cars	Shower curtains	Lipstick	Antihistamines	Bearing Grease
Folding doors	Guitar strings	Denture adhesive	Purses	Ink
Hair curlers	Luggage	Linoleum	Shoes	Floor wax
Cold cream	Aspirin	Ice cube trays	Dashboards	Ballpoint pens
Movie film	Safety glasses	Synthetic rubber	Cortisone	Football cleats
Soft contact lenses	Antifreeze	Speakers	Deodorant	Upholstery
Drinking cups	Football helmets	Plastic wood	Footballs	Sweaters
Fan belts	Awnings	Electric blankets	Putty	Boats
Car enamel	Eyeglasses	Glycerine	Dyes	Insecticides
Shaving cream	Clothes	Cassettes	Panty hose	Bicycle tires
Ammonia	Toothbrushes	Dishwasher parts	Refrigerant	Sports car bodies
Refrigerators	Ice chests	Tool boxes	Dresses	Nail polish
Golf balls	Footballs	Shoe polish	Tires	Fishing lures

Figure 1:2 A selection of the variety of products that are derived from fossil resources. Adapted from reference [4].

However, whereas solar electricity is an established technology, artificial photosynthesis is still in its infancy. Even though the goal of artificial photosynthesis has been rigorously pursued since the first report of electrochemical photolysis of water by Fujishima and Honda in 1972 [10] (using a photoelectrochemical approach based on the *n*-type semiconductor TiO_2), systems developed thus far rarely possess efficiencies above 5% (notable exceptions are given in references [11-17]). The aim is to produce devices with efficiencies greater than 10%, increasing to 20% in the longer term. A vision on how a future centred on energy provision by solar fuels could look like is depicted in Figure 1:3: provided a 'hydrogen economy' [18] will be established and the challenge of hydrogen storage solved [19,20], solar hydrogen can be used as a 'clean' transportation fuel. Alternatively, carbon-based fuels such

as methanol [21] can be used to power transport, complementing their use as feedstock in a future solar chemicals industry, where they would provide replacements for exiting petrochemicals and value-added downstream products.

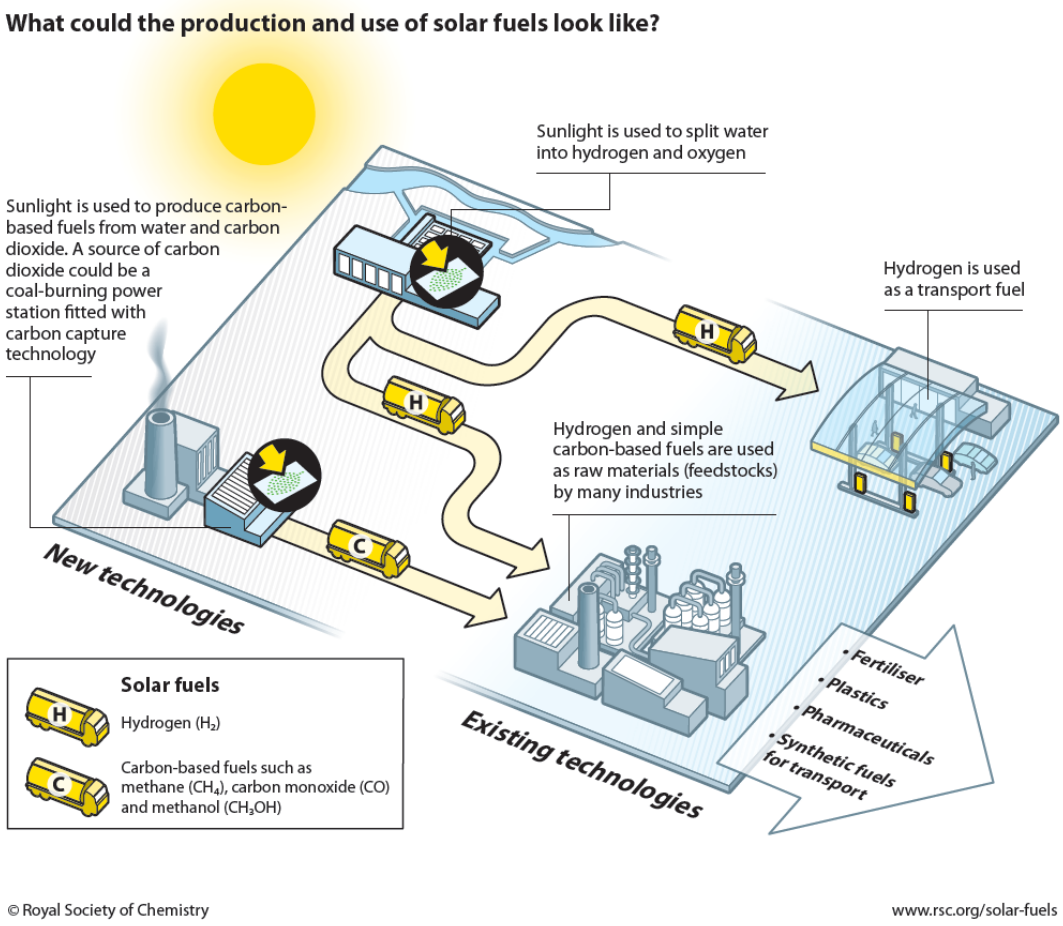


Figure 1:3 Schematic representation of possible future energy provision by solar fuels, their use as transportation fuels, and integration into existing chemical technologies. Reprinted with permission from the Royal Society of Chemistry. Copyright The Royal Society of Chemistry 2012.

1.2 Principles of photosynthetic energy conversion

1.2.1 Energy flow in biology and photosynthetic efficiencies

Biology developed the capacity to efficiently capture solar energy and use it to power the synthesis of organic molecules more than 3 billion years ago (oxygenic photosynthesis appeared on our planet approximately 2.5 bn years ago [22]); today, photosynthesis produces more than 100 billion tons of dry biomass annually [23]. All fossil fuels burned in our time, *i.e.* oil, gas, and coal, were provided by photosynthesis with energy originally derived from sunlight [24]. A general understanding of how Nature uses photosynthesis to convert sunlight into chemical energy is needed to identify the key components chemists have to mimic in their pursuit to devise efficient artificial photosynthetic systems.

Biological energy flow is schematically depicted in Figure 1:4 [22,23,25]. The resources needed for photosynthetic energy conversion, water, sunlight, and carbon dioxide, are of almost unlimited abundance. As illustrated in Figure 1:4, water is split into oxygen and hydrogen (equivalents) in the photosynthetic light reactions – O_2 is released into the atmosphere whereas 'hydrogen' is combined with carbon dioxide to form sugars and other organic matter [22] (the immediate end product being the monosaccharide D-glucose [26]). Combustion of biomass and fossil fuels originating from photosynthesis (or metabolisation of organic molecules that constitute food by the process of respiration, *i.e. in vivo* oxidation) leads to recombination of the stored hydrogen equivalents with oxygen, thereby completing the cycle. From an energetic point of view, the synthesis of organic molecules represents a way of storing hydrogen and therefore storing solar energy in the form of chemical bonds [22].

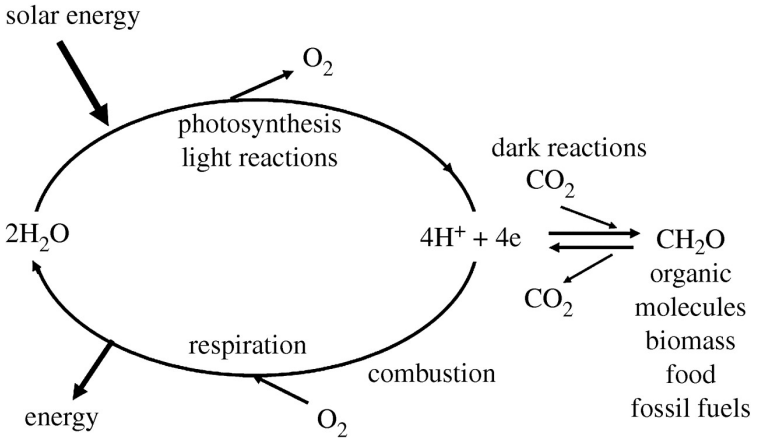


Figure 1:4 Diagram depicting the flow of energy in biology [22,23,25]. Solar energy is used by photosynthesis to oxidise water to oxygen and hydrogen equivalents, which are stored in the form of organic molecules such as glucose. Upon combustion or metabolisation, energy is released while oxygen is consumed. Reprinted with permission from reference [22]. Copyright 2009 The Royal Society of Chemistry.

A maximum efficiency for the conversion of light to stored chemical energy (dry carbon matter) of approximately 5% has been calculated [23,26], a value that is rarely reached due to several loss mechanisms, illustrated in Figure 1:5. The net efficiency of photosynthesis averaged over Earth's surface (both land and oceans) is ~0.15%; for modern food crops energy storage efficiencies of 0.5 – 1.0% are typical, and only short-term yields can be as high as ~4% [26]. Despite these low efficiencies, about ten times the amount of the current world energy consumption is stored annually by photosynthesis and it is important to note that the imperative for any photosynthetic organism is replication, not the accretion of biomass [26]. The different loss mechanisms illustrated in Figure 1:5 make immediately apparent that an intrinsically simpler synthetic device, solely dedicated to converting solar to chemical energy *and* capable of utilising the solar spectrum to a maximum extent offers possibilities for much higher conversion efficiencies.

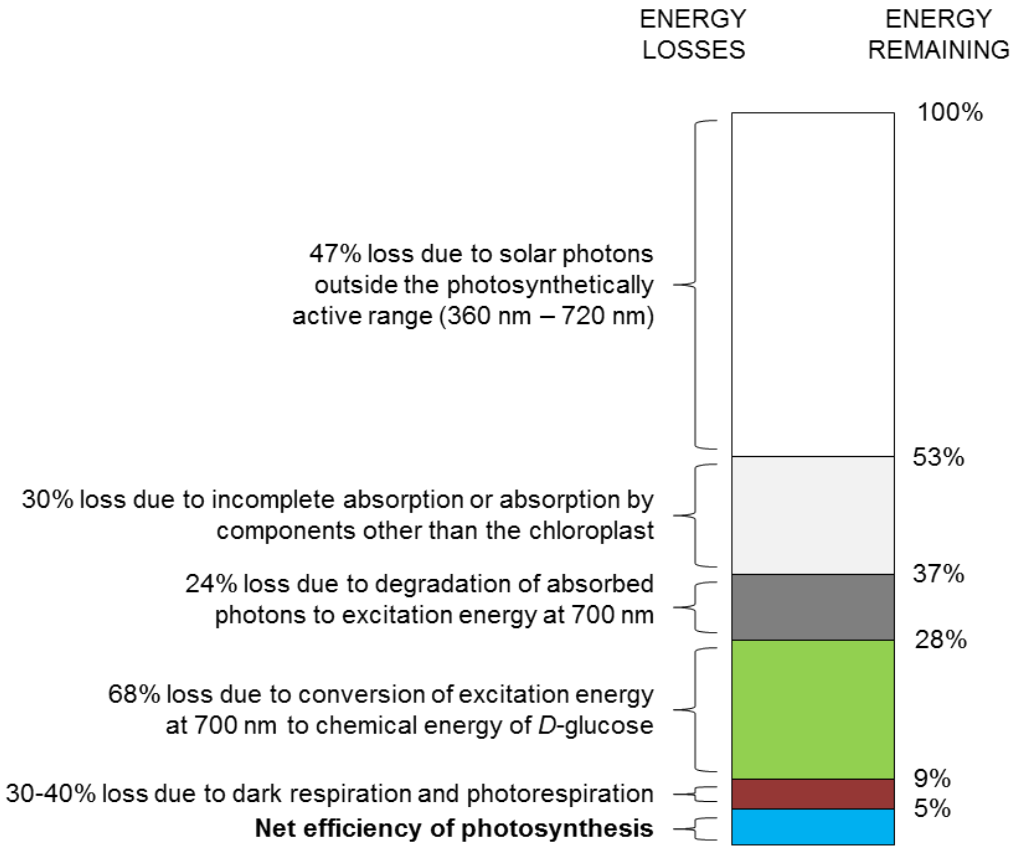


Figure 1:5 Energy losses in photosynthesis according to reference [26].

1.2.2 The photosynthetic reactions

1.2.2.1 From light-absorption to carbon dioxide fixation – a brief overview

In oxygenic photosynthetic organisms (plants, algae, and cyanobacteria), the photosynthetic apparatus involved in the light reactions is embedded in the thylakoid membrane [26]. Two reaction centres (protein complexes in which light energy is converted to electrochemical potential) termed Photosystem I (PSI) and Photosystem II (PSII) are coupled to provide sufficient energy to oxidise water and reduce CO_2 (Figure 1:6). Two photons are required to drive each electron through this system, commonly termed the 'Z-scheme'. Energy storage is accomplished by rapid separation of the initial oxidants and reductants of the primary charge separation events so as to avoid wasteful recombination reactions [26].

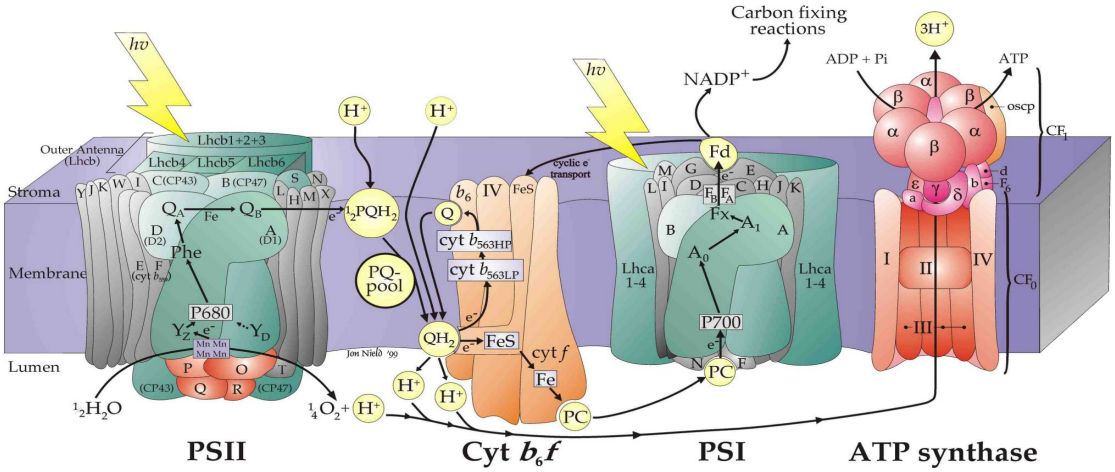


Figure 1:6 Cartoon showing the electron-proton transport chain of oxygenic photosynthesis in the thylakoid membrane. Copyright Professor James Barber, Imperial College. See main text for key abbreviations.

In all types of photosynthetic organisms, light-harvesting antenna systems funnel excitation energy rapidly to the respective reaction centre [27,28] through Förster resonance energy transfer on a sub-nanosecond time domain. The overall energy transfer rates are faster than the singlet excited state lifetimes of the pigments involved, requiring these to be located in close proximity, with typical centre-to-centre distances being 10 – 15 Å [26]. Approximately 250 pigments service a reaction centre in plants and algae; the main molecules bound to light-harvesting proteins are chlorophyll *a*, chlorophyll *b*, and carotenoids [26].

Once excitation energy arrives at the reaction centre from the light-harvesting system, primary charge separation occurs, followed by secondary electron flow to a terminal electron acceptor, ferredoxin (Fd) in PSI and quinone (Q_B) in PSII (see Figure 1:6) [26]. As mentioned above, in oxygenic photosynthetic organisms the two photosystems work together to oxidise water and reduce ferredoxin; two photons are needed to drive one electron from water to Fd.

PSI and PSII are coupled by cytochrome (Cyt) b_6f, which acts as a plastoquinol-plastocyanin oxidoreductase and facilitates the maintenance of the electrochemical potential

gradient of protons across the thylakoid membrane needed to convert ADP to ATP [26]. Reduced ferredoxin is used to convert $NADP^+$ to NADPH, which, together with ATP, is required to convert CO_2 to carbohydrates.

Carbon dioxide fixation takes place separately from the light-driven reactions in the stroma or cytoplasm [26]. Photosynthetic organisms can carry out the required transformational sequences in the dark; hence, the processes of carbohydrate formation are often referred to as the 'dark' reactions. The most common pathway of photosynthetic carbon assimilation is the C_3 or reductive pentose cycle, which operates in algae and most plants [26]. Central to this sequence is the Calvin cycle, the complex metabolic pathway by which plants incorporate CO_2 as carbohydrates [29]. In short, carboxylation of the CO_2 acceptor ribulose-1,5-biphosphate (RuBP), catalysed by the enzyme RuBisCO (ribulose-1,5-biphosphate carboxylase–oxygenase), is followed by reduction of the primary product to a 3-carbon sugar phosphate and regeneration of RuBP [30].

When comparing the reversible potential for water splitting into hydrogen and oxygen (eq. (1:1)) with the reversible potential for the reduction of CO_2 to carbohydrate and water (eq. (1:2)) it becomes apparent that, from an energetic standpoint, water splitting lies at the heart of photosynthetic solar energy storage [31,32]. Only a mere 0.01 eV more energy (on an electron equivalency basis) is stored in the production of carbohydrates:

$$2H_2O \rightarrow 2H_2 + O_2 \qquad \Delta G° = 1.23 \text{ eV} \qquad (1:1)$$

$$6CO_2 + 6H_2O \rightarrow C_6H_{12}O_6 + 6O_2 \qquad \Delta G° = 1.24 \text{ eV} \qquad (1:2)$$

The light-driven redox chemistry of PSII (eq. (1:3)) closely resembles the water splitting reaction described in eq. (1:2): water is oxidised to dioxygen and the reducing equivalents ('hydrogen') leave the photosystem in the form of reduced plastoquinol (Q_BH_2) [22], at an

estimated [33,34] midpoint potential (E_m (Q_BH_2/Q_B) = –0.06 V [35,36]) similar to the thermodynamic potential for H^+/H_2 interconversion.

$$2H_2O + 2Q_B + 4h\nu + 4H^+_{Stroma} \rightarrow 2Q_BH_2 + 4H^+_{Lumen} + O_2 \quad (1:3)$$

The reaction described in eq. (1:3) is coupled to acidification of the lumen and alkalisation of the stroma [37] (see Figure 1:6). Because of the important similarities between eq. (1:2) and eq. (1:3), the next section will cover the processes occurring in PSII in more detail.

1.2.2.2 Water splitting by Photosystem II

Figure 1:7A depicts a cartoon representation [37] of a 1.9 Å resolution crystal structure of PSII [38]. Photosystem II is a homodimeric complex [39], the reaction centre consists of two proteins, D1 and D2, with the electron transfer processes occurring mainly on the D1-side [40]. Some of the symmetrically related D2 cofactors are non-functional, whereas others are functionally active and seem to play a role in protecting PSII against photoinduced damage [22].

As illustrated in Figure 1:7B, initial electron-hole separation occurs after excitation of the primary electron donor P680, which is composed of four chlorophylls located in close proximity (known as P_{D1}, P_{D2}, Chl_{D1}, and Chl_{D2}). In $P680^*$,[i] the excited-state electron is likely delocalised over all four chlorophyll centres, but the initial electron donation occurs from Chl_{D1} [22]. Electron transfer to the primary electron acceptor pheophytin *a* (denoted 'Phe' in Figure 1:7) occurs on the ultrafast time domain with a lifetime of approximately 3 ps; subsequent electron transfer to the intermediate, bound plastoquinone Q_A occurs within 300 ps [33,34,37,41]. The latter event, termed 'stabilisation step' [42] comes at an energetic cost in the range of 0.6 eV [43]. These two electron transfer events are followed, on the kinetic timeline, by hole injection from $P680^+$ into the redox active tyrosine Y_z, regenerating

[i] The superscript '*' commonly refers to the excited that of a molecule/group. This notation is used throughout this thesis.

the ground state of the former [42]. This step is accompanied by proton transfer to the nearby (with respect to Y_z) D1His190, resulting in the formation of a neutral tyrosine radical [42], which then oxidises the oxygen evolving cluster OEC (as described in more detail below). Finally, electron transfer from the reduced primary quinone acceptor Q_A^- to the secondary two-electron acceptor plastoquinone Q_B occurs on the μs to ms regime, mediated by a non-haem Fe centre that is ligated by four histidine ligands [22]. Once Q_B has accumulated two electrons and two protons (compare eq. (1:3)) it departs from the reaction centre *via* the hydrophobic lipid phase of the membrane and enters the electron/proton transfer chain illustrated in Figure 1:6 [22]; it is replaced by an oxidised plastoquinone molecule from the membrane-soluble plastoquinone pool [39].

Although the series of electron transfer events described above comes at a significant energetic cost (see Figure 1:7B), Nature has engineered and optimised these processes, making the quantum efficiency of charge separation approach 100% [41,44]: 'barrierless' forward electron transfer over great distances occurs at maximum rate, while destructive recombination is greatly retarded and rendered kinetically unfavourable. The theory that mathematically links the thermodynamics and kinetics of electron transfer events, developed first and foremost by Marcus, is discussed in section 2.4.

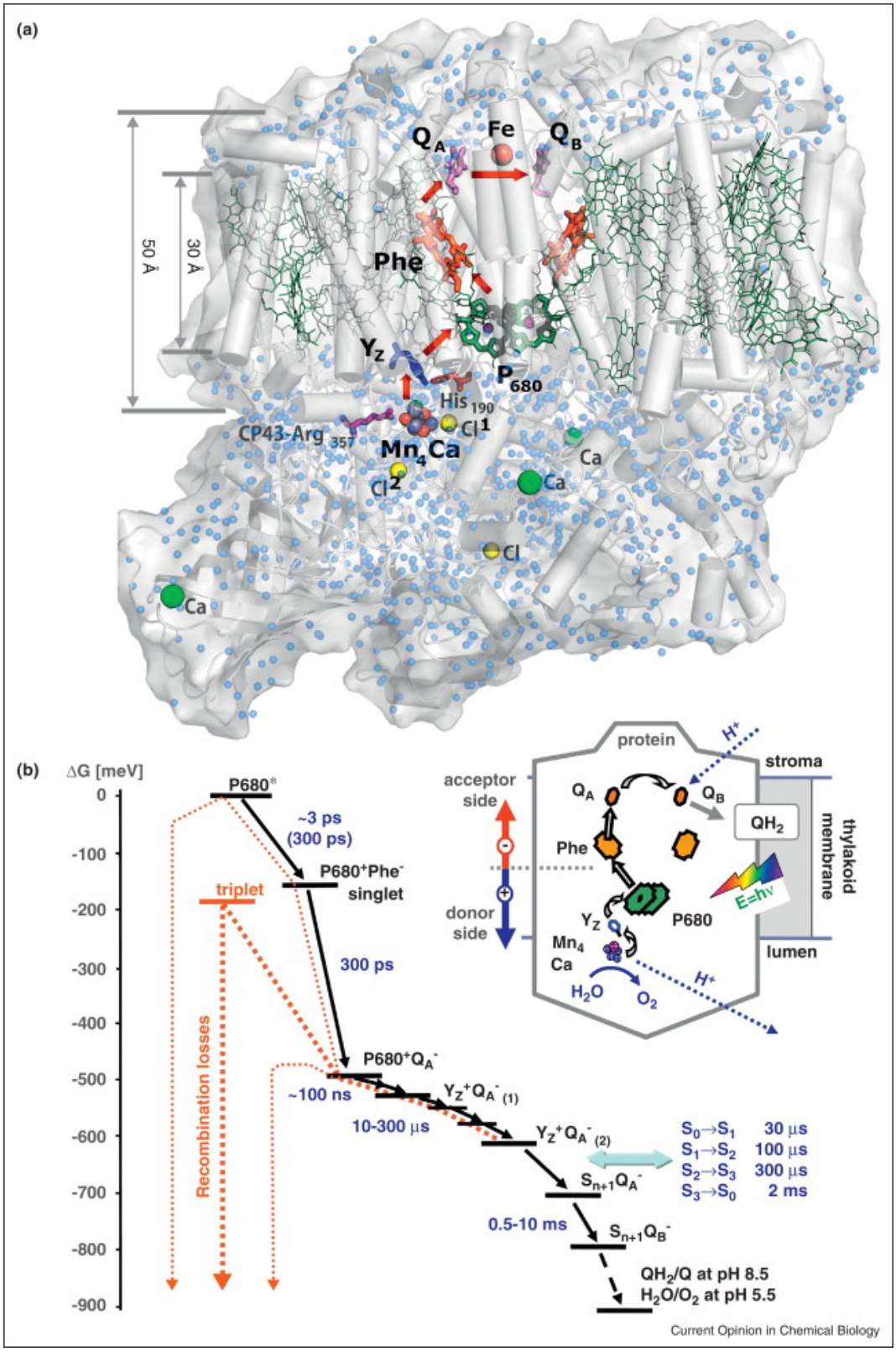


Figure 1:7 (A) Cartoon representation of Photosystem II based on a recent 1.9 Å resolution crystal structure (PDB code 3ARC) [38]. The main electron transfer components and the OEC are highlighted. (B) Schematic illustration of kinetic and thermodynamic parameters of the charge-separation events in PSII. Key abbreviations are defined in the main text. Reprinted with permission from reference [37]. Copyright 2012 Elsevier.

The processes in Figure 1:7 that govern the splitting/oxidation of water to dioxygen occur in the OEC, located off-centre towards the D1 side of the core reaction centre complex of PSII [29]. To achieve O_2 evolution, a catalyst must survive the production of very electrophilic and highly oxidising intermediates, which seems at first incompatible with organic chemistry. Biology has indeed adopted a cofactor that is 'mineral-like' but housed in a subunit that is regularly replaced to offset oxidative damage (*vide infra*). The OEC has a composition of [4MnCa-5O] (where the Mn ions are commonly designated Mn1 to Mn4 and the oxygens are referred to as O1 to O5) and serves as the 'benchmark' catalyst for O_2 evolution: it is capable of operating at neutral or near-neutral pH under ambient conditions [31], achieving turnover frequencies (TOFs) $> 100\ s^{-1}$ (the hypothetical maximum being *ca.* $500\ s^{-1}$ [39]) at a relatively modest overpotential, compared to synthetic analogues, of approximately 400 mV [36]. The [4MnCa-5O] complex self-assembles by an oxidative mechanism [45] involving the photooxidation of Mn(II) ions bound to the apo-coordination environment [46] of the PSII complex to Mn(III), with the oxidising equivalents being passed through the P680-Y_z pathway depicted in Figure 1:7 [31].

As the water splitting reaction produces toxic reactive oxygen species, the turnover number (TON) of the OEC is limited to approximately 10^6; subunit D1, which supplies most of the ligands to the [4MnCa-5O] cluster, is replaced as frequently as every 30 minutes [31,47], being damaged by the intense photocatalytic activity. This process is accompanied by the disassembly of the OEC, which reassembles upon re-insertion of D1 [31].

The crystallographic model of PSII resolved to 1.9 Å resolution firmly established the cubane motif of the OEC depicted in Figure 1:8A, proposed by Barber (apart from the position of Mn4 [40]), Dau [48], and Siegbahn [49,50], even though photoreduction of the electrophilic Mn-complex upon X-ray exposure caused significant Mn-O/N and Mn-Mn/Ca distance elongations (reviewed in reference [37]).

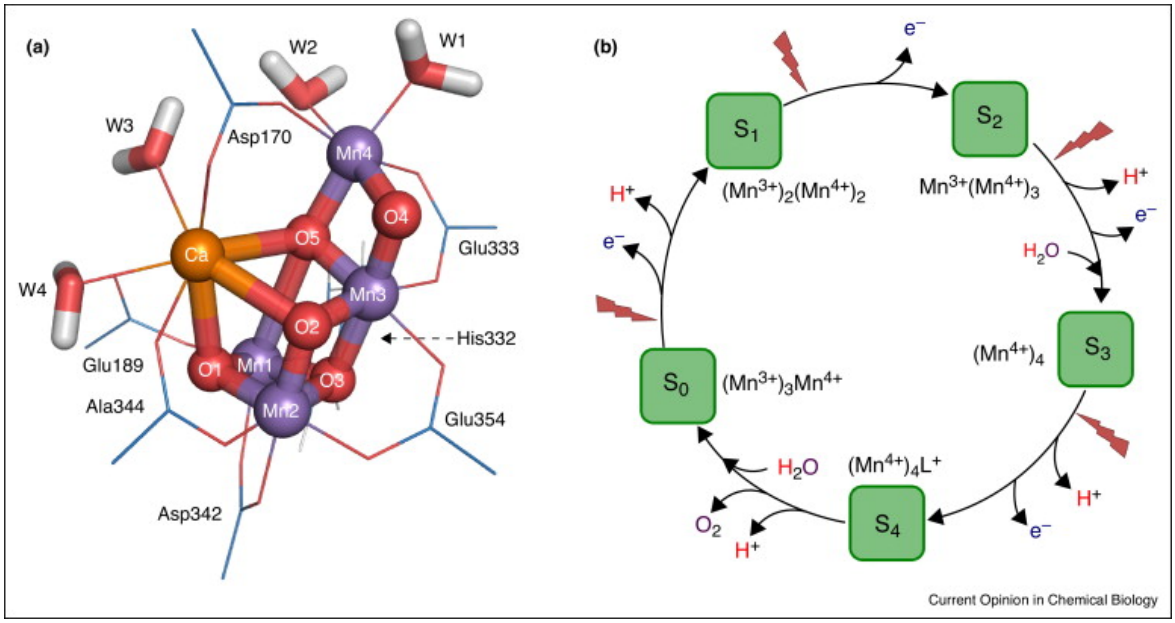


Figure 1:8 (A) Structural representation of the OEC and coordinating residues according to the crystal structure presented by Shen *et al.* [38], computationally optimised for the dark-stable S_1 state [51]. All labelled side chains apart from Glu354 belong to the D1 protein. Abbreviations are defined in the main text. (B) Sequential steps leading to O_2 formation according to Kok [52]: electrons and protons are released in an alternating pattern, starting from the S_1 state, until O_2 release spontaneously occurs in the S_4 state. Reprinted with permission from reference [39]. Copyright 2015 Elsevier.

As established by Kok [52], the OEC undergoes a series of five different redox states known as S_0 to S_4 (see Figure 1:8B), which represent successively more oxidised forms [29]. According to this model, the system advances through the cycle by single electron/proton transfer steps, each following excitation of P680, until O_2 is spontaneously, *i.e.* within 1 ms [53], released upon formation of the transient S_4 state. In the dark, S_2 and S_3 decay back to the dark-stable S_1 state, meaning approximately three-fourths of the OEC appear to be in the S_1 state, with one-fourth being in state S_0 (S_4 is unstable and occurs only transiently) [29].

Whilst the Kok cycle formally explains the observed pattern for O_2 release, it does not provide mechanistic details on how O–O bond formation occurs. Although the precise mechanism is still under debate [36,37,39,54,55], a more detailed picture is emerging thanks to recent progress from both experimentalists and theoreticians. Two main, competing mechanistic proposals have evolved over the last one and a half decades: Brudvig and co-

workers put forward a mechanism in which O_2 formation occurs by nucleophilic attack of a Ca-bound water molecule on a highly electrophilic Mn(V)-oxo species at Mn4 [56,57]. In contrast, a radical coupling mechanism, in which dioxygen is formed between an oxyl radical in the centre of the cluster and a Mn-bridging μ-oxo ligand, has been championed by Siegbahn [49,50,58-60].

Recently, multifrequency, multidimensional magnetic resonance spectroscopy revealed a detailed picture of the electronic configuration of the S_3 state [61], meaning that all S-states prior to O_2 release in the transiently occurring S_4 state have now been trapped at low temperatures and characterised [54,62]. As indicated in Figure 1:8B, the [4MnCa-5O] cofactor is assigned to an all-octahedral $(Mn(IV))_4$ complex, with all Mn ions being coordinatively saturated through six-fold coordination. Hence, all S-state transitions before S_4 represent Mn-centred oxidations.

Lubitz and co-workers established that this all–octahedral coordination geometry is achieved through inclusion of an additional, water-derived hydroxyl ligand at Mn1 (along the Mn4-Mn1 axis) upon one electron oxidation of S_2 [61] (see Figure 1:9). However, it remains to be determined whether this second, late binding substrate represents an additional water molecule binding from bulk solvent or a repositioned terminal oxygen ligand of Mn4 (W2 in Figure 1:8A) or Ca (W3 in Figure 1:8A). Conversely, the early binding substrate water is incorporated into the cluster *via* Ca(II) at the start of the Kok cycle, *i.e.* at S_0 [54]. Presumably, the structural flexibility the OEC shows in the S_2 state ('open' *vs.* 'closed' geometry in Figure 1:9) makes the inclusion of this additional, late binding water ligand possible. The S_3 state characterised by Lubitz *et al.* is similar to recent S_3 models proposed by Siegbahn [60], the calculations of whom suggest that the flexibility of the S_2 state is lost upon formation of the S_3 state [63], with the cluster then adopting an 'open' geometry.

Regardless of the precise identity and origin of the additional hydroxyl ligand at Mn1 in S_3, O–O bond formation most likely proceeds by coupling of the two proximal oxygens ligated to Mn1 and Mn4, as depicted in Figure 1:9 [61], in contrast to the reaction of an Mn4-oxo species with a Ca-bound water/hydroxide ligand. The final oxidation towards S_4 can then either be substrate-centred [64], generating the Mn(IV)-oxyl radical proposed by Siegbahn [50,58,60], or metal-centred, resulting in the formation of a Mn(V)-oxo species proposed by Brudvig *et al.* [56]. While such high-spin Mn(V)-O species are unknown in other biological contexts [53], a metalorganic variant has been synthesised [65]. The fact that the Mn4 and Mn1 ions carry opposite spin in S_3 [61] would, in a radical-coupling mechanism, lead to the development of opposite spin on the two substrate oxygens in the S_4 state, decreasing the barrier for O–O bond formation [50,58,60] such that it is significantly lower than for the nucleophilic attack mechanisms preferred by Brudvig and colleagues [36]. An oxo/oxyl radical coupling mechanism is also supported by substrate water exchange studies, reviewed in references [54,55,62].

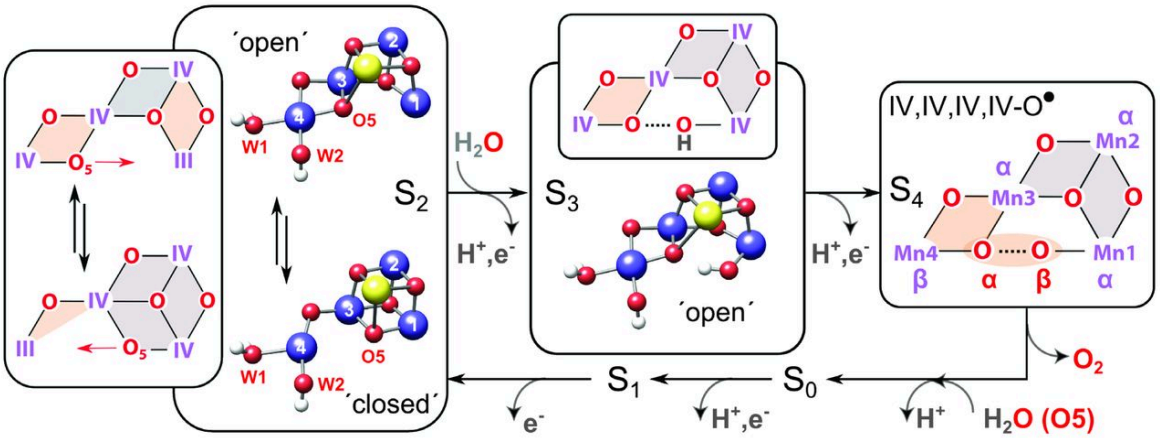


Figure 1:9 Theoretically calculated structures of the S_2 and S_3 states and proposed mechanism of O–O bond formation. The structural models are based on a recent X-ray crystal structure, as well as EXAFS and magnetic resonance data. Colour coding: Mn, purple/blue; O, red; Ca, yellow. Shaded boxes in the two-dimensional representations represent the antiferromagnetic (orange) and ferromagnetic (grey) interactions of the OEC during the Kok cycle. Antiparallel alignment of the spin on the two substrate oxygens in the proposed S_4 state may facilitate low barrier O–O bond formation. Reprinted with permission from reference [61]. Copyright 2014 The American Association for the Advancement of Science.

Although we cannot *yet* discriminate between the two putative pathways, the scientific community is rapidly advancing to close the remaining gaps in the mechanism of photosynthetic dioxygen formation. Emerging experimental techniques such as time-resolved X-ray spectroscopy and diffraction [66,67], which allow studying the structural and chemical dynamics of the OEC under functional conditions, could soon provide concluding evidence.

1.2.3 Using Photosystem II as a guide for assembling an artificial photosynthetic system

The highly engineered processes of natural photosynthesis, 'perfected' by evolution, are highlighted in section 1.2.2. Understanding the Natural system allows identification of the essential components chemists have to mimic for assembling artificial photosynthetic systems and, moreover, the processes that Nature does not carry out with sufficient efficiency. Hence, there is room for improvement, as discussed below.

First, despite the complexity and intricacy of photosynthetic organisms, biology has no difficulty in constructing these in rapid and reliable stages by 'polymerisation' and *self-assembly* processes that follow a blueprint. Hence, the problem of short-lived activities can be compensated by the replacement of worn-out parts, such as *catalyst repair* of the OEC described in section 1.2.2.2. Herein lies a lesson for artificial photosynthesis, because outside biology there is no automatic repair mechanism for oxidative damage: a useful synthetic oxygen evolution catalyst must therefore be stabilised under oxidising conditions and avoid organic ligands.

Second, the photosynthetic reaction centres are not only able to efficiently generate free charge carriers (by utilisation of low-energy near-infrared photons), but, crucially, can achieve *spatial electron-hole separation across long-distances*, with carefully tuned redox potentials so as to minimise energy loss as heat.

Third, even a reaction as thermodynamically demanding as water oxidation (compare eq. (1:1)) is catalysed *with high turnover frequencies under environmental conditions*, *i.e.* by *proton-coupled electron transfer catalysis* using earth-abundant elements at (near) neutral pH, ambient pressure and temperature, and with minimal driving force (overpotential). An important feature, identified by Lubitz *et al.* [61], could be the ability of the OEC to incorporate the second substrate water late in the catalytic cycle in a concerted process coupled to S_2 oxidation, to avoid slow, two-electron reactivity. Replicating these features constitutes a grand challenge for the synthetic community.

However, the natural photosynthetic apparatus (Figure 1:6) imposes certain limitations an artificial system needs to address and overcome. First and foremost, these are the complexity of the photosynthetic organism and the resulting efficiency limitations. An engineered device has to be intrinsically simpler in design, with its sole purpose being the conversion of solar energy to chemical molecules. Further, even a process as highly optimised as photosynthesis suffers from some form of energy-mismatch, *i.e.* the limited ability to reconcile single-photon charge-generation with two types of multi-electron catalysis – the four-electron chemistry of water oxidation and two-electron 'hydrogen' formation. While the OEC has a hypothetical maximum TOF of approximately 500 s^{-1}, the observed turnover rate of PSII is $25 - 88\ O_2\ s^{-1}$, with kinetic limitations arising mainly from slow plastoquinol (H_2Q_B) exchange [39].

To summarise, a future artificial system has to be made from robust materials comprising earth-abundant elements, using inexpensive and scalable processes. Independent of its design architecture, it must contain light-absorbers that can utilise the electromagnetic spectrum to a maximum extent, even 1000 nm infrared light contains enough energy to effect water splitting. Further essential components include charge-separators such as membranes that prevent recombination and back reactions, and multi-electron catalysts for both water

oxidation and fuel-formation that can keep up with the solar-flux, have the ability to synchronise proton and electron transfer to avoid high-energy intermediates, operate at the limit of reversibility and do not kinetically limit the overall process, and, last but not least, work under benign conditions.

These restrictions make apparent that an artificial photosynthetic system will have to *functionally* mimic natural photosynthesis, not *structurally*. One ought to remember that, as Blankenship puts it [29], "although both airplanes and birds are devices that fly, they work in very different ways. Yet, they must obey the same laws of physics. If birds and other flying creatures did not exist, it is unlikely that people would have ever invented airplanes, as the idea would simply have been too far outside of the realm of possibility. The existence of natural photosynthetic systems provides the inspiration and the conceptual framework for artificial photosynthetic devices, even if the details of the implementation are entirely different in the two systems."

1.3 The individual components of artificial photosynthetic systems

1.3.1 Light-absorption and charge-separation

1.3.1.1 General considerations

Independent of the type of light-harvester employed (*e.g.* molecular dye or semiconductor), optimal electronic coupling to the respective, ideally reversible and highly efficient multi-electron catalyst for oxygen evolution and fuel-formation needs to be ensured. Properties to be enhanced are, amongst other things, wavelength and absorption efficiency, exciton propagation and charge separation, and the lifetime(s) of the charge-separated state(s).

1.3.1.2 Molecular dyes

Building on the principles of photosynthetic light-absorption and charge-separation, much effort has been put into mimicking naturally occurring antenna systems. Many organic or organometallic pigment architectures have been designed over the past decades, examples include tris(bipyridine)ruthenium(II) derivatives [68] or supramolecular porphyrin based systems [69,70] including the recently developed 'high-potential' porphyrins [71]. A distinct advantage of these types of molecular light-absorbers is that their (excited-state) energy levels can be precisely tailored through synthetic modifications. Further, their photochemistry, particularly the kinetics of charge-separation and recombination, is well established: in addition to having large extinction coefficients in the visible region, these types of dyes possess long-lived charge-separated (triplet) states, allowing for electron/hole injection into a catalyst before recombination occurs [68,72,73]. Yet, their lack of robustness and durability, especially under the harsh conditions of water oxidation, makes molecular dyes unsuitable for incorporation into tightly integrated systems.

1.3.1.3 Metal-to-metal-charge-transfer units

An interesting approach toward visible-light capture and electron-hole separation has been developed by Frei: all-inorganic oxo-bridged binuclear metal-to-metal charge-transfer (MMCT) units [74] combine the advantage of broad absorption well into the visible region, known for molecular dyes, with the robustness of metal oxides. Integration of MMCT units into silica scaffolds allows scalability and provides opportunities for separating reduction and oxidation sites, while the redox potentials can be tailored through the use of different abundant first row transition metal centres [75]. These units, some of which show remarkable charge-separated state lifetimes (μs-regime) [76], have been employed to drive water oxidation [77,78], as well as CO_2 reduction [79,80]. Recently, MMCT units have been incorporated into an integrated system capable of reductively activating CO_2 using water as the electron source [81].

1.3.1.4 Semiconductors

Natural photosynthetic light-harvesting pigments can also be mimicked by semiconductors, *e.g.* in the form of particles (nano, micro) or (porous) electrodes. A guide to optical and electronic properties of some important semiconducting materials is shown in Figure 1:10, alongside electrochemical data (reduction potentials) for fuel- and O_2-forming reactions under neutral conditions. The investigator needs to consider both *n*- and *p*-type conductivity of materials, their carrier mobilities and band gaps, and how the conduction and valence band potentials are suited, respectively, for fuel formation or O_2 evolution. The values shown are for the bulk materials, but they still provide a good guide as to what is expected for the respective nanoparticles and highly porous structures. Attachment of external, visible-light-absorbing sensitisers such as the pigments described in section 1.3.1.2 can greatly enhance the absorptive abilities of wide-band gap materials that would otherwise be transparent in the visible region of the electromagnetic spectrum; this approach is based on the advent of dye-

sensitised solar cells (DSSCs) [82], which commonly use *n*-TiO_2 as large band gap semiconductor, modified with ruthenium polypyridyl sensitisers. The surface chemistry of the material becomes important when considering strategies for attaching sensitisers and catalysts.

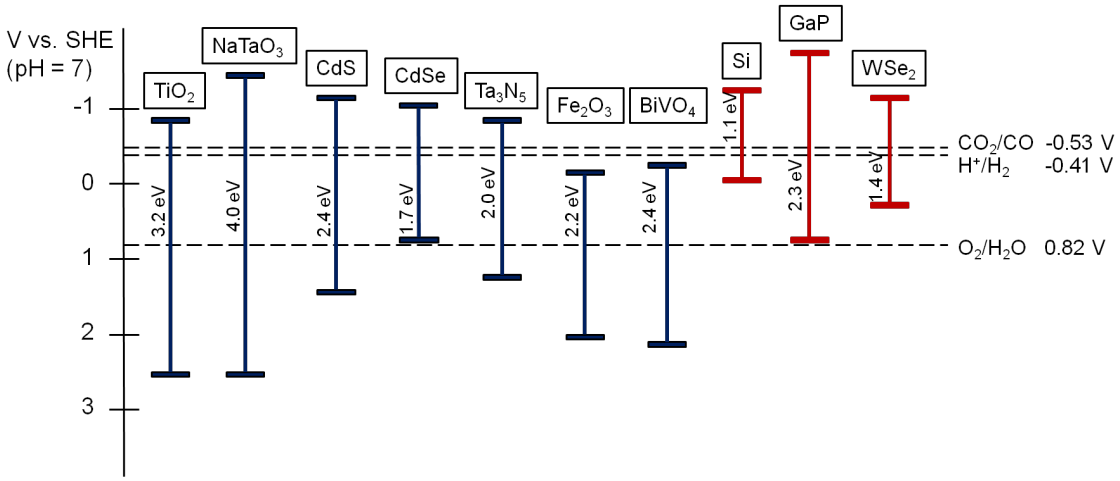


Figure 1:10 Electronic band structures of selected *n*-type (*blue*) and *p*-type (*red*) semiconductors at neutral pH, as well as reduction potentials for O_2 evolution, CO_2 reduction, and H_2 formation from water [83].

In Figure 1:10 the electronic band structures of selected *n*-type and *p*-type semiconductors are represented by blue and red lines, respectively. To be useful for artificial photosynthesis, the conduction band minimum must be more negative than the reduction potential of the fuel-forming reaction (H_2 evolution or CO_2 reduction), and the valence band maximum must be more positive than the reduction potential of the oxidation reaction (ideally O_2 evolution from water). Metal oxides such as TiO_2 satisfy these conditions, but at the cost of a wide band gap, resulting in lower utilisation of the solar spectrum. Some non-oxide materials, *e.g.* chalcogenides and nitrides, can have a smaller band gap due to the contribution of less electronegative S and N atoms to the valence band. The stability of the semiconductors in water must also be considered, as chalcogenides, among other materials, can undergo self-decomposition in water under irradiation [84].

Some materials are only suitable for half of the overall reaction, due to insufficient positioning of either the conduction band or valence band. For example, $BiVO_4$, an *n*-type material that has been used in conjunction with a variety of water oxidation electrocatalysts [85,86], is only useful for O_2 evolution due to its conduction band minimum lying more positive than the H_2 evolution potential [87]. To construct an overall water splitting system, such materials can be used with an applied bias in a photoelectrochemical set-up or in conjunction with another light-absorbing material that is able to evolve H_2 or reduce CO_2 (see section 1.4).

1.3.1.5 Photovoltaics

Due to rapid progress of the photovoltaic community [9], especially in emerging PV technologies (see Figure 1:11), the 'brute force' approach of directly using solar cells to power 'dark' electrocatalysis can also be considered. Whereas the multi-junction cells that have previously been deployed in artificial photosynthetic systems [11-15] were too intricate and costly to allow for scale-up, new technologies are on the horizon that have the potential to overcome the Shockley-Queisser efficiency limit for single band gap cells of approximately 34% [88]. These include third generation cells [89-91] and strategies such as multiple-exciton generation [92] and singlet-fission [93,94].

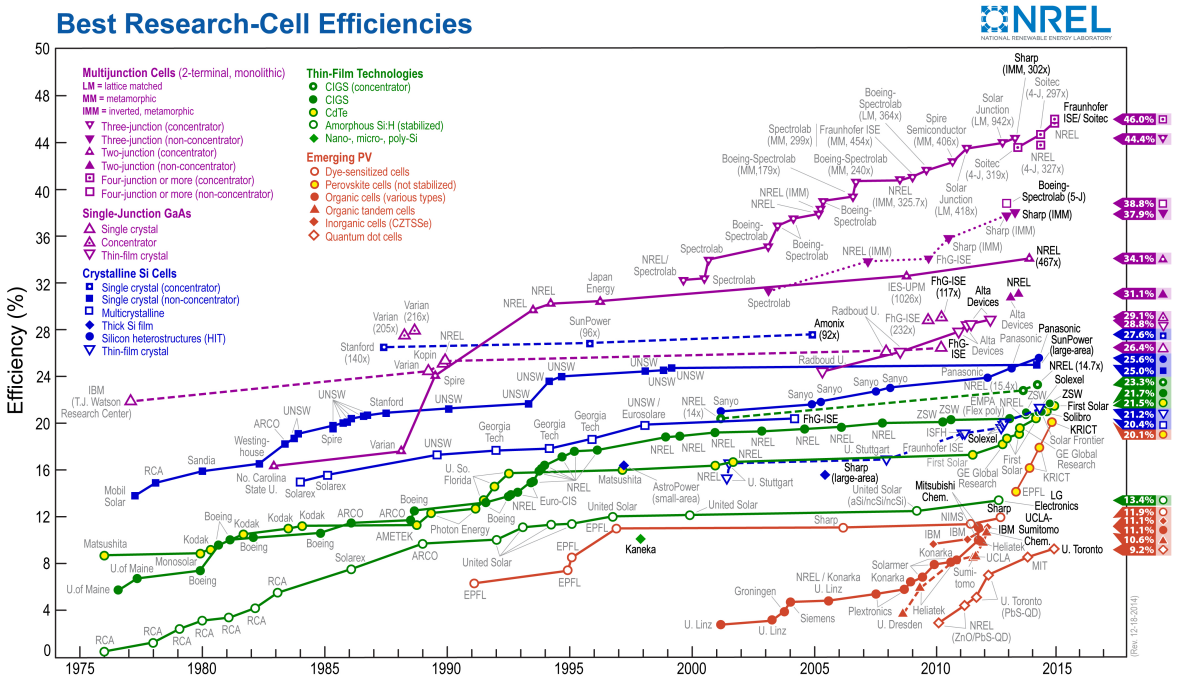


Figure 1:11 Compilation of the highest confirmed conversion efficiencies for research cells of different photovoltaic technologies, confirmed by independent, recognised test laboratories. This plot is courtesy of the National Renewable Energy Laboratory, Golden, CO, USA.

Of particular interest are organometal trihalide perovskite-based solar cells [95-97], most commonly using methylammonium lead triiodide as the light-absorber [98] (see Figure 1:12 for a structural representation). Originally employed as visible-light sensitisers for liquid-electrolyte TiO_2-based DSSCs [99], a paradigm shift occurred when Snaith established, using mesoporous Al_2O_3 instead of TiO_2 (the former being unable to accept electrons from the sensitiser), that the perovskite itself acts as the charge-transporter and must therefore have a high charge-carrier mobility [100]. Indeed, the effective diffusion length is relatively large in $CH_4NH_3PbI_3$ [101,102]; values exceeding 1 μm have been reported for a mixed halide (iodide-chloride) variant [101]. With a reported efficiency of 10.9%, this new, unoptimised type of cell already rivalled highly optimised DSSCs [103]. Subsequent to this seminal discovery, it was established that complex nanostructures are not vital to cell performance and thin films created by vapour deposition offer even higher efficiencies [104]. Values as high as 20% [105] have been realised only two years after the initial report by Snaith.

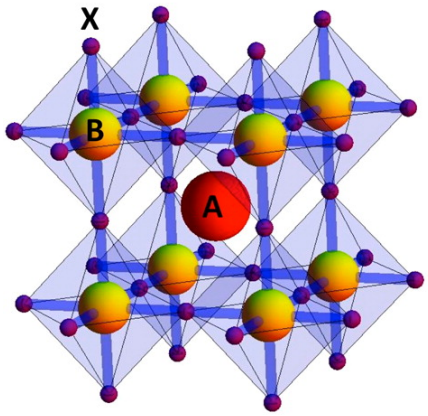


Figure 1:12 Ideal cubic structure of perovskite, with the general formula ABX_3, consisting of corner-sharing octahedra (BX_6) with the A-cation occupying a 12-fold coordination site. In $CH_3NH_3PbI_3$, A is the monovalent cation $CH_3NH_3^+$, B represents the divalent cation Pb^{2+}, and X corresponds to the monovalent halide anion I^-. Reprinted with permission from reference [106]. Copyright 2015 American Chemical Society.

Although few stability studies have been performed so far [107,108] and it is yet unclear whether these perovskite-based cells can meet the stringent norms for outdoor photovoltaic applications [97], a reported efficiency decrease of less than 20% after 500 h of operation [107] can certainly be regarded as encouraging [98]. The toxicity of lead also needs to be addressed, as $CH_3NH_3PbI_3$ converts to the known carcinogen PbI_2 under humid conditions [97]. However, less than 10,000 tons of lead would be needed for a production capacity of 1000 GW per year compared to 4 million tons used per year for lead-acid batteries [98]. The spectacular rise of perovskite cells prompted their integration into artificial photosynthetic systems and, indeed, Grätzel and colleagues realised a device with a solar-to-hydrogen (STH) efficiency of 12.3% [16], using two perovskite cells connected in electrical series. Their approach takes advantage of the high photovoltage offered by $CH_3NH_3PbI_3$; a related study using silicon photovoltaics relies on four cells connected in series [17].

1.3.2 Water oxidation catalysis

As outlined in section 1.2.2.2, the four-electron/hole chemistry of water oxidation is thermodynamically and kinetically challenging. Following billions of years of evolution, Nature has evolved the mineral-like OEC that serves as the benchmark, both in terms of achieved turnover frequencies at low driving force and its composition of earth-abundant elements.

In the synthetic world, the best contenders are transition metal oxides, apart from a few transition metal complexes that are, most notably, based on Ru (originally developed by Meyer [109,110]) or Ir (pioneered by Crabtree [111-113]). Furthermore, a bipyridine-isoquinoline ruthenium complex co-developed by Llobet and Sun exhibits a water oxidation TOF of 300 s^{-1} under acidic conditions, which is comparable to the rates of PSII *in vivo* (100-400 s^{-1}) [114]. Although the TON of 8,400 might indicate chemical stability, the compound degrades within a minute. Furthermore, these performance measures were achieved under the large driving force provided by the highly oxidising Ce(IV) ion ($E^0 = +1.76$ V *vs*. the standard hydrogen electrode, SHE) [115]. The development of other molecular water oxidation electrocatalysts has recently been reviewed by Åkermark and colleagues [116]. Several groups have achieved photocatalytic O_2 evolution catalysed by molecular catalysts interacting with/coupled to different types of light-absorber such as tris(bipyridine)ruthenium(II) sensitisers [117-119], perylene diimide derivatives [120], dye-sensitised TiO_2 [110,121-125], WO_3 [126], and $BiVO_4$ [127].

The catalytic activity and stability of several heterogeneous oxygen evolution catalysts has recently been 'benchmarked' by Jaramillo and co-workers, at a current density of 10 mA cm^{-2} that corresponds to a 10% solar-to-fuel conversion efficiency (Figure 1:13) [128]. In alkaline solution, every non-noble metal system achieved this current density at

similar operating overpotentials between 0.35 and 0.43 V. However, only iridium oxide (IrO_x) is stable under oxidative conditions in acidic solutions. It is important to note that although benchmarking experiments are easiest to carry out in acidic or basic media, a future artificial photosynthetic system will have to operate at neutral pH, ideally using waste or sea water. Iridium oxide closely approaches the efficiency and stability required for the ultimate use in integrated artificial photosynthetic systems, demonstrated both under electro- (see Figure 1:13) and photocatalytic conditions – for example, a TOF of 40 s^{-1} has been demonstrated for colloidal IrO_2 particles under a modest overpotential of 370 mV [129]. Iridium oxide has also been deposited onto semiconductor surfaces such as hematite [130] and TiO_2 [131,132] for light-driven photoelectrocatalytic water oxidation. However, iridium oxide is not a viable catalyst for future large-scale systems as it is the least abundant stable element in the upper continental earth crust [133].

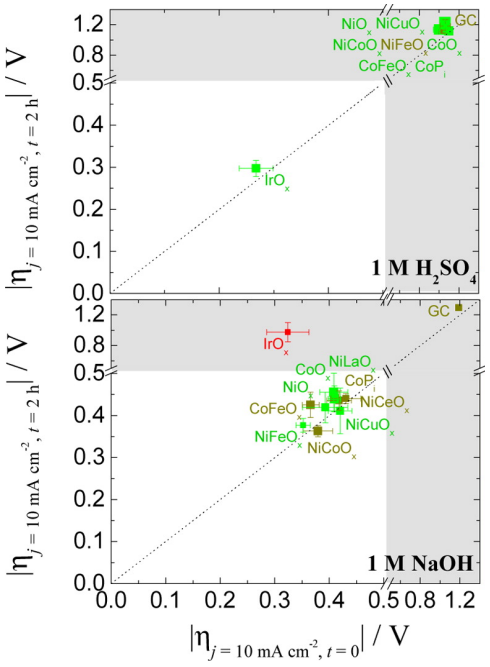


Figure 1:13 Comparison of catalytic activity, stability, and electroactive surface area for heterogeneous water oxidation catalysts in acidic and basic media. The overpotential requirement for operation at 10 mA cm^{-2} of a given catalyst after $t = 2$ h is plotted against the overpotential requirement at $t = 0$. Hence, the dashed line indicates a stable catalyst. Only catalysts with activity and stability parameters falling into the non-shaded area of the plot have sufficient activity to be considered benchmarks. Adapted with permission from reference [128]. Copyright 2013 American Chemical Society.

The good news, however, is that in the context of the ability to operate efficiently at neutral pH, first-row transition elements feature well: even the *isolated* OEC is predicted to be a good O_2-evolving catalyst [83]. To be efficient, the catalyst must be able to store four oxidising equivalents at the right potential and/or stabilise intermediates just sufficiently so that they are not too tightly bound. Further, as described in section 1.2.3, the water oxidation catalyst must either be durable and robust, or have the ability to undergo self-repair. The Co ('Co-Pi') and Ni oxide catalysts developed by Nocera and co-workers are good examples of heeding this latter requirement [134,135]. Interestingly, the amorphous cobaltate films in Co-Pi, as established by X-ray absorption spectroscopy [136,137], are nearly identical structural congeners of the PSII-OEC: both systems are of partial cubane structure with identical metal-metal (d = 2.82 Å) and metal-oxo (d = 1.89 Å) distances [31]. The discovery of this type of catalyst sparked intense research activity across the scientific community. Several groups have achieved photoelectrocatalytic water oxidation by interfacing cobalt oxide electrocatalysts with semiconductor electrodes made of ZnO [138], Si [139,140], TiO_2 [141], Fe_2O_3 [142,143], WO_3 [144], and $BiVO_4$ [145-149].

Another class of emerging heterogeneous electrocatalysts for water oxidation are metal oxyhydroxides such as FeOOH and NiOOH [150,151], recently interfaced with photoanodes made of TiO_2 [152] and $BiVO_4$ [153,154]. Choi *et al.* serially applied dual layers of both FeOOH and NiOOH on a nanoporous $BiVO_4$ photoanode, with the former reducing interface recombination at the $BiVO_4$/OEC junction and the latter creating a more favourable Helmholtz layer potential drop at the OEC/electrolyte junction (NiOOH) [155]. The resulting $BiVO_4$/FeOOH/NiOOH photoanode achieves a photocurrent density of 2.73 mA cm^{-2} square at a potential as low as 0.6 V *vs.* the reversible hydrogen electrode (RHE), even without doping the underlying $BiVO_4$ semiconductor layer.

Yet, despite progress being made in the area of water oxidation catalyst development, new materials will have to be developed to collectively address efficiency, durability, and abundance of materials. Novel experimental techniques such as pulsed-laser ablation [156,157] or photochemical metal-organic deposition [158], in combination with high throughput screening techniques [159-162], may greatly accelerate this search.

1.3.3 H_2 formation

1.3.3.1 Molecular catalysts

Platinum is well established as a reversible catalyst for hydrogen production, but it is too rare to allow it to be scaled up for global artificial photosynthesis and there is much interest in finding alternatives. Hence, extensive research activities are being carried out, most promisingly in the areas of organometallic and solid-state chemistry. Well-known contenders from the organometallic world are cobalt tetraazamacrocycles [163-167] such as cobaloximes [168,169]. Originally developed as model compounds for vitamin B_{12} [170], these species have been explored extensively as catalysts for the hydrogen evolution reaction over the past three decades. Mechanistically, Gray and colleagues established that a transiently generated Co(III)-hydride is reduced to the Co(II) hydrido complex, which, upon protonation, yields molecular hydrogen [171]. Theoretical calculations from Hammes-Schiffer [172] showed that in addition to this monometallic pathway, favoured at high acid concentrations, these complexes can also undergo bimetallic reactions in which both two Co(III)-H or two Co(II)-H complexes can react to produce H_2. It is worth noting that despite the great deal of mechanistic insight these complexes offer, there is still much room for improvement, particularly in terms of stability (TON), TOF, overpotential requirement, and solubility in water.

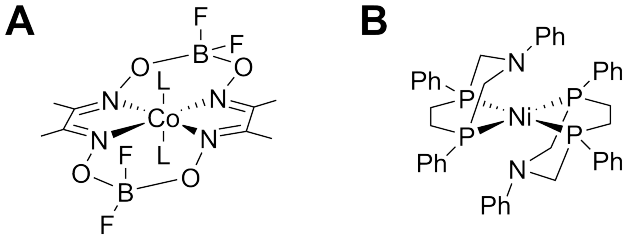


Figure 1:14 Well-known molecular hydrogen evolution catalysts. A) Cobaloxime complex (L is typically H_2O or CH_3CN) [169]. B) Nickel bisdiphosphine catalyst developed by DuBois [173].

More recently, a family of nickel bisdiphosphine electrocatalysts have been pioneered by DuBois [174,175]. These molecules are based on a nickel (II) redox platform and feature a pendant amine base in close proximity to the metal. Mechanistically, dihydrogen formation occurs by reaction of a Ni(II)-hydrido complex with a protonated amine-N. The Ni(II) hydride is proposed to be generated by initial reduction of a Ni(II) species to Ni(I) followed by protonation of the pendant amine, transfer of a second electron leading to a monoprotonated Ni(0) complex and eventual hydride formation after protonation of a second pendant amine-N [176]. Alternatively, two consecutive reductions can occur prior to the first protonation step, leading to an unprotonated Ni(0) intermediate [177].

Both turnover frequencies and overpotential requirements of this family of catalysts can be tailored through ligand modification. Through rational design, turnover frequencies of 106,000 s^{-1} have been achieved in a mixture of acetonitrile and water [173]. Derivatives modified with amino acids have been shown to catalyse H_2 production/oxidation fully reversibly at elevated temperatures in aqueous suspension, highlighting the importance of the outer coordination sphere [178]. This study, where an arginine-modified variant emerged as particularly proficient catalyst, addresses the lack of water solubility most of the DuBois-type complexes suffer from [166], albeit at the cost of synthetic complexity.

Both cobaloximes and DuBois-type catalysts have been 'heterogenised' through immobilisation on a variety of materials, including carbon nanotubes [179-181], and, for

light-driven H_2 evolution, semiconducting materials such as TiO_2 [182-185], CdSe [186], Si [187], NiO [188], and GaP [189], as well as 'soft' materials including self-assembling hydrogel scaffolds [190]. Advances in the development of hybrid photocatalysts for solar-fuel production are reviewed by Loo *et al.* [191].

1.3.3.2 Solid-state catalysts

The activities of a variety of heterogeneous hydrogen evolution catalysts have been evaluated under standardised conditions, showing that most catalysts exhibit much lower specific activity than Pt, which still serves as benchmark in both acidic and alkaline solutions [192]. However, progress is being made and several new non-precious metal electrocatalyst materials, sulphide and phosphide derivatives in particular, have emerged as promising contenders for electrochemical hydrogen evolution under harsh acidic conditions, offering nearly platinum-like catalytic performance [193].

The isostructural materials molybdenum sulphide (MoS_2) and tungsten sulphide (WS_2) [194-196] (the latter being slightly less active [166]), both well established catalysts for hydrodesulphurisation [197], are considered promising due to their high electrocatalytic activities and stabilities over a wide pH range [166]. Although the precise mechanism of H_2 formation by these layered S–M–S (M = Mo or W) materials is still unclear, Jano and colleagues recently established that terminal disulphide units are involved in the reduction of protons by amorphous molybdenum sulphide [198]. Light-driven H_2 evolution has been demonstrated with molybdenum sulphide catalysts deposited on light-absorbing *p*-Cu_2O cathodes [197,199], Si photoelectrodes protected by thin Ti [200] and MoS_2 layers [201], Si nanowire photoelectrodes [202], an organic photovoltaic cell [203], and CdSe-seeded CdS nanorods [204].

Cobalt phosphide (CoP) is another well established hydrodesulphurisation material that was recently rediscovered as an efficient HER catalyst. Being of the MnP structure, electrodes constructed from CoP nanoparticles display high stability[ii] in acid, *i.e.* no significant degradation occurs over 24 h of continuous operation at −20 mA cm^{-2}, and show an overpotential requirement of −85 mV at this cathodic current density, compared to −25 mV for the Pt control electrode [205]. An estimated per active site TOF of 0.046 s^{-1} has been reported.

Nickel-based materials have also received much attention as hydrogen evolution electrocatalysts, with Ni being a significantly more abundant element than molybdenum (which is part of MoS_2 catalysts) [206]. Most Ni-alloys are unstable in acidic solution, in contrast to two recently explored nickel phosphide phases, Ni_2P [206], another well-known hydrodesulphurisation catalyst, and Ni_5P_4 [207]. Nanostructured Ni_2P, which adopts the hexagonal Fe_2P structure, has been predicted to be a highly efficient HER catalyst by density functional theory already in 2005 [208]. Of particular interest is its (001) surface, which has exposed Ni and P sites and exhibits an 'ensemble' effect, whereby proton acceptor and hydride acceptor centres are both present to facilitate catalysis. The overpotential requirements of Ni_2P compare favourably with other non-Pt HER electrocatalysts in acidic solutions [206]. However, the catalyst electrodes are not stable in base; Ni_2P quickly degrades to Ni in 1.0 M KOH under rapidly declining HER performance. This stands in contrast to Ni_5P_4, which is stable in both acid and base. This nickel phosphide phase shows geometric activities on par with bulk platinum catalysts and superior catalytic efficiency compared to Ni_2P [207], with estimated turnover frequencies per surface atoms being 200 times greater in both acidic and basic media (3.5 s^{-1} and 0.8 s^{-1} at $\eta = 0.1$ V, respectively). However, on a per active site basis, Pt-foil still displays a two orders of magnitude higher

[ii] From a basic research perspective.

TOF in acid (assuming an atomically flat surface). Apart from one report dealing with iron phosphide nanoparticles immobilised on TiO_2 particles [209], light-driven hydrogen evolution using recently established transition metal phosphide materials has yet to be demonstrated.

1.3.3.3 Hydrogenases

Looking at nature for inspiration, hydrogenase enzymes are exceptional catalysts for H_2 production and oxidation. With turnover frequencies exceeding 10^3 s^{-1} [210], their active sites rival Pt in performance [211,212]. Both main classes of enzyme, [FeFe]- and [NiFe]-hydrogenases [210,213] (see Figure 1:15 for structural representations of the respective active sites), catalyse the two-electron interconversion of protons and dihydrogen in mechanisms involving a metal-bound hydride and a proton (bound to a nearby base), similar to the type of mechanism favoured for the molecular electrocatalysts synthesised and investigated by DuBois (described in section 1.3.3.1), which can thus be considered functional analogues of the enzymes. Yet, these molecular catalysts show inferior performance on a per catalyst active site basis when compared to hydrogenases incorporated into artificial photosynthetic systems [214].

Although [FeFe]-hydrogenases are more active H_2 producers than the [NiFe] analogues, they are inactivated irreversibly by trace O_2 [213]. The [NiFe]-hydrogenases are less sensitive to O_2 and some even function in air, but they are less active H_2 producers, partly because H_2 binds tightly and is a strong inhibitor. One exception is the subclass known as [NiFeSe]-hydrogenases: these enzymes, in which one cysteine ligand to Ni is replaced by selenocysteine, are excellent H_2 producers that retain some activity in the presence of O_2 [215]. The respective mechanisms of the two classes of hydrogenases are described in more detail in section 1.6.

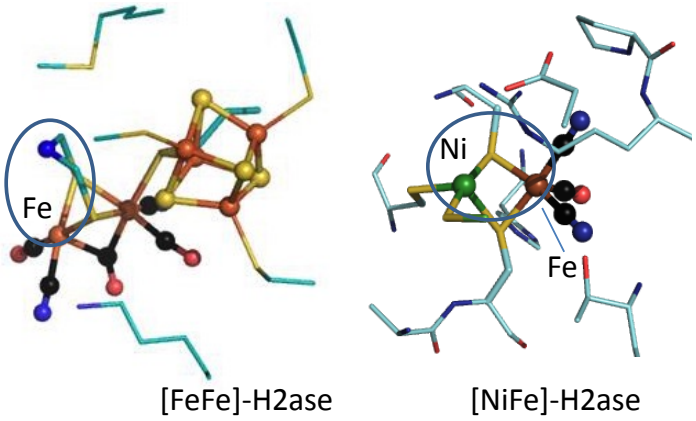


Figure 1:15 Active sites of [FeFe]-hydrogenase from *Clostridium pasteurianum* (left, PDB code 3C8Y) and [NiFe]-hydrogenase from *E. coli* (right, PDB code 3USC). Regions considered to be at the focus of the catalytic transformation are indicated by ovals. Note the structural similarity between the [FeFe]-Hydrogenase active site and the functional analogue depicted in Figure 1:14B, *i.e.* a pendant amine base placed above the reactive metal centre.

1.3.4 CO_2 reduction

1.3.4.1 General considerations on the reduction of carbon dioxide to fuels and chemicals

We established in section 1.2.2.1 that it is the water splitting chemistry of PSII that accounts for virtually all of photosynthetic energy storage; fixation of CO_2 in the photosynthetic dark reactions does not store additional energy (eqs. (1:1) – (1:2)). However, from a practical perspective, transforming CO_2 in the reduction half-reaction can be beneficial. Carbon dioxide can be reduced to liquid fuels such as methanol, which offer much higher *volumetric* energy densities than hydrogen. Such an approach would obviate the need to develop a hydrogen storage infrastructure for later use as transportation fuel [75]. Further, CO_2 could form the basis of a future solar-chemicals industry, in which drop-in replacements for existing petrochemicals and other value-added products derived from petroleum (compare Figure 1:2) will be made by artificial photosynthesis, for example *via* formation of methanol as a C1 intermediate [216].

Multi-electron catalysts are required to achieve the reduction of CO_2 to liquid fuels/chemicals. Carbon dioxide is a difficult molecule to activate: the HOMO is localised on the two O-atoms and the linear molecule must bend and convert to a C-bonded carbonyl. The large reorganisation energy required to form this bent 1-electron reduced radical anion $CO_2^{\bullet-}$ is reflected in its thermodynamic potential of –1.9 V (eq. (1:4)) [217].

From a thermodynamic perspective, the most demanding step in multi-electron reduction of CO_2 is its initial two-electron reduction to CO or formate intermediates [218,219] (eqs. (1:5) – (1:6)). Indeed, provided upon the availability of suitable reversible catalysts, the thermodynamic potentials for HCHO, CH_3OH and CH_4 formation [218,219] from CO_2 given in eqs. (1:7) – (1:9) suggest that coupled multi-electron, multi-proton steps can be performed at less cathodic potentials [220] (the standard potentials summarised in eqs. (1:4) – (1:9) are referenced to pH 7 under aqueous conditions, 1 atm gas pressure, 25 °C, and 1 M solutes).

$$CO_2 + e^- \rightarrow CO_2^{\bullet-} \qquad E^0 = -1.90\ \text{V} \qquad (1:4)$$

$$CO_2 + 2H^+ + 2e^- \rightarrow CO + H_2O \qquad E^0 = -0.53\ \text{V} \qquad (1:5)$$

$$CO_2 + 2H^+ + 2e^- \rightarrow HCOOH \qquad E^0 = -0.61\ \text{V} \qquad (1:6)$$

$$CO_2 + 4H^+ + 4e^- \rightarrow HCHO + H_2O \qquad E^0 = -0.48\ \text{V} \qquad (1:7)$$

$$CO_2 + 6H^+ + 6e^- \rightarrow CH_3OH + H_2O \qquad E^0 = -0.38\ \text{V} \qquad (1:8)$$

$$CO_2 + 8H^+ + 8e^- \rightarrow CH_4 + 2H_2O \qquad E^0 = -0.24\ \text{V} \qquad (1:9)$$

Numerous synthetic homogeneous and heterogeneous electrocatalysts have been developed and interfaced with light-absorbers to achieve photodriven reduction of CO_2 [219,221]. However, progress in this field has been quite limited compared to other areas of artificial photosynthesis research [222] and most synthetic catalysts do not afford reactivity beyond the two-electron reduction of CO_2 to CO or formate. Nonetheless, it is important to note that although an ultimate goal of artificial photosynthesis is to produce liquid fuels (such as

methanol) directly, both CO and HCOOH are valuable feedstock in industrial processes, *e.g.* the Fischer-Tropsch process that converts carbon monoxide and hydrogen into hydrocarbons [223].

1.3.4.2 Heterogeneous electrocatalysts for CO_2 reduction

Most heterogeneous electrocatalysts for CO_2 reduction suffer from high overpotential requirements and low faradaic efficiencies that result in product mixtures [224,225], a direct consequence of the multiple reduction pathways illustrated in eqs. (1:4) – (1:9).

Much research has focused on using transition metals as catalysts, which have been shown to produce a variety of CO_2 reduction products [222]. However, evolution of H_2 is the preferred pathway at most of them [226]. Copper, for which CO_2 reduction has been first demonstrated in 1985 [227], has been extensively investigated [228-231]. Even so, large overpotentials are typically required and up to 16 different CO_2 reduction products (C1-C3) have been identified [232]. Yet, despite its lack of specificity, Cu is the only known transition metal capable of reducing CO_2 in multiple reducing steps to yield carbon-based chemicals such as methane, ethylene, etc. [222,232]. Other transition metal electrodes and nanostructures [233] that show activity towards CO_2 activation, with varying selectivity, are Au [234-236] and Ag [237-239], both selective and active for CO [236], as well as Sn, which shows pronounced activity towards the formation of formate [226,240,241]. However, all of these examples suffer from significant overpotential requirements.

In a density functional theory study, Nørskov examined the mechanism of CO_2 reduction on metal surfaces, considering the following steps for the two electron reduction to CO [236]:

$$CO_2(g) + * + H^+(aq) + e^- \leftrightarrow COOH* \quad (1:10)$$

$$COOH* + H^+(aq) + e^- \leftrightarrow CO* + H_2O(l) \quad (1:11)$$

$$CO^* \leftrightarrow CO(g) + * \quad (1:12)$$

In eqs. (1:10) – (1:12), COOH* and CO* denote adsorbed intermediates and * refers to a free step site. Figure 1:16 shows the calculated free energy diagram for CO_2 reduction through this scheme on Au(211) and Pt(211) surfaces. On Au(211), the free energies of the initial and final states are the same and the standard free energy of CO desorption is close to zero, but initial formation of adsorbed COOH* is associated with a high increase in free energy at the reversible potential. Therefore, increasing the driving force makes COOH formation easier and results in increased CO production. In contrast, for Pt(211), COOH* is very stable and CO_2 activation will be exergonic. However, desorption of CO is associated with a large change in free energy, but this 'non-electrochemical' step does not affect the free energy directly. Comparing the reaction pathways at the two different metals, Nørskov *et al.* suggest accordingly that improved CO evolution activity could be obtained by finding a catalyst where the binding of COOH is stronger than on Au(211) or where the binding of CO is weaker than on Pt(211) [236].

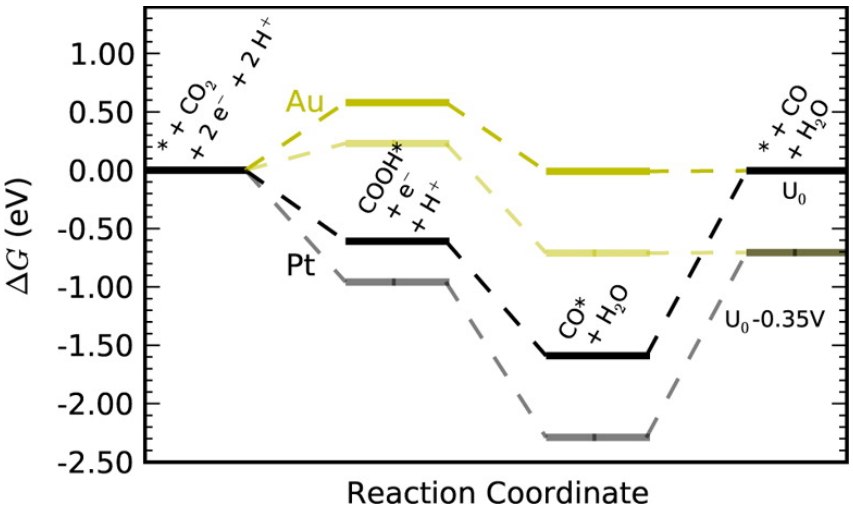


Figure 1:16 Free energy diagrams for CO_2 electroreduction to CO on Au(211) and Pt(211) at the reversible potential, denoted U_0, and at an overpotential of 0.35 V. Reprinted with permission from reference [236]. Copyright 2013 American Chemical Society.

In an interesting recent development, Koper and co-workers devised a system capable of *reversibly* interconverting CO_2 and formate (**Figure 1:17**) [242] by electrodepositing palladium onto a polycrystalline platinum substrate. The authors hypothesised that a Pd-Pt alloy electrode is formed, which slows down CO poisoning compared to bare Pd. Further, it is assumed that the alloy is covered by a thin layer of Pd, the effect of which is to suppress hydrogen adsorption. However, the activity decreases significantly over the course of the 20 voltammorgams depicted in **Figure 1:17**; this decay is attributed to electrode-poisoning by CO, which is also formed in the potential window around the reversible potential for HCOOH formation/oxidation. Simultaneous evolution of hydrogen during CO_2 reduction is also detected. Hence, despite the important demonstration of reversible behaviour for CO_2/CO interconversion, the system is severely limited by both lack of stability and selectivity.

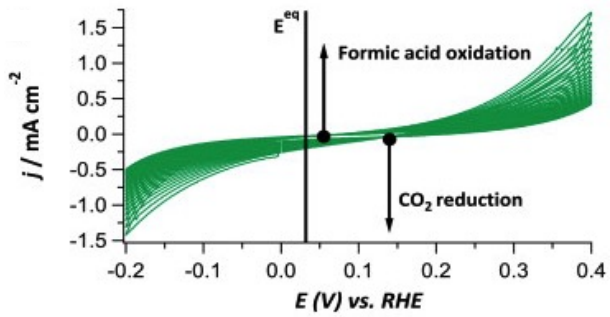


Figure 1:17 Cyclic voltammograms (20 consecutive cycles) showing reversible formic acid oxidation and CO_2 reduction by a Pd-Pt electrode. Experimental conditions: scan rate = 50 mV s^{-1}, 0.2 M NaH_2PO_4/0.2 M Na_2HPO_4 buffer (pH 6.7, saturated with CO_2), 25 mM NaHCOO. Reprinted with permission from reference [242]. Copyright 2015 Elsevier.

Over the past decade, the transition metal catalysts described above have been interfaced with light absorbing materials for photoinduced CO_2 reduction. Notable examples include Cu-sensitised *p*-Si nanowires [243], photocatalytic CO_2 reduction by Cu-Au nanoalloys supported on TiO_2 [244], as well as Cu-nanoparticle decorated graphene oxide [245]. Several recent review articles [219,246-248] provide comprehensive overviews on approaches

towards photocatalytic CO_2 reduction by heterogeneous transition metal catalyst/semiconductor light-absorber composites.

1.3.4.3 Molecular CO_2 reduction catalysts

Notable organometallic CO_2 reduction electrocatalysts include Ni(II)-cyclam systems originally devised by Sauvage and co-workers [249], and Lehn's $Re(bpy)(CO)_3X$ catalysts, with X being Cl^- or Br^- [250,251]. Both classes of catalyst have been intensively studied and developed further by many research groups [218]. However, rhenium is among the least-abundant elements on Earth. A recent advance is the incorporation of an earth-abundant manganese ion as the metal centre into the bipyridyl-tricarbonyl ligand environment, which lowers the overpotential for CO_2 reduction by 0.4 V while maintaining selectivities and Faradaic efficiencies that are comparable to the rhenium analogues [252]. Both cyclam [253] and bipyridyl-carbonyl (Re and Ru) complexes have been used in systems for light-driven CO_2 reduction [254-256].

Iron tetraphenylporphyrins developed by Savéant and colleagues represent another class of molecular electrocatalysts for the conversion of CO_2 to CO that are based on earth-abundant metal ions [257]. Modification of the porphyrin-framework with *ortho*-phenol moieties results in a high local concentration of protons being available, which significantly enhances catalysis by the transiently generated iron(0) complex. Reduction of CO_2 is catalysed with an average TOF of 3500 s^{-1} over 4 h at an overpotential requirement of approximately 0.5 V, which represents a significant advance for synthetic catalysts, but still constitutes a substantial energetic cost. This catalyst has been employed to effect photocatalytic CO_2 reduction in acetonitrile (but not water), using the organic photosensitiser 9-cyanoanthracene and trimethylamine as electron donor [258].

A further, interesting approach developed by the group of Bocarsly constitutes the utilisation of the pyridinium ion as homogeneous catalyst for the six-electron reduction of CO_2 to methanol, with comparatively modest overpotentials of 200 mV being sufficient to drive the reaction [259]. Photoreduction of CO_2 using the pyridinium ion in conjunction with a *p*-GaP photocathode has also been demonstrated [260], and initial mechanistic studies suggested that the one-electron reduced pyridyl radical $PyH^{\bullet}$ acts as electron shuttle and activates CO_2 [261,262]. However, this proposal has been questioned in a recent mechanistic study conducted by Savéant [263], who calls for a more careful examination of the actual role of the pyridinium ion, as the reduction of this species in conjunction with a platinum electrode did not involve the pyridyl radical and neither methanol nor formate could be detected in preparative-scale electrolyses.

Approaches toward photo- and photoelectrocatalytic reduction of CO_2 using the molecular catalysts described in this section have recently been reviewed by the groups of Fujita [264], Loo [191], Kubiak [219], and Perutz [265].

1.3.4.4 CO_2 reduction in biology

Although they are not suitable for large-scale applications, enzymes lead the way as CO_2 reduction catalysts, meeting the criteria of minimal driving force requirement, high stability, as well as high selectivity, *i.e.* the ability to form *specific* products with high Faradaic efficiencies [222]. Similar to hydrogenases that are able to reversibly catalyse the hydrogen evolution reaction (section 1.3.3.3), certain enzymes act as reversible CO_2 reduction catalysts with unprecedented efficiency and specificity: in biology, two-electron reduction of CO_2 is catalysed by two very different types of enzymes, formate dehydrogenases and carbon monoxide dehydrogenases (Figure 1:18). Both are electroactive on conducting electrodes and set excellent benchmarks for the performance that must be possible with small molecular or surface catalysts. Through proton-coupled electron transfer (PCET), these enzymes are

capable of avoiding the high energy $CO_2^{\bullet-}$ radical intermediate in favour of the two-electron reduced species CO or HCOOH.

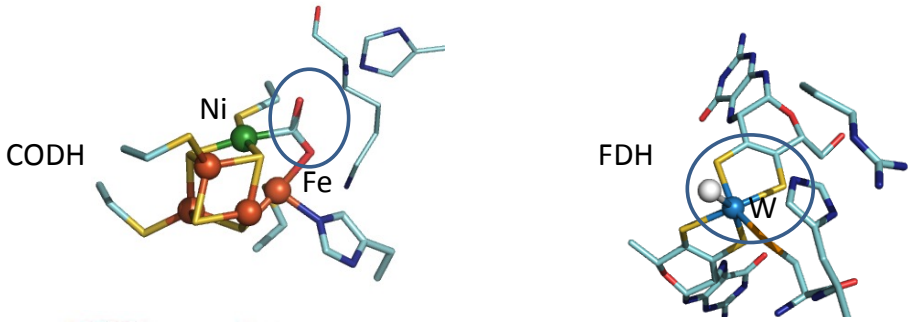


Figure 1:18 Active sites of CO dehydrogenase II (CODH) from *Carboxydothermus hydrogenoformans* (left, PDB code 3B52) and tungsten containing formate dehydrogenase from *Desulfovibrio gigas* (right, PDB code 1H0H). Regions considered to be at the focus of the catalytic transformation are indicated by ovals.

Formate dehydrogenase (FDH) was among the first enzymes to be studied in the context of artificial photosynthesis. A paper published by Parkinson and Weaver in 1984 describes how electrons from a photoexcited *p*-InP photocathode are transferred *via* methyl viologen to the enzyme, which carries out CO_2 reduction to formic acid [266]. Photogenerated electrons in the semiconductor can be produced with wavelengths of up to 900 nm. More recent work has shown that both tungsten- [267] and molybdenum-containing [268] FDH are reversible electrocatalysts when adsorbed directly on graphite electrodes, although immobilisation on semiconducting materials for photodriven CO_2 reduction has yet to be demonstrated.

Carbon monoxide dehydrogenases (CODHs) fall into two main types, aerobic and anaerobic, but it is the latter class, containing a [Ni4Fe-4S] cluster, that were established to be excellent electrocatalysts for CO_2 reduction to CO [269]. The anaerobic enzymes operate virtually reversibly, contrasting markedly with the situation for small molecular and heterogeneous catalysts described in the previous two sections. As is the case with hydrogenases, the surrounding outer-shell environment probably holds the secret to the very high activity. Evidence suggests that a bond forms between the C-atom and the Ni subsite,

which is very nucleophilic in the reduced enzyme: an O-atom is then removed (as oxide/hydroxide) by the pendant Fe in a PCET process that is exquisitely organised by the side chains of appropriately positioned residues [269,270]. Considerations regarding the mechanism of CO_2 reduction by CODH will be presented in more detail in section 1.6.

The supremacy of CODH over metal electrocatalysts inspired an interesting comparison by Nørskov and co-workers [236], who argued the importance of the active site of CODH being able to attack CO_2 at *two* atoms (Ni–C and Fe–*departing* O) simultaneously, stabilising a bound intermediate without also stabilising bound CO, in contrast to metallic surfaces. Figure 1:19 compares the calculated electrocatalytic activity towards CO_2 reduction, *i.e.* the TOF per site *vs.* applied potential, for CODH and Au(211), showing reversible behaviour for CODH and significant overpotential requirements in either direction for the Au surface.

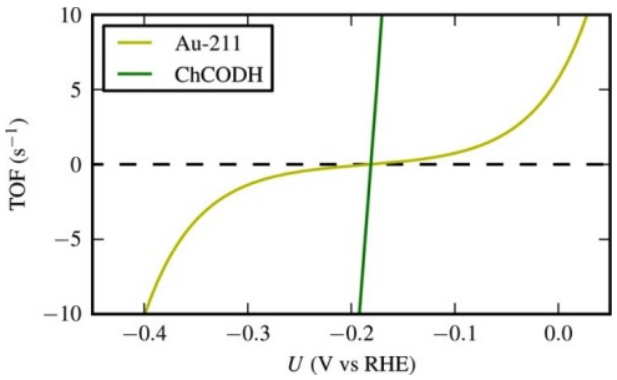


Figure 1:19 Comparison of electrocatalytic activity for CO_2/CO interconversion as a function of applied potential at a metal surface (Au(211)) and an enzyme (CODH). On CODH, the turnover changes sharply through the equilibrium potential, suggesting a reversible interconversion of CO_2 and CO, while a significant overpotential is required on Au(211). Reprinted with permission from reference [236]. Copyright 2013 American Chemical Society.

To summarise, major scientific breakthroughs are needed to make each of the different components described in section 1.3 efficient, robust, scalable, and, last but not least, composed of inexpensive and abundant materials. All these are necessary requirements for artificial photosynthesis to achieve scalability and, ultimately, commercial viability.

1.4 Strategies for integrated systems

1.4.1 Integrating the individual components

As described in section 1.3, the essential components of a solar-fuels device are a light-absorber, multi-electron electrocatalysts for water oxidation and fuel-formation, a conducting electrolyte, and a means of product separation, such as a proton conducting but gas impermeable membrane. A major challenge in integrating these different components, independent of the actual design architecture, is to achieve efficient charge transport between the different components, without losing large fractions of transient carriers in side or back reactions, or being trapped at defect sites [75]. A further inherent difficulty is the need to reconcile single-photon, charge generation events with multi-electron catalysis.

The individual components can be assembled to form integrated systems of varying intricacy. The two limiting cases, categorised by Gray according to their complexity, technological maturity, and projected manufacturing cost [271], are aqueous photocatalyst colloids and commercial photovoltaic modules connected to discrete electrolysers, with various integrated photoelectrochemical design architectures lying somewhere in-between (Figure 1:20). Some of these approaches have recently been evaluated in terms of efficiency criteria and resulting design implications [272], and from a technical and economic feasibility perspective [273-275].

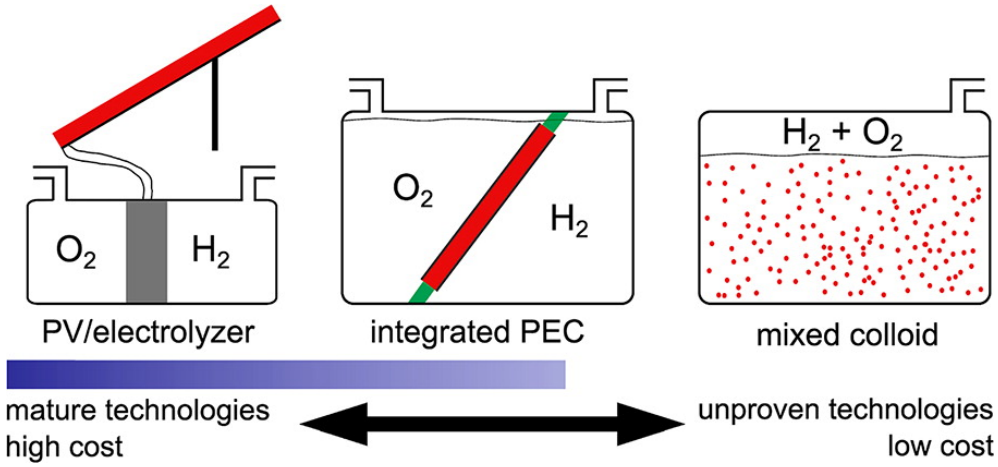


Figure 1:20 Schematic of three device architectures available for solar-driven water splitting, ordered according to their relative technological maturity and projected costs to manufacture. Reprinted with permission form reference [271]. Copyright 2013 American Chemical Society.

It is important to remember that even though individual components might be efficient, robust, and scalable, this does not imply that they can be arbitrarily combined to form viable integrated systems [271], they must be *compatible* with each other. Moreover, new challenges arise when reactions are being driven under real operating conditions by transiently generated carriers instead of half systems relying on sacrificial reagents or externally applied bias: it is now becoming a recurring theme that the electrocatalytic activities of catalysts for artificial photosynthesis observed in standard, 'dark' electrochemistry experiments are often orders of magnitude higher than the turnover frequencies observed under photo- and photoelectrochemical conditions. Although this is yet to be firmly established, it seems that the major reason for the lower rates observed in light-driven experiments is that the charge carriers are transient and there is unfavourable competition with destructive charge carrier recombination, which is thermodynamically preferred – a formidable challenge that needs to be addressed.

1.4.2 Photochemical *vs.* photoelectrochemical water splitting

1.4.2.1 Photoelectrochemical cells

The first proof-of-concept example of photoinduced water splitting was a photoelectrochemical cell (PEC) developed in 1972 by Fujishima and Honda [10]. In this system, the reactions are driven by UV light absorbed by a TiO_2 photoanode. The electrons excited into the TiO_2 conduction band are transferred through an external circuit to a 'dark' platinum cathode, where the H_2 evolution reaction takes place. Water is oxidised by high-energy holes in the TiO_2 valence band, the latter reaction being energetically costly as it proceeds *via* high-energy intermediates such as hydroxyl radicals [276].

Photoelectrochemical cells can be constructed from single *p*-type or *n*-type semiconductor materials to give single band gap devices (where the second half-reaction takes place at a dark electrode similar to the Fujishima–Honda system above) or from two semiconductors connected in series, *i.e.* forming a dual band gap device [277]. In dual band gap photoelectrochemical cells, combinations of semiconductor materials with different band gaps and complementary absorption characteristics should be employed to utilise the solar spectrum to its maximum extent, particularly to harvest low-energy photons in the near-infrared region. A dual band gap photoelectrochemical cell is depicted schematically in Figure 1:21.

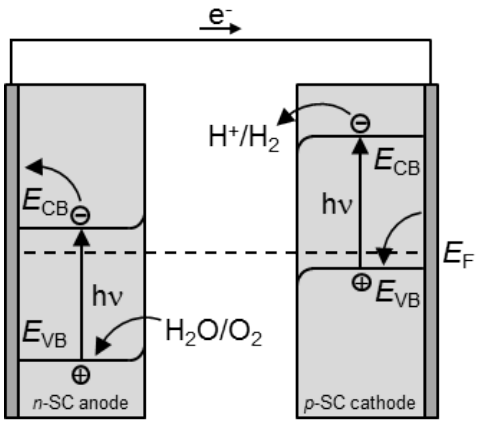


Figure 1:21 Schematic representation of a dual band gap photoelectrochemical cell for water splitting with water oxidation taking place at the *n*-type photoanode and proton reduction at the *p*-type photocathode.

In Figure 1:21, the minority carriers generated in the photoelectrodes carry out the electrochemical reactions, with charge separation being assisted by the electric fields that arise at the semiconductor/electrolyte (or semiconductor/catalyst) interface. In the case of an *n*-type semiconducting photoanode, a depletion layer prevents oxidative currents in the dark (see section 2.3 for a general description of the underlying principles). Upon illumination, the electron-hole pair is separated by the electric field of the space-charge region, resulting in a photooxidation current: electrons, the majority carriers, move through the conduction band into the bulk of the material (and to the counter electrode for fuel-formation). In the valence band the minority carriers, holes, move to the semiconductor/electrolyte interface where they drive the water oxidation reaction. *p*-Type materials show analogous behaviour, but with holes as majority carriers; they are dark anodes and photocathodes.

One of the inherent advantages of a 'wired' photoelectrochemical cell is that this design utilises fast electronic conductivities: an electronic conductor completes the circuit between the anode and the cathode by a relatively long path, but with the ionic path being as short as possible [278]. Placing the two electrodes in close proximity limits 'bottleneck' effects of the intrinsically lower ionic conductivities. Progress made on photoelectrochemical

cells for artificial photosynthesis has been reviewed by several authors [277,279-284] and notable examples of recently developed photoelectrochemical cells for artificial photosynthesis are given in references [11,12,131,243,285-300].

In ground-breaking work from 1998, Khaselev and Turner established the proof-of-principle for efficient photoelectrocatalytic water splitting using visible-light, achieving a solar-to-hydrogen efficiency of 12.4% [12]. The reported cell structure (Figure 1:22) consists of a top layer of *p*-$GaInP_2$, connected in series, *via* a tunnel junction, to a GaAs *p*/*n* bottom photovoltaic cell on a GaAs substrate. In this 'D4'-configuration ('dual-absorber – four-photons'), two-photons are required to produce one electron in the external circuit and four-photons are required for the formation of H_2. Hydrogen is produced at the semiconductor electrode and the water oxidation reaction takes place at the Pt counter electrode. However, despite proving that STH efficiencies > 10% are possible using a single integrated device, the instability of the materials (degradation under use within days) and the use of non-abundant materials make this device unsuitable for manufacturing on the scale needed for global fuel generation [75].

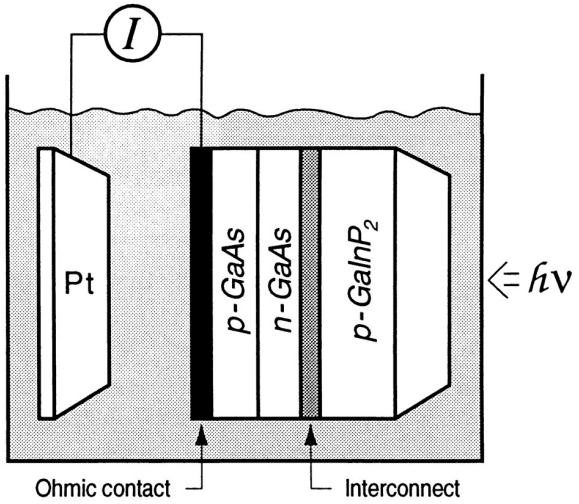


Figure 1:22 Schematic of a monolithic PEC/PV device for photoelectrochemical water splitting developed by Turner. Reprinted with permission from reference [12]. Copyright 1998 The American Association for the Advancement of Science.

'Wireless' PEC architectures, in contrast to the wired cell designs described above, provide a direct connection between anode and cathode with the ionic conductor taking a much longer path. The 'wireless' p/n-PEC device configurations, first developed by Nozik and referred to as 'photochemical diodes' [301], are intrinsically simpler in structure and are thus projected to be more suited for a low-cost, manufactured device [277]. The intimate integration of the light-harvesting, charge-separation and chemical bond-forming functions into one single structure is advantageous compared to a multi-component process in which electricity is a tangible intermediary: integration avoids the cost and system constraints associated with electrical contacts, wires, and inverters [3]. Consequently, several 'wireless' integrated architectures for artificial photosynthesis have been designed and evaluated both theoretically [302-305] and experimentally [15,306-309] in recent years; an example of an artificial leaf is depicted in Figure 1:23 [31]. Notably, a 'free-standing' monolithic device developed by Jacobsson *et al.* [15], consisting of three series interconnected copper indium gallium selenide (CIGS) PV light-absorbers coupled with two platinum catalysts for water oxidation and hydrogen evolution, achieves a STH efficiency of 10% (the US Department of Energy

target [11] and threshold for economic and technological compatibility [15]), rivalling the efficiency achieved by Turner (Figure 1:22). Although the use of non-cost effective precious metal catalysts prevents further scale-up, the device has important value from a proof-of-principle viewpoint.

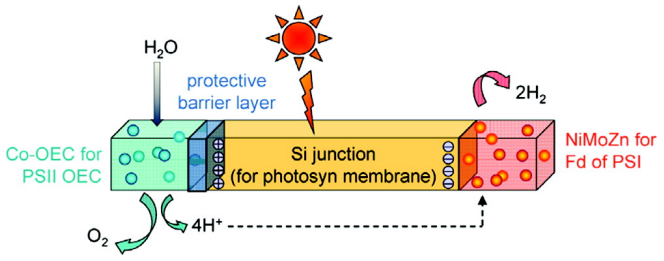


Figure 1:23 Wireless solar-fuel generator ('artificial leaf') developed by Nocera and co-workers, comprising a Co-Pi oxygen evolving catalyst (section 1.3.2) and a NiMoZn alloy for H_2 evolution. Reprinted with permission from reference [31]. Copyright 2012 American Chemical Society.

1.4.2.2 Photochemical systems

To study the mechanistic interplay between catalysts and light-absorbing components, it is advantageous to examine the water oxidation or fuel-forming 'half-systems' separately through photochemical experiments in (ideally homogeneous) solution: equilibria can be shifted in the desired direction and reaction rates can be controlled through the use of sacrificial reactants (in very large excess). Mechanisms can be elucidated through a variety of spectroscopic tools (*e.g.* steady-state UV/Vis or time-resolved optical spectroscopy), most of which are easiest to perform in solution.

Aside from the difficulty of product separation in a colloidal approach, it is extremely unlikely that light-driven overall water splitting, *i.e.* simultaneous water oxidation and fuel production could occur efficiently at a single nanoparticle site. Reasons include the lack of spatial charge separation to suppress recombination and destructive back reactions, as well as the difficulty in dealing with two sets of highly reactive intermediates during a four-photon cycle. Nevertheless, colloidal semiconductor nanocrystals are excellent light-harvesting

elements for artificial photosynthetic model systems because they are strong light-absorbers with tuneable particle size, shape, electronic structure, absorption spectra and surface chemistry [310-317].

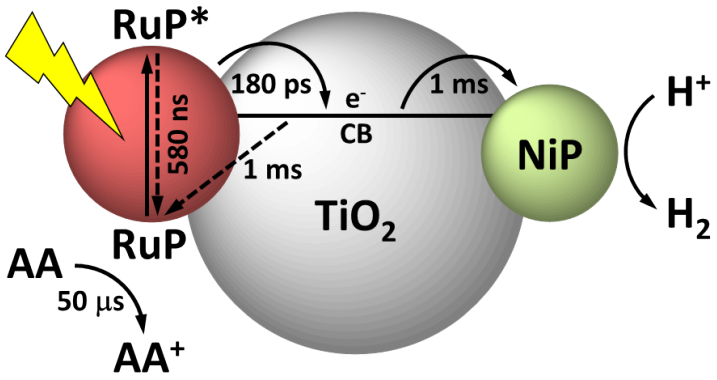


Figure 1:24 Cartoon representation of a semiconductor nanoparticle-based 'half'-system for hydrogen evolution in colloidal solution [184]. A molecular DuBois-type hydrogen evolution catalyst (NiP) is immobilised on a TiO_2 semiconductor particle, co-sensitised with a visible-light-absorbing tris(bipyridine)ruthenium(II) dye (RuP). Ascorbic acid (AA) acts as sacrificial electron donor and respective carrier dynamics are indicated.

Figure 1:24 schematically illustrates the principle for a system catalysing fuel-formation driven by a sacrificial electron donor [184]. Domen pioneered the approach of using semiconductor powders for photocatalytic water splitting, such as in his laboratory's elegant study from 2006: using a solid solution of $(Ga_{1-x}Zn_x)(N_{1-x}O_x)$, impregnated with nanoparticles of rhodium-chromium mixed oxide [318], hydrogen and oxygen have been shown to evolve stoichiometrically in the expected 2:1 ratio under visible-light irradiation ($\lambda > 400$ nm), with an external quantum efficiency of approximately 2.5% at 420 – 440 nm. The system shows remarkable stability, no noticeable degradation was observed after repeated runs for 35 h. Following Domen's seminal work, a variety of fuel-forming catalysts have been coupled with nanoparticulate, colloidal semiconductor materials (both for CO_2 reduction and H_2 evolution), either through directed immobilisation or non-specific 'bimolecular' interactions, and integrated 'colloidal' systems have also been devised [319-337].

Many of the semiconductor/molecular catalyst systems developed thus far focus on dye-sensitised TiO_2 nanoparticles and Cd-chalcogenide nanostructures of various geometries. Both types of materials offer several advantages: their photochemistry and excited-state kinetics are well established [338,339] and the conduction band edges (see Figure 1:10 for a guide) provide enough driving force to effect the fuel-forming reactions.

Both TiO_2 and CdS are *n*-type semiconductors that normally form a depletion layer at open circuit potential. A positive charge is associated with the space-charge region (section 2.3.3), which is reflected in an upward bending of the band edges at the semiconductor/electrolyte interface [340]. Size becomes crucial: at the *macroscale*, excited electrons in the conduction band migrate from the surface into the interior and render the material unsuitable for light-harvesting applications for the fuel-generating half-reaction. However, at the *nanoscale*, formation of a space-charge layer is improbable due to the tiny dimensions. Semiconductor nanocrystals with very small particle diameters do not contain enough electrons to support an effective space-charge layer. In practice, this lack of space-charge effects applies to both nanoparticle suspensions and highly porous electrodes [341]. Hence, on the nanometre scale, both TiO_2 and CdS are useful light absorbers for light-driven fuel formation.

Commercially available TiO_2 nanoparticles (such as 'P25', an 80:20 mixture of rutile and anatase) are widely used in self-cleaning wall paint (exploiting hydroxyl radicals generated by UV radiation). The disadvantage for artificial photosynthesis is their transparency towards visible light, with band gaps of 3.03 eV for rutile and 3.20 eV for anatase, respectively [342]. To overcome this issue, TiO_2 is commonly sensitised with molecular dyes, most commonly tris(bipyridine)ruthenium(II) derivatives [68,82] and high-potential porphyrins [71]. These types of sensitiser have large extinction coefficients in the visible region and long-lived charge-separated (triplet-) states, leading to efficient charge

injection from the chromophore to the semiconductor [73,338]. Due to the position of its conduction band potential (Figure 1:10), TiO_2 provides only a marginal driving force for fuel formation, especially for CO_2 reduction. This disadvantage however will pose little problem for a reversible electrocatalyst. Owing to a combination of advantages that include low cost, TiO_2 has been widely used in research on DSSCs and is one of the best-characterised semiconductor materials.

In contrast to TiO_2, CdS, which has a band gap of 2.3 eV, absorbs visible light below a wavelength of about 540 nm. The conduction band edge of bulk CdS lies at a significantly more negative potential than for TiO_2: with $E_{cb} = -0.87$ V *vs.* SHE (pH 6.0) [343], a much larger driving force is available for fuel-forming reactions (consider for example the reduction of CO_2 to CO, which has a reduction potential of −0.46 V *vs.* SHE, at pH 6.0).

1.4.3 The combination of photovoltaics and electrolysis

Despite the additional complexities, constraints, and potential costs imposed by the need for electrical contacts, wires, inverters, etc. [3], an approach in which light absorption by photovoltaic devices is physically separated from 'dark' electrocatalysis has several distinct advantages: firstly, the rapid advancement of photovoltaic cell development (section 1.3.1.5) offers the potential for solar-conversion efficiencies much higher than what is achievable with conventional semiconductor photoelectrodes. Further, there is no need to precisely match the light-absorber with the catalysts in order to make them compatible for device integration. Instead, the type of light-harvester is irrelevant for catalysis as long as sufficient voltage is (steadily) supplied to drive the water oxidation and fuel-forming reactions. To overcome restrictions imposed by the intermittency of solar irradiation, other sources of renewable electricity such as wind power could also be utilised. Professor Stephen Chu,

former US Secretary of Energy, for example proposed to use cheap night-time electricity to split water and produce liquid hydrocarbons through the concomitant reduction of CO_2 [344].

Many non-oxide semiconductor electrodes undergo decomposition by photocorrosion or photopassivation when in contact with aqueous electrolytes in solution [84]. Attempts at protection have been undertaken and, among others, amorphous TiO_2 [345-347] and NiO_x [348] coatings have been demonstrated to stabilise and protect Si, GaAs, GaP, and CdTe photoanodes. However, it remains to be seen whether such an approach will be viable in the long-term. Conversely, there is no need to protect intricate and fragile semiconductor surfaces from aqueous environments when catalysis is separated from the light-harvesting events. Recently, two papers established the general feasibility of this approach on a bench-scale level. Nocera and Grätzel respectively achieved solar-to-hydrogen efficiencies greater 10% using photovoltaic cells based upon silicon (10% STH [17]) and $CH_3NH_3PbI_3$ (12.3% STH [16]) connected in series to dark electrocatalysts. Importantly, both architectures consist of earth-abundant materials.

Grätzel's example (Figure 1:25) is particularly elegant: the simplistic design (Figure 1:25A) features the same catalyst material for both the OER and the HER, a bi-functional Ni-Fe layered double hydroxide material that is grown on a Ni foam surface. The high photovoltage of the perovskite absorber permits the use of only two PV cells connected in series (Figure 1:25B), as opposed to the system devised by Nocera, which relies on four cells connected in series. As depicted in Figure 1:25C, the operating point of the water-splitting cell lies very close to the maximum power-point of the perovskite photovoltaic tandem cell. A photovoltaic efficiency of 15.7% is converted into 12.3% STH efficiency, *i.e.* minimal

energy is lost in converting electrical to chemical energy. Currently, the system is limited by the instability of the perovskite solar cell, which degrades within hours.[iii]

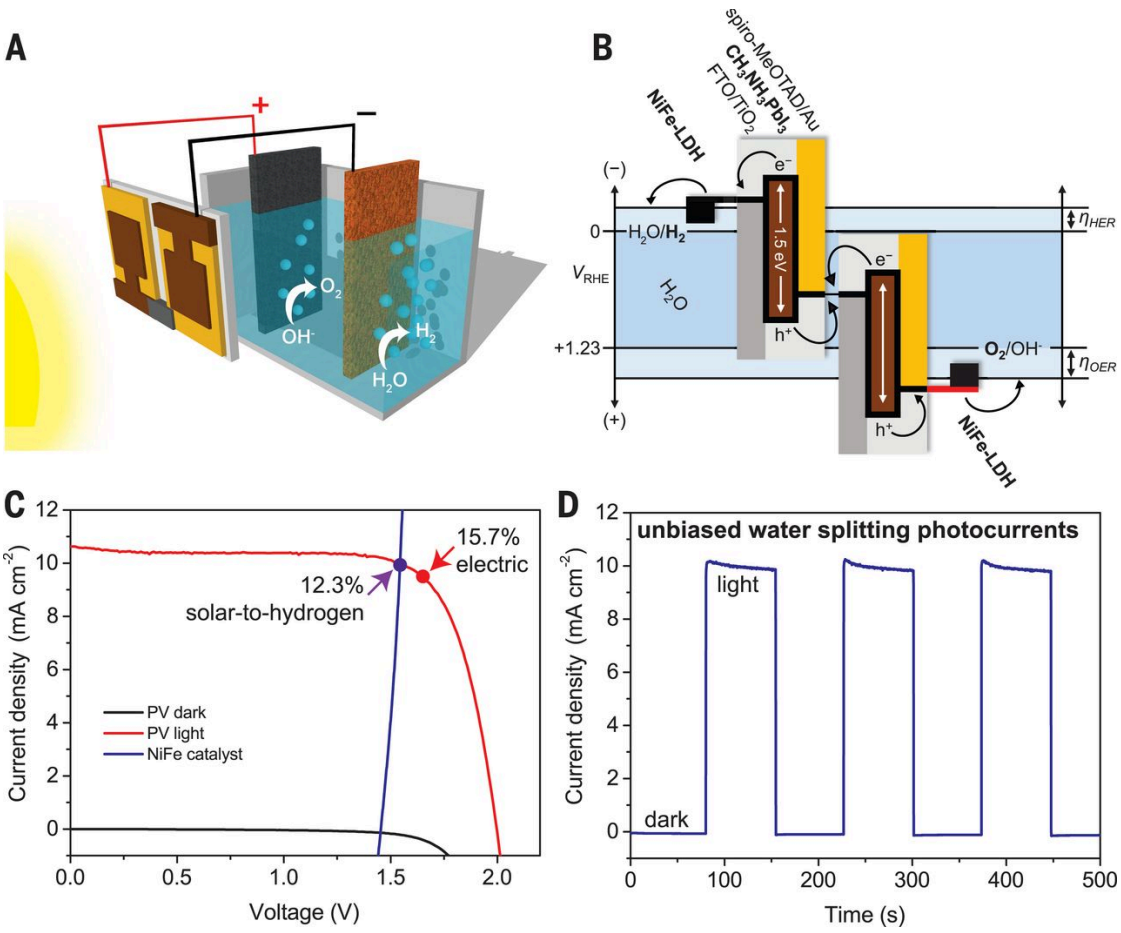


Figure 1:25 Combination of a perovskite tandem water-splitting cell developed by Grätzel *et al.* (A) Schematic diagram of the water-splitting device. (B) A generalised energy schematic of the perovskite tandem cell for water splitting. (C) *j–V* curves of the perovskite tandem cell in the dark (black) and under simulated AM 1.5G 100 mW cm^{-2} illumination (red), and of the NiFe/Ni foam electrodes in a two-electrode configuration (blue). The illuminated surface area of the perovskite cell was 0.318 cm^2, and the catalyst electrode areas (geometric) were ~5 cm^2 each. (D) Current density–time curve of the integrated water-splitting device without external bias under chopped simulated AM 1.5G 100 mW cm^{-2} illumination. Reprinted with permission from reference [16]. Copyright 2014 The American Association for the Advancement of Science.

Further, there is still room for catalyst improvement: more proficient catalysts with lower overpotential requirements are needed keep up with the development of future photovoltaic cells of even higher efficiency, or to compensate for some loss in available photovoltage by substitution of one of the PV components by a lower-voltage silicon cell.

[iii] Use of a single band gap material in a tandem configuration is also not ideal: combining a perovskite cell with a different semiconductor of similar band gap could further enhance the solar conversion efficiency [349].

1.5 The role of enzymes in artificial photosynthesis

1.5.1 General considerations

Enzymes set the benchmark for water oxidation, hydrogen production, and CO_2 reduction catalysis (see sections 1.3.2 – 1.3.4). Thus, the obvious question arises if enzymes can add value to artificial photosynthesis, not for technology development and scale-up, but to gain mechanistic insight at a fundamental level and establish design criteria for future all-inorganic devices.

Enzymes make possible the design and construction of bench-scale test systems that are instructive because the chemical reactions of solar-fuel production are rendered so fast and efficient that they are expected not to limit the overall performance of a device. If attached to light-absorbers so that interfacial electron transfers are fast, metalloenzymes can serve as smooth, proficient depolarisers to allow electron flow. Exploitation of enzymes in this way makes possible the evaluation of semiconducting materials for artificial photosynthesis development in cases where those materials may be highly suited for light harvesting but very poor catalysts.

There is an interesting connection between redox catalysis that occurs on the surface of a photoexcited semiconductor and electrocatalysis that occurs at electrodes [343]. Extensive investigations using a suite of techniques called protein film electrochemistry (PFE, section 2.2), have established that many redox enzymes catalysing artificial photosynthetic transformations are extremely fast and efficient, despite their giant size [213,350]. This information is implicit in numerous observations: fuel-forming electrocatalytic reactions such as H_2 evolution and CO_2 reduction are reversible when catalysed by the appropriate enzyme and require only a minimal overpotential to operate in

either direction. Given the crucial importance, for scaling up artificial photosynthesis, of having catalysts based upon inexpensive, abundant materials, it is highly significant that these investigations have proved that solar-fuel production *does not* require precious metal catalysts like Pt, Ru, or Ir. Indeed, experiments with enzymes show instead that in the right atomic environments, the 3d elements Mn, Fe, Ni, and Cu perform excellently. Importantly also, these inexpensive, 'dressed-up' catalysts perform under ambient, neutral conditions. Studies with enzymes provide hints at other advantages, such as the ability of an enzyme to trap and accumulate all the charge carriers (electrons or holes) required for the reaction (*e.g.* two for H_2 evolution, four for water oxidation).

1.5.2 Photosystem II in artificial systems

Highly electrophilic intermediates have to be stabilised under the harsh conditions of water oxidation, prohibiting the use of any soft material. Nonetheless, PSII has been incorporated and studied in a variety of artificial photosynthetic systems. The enzyme displays *photoelectro*catalysis when interfaced with different light-absorbing nanomaterials – the light-harvesting and catalytic components being inseparable parts of the same super-molecule.

Using the technique of protein film photoelectrochemistry [351], cyanobacterial PSII has been shown to be electroactive on mesoporous indium tin oxide (*meso*-ITO) electrodes, and catalytic water oxidation was observed under red light irradiation [352]. Orientation-controlled adsorption of PSII on *meso*-ITO through electrostatic or covalent interaction with self-assembled monolayers of organic linker molecules on the ITO surface improved interfacial electron transfer and substantially enhanced the turnover frequencies for light-driven oxygen evolution [353]. Other recent reports include O_2 evolution by His-tagged PSII

immobilised on Au-nanoparticles [354] and incorporation into redox-active polymers [355-357]. Enzyme-based photovoltaic cells have also been devised [35,358].

However, it has to be re-emphasised that there is no repair mechanism outside biology and artificial photosynthetic systems using PSII *in vitro* are prone to quick degradation [210], limiting the value such systems can bring about.

1.5.3 Fuel-forming enzymes for artificial photosynthesis

1.5.3.1 Configurations

In contrast to water oxidation, the reducing chemistry of fuel-formation relies on nucleophilic attacks and insight from molecular and/or biological components incorporated into artificial photosynthetic systems can be very useful: enzymes can remove the related burden of poor catalytic activity and high overpotential requirement.

Following seminal demonstrations of photochemical reduction of CO_2 and H^+ by metalloenzymes in 1984 [266,359], various strategies have been used to link redox enzymes to light-harvesters. Tight electronic integration between enzymes and light-absorbers can be achieved through four main strategies (Figure 1:26): (A) non-specific interaction with light-absorbing components, (B) specific covalent-linkage, (C) immobilisation on porous semiconductor nanoparticles, and (D) photoelectrodes. (Much less advantageous in this respect are multi-component 'cascade' systems, which depend on regenerating freely diffusing components such as NAD(P)H, as devised for light-driven, FDH-catalysed CO_2 reduction [360-362].)

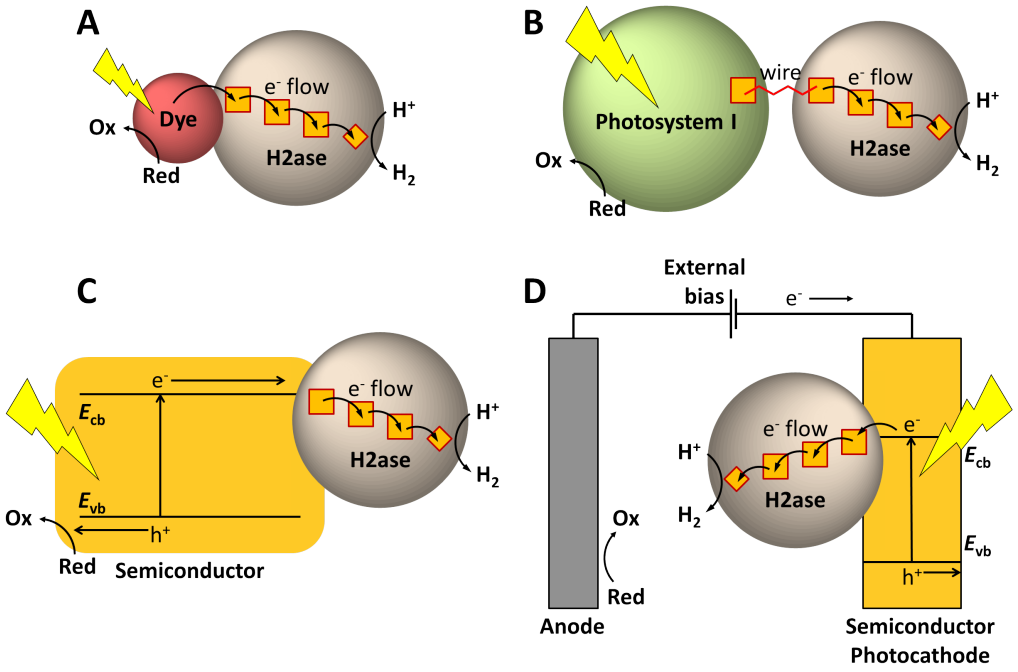


Figure 1:26 Cartoons depicting different strategies for enzyme-light-absorber interaction, exemplified with a hydrogenase enzyme. (A) 'Photoenzyme', (B) 'fusion protein' comprising hydrogenase wired to Photosystem I, (C) hydrogenase immobilised on a semiconductor nanoparticle, (D) photoelectrochemical cell with hydrogenase attached to a semiconductor photocathode. Reprinted with permission from reference [363]. Copyright 2015 Elsevier.

1.5.3.2 Photoenzymes

'Photoenzymes' can be formed as short-lived encounter-complexes between sensitiser and protein in bimolecular reactions, or by covalent dye-attachment on selected protein sites (created by introducing specific anchoring groups *via* site-directed mutagenesis). A photoenzyme formed by covalently attaching a polypyridine Ru(II) photosensitiser to a [NiFe]-hydrogenase was reported by Peters and co-workers [364]. The authors used an amine functionality on one of the Ru-ligands to form amide bonds with various carboxylates on the protein surface. Visible-light-driven H_2 production was observed (even in the presence of O_2) using ethylenediaminetetraacetic acid as a sacrificial electron donor, but the system still relied on a soluble mediator (methyl viologen), reflecting the poor electron transfer rates resulting from nonspecific coupling. Reisner and co-workers used Eosin Y, a polyaromatic photosensitiser that drives H_2 evolution by [NiFeSe]-hydrogenase through efficient

bimolecular electron transfer, without the need for a redox mediator, using triethanolamine (TEOA) as sacrificial donor [365]. The powerfully reducing nature of excited Eosin (E = –0.91 V *vs.* NHE) also ensured adequate O_2 tolerance.

1.5.3.3 From photoenzymes to fusion-complexes: the limiting case of stoichiometric architectures

Lacking specific linkages, the aforementioned photoenzymes depend on a proportion of orientations being productive, as well as bimolecular reactions. An alternative approach is to attach enzymes stoichiometrically to light-harvesting components using specific linkages. Photocatalytic activity of nitrogenase, for example, has been achieved in this manner [366]: a variant of the molybdenum-iron-protein, specifically derivatised with a Ru-photosensitiser, reduces protons to H_2 and acetylene to ethylene when illuminated.

Photosystem I can be fused with hydrogenases [367], such as in the intricate example from Golbeck and co-workers, where a fusion complex is produced by tethering PSI to the [FeFe]-Hydrogenase *Ca*HydA from *Clostridium acetobutylicum* through an alkane-dithiol molecular wire [368]. The dithiol tether connects the two enzymes by binding at their respective solvent-exposed [4Fe-4S] clusters. Overcoming the diffusion limit, the nanoconstruct is, under illumination, twice as active as natural cyanobacterial photosynthesis in terms of electrons per second per PSI.

1.5.3.4 Enzymes on semiconductor nanoparticles

Overall rates of 1:1 fusion systems, comparable to synthetic molecular ‘dyads’ [120,369], will always be controlled by the slower component, a limitation that need not apply if enzymes are attached to nanoparticles. The amount of immobilised catalyst (and, if necessary, molecular sensitiser) can be varied, allowing control over the reaction rates of the different components. The band gap determines the spectral region that can be utilised, while

valence and conduction band potentials determine, respectively, the oxidising and reducing ability of the photoexcited material. The challenge is to find materials that present these fundamental properties to greatest advantage for specific enzymes: several successful systems have been described, each assembled using electrostatic interactions or small linker molecules.

Obtaining stable and efficient linkages between catalysts and semiconductor surfaces is crucial but far from being a simple task. The linkage can be a deciding factor in terms of charge transport yields and chemical robustness under reaction conditions. A large fraction of electrons or holes is typically diverted by destructive side or back reactions, or trapped at defect sites, resulting in low photochemical quantum yields. Ideally, enzymes should be attached such that the electron entry/exit point, usually lying close to the protein surface, comes into close contact with the semiconductor surface, thus minimising the interfacial electron tunnelling barrier. Due to their relatively large dimensions, this problem is far greater for enzymes than for molecular catalysts. A covalent linker improves stability but need not improve interfacial electron transfer rates. Efficient charge transport is crucial at every stage of the catalytic cycle, but for efficient catalysts that operate close to reversibility, charge injection from the excited semiconductor to the catalyst is most critical. This step is always in direct competition with several destructive decay processes in the semiconductor such as photoemission, non-radiative decay, and intersystem crossing.

Several strategies for linking enzymes to semiconductor materials are in use. Electrostatic interactions can be exploited, using variations in pH and ionic composition, and utilising favourable charge distributions on the enzyme surface. For example, the surface of TiO_2 is covered with hydroxyl groups that are in acid–base equilibrium with H_2O, and the enzyme's electrostatic surface can be computed from a crystal structure. Electrostatic interactions alone usually result in a wide distribution of enzyme orientations on the

semiconductor and may limit experiments to certain narrow pH regimes in which semiconductor and the optimal contact region on the enzyme have opposite charges.

Semiconductor surfaces can be modified with small linker molecules to give more specific enzyme attachment. The [FeFe]-hydrogenase *Ca*HydA, for example, has a positively charged region of surface close to the 'distal' [4Fe-4S] cluster lying at the end of the relay system [370]. This is the site at which electrons enter or leave the enzyme and, *in vivo*, engages in a dynamic ET complex with its natural redox partner ferredoxin. Exploiting this knowledge, *Ca*HydA was attached to CdS nanorods capped with a monolayer of negatively charged 3-mercaptopropionic acid (MPA) [310,371].

Enzymes can be immobilised on carbon nanotubes, resulting in excellent electron transfer kinetics – usually measured by electrochemical methods. By attaching *Ca*HydA directly to single-walled carbon nanotubes [372], King and co-workers obtained an order-of-magnitude increase in catalytic rates for both H^+ reduction and H_2 oxidation [373]. Another example has been developed in the course of electrochemical studies where the aim has been to maximise coverage and stability for a membraneless H_2/O_2 fuel cell [374]: first, a graphite electrode is pre-coated with multi-walled carbon nanotubes, modified by binding of 1-pyrenebutyric acid (through π–π interactions), producing a dense, permeable conducting layer. Second, a [NiFe]-hydrogenase (Hyd1) from *E. coli* is introduced to the modified electrode surface, where it becomes covalently linked to the 1-pyrenebutyric acid units *via* peptide coupling to surface lysines. This modification leads to an order-of-magnitude enhancement of an enzymatic hydrogen–air fuel cell compared to analogous cells in which the enzymes are conventionally adsorbed on graphite.[iv]

[iv] The powerful π–π -stacking capability of pyrene moieties has also been exploited to attach small *molecular* fuel-forming catalysts to electrodes: Gray and co-workers attached small organometallic H_2 evolving and CO_2

Another strategy to link hydrogenases covalently to graphite electrodes is *via* amide coupling to graphite surfaces pre-functionalised with a layer of either 4-aminophenyl or 4-carboxyphenyl moieties, depending on the surface charge of the respective enzyme [376]. Covalent bond formation is again achieved through peptide coupling (with *N*-hydroxysuccinimide).

Figure 1:27 depicts H^+ and CO_2 photoreduction by semiconductor-enzyme systems. The prototype was established by immobilising hydrogenases on TiO_2 nanoparticles co-modified with the visible-light sensitiser RuP (Figure 1:27A) [377]. A [NiFeSe]-hydrogenase was identified as a particularly proficient catalyst, the optimised system (enzyme-RuP-TiO_2 with TEOA as donor) achieving a reproducible TOF of 50 s^{-1} (total) $enzyme^{-1}$ under ambient conditions, thus providing a benchmark for subsequent systems [378]. Similar dye-sensitised metal oxide systems have been devised for CODH-catalysed conversion of CO_2 to CO, and one based on RuP-sensitised TiO_2-P25 (a rutile-anatase mixture) emerged as clear winner among several metal oxides, including ZnO and $SrTiO_3$ [379,380]. A simpler construct, which uses band gap excitation, was assembled using CdS nanocrystals (Figure 1:27B) that absorb visible light [381]. Both quantum-dots and nanorods were investigated, the CODH-nanorod assemblies proving superior, with an average TOF of 1.23 s^{-1} $enzyme^{-1}$. Semiconductor nanocrystals have also been utilised for solar H_2 production with the [FeFe]-hydrogenase *Ca*HydA, which is more active than [NiFeSe]-hydrogenase [310,371,382]. Using CdTe nanoparticles (and ascorbic acid as donor), a STH efficiency of 1.8% was achieved under simulated sunlight with a TOF of 25 s^{-1} $enzyme^{-1}$ [382]. In a major step forward, a per-enzyme TOF in excess of 380 s^{-1} has recently been achieved for *Ca*HydA adsorbed on CdS nanorods [371].

reducing catalysts to a graphite electrode *via* pyrene-appended bipyridine ligands; even so, the resulting electrocatalytic rates were much lower than observed with enzymes as catalysts [375].

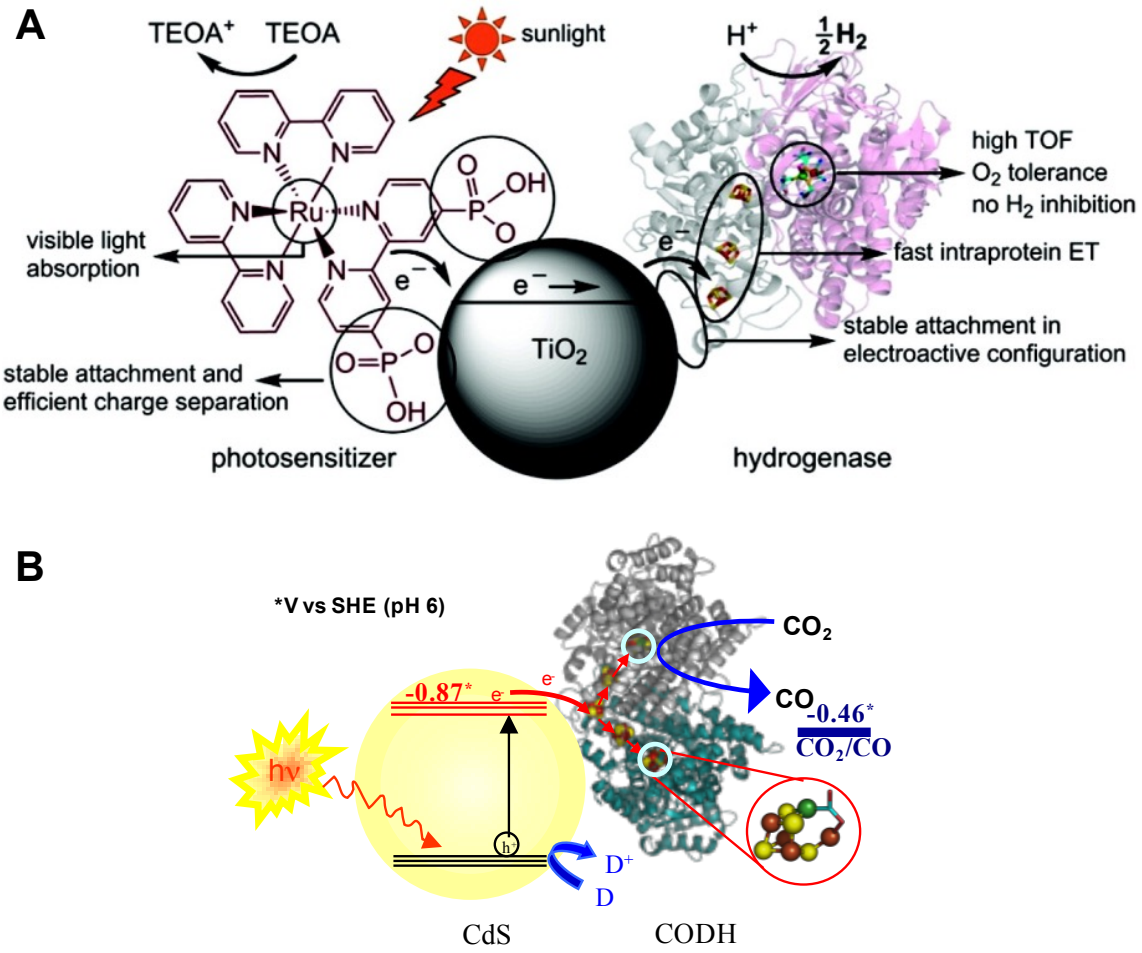


Figure 1:27 Cartoons depicting visible-light-driven photocatalytic fuel formation catalysed by hydrogenase and CODH enzymes immobilised on semiconductor nanoparticles. (A) [NiFeSe]-hydrogenase adsorbed on dye-sensitised TiO_2 particles. Reprinted with permission from reference [378]. Copyright 2009 American Chemical Society. (B) CODH attached to visible-light-responsive CdS nanocrystals. Reprinted with permission from reference [381]. Copyright 2012 The Royal Society of Chemistry.

Performances of the aforementioned systems for photocatalytic hydrogen evolution and CO_2 reduction are summarised in Table 1:1.

Table 1:1 Overview of enzyme-semiconductor systems for photochemical solar-fuel generation.

Semiconductor	Enzyme	Evolved gas	TOF (s^{-1} enzyme^{-1})	Φ (%)	Reference
RuP/TiO_2	NiFeSe	H_2	50	N/A	[378]
RuP/TiO_2	CODH	CO	0.14	0.07 at 420 nm	[380]
CdS	CODH	CO	1.23	N/A	[381]
CdTe	*Ca*HydA	H_2	25	9 at 532 nm	[382]
CdS	*Ca*HydA	H_2	380 – 900	20 at 405 nm	[371]

1.5.3.5 Photoelectrode assemblies for fuel-formation

With regard to closing the photosynthetic cycle and creating an integrated photoelectrochemical device, linking enzymes to semiconductor photo*electrodes* would constitute a further evolutionary step compared to the approaches described thus far. Enzyme-photoelectrode assemblies do not depend on sacrificial reactants and an external bias can be applied to supply additional driving force if needed. Product separation is possible by compartmentalisation of the electrochemical cell using a porous membrane.

A notable example of this approach, using a molecular cobalt cobaloxime catalyst, comes from Sun and co-workers who achieved light-driven H_2 evolution by co-adsorbing the organic pigment P1, developed as organic photosensitiser for *p*-type DSSCs [383], and the metalorganic catalyst on NiO [188]. Few other systems using molecular catalysts anchored on *p*-type semiconductors exist [189,253,255,291,384,385] and no such system building upon a fuel-forming enzyme has been devised yet. Chapter 5 will address this issue on a proof-of-concept level.

1.6 The mechanisms of fuel-forming enzymes

1.6.1 Common mechanistic principles

This section will examine in detail the mechanisms and important structural features of the three classes of fuel-forming enzymes that are of central relevance to this thesis, [NiFe]-hydrogenases, [FeFe]-hydrogenases, and CODH. The active sites of these enzymes have evolved to optimise selectivity and reaction rates by tuning reduction potentials, coupling proton and electron transfers so they are synchronous, and stabilising intermediates by just the right degree (*i.e.* avoiding high-energy states). Most attempts to mimic enzymes have focused on the active site, but it is important to consider how and why the inner coordination complex is held in such a special environment (the outer shell). Away from the active site, which is buried and shielded from bulk solvent, electron relay centres have evolved to have small reorganisation energies, optimal reduction potentials, and separation distances just short enough to allow fast and efficient electron transfer. The complete enzyme has the capacity to store all the charge carriers (electrons or holes) that are required to perform a complete half-cell reaction – a property that contrasts with most small metal-complex catalysts. The charge carriers may be 'trapped' within the enzyme, thus impeding recombination within the semiconductor. How important then is the outer shell, with its special environment – a factor distinguishing redox enzymes from small-molecule electrocatalysts? In enzymes, the outer shell can be engineered to produce bespoke variants, with atoms and their positions altered precisely. All this is achieved with earth-abundant elements – demonstrating what is possible *without* rare or expensive elements.

Crucially, the active sites shown in Figure 1:15 and Figure 1:18 are two-centre catalysts, *i.e.* they possess acid and base functionalities, located at precise distances apart (a prime example is the active site of [FeFe]-hydrogenases, where an amine-moiety is placed

right above the Fe-coordination site). Inorganic surfaces can mimic some of these principles at defects or bimetallic interfaces – but can chemists realise all of these necessary requirements?

1.6.2 [FeFe]-Hydrogenases

1.6.2.1 Structural features

Most of the [FeFe]-hydrogenases that have been studied are from green algae, *Clostridia*, and *Desulfovibrio* species [210]. Three enzymes have been crystallised: the hydrogenase HydA1 from the green alga *Chlamydomonas reinhardtii* (*Cr*) has been crystallised in its apo-form, *i.e.* lacking a di-iron subdomain that is part the active site [386]. Structures of the complete holo-enzymes were determined for the periplasmic hydrogenase from *Desulfovibrio desulfuricans* (*Dd*H) [387] and the cyctoplasmic Hydrogenase I from *Clostridium pasteurianum* (*Cp*I) [388], depicted in Figure 1:28. The active site, known as the H-cluster, is structurally conserved among the different types of [FeFe]-hydrogenases. In prokaryotic hydrogenases, it is buried inside the protein and pathways associated with substrate/product transport such as gas channels exist, as well as components for electron and proton transfer [210].

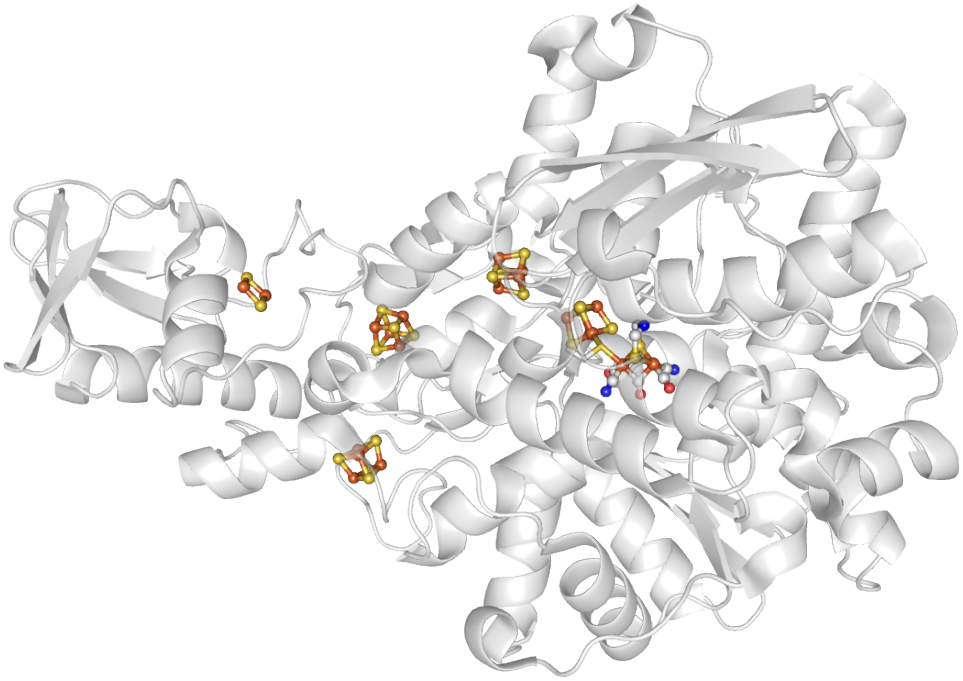


Figure 1:28 X-ray crystal structure of the [FeFe]-hydrogenase I from *Clostridium pasteurianum* (*Cp*I, PDB structure 3C8Y). The active site and the FeS centres are represented as spheres and sticks. Colour coding: iron, *orange*; sulphur, *yellow*; carbon, *grey*; nitrogen, *blue*; oxygen, *red*.

Many of the [FeFe]-hydrogenases contain additional FeS clusters ('F-clusters'), which are typically spaced within 11 Å [210] and act as an electron relay chain, providing efficient electron transport between the active site and external redox partners at the protein surface [389,390]. The [FeFe]-hydrogenase from *Dd* consists of two subunits, with the active site and the two additional [4Fe-4S] relay centres being housed in the large subunit [387]. Its monomeric congener *Cp*I contains four F-clusters, three [4Fe-4S] and one [2Fe-2S] centre (Figure 1:28) [388]. Theoretical calculations on this enzyme found the electron-transport process to activate a water channel, suggesting a coupled mechanism for proton and electron transport to the active site [391]. The algal enzyme *Cr*HydA1 is unique in that it does not contain any further FeS clusters in addition to the one that is part of the active site [386].

Substrate and inhibitors access the active site through hydrophobic gas-access channels, which are, according the crystal structures obtained so far, much shorter than the

channels in [NiFe]-hydrogenase enzymes [210]. Three putative pathways that extend from the solvent to the H-cluster and the so-called central 'C' cavity (which leads to the active site) have been suggested [210,392]. The static 'A' channel comprises an elongated cavity, connecting the protein surface to the central C cavity [387]. A recent computational study suggested O_2 diffusion into the protein proceeds *via* this channel [392]. A 'dynamic' channel, 'B', which extends from the protein to the central cavity, was identified by molecular dynamics simulations: it was previously suggested to be the dominant route for oxygen transport [393]. A third channel ('W') is lined by hydrophilic amino acids that stabilise water molecules [392].

Putative proton pathways in both *Dd* and *Cp*I have been investigated *in silico* [394,395]. In both enzymes, proton transfer to the active site takes place *via* three Glu residues, one Ser, one water molecule and one Cys, the latter being located close to the azadithiolate bridgehead atom of the active site (Figure 1:29). Genetic modification of any of the highly conserved residues leads to a drastic reduction in activity [396], corroborating the computational results. A molecular dynamics study suggests the same pathway [397].

1.6.2.2 Active site and redox states

The 'H-cluster' (Figure 1:29) consists of two components: a binuclear iron subcluster $[2Fe]_H$ that is connected, *via* a cysteine sulphur ligand, to a cubane $[4Fe\text{-}4S]_H$ cluster [210]. The Fe atoms in $[2Fe]_H$, designated 'distal' (Fe_d) or proximal (Fe_p) according to their position with respect to the $[4Fe\text{-}4S]_H$ domain, are each coordinated by CO and CN^- ligands and are bridged by an unusual azadithiolate (adt) ligand that positions a pendant amine-N above Fe_d.

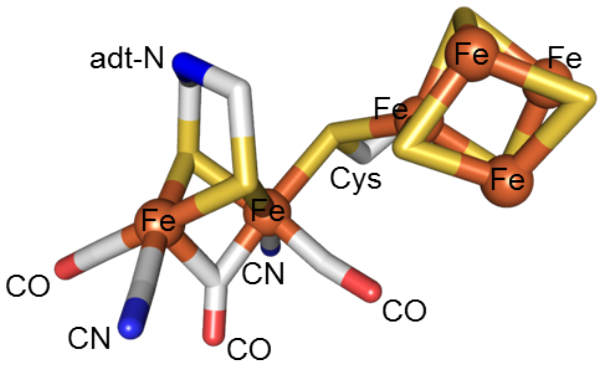


Figure 1:29 The active site of [FeFe]-hydrogenases, known as the H-cluster. The overall charge of $[4Fe\text{-}4S]_H$ is 2+, but individual charges on Fe_p and Fe_d are still under debate [398] – both $Fe_p(II)$-$Fe_d(I)$ and $Fe_p(I)$-$Fe_d(II)$ are possible combinations.

Aside from an inactive oxidised form known as H_{ox}^{inact} (where both Fe atoms of $[2Fe]_H$ are Fe(II) and the $[4Fe\text{-}4S]_H$ domain is oxidised (2+)) and the non-catalytic one-electron reduced form referred to as H_{trans} ($[4Fe\text{-}4S]_H^{1+}$ [Fe(II)Fe(II)]), three active oxidation levels of the H-cluster have been identified by spectroscopy – H_{ox}, H_{red} and a 'super-reduced' state known as H_{sred} [210]. The H_{ox} state (($[4Fe\text{-}4S]_H^{2+}$ [Fe(I)Fe(II)]), which is found in all known [FeFe]-hydrogenases, has the same overall electron count as $H_{trans,}$ but contains a mixed valence binuclear subdomain. One-electron reduction of H_{ox} leads to the formation of H_{red} ($[4Fe\text{-}4S]_H^{2+}$ [Fe(I)Fe(I)]), in which the H-cluster is EPR-silent. Addition of a further electron yields the 'super-reduced' state, which has been characterised by EPR and FTIR spectroscopy in the algal hydrogenase *Cr*HydA1, where no F-clusters that would interfere with the EPR spectrum of the active site are present [376]. In the spectroscopically accessible resting-form of H_{sred}, the EPR spectrum is typical for a reduced FeS cluster, $[4Fe\text{-}4S]^{1+}$, implicating that both the proximal and distal iron are Fe(I). Lubitz and colleagues proposed that this resting state cannot be stabilised in other [FeFe]-hydrogenases, as the additional F-clusters present in these enzymes are expected to quickly reoxidise the reduced cubane subdomain of the H-cluster [376].

A detailed EPR and FTIR study by King and co-workers, also carried out using *Cr*HydA1, corroborates the characterisation of H_{sred} by Lubitz, but suggests that the overall picture is more complex [399]. Further states in which an electron is transiently housed on the H-cluster cubane (*i.e.* $[4Fe\text{-}4S]_H^{1+}$-moieties) have been identified. Armstrong and co-workers introduced a nomenclature in which the steady-state redox levels of the H-cluster dominating at different potentials are distinguished as H_{ox}, $H_{ox\text{-}1}$, and $H_{ox\text{-}2}$, rather than using the spectroscopic labels H_{red} and H_{sred} [400]. This nomenclature allows for discrimination between catalytic oxidation levels that have clear overall electronation states, but may have different protonation states and the oxidation numbers of the individual iron centres are still vague. The different redox levels of the H-cluster are summarised in Figure 1:30.

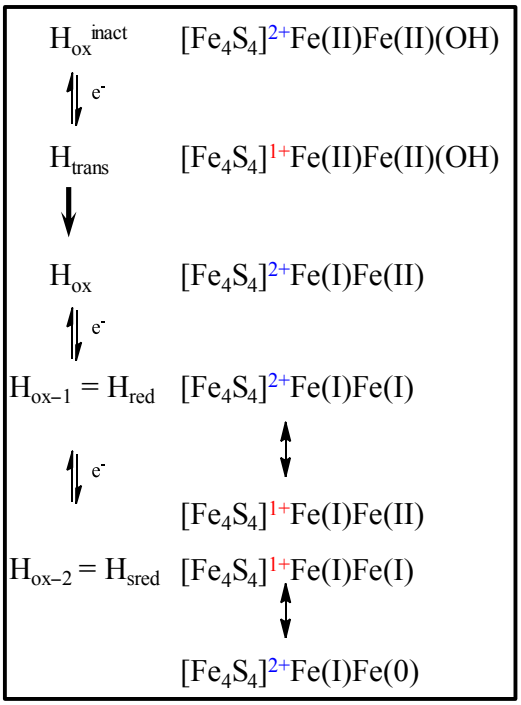


Figure 1:30 Overview of the redox levels and corresponding spectroscopic states of the H-cluster in [FeFe]-hydrogenases.

Carbon monoxide, a potent inhibitor of [FeFe]-hydrogenases, binds strongly to H_{ox} and X-ray crystallography shows CO to bind to Fe_d [401]. The extrinsic CO ligand is photolabile and reactivation of the inactivated H-cluster is greatly enhanced under illumination [402]. From

CO inhibition, it follows that Fe_d is most likely the site at which H_2 binds. Carbon monoxide binds less strongly to H_{red} (it destabilises the H-cluster [403]) and does not bind to H_{sred} [400]. The fact that CO protects against irreversible inactivation by O_2 has been interpreted in terms of O_2 also binding, initially, at Fe_d [402,404], leaving an inactive $[4Fe\text{-}4S]_H$ domain that can be reactivated *in vitro* [405].

1.6.2.3 Artificial maturation

An excellent example of the special nature of the active sites of metalloenzymes is provided by a recent discovery made during investigations of the biosynthesis of [FeFe]-hydrogenases. Two papers which appeared in 2013 showed how the Fe-carbonyl precursor of $[2Fe]_H$ (which shows little catalytic activity *in vitro*) becomes extremely active when inserted into the $[2Fe]_H$ binding cavity of the preformed 'apo-enzyme' that is already equipped with the [4Fe-4S] cluster [406,407]. The conversion is shown pictorially in Figure 1:31A. All that occurs in terms of the inner-sphere coordination chemistry is that one CO is replaced by the cysteine-S ligand to link the two components together. The structures of the $[2Fe]_H$ precursor, the apo-enzyme, and the active site of the assembled H-cluster within the binding cavity are depicted in Figure 1:31B.

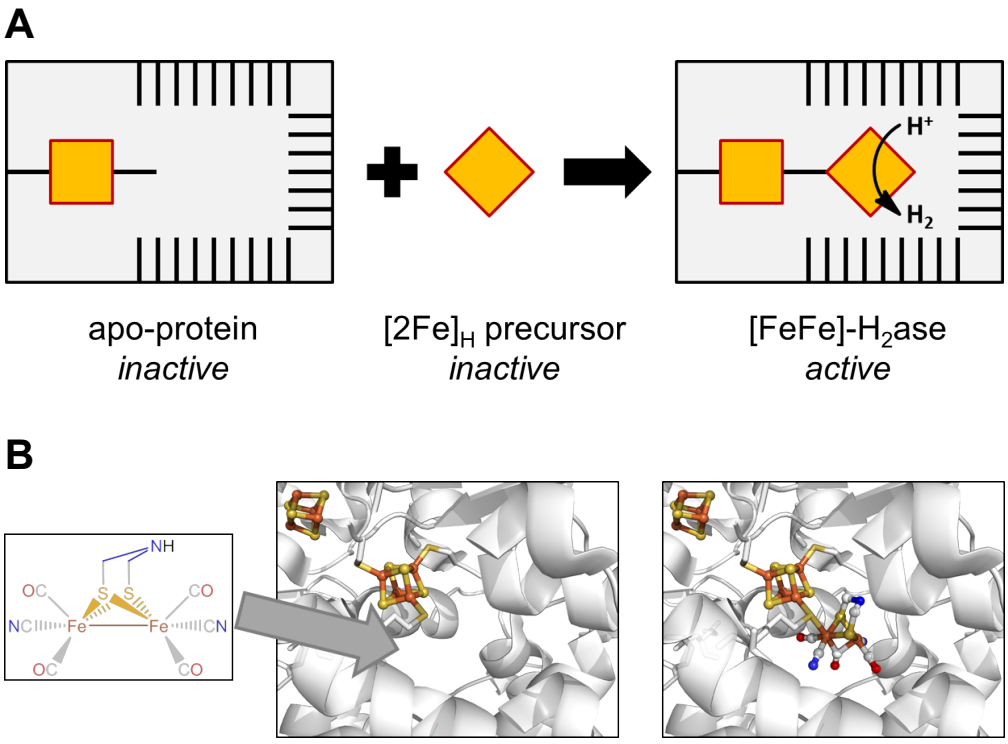


Figure 1:31 (A) *Cartoon* showing the insertion of the $[2Fe]_H$ precursor into the hydrogenase apo-protein to give active enzyme. Binding of $[2Fe]_H$ to the $[4Fe\text{-}4S]_H$ domain *via* a cysteine-S ligand occurs after loss of one CO ligand. The *grey box* represents the binding cavity, with amino acids surrounding the active site depicted as *black lines*. The [4Fe-4S] fragment is shown as an *orange square*, and $[2Fe]_H$ is depicted as an *orange rhombus*. (B) Structural representation of the insertion reaction. Depictions of the active site and the surrounding cavity were generated in PyMOL using the PDB structure 3C8Y. Some amino acids are omitted to provide an unobstructed view of the active site and the surrounding environment. Colour coding: iron, *orange*; sulphur, *yellow*; carbon, *grey*; nitrogen, *blue*; oxygen, *red*.

Significant catalytic activity is *only* achieved upon completion of the insertion reaction, *i.e. formation of the 'holo'-enzyme*, as visualised in an elegant electrochemical study by Dr. Suzannah Hexter [408] (Department of Chemistry, University of Oxford). Figure 1:32A shows cyclic voltammograms of the *Cr*HydA1 apo-protein adsorbed on a pyrolytic graphite electrode, catalytic activity only commences upon injection of the $[2Fe]_H$ precursor complex and increases until the voltammograms are virtually indistinguishable from native enzyme. Artificially maturated *Cr*HydA1 displays reversible electrocatalysis and the voltammetric scans cross the zero-current axis sharply at precisely the thermodynamic equilibrium potential for H^+/H_2 interconversion. The kinetics of the insertion reaction/enzyme activation

are depicted in Figure 1:32B. These experiments demonstrate that the integrity of the whole enzyme is essential for catalytic activity.

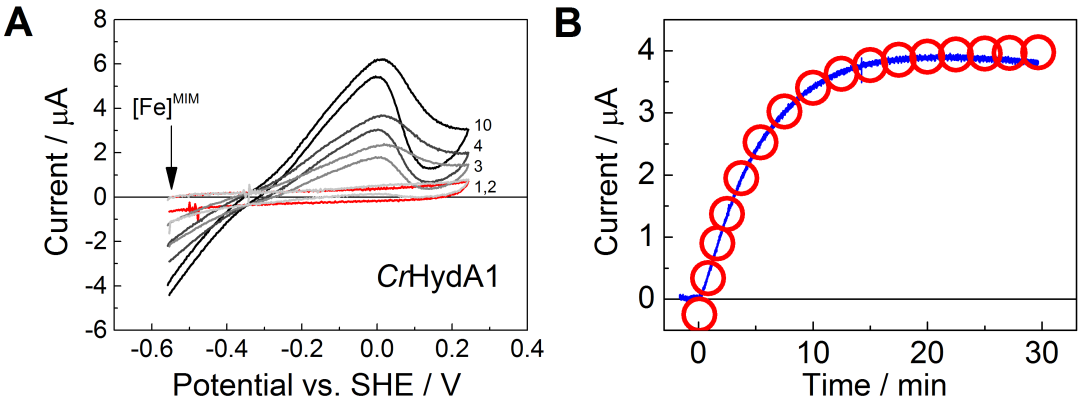


Figure 1:32 Insertion of the $[2Fe]_H$ H-cluster precursor ('$[Fe]^{MIM}$') into the apo-hydrogenase *Cr*HydA1, monitored by protein film electrochemistry. (A) Set of cyclic voltammograms, in which apo-*Cr*HydA1 is adsorbed on a pyrolytic graphite electrode (PGE). $[Fe]^{MIM}$ is introduced into the electrochemical cell solution (final concentration 230 nM) at –560 mV after the first scan (shown in red). Consecutive scans are depicted in shades of grey. Conditions: pH 6.1; 5 °C; scan rate = 30 mV s^{-1}; ω = 1000 rpm; 100% H_2. (B) Current response (blue line) observed upon injection of $[Fe]^{MIM}$ (c_{final} = 230 nM) at t = 0. A single-exponential fit of the kinetics of enzyme activation is depicted as red circles ($k_{obs} = 3.3 \cdot 10^{-3}$ s^{-1}). Conditions: E = –40 mV; pH 6.1; 15 °C; ω = 1000 rpm; 100% H_2. Adapted with permission from reference [408].

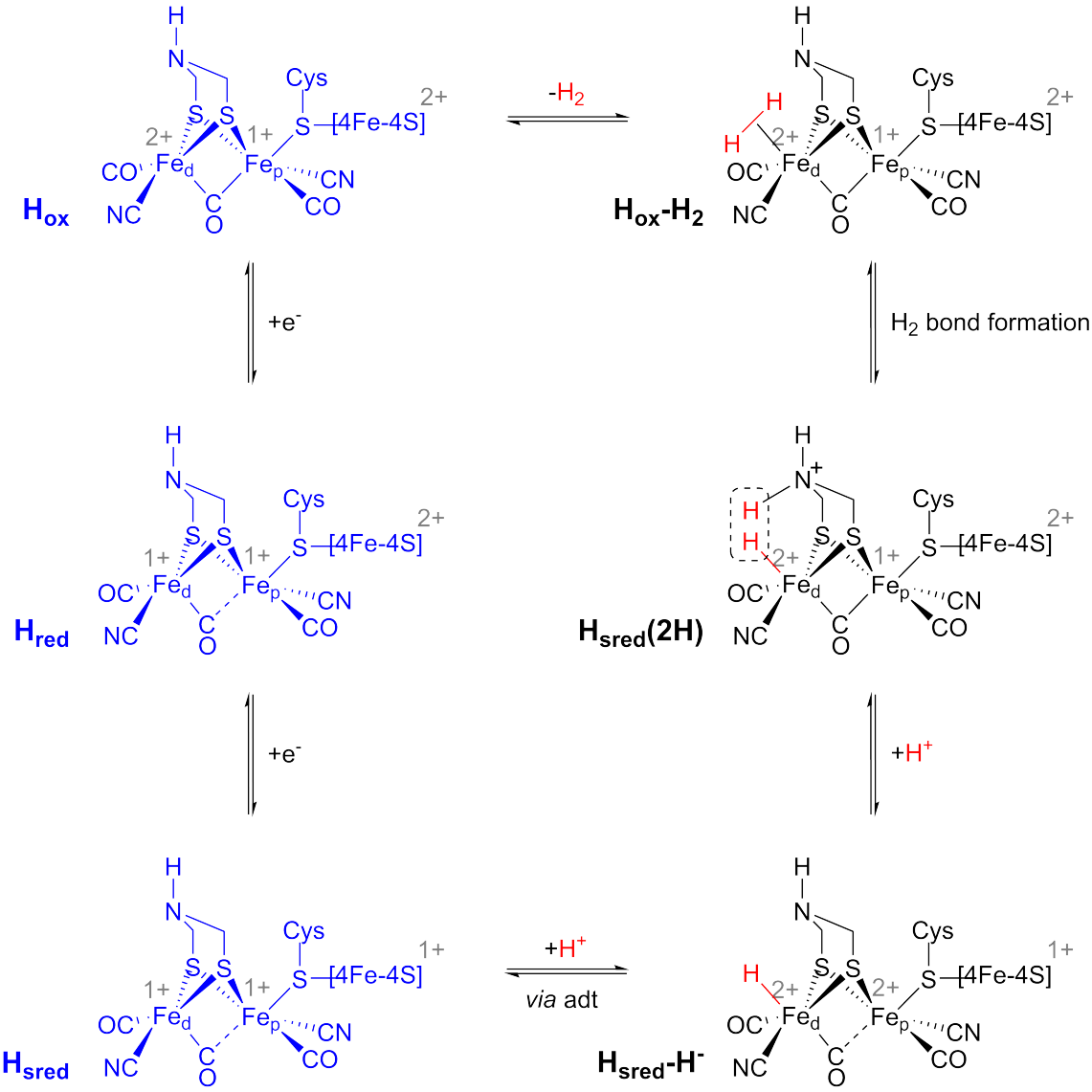
One important possibility is that only the complete H-cluster is able to delocalise, or accommodate more easily, a second electron. A recent experiment by Rauchfuss *et al.* showed that attaching a ferrocene unit to an Fe-carbonyl analogue of $[2Fe]_H$ conferred catalytic activity for H_2 oxidation that was previously absent [409]. However, the activity remained orders of magnitude lower than for the enzyme. The discovery outlined above further establishes the importance of optimising the *total* environment (*i.e.* the second- and outer-shell atoms, not just the first coordination shell). Despite the much longer distance that is required to transfer electrons to and from the buried active site of the enzyme compared to the small complex, the enzyme is the clear winner. A buried active site poses no problem if electron relay centres are present. In addition to providing a fast 'wire', these relay centres, noted as having small reorganisation energies, can trap and store electrons (or 'holes') within the macromolecule.

1.6.2.4 Mechanism

In principle, H_2 molecules are formed by the reaction of a metal-hydride ($Fe–H^-$) with a nearby, protonated base, most likely the bridgehead adt-N (a H^+NHR_2 moiety). However, due to the high activity of [FeFe]-hydrogenases, it is very difficult to trap intermediates in the catalytic cycle. During catalytic turnover, the H-cluster is thought to interchange between three one-electron separated redox states that have been spectroscopically characterised and identified as/proposed to be part of the catalytic cycle: H_{ox}, H_{red}, and H_{sred} (compare Figure 1:30) [210,376,399]. Starting from H_{ox}, two electrons and two protons are needed to evolve H_2. However, it has not yet been established, experimentally and in a kinetic study, in which order these events occur.

Scheme 1:1 shows a proposed mechanism, which takes into account recent observations from both experiment and theory. Therein, formation of a terminal [410] Fe_d-hydride and subsequent creation of the dihydrogen-bond is hypothesised to take place when the enzyme is in the super-reduced electronation level. Recent experimental evidence for Fe_d being unprotonated in the reduced H_{red} state stems from X-ray absorption and emission (XAE) spectroscopy [411]. Lubitz *et al.* [376] conclude from combined EPR/FTIR studies that Fe_d is also unprotonated in the spectroscopically accessible resting-form of H_{sred} [210]. A terminal hydride at Fe_d ('$H_{sred}–H^-$') is proposed to be formed in a rapid, exothermic process following the first protonation of the adt-bridge in H_{sred} [210]. Theoretical calculations suggest that the unpaired electron in $H_{sred}–H^-$ still resides on the cubane subcluster and only the second protonation of the adt-ligand triggers electron transfer to the $[2Fe]_H$ moiety, which in turn leads to facile H_2 formation [412] in a mechanism similar to the functional DuBois-type analogues discussed in section 1.3.3.1.

Scheme 1:1 *Proposed* catalytic mechanism for hydrogen formation at the H-cluster based on recent spectroscopic observations and theoretical investigations [210,376,399,412]. The three previously characterised redox states H_{ox}, H_{red}, and H_{sred} are depicted in blue. Note that due to lack of conclusive experimental evidence the Fe oxidation states in the $[2Fe]_H$ subsite can only be tentatively assigned to the two individual Fe centres.



Investigations into the mechanism of H_2-formation by [FeFe]-hydrogenases and the sequential order of protonation and electronation steps are presented in chapter 3; [FeFe]-hydrogenase electrochemistry studies presented therein utilise the hydrogenase *Ca*HydA from the strictly anaerobic bacterium *Clostridium acetobutylicum*. As depicted in Figure 1:33, this enzyme shows little inactivation at high potentials, in contrast to other [FeFe]-hydrogenases, and can therefore be characterised within a relatively large potential window

[213]. Also containing a series of three [4Fe-4S] clusters and one [2Fe-2S] cluster, monomeric *Ca*HydA (64.3 kDa) [413] is very similar to the crystallographically characterised hydrogenase *Cp*I (Figure 1:28) – both enzymes share 71% sequence identity [414]. EPR-spectroscopy experiments presented in chapter 3 were undertaken using the [FeFe]-hydrogenase *Cr*HydA1 from the green alga *Chlamydomonas reinhardtii*, due to its lack of F-clusters (*vide supra*).

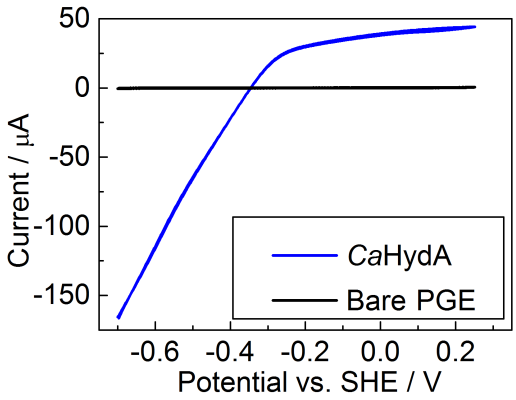


Figure 1:33 Typical cyclic voltammogram of the [FeFe]-hydrogenase *Ca*HydA adsorbed on a pyrolytic graphite edge electrode, recorded under a H_2 atmosphere at pH 6.0. The voltammogram illustrates the relative stability of this enzyme under oxidising conditions, as well as the reversibility of catalysis. The zero-current axis is cut sharply at the thermodynamic equilibrium potential for H^+/H_2 conversion.

1.6.3 [NiFe]-Hydrogenases

1.6.3.1 Structural features

[NiFe]-hydrogenase enzymes can be broadly categorised into three main subclasses: (i) 'standard', oxygen-sensitive [NiFe]-hydrogenases, (ii) O_2-tolerant [NiFe]-hydrogenases, and (iii) [NiFeSe]-hydrogenases. The [NiFeSe]-hydrogenase from *Desulfomicrobium baculatum* (Figure 1:34) [415] (henceforth simply [NiFeSe]-hydrogenase) was used in semiconductor protein film electrochemistry experiments described in chapter 4. Forming a subclass of [NiFe]-hydrogenases in which one cysteine ligand to Ni is replaced by a selenocysteine,

[NiFeSe]-hydrogenases are excellent H_2 producers that retain some activity in the presence of O_2 [215].

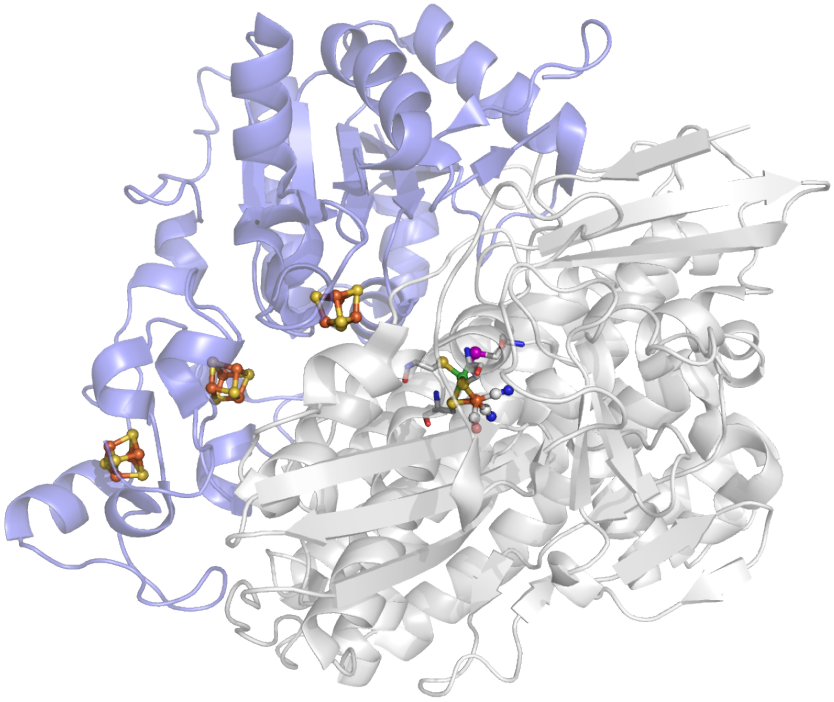


Figure 1:34 X-ray crystal structure representation of the [NiFeSe]-hydrogenase from *Desulfomicrobium baculatum* (PDB code 1CC1). The large and small subunits are depicted in grey and blue, respectively. FeS clusters and the active site are shown as sticks and spheres. Colour coding: iron, *orange*; sulphur, *yellow*; carbon, *grey*; nitrogen, *blue*; oxygen, *red*; nickel, *green*; selenium, *purple*.

The overall structures of the [NiFe]-hydrogenases show a great deal of similarity across the three above-mentioned subclasses and most of the enzymes are purified as heterodimers, with the small subunit containing an FeS electron transport chain, 'wired' to the deeply buried catalytic centre that is housed in the large subunit, as for example in Figure 1:34 [210]. A substrate/inhibitor pathway and a putative proton pathway have also been found [210].

Similar to the [FeFe]-hydrogenases, [NiFe]-hydrogenases contain additional FeS clusters. The electron transfer chain in all three subclasses consists of three FeS clusters – termed 'proximal', 'medial', and 'distal' with respect to the active site – located in an almost linear fashion in the small subunit with intercluster distances of approximately 12 Å [210]. In O_2-sensitive [NiFe]-hydrogenases the proximal and distal cluster are [4Fe-4S] clusters, and

the medial cluster is [3Fe-4S]. Conversely, [NiFeSe]-hydrogenases contain a [4Fe-4S] medial cluster. Oxygen-tolerant [NiFe]-hydrogenases in turn have a modified proximal cluster, [4Fe-3S], ligated by two additional cysteine residues compared to the standard [NiFe]-hydrogenases. One of the thiolates of the cysteine residues substitutes a sulphide ligand in this FeS centre [210].

The hydrophobic gas channels through which the known gaseous reactants H_2, O_2, and CO transfer to the active site in standard [NiFe]-hydrogenases have been probed experimentally through crystallisation under a xenon-atmosphere [416]. Although the cavities derived from these xenon-bound structures are static models, they reveal several hydrophobic channels on the molecular surface, which combine close to the active site [210]. In the [NiFeSe]-hydrogenase, a computational study identified a hydrogen diffusion pathway in addition to the gas channel found in the crystal structure [417]; it has been suggested that the existence of such alternative pathways is required to yield higher amounts of H_2 accumulation near the active site, compared to standard [NiFe]-hydrogenases [210]. Although it has been suggested that one of the origins of the O_2-tolarance displayed by certain [NiFe]-hydrogenases lies in the substrate transfer channels, and a site-directed mutagenic study [418] created a bottleneck in the hydrophobic gas channel, leading to a lower gas-diffusion rate, enhanced CO inhibition, and increased O_2 sensitivity, it is not considered essential for O_2 tolerance [210]. In order to sustain catalytic activity in the presence of O_2, oxygen is reduced quickly and efficiently to water [419,420], which is thought to leave the enzyme *via* hydrophilic water-filled cavities near the active site that lead to the molecular surface [421].

Despite several investigations, both experimentally and computationally, a definitive proton pathway has yet to be established [210]. One model suggests a pathway wherein a structurally conserved Arg residue positioned opposite the μ-hydrido ligand at the active site

acts as initial proton acceptor [422], further transfer away from the active site is thought to take place (with increasing distance) *via* Asp, His, and Glu residues. Substitutions of the conserved amino acids of this presumed transfer route impaired the activity of the hydrogenase. A different model suggests a terminal cysteine at the active site as initial proton acceptor [423], followed by transfer to a nearby glutamate [424]. It is entirely conceivable that both pathways play a role in the heterolytic splitting of H_2 by [NiFe]-hydrogenases, one acting as a shuttle for H^+, the other one transferring the proton that originally stems from the hydrido ligand, the other immediate product of H_2 cleavage.

1.6.3.2 Active site and redox states

Similar to the H-cluster, the active site of [NiFe]-hydrogenases (Figure 1:35A) also contains CO and CN^- ligands, unusual for biological systems. Four sulphurs from four strictly conserved cysteine residues are coordinated to the Ni, two of which are bridging to the adjacent Fe centre and the other two being bound to the Ni in a terminal fashion [210]. The low-spin Fe(II) ion is coordinated by one CO ligand and two CN^- ligands, strong σ-donors that form hydrogen bonds to amino acids surrounding the active site. A third bridging ligand (not shown in Figure 1:35), the nature of which changes depending upon the redox state of the enzyme (*vide infra*), is ligated to both the Ni and the Fe centres [210]. Figure 1:35B depicts the active site of [NiFeSe]-hydrogenase, the only structural difference being the replacement of one of the terminal cysteine residues by a selenocysteine (SeCys) [415].

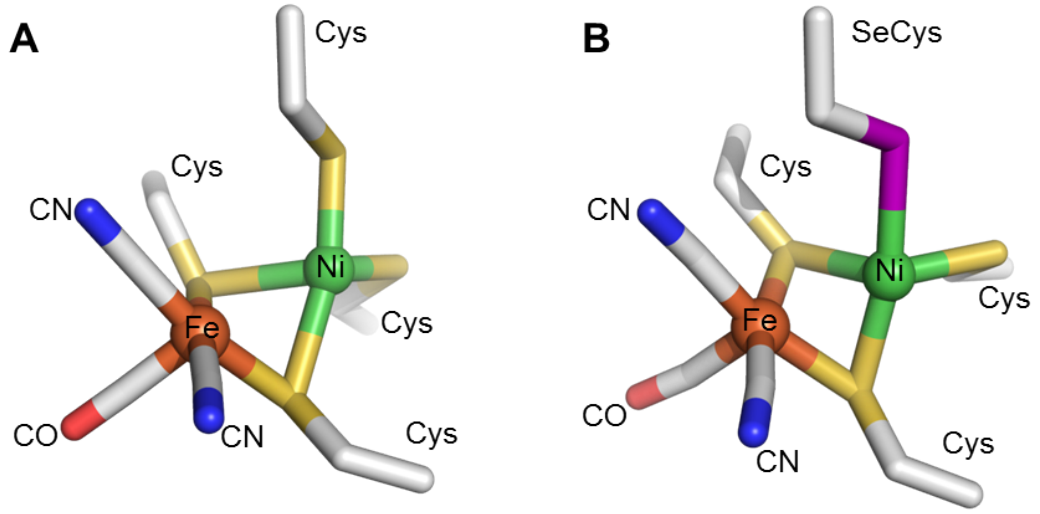


Figure 1:35 Structural representations of the active sites of (A) [NiFe]-hydrogenase from *Desulfovibrio gigas* (inactive, oxidised 'unready' form, bridging ligand not shown, and PDB code 1YQ9) and (B) [NiFeSe]-hydrogenase from *Desulfomicrobium baculatum* (reduced, active from, PDB structure 1CC1).

The most oxidised states of [NiFe]-hydrogenases are known as Ni-A (commonly termed 'unready') and Ni-B ('ready'). Both states are catalytically inactive and assigned as [Ni(III)Fe(II)], they can be obtained upon exposure to oxygen or through anaerobic inactivation at high potentials [210]. In Ni-B the bridging ligand was assigned as hydroxide [425-427], whereas the exact nature of this ligand in Ni-A is still under debate (a hydroperoxide species was postulated [425,426]). Whereas Ni-B is quickly reactivated by H_2 (typically within one min), Ni-A requires a much longer reactivation time (> 1 h) [210].

One-electron reduction of the inactive oxidised states leads to the formation of different EPR-silent states, which are all in the [Ni(II)Fe(II)] electronation level. Ni-A reduction yields Ni-SU ('silent unready'), one-electron reduction of Ni-B results give the Ni-SI_r state ('silent ready'). The latter is in acid/base equilibrium with Ni-SI_a [428], the most oxidised catalytically active state. Protonation and dissociation of the bridging OH^- ligand is thought to be responsible for conversion of Ni-SI_r to Ni-SI_a.

Further reduction by one-electron converts the Ni-SI_a state into the active, reduced Ni-C state. Here, H^- is the third bridging ligand and the nickel centre is formally assigned as

Ni(III). Photolysis of Ni-C at cryogenic temperatures yields distinctive EPR-active states, collectively termed Ni-L [210], in which the bridging hydride has migrated as a proton to a nearby basic ligand such as a terminal cysteine sulphur, leaving behind a [Ni(I)Fe(II)] bimetallic core. The conversion is reversible; Ni-C can be recovered at elevated temperatures. Ni-L has mainly been regarded as an artefact of no mechanistic relevance, however, Hidalgo *et al.* demonstrated that Ni-L can be generated reversibly in the dark at ambient temperature under turnover conditions and that it is present under all potentials during turnover under H_2 [429]. More recently, Murphy *et al.* showed that the interconversion (in *E. coli* Hyd1) is a pH-dependent process that proceeds readily in the dark, suggesting that Ni-L is a true catalytic intermediate of [NiFe]-hydrogenases [430].

Additional one-electron reduction of Ni-C leads to the formation of Ni-R, the most reduced catalytically active state, which has recently been crystallised to a resolution of 0.89 Å [423]. Ni-R is EPR-silent and is characterised by a bridging hydrido ligand bound to the [Ni(II)Fe(II)] binuclear site.

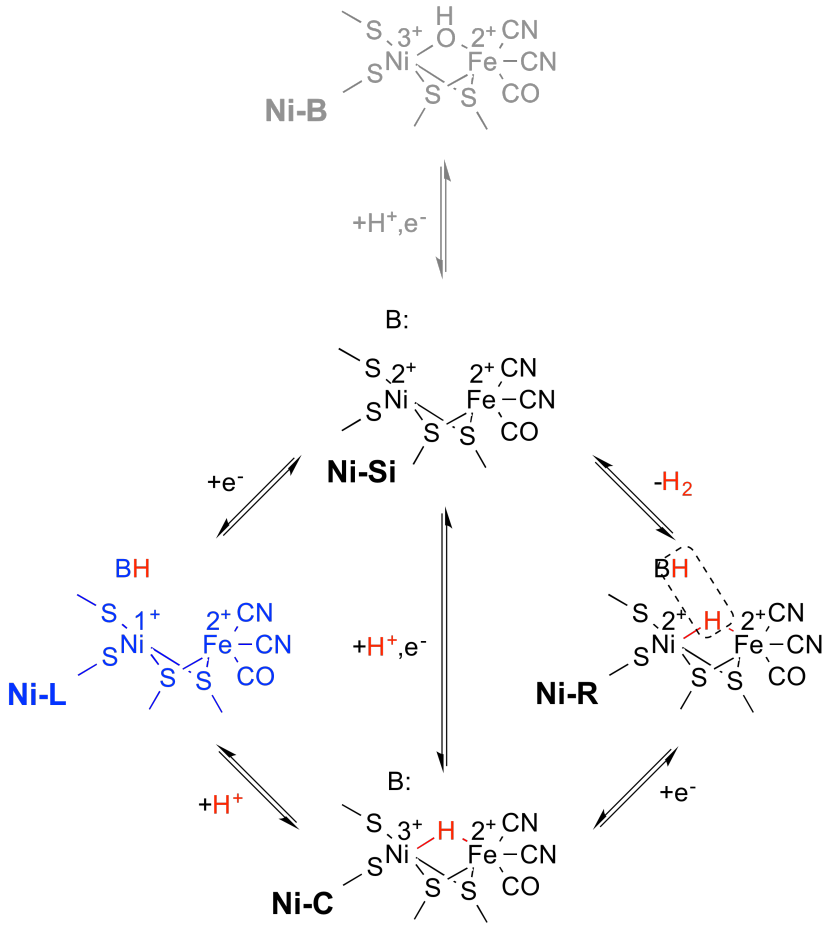
1.6.3.3 Catalytic mechanism

Although more [NiFe]-hydrogenase states have been characterised by spectroscopy than for the [FeFe] analogues, the catalytic mechanism of the former is less clear. A general consensus exists that, following addition of H_2 to the open-bridge Ni-SI_a state, heterolytic H–H bond cleavage leads to formation of Ni-R (Scheme 1:2). As indicated in section 1.6.3.1, two residues are currently favoured to act as base for initial proton removal, a terminal cysteine ligated to Ni [423], or a strictly conserved arginine residue positioned opposite the Ni-Fe site, at a distance of approximately 4.5 Å to the Ni [422]. Recently, a variant of hydrogenase 1 from *E. coli* has been crystallised (PDB structure 4UE3), in which this arginine has been exchanged for a lysine by site-directed mutagenesis. The resulting enzyme

is stable and fully assembled, but shows a 100-fold decreased activity [431], indicating that this arginine has indeed mechanistic relevance and might serve as initial proton acceptor in a frustrated Lewis pair mechanism, similar to the adt-N bridgehead in [FeFe]-hydrogenases.

Oxidation of Ni-R yields Ni-C, which is, upon loss of a further electron and proton from the μ-hydrido ligand, converted back into the Ni-SI_a state. It is conceivable that this second proton leaves the active site through a different pathway, *e.g. via* one of the terminal cysteine ligands. As suggested in section 1.6.3.2, conversion of Ni-R into Ni-SI_a can also proceed *via* Ni-L as catalytic intermediate, if electron transfer is sufficiently slower than proton transfer [429,430].

Scheme 1:2 Proposed catalytic cycle of hydrogen formation by [NiFe]-hydrogenases, taking into account recent findings by that suggest Ni-L (blue) is a true catalytic intermediate [429,430]. Anaerobic inactivation (Ni-B) is shown in grey.

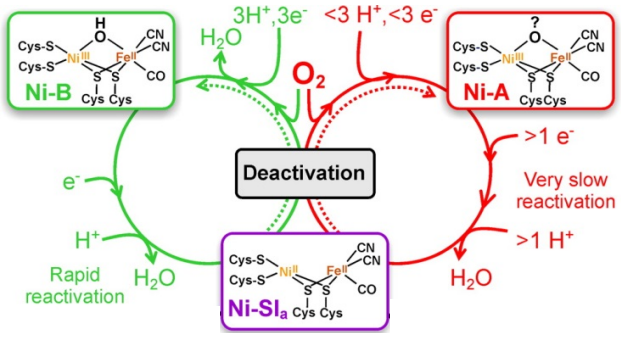


1.6.3.4 Oxygen tolerance

The two oxidised states Ni-A and Ni-B are involved in inactivation by O_2. In oxygen tolerant [NiFe]-hydrogenases, Ni-B is formed almost exclusively, and O_2 is split into H_2O [419,420] and OH^- in a four-electron, three-proton process [210] (Scheme 1:3). Of special importance in this reactivation mechanism is the unique proximal [4Fe-3S] cluster [432], which provides two electrons through its ability to undergo two redox transitions at high potentials: the first electron in the four-electron Ni-B reactivation is provided by the active site, the second and third electrons come from the proximal cluster's $[4Fe\text{-}3S]^{3+/4+}$ and $[4Fe\text{-}3S]^{4+/5+}$ transitions, respectively, and the fourth electron is provided by the $[3Fe\text{-}4S]^{0/1+}$ couple of the medial

cluster [210,421,433-435]. The precise mechanism of Ni-B reactivation, *i.e.* the elementary steps, is still under debate and it has yet to be established that the oxygen species in the bridge originates from complete O_2 reduction [210].

Scheme 1:3 The reaction of [NiFe]-hydrogenases with oxygen. O_2-tolerant hydrogenases form Ni-B, which can be rapidly reactivated (green pathway). In 'standard' hydrogenases Ni-A is formed accumulatively (red pathway), a state that requires low potentials and long reactivation times to restore activity. Anaerobic inactivation is represented by dotted lines. Adapted with permission from reference [210]. Copyright 2014 American Chemical Society.



Neither Ni-A nor Ni-B have been observed in [NiFeSe]-hydrogenases [436], which form EPR-silent oxidised states and can only sustain activity in the presence of O_2 when low potentials are applied, *i.e.* in the hydrogen production regime [215]. Their inability to form the [Fe(II)-O(X)-Ni(III)] inactive states found in other [NiFe]-hydrogenases suggests a different pathway exists for oxygen inhibition [436]: the medial [4Fe-4S] cluster, ligated by three Cys and one Ser might play a role [210], coordination by the more electronegative serine should perturb the redox potential of the cluster and impact the electronic structure [436]. Further, oxygen exposure converts the selenocysteine ligated to Ni into oxidised seleninate [437] or selenate [438] species. Compared to sulphur-oxygen bonds, selenium-oxygen bonds are more labile [439], a potential reason why the inactivated protein is readily reactivated and thus exhibits little oxygen sensitivity [215,440] at low potentials.

1.6.4 Carbon monoxide dehydrogenase

1.6.4.1 Structural features and active site

Carbon monoxide dehydrogenases can be classified according to two main categories: the aerobic Mo-CODHs with a Cu-S-Mo(pyranopterin) centre [441] and the anaerobic Ni-CODHs, which contain a [Ni4Fe-4S] cluster as their active site [442]. Both classes are monofunctional enzymes. Ni-CODHs are frequently associated with acetyl coenzyme A synthase (ACS), forming a bifunctional enzyme which couples CO_2 reduction with formation of acetyl-CoA [442].

This work utilises the Ni carbon monoxide dehydrogenase CODH I from the thermophilic eubacterium *Carboxydothermus hydrogenoformans* (*Ch*), a chemolithoautotroph that is able to grow with CO as its only source of carbon and energy [269]. This bacterium expresses five different Ni-CODH enzymes [443], two monofunctional proteins (CODH I and CODH II) which reversibly catalyse the oxidation of CO [444], the bifunctional CODH III, which is found in a stable complex with ACS and supports autotrophic carbon assimilation [445], CODH IV, which based on genomic analysis is suggested to be associated with a multisubunit enzyme complex for oxidative stress response [270], and CODH V, the role of which remains unclear.

The crystal structure of CODH II has been determined (Figure 1:36) [446]. The homodimeric enzyme contains five metal clusters, three [4Fe-4S] cubanes (two B clusters and one known as D cluster), as well as two active site clusters, known as C-clusters. The D-cluster, which lies close to the protein surface, covalently links both monomers; it is coordinated by two cysteines of each monomer at the dimer interface [443]. Although it is not yet established if it is part of the electron transfer chain, the D-cluster is ideally positioned to serve as electron entry/exit point. However, it is not reducible at potentials as low as

−530 mV, indicating that it may serve a structural, rather than an electron-transfer role [447]. The two B-clusters, each coordinated by the *other* subunit, are positioned about 10 Å away from cluster D and approximately 10 Å from the respective active site, *i.e.* within typical biological electron transfer distances [389,448]. In short, the electron transfer chain may encompass D ↔ B' ↔ C. The active site itself comprises a [Ni4Fe-4S] cluster [449] (Figure 1:37), which can be described as [Ni3Fe-4S] cubane cluster with an extra-cuboidal 'pendant' or 'dangling' Fe [270].

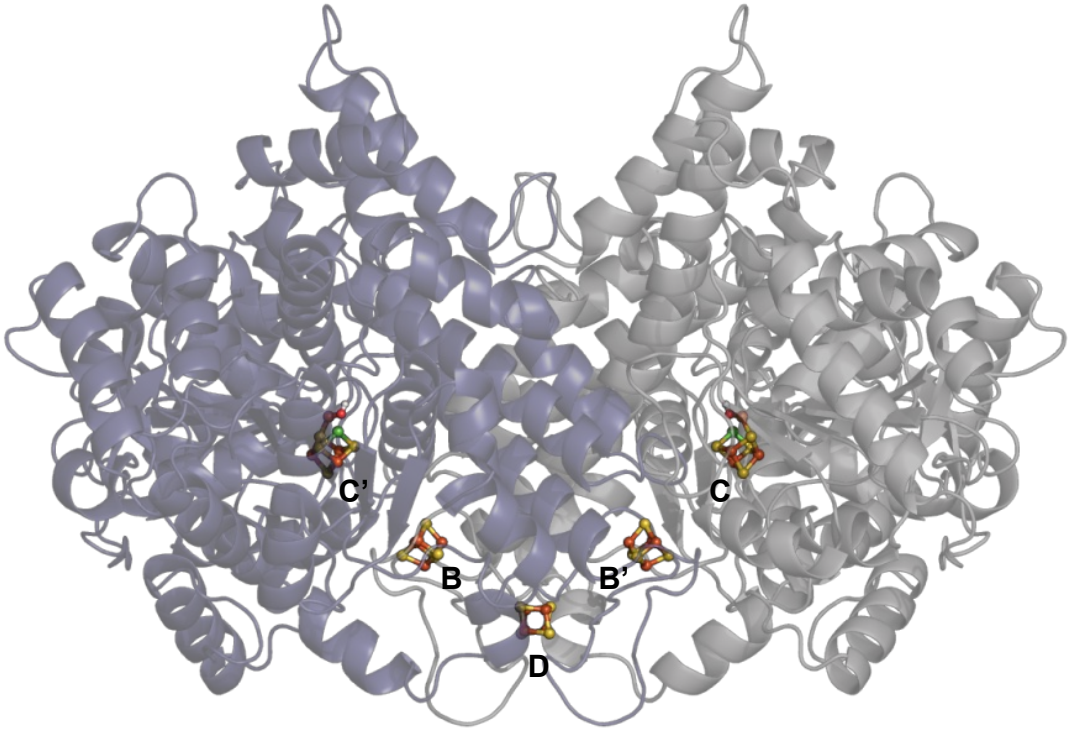


Figure 1:36 X-ray crystal structure of CODH II from *Carboxydothermus hydrogenoformans* (PDB code 1SU7). The two subunits of the homodimeric enzyme are depicted in grey and blue, respectively. The FeS conduit and the active site are shown as sticks and spheres. Colour coding: iron, *orange*; nickel, *green*; sulphur, *yellow*; oxygen, *red*; hydrogen, white.

Ni-CODHs employ two sets of gas channels [443]. One channel is unique to the monofunctional enzymes and, as revealed by a recent X-ray crystallisation study in the presence of the inhibitor *n*-butyl isocyanide, directed to the solvent, allowing CO and CO_2 to rapidly transfer to/escape from the active site [450]. This channel is blocked by several

residues in bifunctional Ni-CODHs, most likely to avoid escape of the substrates [269]. A second channel coincides with the tunnel that connects the C-cluster and the active site of ACS (A-cluster) in bifunctional Ni-CODHs [443]. A recent molecular dynamics and DFT study provides evidence for a further, dynamically formed gas channel in bifunctional CODH/ACS, through which CO_2 might diffuse from the solvent to the C-cluster: Blumberger and colleagues proposed that this channel is formed by two cavities that are transiently created by protein fluctuations and are thus not apparent in the X-ray crystal structures [451].

A network of hydrophilic, charged residues is responsible for water transfer from the surface to the C-cluster; protons leave the active site through a chain of four consecutive histidine residues (His93, 96, 99, and 102), the last of which is in contact with the solvent [443].

1.6.4.2 Redox states and catalytic mechanism

Four redox states have been identified by spectroscopy, they are referred to as C_{ox}, C_{red1}, C_{int}, and C_{red2}, in order of decreasing oxidation level [452,453]. The most oxidised state, C_{ox}, is EPR-silent and catalytically inactive, but can be reductively activated at potentials below −200 mV [454]. Using Mössbauer spectroscopy, C_{ox} was assigned as $[Ni(II)Fe_{pendant}(III)]:[3Fe\text{-}4S]^{1-}$[452]. One-electron reduction of C_{ox} yields the paramagnetic ($S = 1/2$) C_{red1} state. Here, the pendant iron is coordinated by an aquo or hydroxyl ligand (OH_x) and Mössbauer spectroscopy suggests $[Ni(II)Fe_{pendant}(II)]:[3Fe\text{-}4S]^{1-}$[452].

C_{red2} is obtained upon transfer of two electrons from CO oxidation; its operational midpoint potential of −530 mV [269] coincides with the redox potential of the CO_2/CO couple (eq. (1:5)). An X-ray crystal structure with CO_2 bound to the active site (Figure 1:37) [455], obtained by incubating crystals of CODH II in a bicarbonate solution adjusted to −600 mV (where C_{red2} prevails) using Ti(III)-citrate, reveals structural insight into CO_2

activation by CODH. A carboxylate bridges Ni and the pendant Fe as a μ_2-η^2 ligand, C-bound to square planar Ni. One of the oxygens of CO_2 replaces the hydroxo/aquo ligand at the extra-cuboidal Fe. An O–C–O angle of 133° shows that CO_2, which is further stabilised through hydrogen bonding to Lys and His residues, is in an activated state.

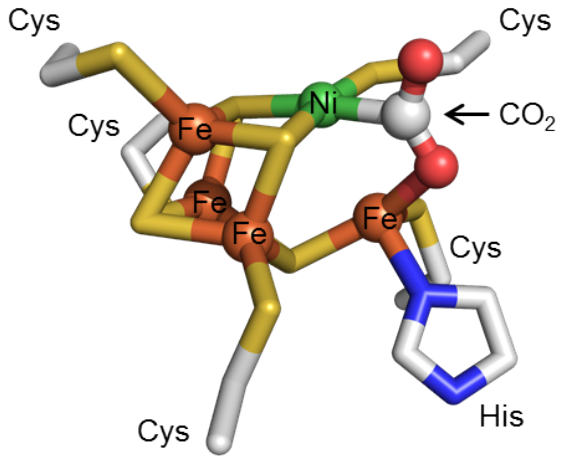


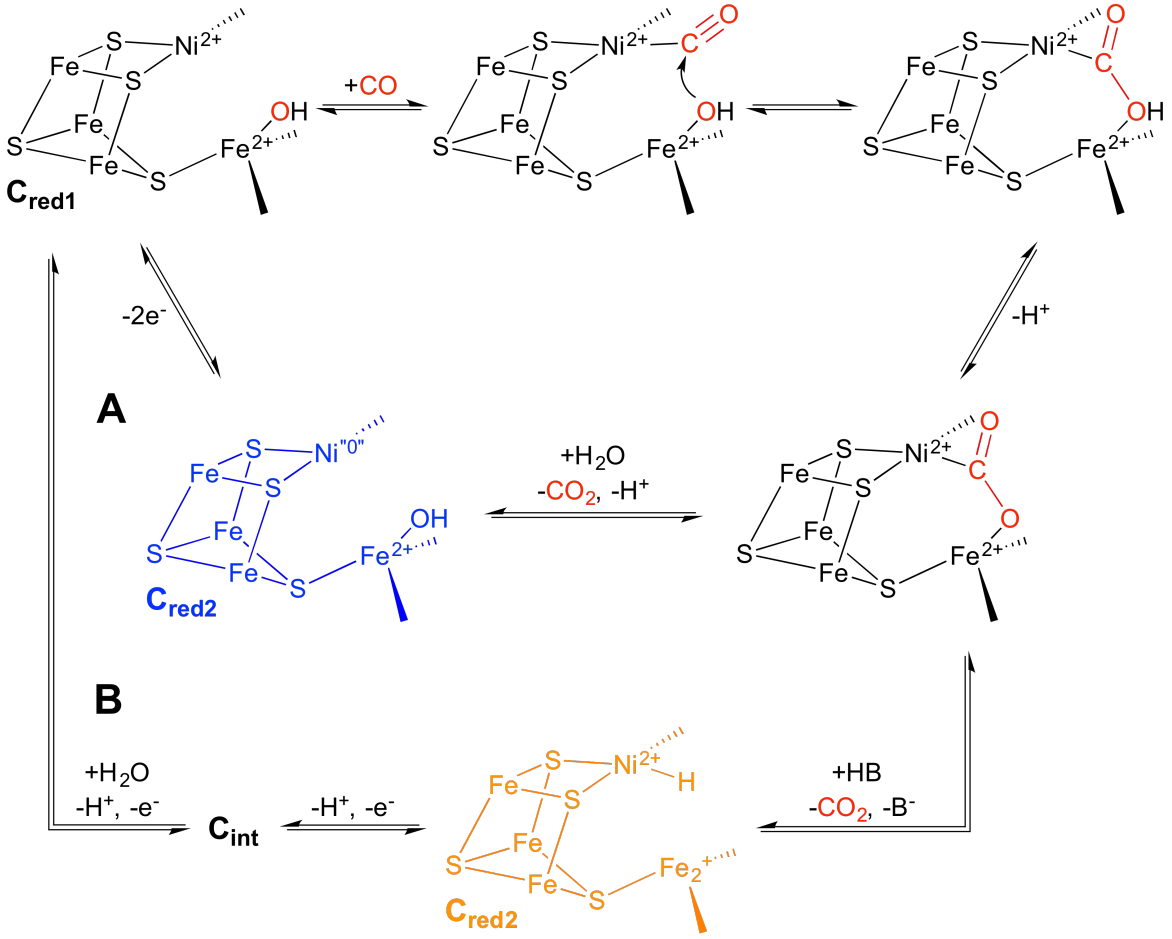
Figure 1:37 Active site of CODH II from *Carboxydothermus hydrogenoformans* in its reduced, CO_2-bound form (PDB structure: 3B52).

It is still unclear where the two additional electrons in C_{red2} reside, involvement of Ni(0) [452], a Ni(II)-hydride [456], and a Ni–Fe bond (dative metal-metal bond) [457] have been proposed. EPR spectroscopy suggests that the [3Fe-4S] core fragment remains unchanged in the two reduced states C_{red1} and C_{red2} [270]. Hence, at least one electron must be transferred to the Ni subsite, as it is unclear as to how a two-electron change could be accommodated by the pendant Fe, which is also coordinated by sulphide, histidine-N, and cysteine-S [270]. Studies using X-ray absorption spectroscopy, carried out on two different CODH enzymes subjected to different oxidation states [458-460], all suggest the Ni subsite is present as Ni(II), irrespective of the redox state of the enzyme [270]. Results, which seem to disfavour formation of a transient Ni(0) state. Half-cycle regeneration to restore the

CO-reactive C_{red1} state proceeds *via* the transient, EPR-silent C_{int} state, formed by intramolecular one-electron transfer to the B-cluster.

Regarding the mechanism of CO_2/CO interconversion by CODH, crystallographic and spectroscopic observations, in particular the CO_2-bound X-ray structure, suggest a mode of CO_2 activation in which the pendant Fe atom abstracts an O-atom from the C-coordinated CO_2 *via* a proton-coupled two-electron process, leaving CO bound to Ni with OH^- on the pendant Fe [270] (Scheme 1:4). In the direction of CO oxidation, CO binding to the C_{red1} state of the C-cluster is diffusion controlled and not rate-limiting [461,462], the rate of reduction of the B-cluster in turn is only slightly higher than the steady-state k_{cat} [269,461], indicating that this step is partly rate-limiting. CO_2 release has also been proposed to be partly rate-limiting [462]. CO is bound to the Ni in a bent fashion at an angle of 103°, which could contribute to the high turnover numbers of the enzyme by destabilising the ground state of the Ni-CO intermediate [269]. When Ni-bound CO is attacked by the $Fe_{pendant}$-hydroxide, a metal carboxylate (*vide supra*) is formed and the nickel coordination geometry changes from tetrahedral to square planar. This step is followed by the generation and release of CO_2 and a proton, and the reduction of the C-cluster from C_{red1} to the C_{red2} state. Scheme 1:4 depicts two possible pathways: formation of a Ni(0) species (A) and formation of a nickel-hydrido intermediate (B).

Scheme 1:4 Possible mechanisms for catalytic CO_2/CO interconversion by Ni-CODHs, adapted from reference [270]. (A) Pathway proposed by proposed by Dobbek [455] and Lindahl [453]; the Ni centre is formally assigned as Ni(0) in the C_{red2} state. (B) Pathway suggested by Fontecilla-Camps *et al.*; in C_{red2} a proton is coordinated to Ni in the form of a Ni(II)–hydrido species [456]. His or Lys residues are possible proton donating/accepting amino acids.



Since only CODH I was used in this thesis, it will henceforth be abbreviated simply as CODH. This enzyme shows great similarity with CODH II: the two isozymes share 58.3% sequence identity and 73.9% sequence similarity, and show similar patterns of behaviour with regard to selective inhibition by small molecule inhibitors [444]. Unprecedented turnover frequencies of 31,000 s^{-1} for CO oxidation have been reported for CODH, with CO_2 reduction occurring around one order of magnitude slower [463].

1.7 Aims of this thesis

One central aim of this thesis is to study and understand the mechanism of [FeFe]-hydrogenases, Nature's most proficient fuel-forming catalysts, specifically by introducing aldehyde molecules as reversible inhibitors (chapter 3). These can intercept and trap reactive intermediates such as the elusive super-reduced state H_{sred}, making them amenable to spectroscopic characterisation. Insights into the mechanism of enzymatic H_2 evolution can provide design principles for future all-inorganic systems.

Another objective of this thesis is to study fuel-forming enzymes in the context of artificial photosynthetic systems, in particular their interaction with semiconducting materials. Chapter 4 deals with the direct electrochemistry of [NiFeSe]-hydrogenase and CODH adsorbed on TiO_2 and CdS electrodes, with the aim of shedding some light on the marked efficiency discrepancies these enzymes display under photo- *vs.* electrocatalytic conditions.

The topic of chapter 5 is the development of a proof-of-concept system for photoelectrocatalytic CO_2 reduction based on the principles outlined in section 1.5.3.5. The aim is to achieve CODH catalysed CO_2 reduction on a *p*-type dye-sensitised NiO photocathode.

Current artificial photosynthesis research is focused on H_2 production or reduction of CO_2, but the low-value products have little immediate opportunity to compete with fossil fuels. Chapter 6 aims at establishing new directions for artificial photosynthesis research, in particular for solar-energy-driven synthesis of organic chemicals. The catalytic conversion of fumarate to succinate (essentially a catalytic hydrogenation reaction) catalysed by the enzyme flavocytochrome c_3 (fcc_3) is studied in two artificial photosynthetic systems. The objective is to achieve and investigate, mechanistically, both photo- and photoelectrocatalytic solar-to-

chemical conversion, and draw implications for future systems capable of effecting solar-driven transformations more elaborate than the production of simple fuel molecules.

In short, using enzymes in model systems for artificial photosynthesis, this thesis asks ‘what can we learn from biology?’

2 Theory of experimental techniques

2.1 Rate and efficiency parameters in artificial photosynthesis

Several spectroscopic and mechanistic tools can be employed to study the intricate mechanisms of interaction between light-absorbing semiconductors and fuel-forming enzymes. First, the efficiencies of the fuel-forming reactions have to be determined, usually *via* monitoring of product formation by gas chromatography (GC). The solar-to-hydrogen (STH) efficiency can then be calculated, according to the following equation [464]:

$$\eta_{\mathrm{STH}} = \left[\frac{(\mathrm{mmol\ H_2\ s^{-1}}) \times (237{,}000\ \mathrm{Jmol^{-1}})}{P_{\mathrm{in}}\ (\mathrm{mW\ cm^{-2}}) \times Area\ (\mathrm{cm^2})}\right]_{AM1.5\ G} \quad (2{:}1)$$

Here, the directly measured rate of H_2 production (mmol H_2 s^{-1}) is multiplied by the change in Gibbs free energy per mole of H_2 ($\Delta G° = 237$ kJ mol^{-1} at 25 °C). In the denominator of eq. (2:1), the incident illumination power density P_{in} is multiplied by the illuminated (geometric) electrode area. The illumination source should closely match the shape and intensity of the air mass 1.5 global standard G173 (AM 1.5 G) [464].

From the amount of enzyme used, the TON and TOF values on a per enzyme basis can be determined. In photoelectrochemical cells, solar energy conversion efficiencies can also be calculated from catalytic current densities, provided the Faradaic efficiencies η_{F} for product formation are known. For solar hydrogen formation, eq. (2:1) then translates to [464]:

$$\eta_{\mathrm{STH}} = \left[\frac{j_{\mathrm{sc}}(\mathrm{mA\ cm^{-2}}) \times (1.23\ \mathrm{V}) \times \eta_{\mathrm{F}}}{P_{\mathrm{in}}\ (\mathrm{mW\ cm^{-2}})}\right]_{AM1.5\ G} \quad (2{:}2)$$

In eq. (2:2), j_{sc} is the short-circuit photocurrent density normalised to the illuminated (geometric) electrode area and the voltage corresponds to the thermodynamic water splitting potential (based on $\Delta G°$). Similar equations can be formulated for the reduction of CO_2.

Enzymes offer much more selectivity than heterogeneous surface electrocatalysts, which often give complex mixtures of products, particularly in the case of CO_2 reduction (see section 1.3.4.2). Therefore, in enzymes, Faradaic efficiencies are often close to 100%. Enzymes are also sensitive to selective inhibitors, which can help to confirm whether or not a product or current arises from catalytic conversion. However, direct product detection is always highly desirable, where possible.

It is important to note that only STH efficiencies (or solar-to-CO_2 reduction efficiencies) measured without the use of sacrificial reagents or applied bias can serve as benchmark values to compare against other materials/systems. 'Half-cell' efficiencies can inflate the apparent performance of a system and cannot be converted into a meaningful device performance metric [464]. Yet, although not suitable for standardisation, the other efficiency parameters described below can still give important information about mechanistic details and are valuable for understanding and improving materials and system performance.

The external quantum efficiency (EQE), equivalent to the incident photon-to-current efficiency (IPCE), is an important characteristic of a solar-fuel system (for a primary photochemical process, quantum efficiency (QE) is identical to quantum yield, Φ). The EQE describes the fraction of catalytic current generated per incoming photon flux ('electrons out per photons in'), taking into account the spectral variation of incident photons at each energy [464]. The IPCEs are usually measured by chronoamperometry experiments (see section 2.2.7) under varying monochromatic light exposure. The internal quantum efficiency (IQE) or absorbed photon-to-current efficiency (APCE) characterises the inherent performance of a material/solar-to-fuel system, since losses from reflected or transmitted photons are subtracted. The APCE can be determined by dividing the IPCE by the

absorptance, η_{e^-/h^+}, which is defined as the fraction of electron-hole pairs generated per incident photon flux and can be estimated from Beer's law [464].

The above-mentioned quantities are important characteristics of solar-fuel systems, but do not give detailed information about the *mechanisms* of light-driven fuel-formation. To characterise the catalytic performances in enzyme/semiconductor systems, TOF, TON, and rates of electron injection and charge transport under catalytic conditions (*i.e.* light exposure and presence of substrate) are the most valuable parameters.

2.2 Protein film electrochemistry

2.2.1 A brief introduction to protein film electrochemistry

Protein film electrochemistry comprises a suite of dynamic electrochemical techniques that reveal intricate mechanistic details of redox enzymes under turnover conditions. Minuscule samples of protein are adsorbed directly on electrodes to give mono- or submonolayer films [465]. Enzymes maintain their native function [466] and their catalytic properties are fully expressed: facile, reversible electron transfer occurs with the electrode, the potential of which now controls the catalytic activity, which is monitored through the observed current that acts as a direct measure of the catalytic turnover rate at any given electrode potential [465].

Carbon is the most common electrode material in protein film electrochemistry. Particularly the 'edge' plane of pyrolytic graphite (PGE) is used, rather than the hydrophobic basal cut, due to the former's diversity of aromatic and oxo species present on the surface and the similarity to a protein's natural environment [466]. Direct enzyme immobilisation obviates the need for redox mediators, diffusion of which is known to kinetically limit the superbly fast rates of electron transfer and catalysis achieved by metalloenzymes such as hydrogenase and CODH.

2.2.2 The electrochemical setup

Typically, a standard three-electrode setup is employed in protein film electrochemistry experiments [467] (Figure 2:1).

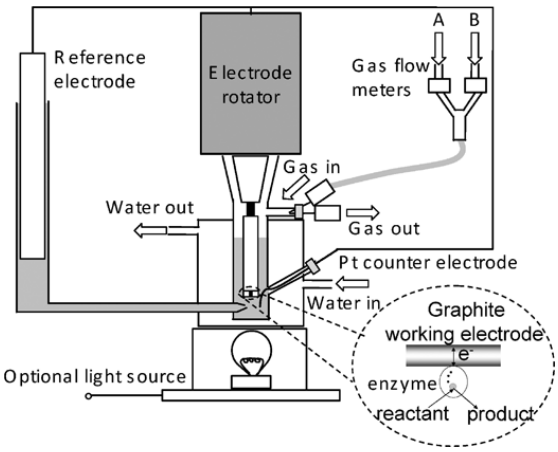


Figure 2:1 Schematic diagram of a typical experimental setup employed in protein film electrochemistry experiments. The electrochemical cell fits tightly against an electrode rotator and is equipped with gas flow controllers for providing accurate mixtures of gases. Reprinted with permission from reference [465]. Copyright 2009 The Royal Society of Chemistry.

Apart from PGE as most commonly used working electrode (WE) material, gold surfaces modified with self-assembled monolayers of alkanethiolate are also used [467]. Different strategies for enzyme-surface immobilisation are described in section 1.5.3.4. Counter electrodes (CE) are typically made of platinum (wire or gauze) and, as the real standard hydrogen electrode (SHE) is rarely practical [468], secondary electrodes such as the saturated calomel electrode (SCE) or the Ag/AgCl electrode are commonly used as reference electrodes (RE). The RE should be placed as closely as possible to the working electrode to limit the effect of electrolyte resistance R_s [464] (*vide infra*). As depicted in Figure 2:1, it can be housed in a separate compartment connected to the cell *via* a Luggin-Haber capillary. Electrode rotation at high frequencies ensures rapid delivery (removal) of substrate (product) to and from the enzyme active site and minimises limiting effects of mass transport. Use of a water jacket allows precise control of the temperature throughout the experiment. Specific gas mixtures can be introduced through the headspace of a gastight cell and the electrochemical setup can be illuminated if necessary.

When a potential is applied between a working electrode and a reference electrode, assuming a finite current i is flowing between the two electrodes, then [469,470]

$$E = (\phi_{\mathrm{w}} - \phi_{\mathrm{s}}^{\mathrm{w}}) + iR_{\mathrm{s}} + (\phi_{\mathrm{s}}^{\mathrm{ref}} - \phi_{\mathrm{ref}}), \quad (2{:}3)$$

where ϕ_{w} and ϕ_{ref} represent the electric potentials of the working and reference electrodes, respectively.[i] $\phi_{\mathrm{s}}^{\mathrm{w}}$ and $\phi_{\mathrm{s}}^{\mathrm{ref}}$ represent the potential of the solution very close to the working and reference electrodes. With R_{S} being the electrical resistance of the solution between the electrodes, iR_{S} represents the voltage drop in solution due to passage of current i between the two electrodes; it is characteristic of the bulk solution and not the electrode reaction [469]. The term $(\phi_{\mathrm{s}}^{\mathrm{ref}} - \phi_{\mathrm{ref}})$ is the potential drop at the reference electrode, which is fixed by its chemical composition [470]. Under conditions when iR_{S} is small (< 1 – 2 mV [469]) such as in microelectrode experiments, a two-electrode cell can be used to determine the *i*-*E* curve, *i.e.* the current i as a function of changes in the potential difference at the working electrode/solution interface ($\phi_{\mathrm{w}} - \phi_{\mathrm{s}}^{\mathrm{w}}$, the driving force for electrolysis) [470]. In the case of large electrodes or more resistive solutions, however, iR_{S} is no longer negligible, and changes in applied potential are no longer confined to changes in $(\phi_{\mathrm{w}} - \phi_{\mathrm{s}}^{\mathrm{w}})$. In addition to the iR_{S} term being altered, the passage of large currents through the reference electrode can change its chemical composition, meaning $(\phi_{\mathrm{s}}^{\mathrm{ref}} - \phi_{\mathrm{ref}})$ may no longer be constant [470].

A *three-electrode* system (the circuit of which is schematically depicted in Figure 2:2), where the current is passed between the working electrode and the counter electrode only, and the potential of the working electrode is held constant (a high input impedance ensures that little current is drawn through the RE [469]) circumvents this problem [470].

[i] Throughout this thesis, electrode potentials (strictly speaking, potential differences) are denoted '*E*' and electric potentials are referred to as 'ϕ', in agreement with eq. (2:3).

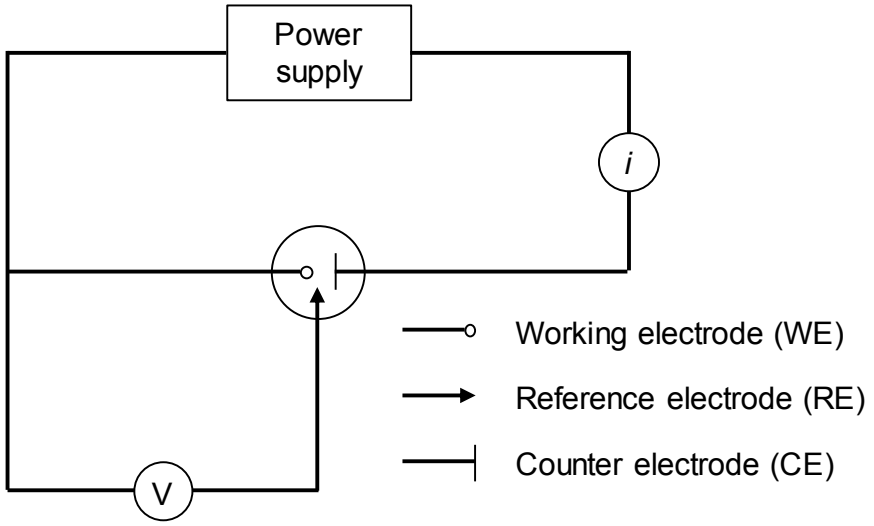


Figure 2:2 Schematic representation of a three-electrode circuit diagram and notation for the different electrodes, adapted from reference [469].

Except when specifically mentioned, *e.g.* in photoelectrochemistry experiments under no external bias described in chapter 6 of this thesis, PFE experiments in this work were carried out using a three-electrode system. Two main types of PFE experiment are presented in this thesis: voltammetry (cyclic voltammetry, CV, and linear sweep voltammetry, LSV) and chronoamperometry. In voltammetry, the current is measured as a function of the applied potential, which is swept between two values. In chronoamperometry, the potential is held constant and the enzymatic current is measured as a function of time.

2.2.3 Non-Faradaic processes

In protein film electrochemistry experiments, the observed current is usually the combination of a Faradaic process (which reveals redox transformations of molecules that come sufficiently close to the electrode, *i.e.* electrons are transferred across the electrode/solution interface) [468] and a non-Faradaic process, where no charge transfer occurs across the electrode/solution interface. The latter process resembles a capacitor:

$$C = \frac{q}{E}, \tag{2:4}$$

where q is the charge stored on the capacitor (in Coulombs, C), E is the potential across the capacitor (in Volts, V), and C is the capacitance (in Farads, F) [469]. Hence, non-Faradaic currents are often termed 'capacitive' or 'charging' currents. When the working electrode potential is swept across a potential range (such as in voltammetry experiments), charge will accumulate on its surface; an effect that has to be counterbalanced by an excess of oppositively charged ions. The result is the formation of an *electrical double layer*. This double layer itself consists of several 'sublayers' [469]: closest to the electrode surface, at the so-called inner Helmholtz plane (IHP), ions are specifically adsorbed to the electrode, stripped off their solvation shell. Solvated ions in turn can approach the electrode only up to a distance that marks the outer Helmholtz plane (OHP). Here, the interaction of these non-specifically adsorbed ions with the electrode is essentially independent of the chemical properties of these ions, because only long-range electrostatic forces are involved [469]. Thermal motion causes the non-specifically adsorbed ions to be distributed in a three-dimensional region called the diffuse layer, which extends form the OHP into the bulk of the solution.

In a voltammetric experiment, the current i that is produced upon modulation of the applied potential equals the change in charge with time:

$$i = \frac{\mathrm{d}q}{\mathrm{d}t}. \tag{2:5}$$

Combining eqs. (2:4) and (2:5), the capacitive current i_c can be formulated as

$$i_c = C\frac{\mathrm{d}E}{\mathrm{d}t} = C\nu. \tag{2:6}$$

Eq. (2:6) shows that i_c is proportional to the scan rate ν (dE/dt). The magnitude of i_c also depends on the resistance in the circuit and, *via* the capacitance, on the electrode area and the applied potential [469].

In chronoamperometry experiments where the potential is held constant, capacitive currents are only observed after potential steps. They occur as exponentially decaying transients ('spikes'), typically decaying within seconds [468]. In general, the non-Faradaic contributions arising in PFE experiments can be measured separately in 'blank' experiments where no enzyme is adsorbed on the bare working electrode surface. Subtraction from the total enzymatic current then allows determination of the Faradaic contribution.

2.2.4 Faradaic current

Faradaic currents arise upon electrode transfer at the electrode, *i.e.* they correspond to redox processes and are governed by Faraday's law, meaning the amount of chemical reaction caused be the flow of current is proportional to the amount of electricity passed [469]. Under equilibrium conditions, there is no net flow of electrons and the Nernst equation (derived in Appendix A) gives the ratio of the activities of oxidised and reduced species, often simplified to concentrations ([Ox]/[Red]) for solutions that show sufficiently ideal behaviour:

$$E_{\mathrm{eq}} = E^0 + \frac{RT}{zF} \ln \frac{[\mathrm{Ox}]}{[\mathrm{Red}]}. \qquad (2:7)$$

In eq. (2:7), E_{eq} is the equilibrium potential, E^0 is the standard reduction potential for the redox couple Ox/Red, R is the ideal gas constant, T is the temperature, z is the number of electrons transferred in the process, and F is Faraday's constant.

In dynamic electrochemistry experiments, a potential is applied that induces a current flow. In PFE experiments where a redox enzyme is adsorbed on an electrode surface, this current provides a direct measure of the catalytic activity of the enzyme. However, it is

important to note that the inherent activity of the catalytic centre is not the only factor contributing to the observed current at the enzyme-modified electrode. Conceptually, an enzyme adsorbed on an electrode can be visualised as a series of resistors (Figure 2:3) [467]. In this model, catalytic electron flow is divided into three stages that express the inherent barriers of (i) interfacial electron transfer (Ω_E), (ii) enzyme catalysis (Ω_{cat}), and (iii) substrate mass transport (Ω_{trans}). To be able to study the intrinsic mechanisms of enzyme action, interfacial electron transfer and substrate mass transport must not be limiting, *i.e.* Ω_E and Ω_{trans} should be as small as possible.

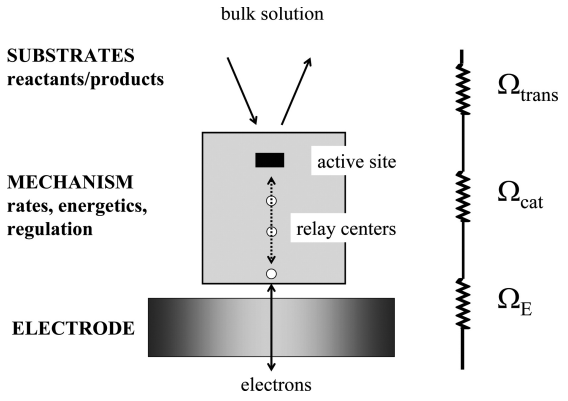


Figure 2:3 Catalytic electron flow through an enzyme immobilised on an electrode in which the possible rate-determining stages are represented by resistors in series. The electron entry/exit site is the lower one of the relay centres indicated as circles. Reprinted with permission from reference [467]. Copyright 2007 American Chemical Society.

2.2.5 Mass transport and interfacial electron transfer

In order to minimise Ω_{trans}, hydrodynamic control over substrate delivery to the active site (and product dispersion away from the catalytic centre) can be exploited by rotating the working electrode at high frequencies. At a planar rotating disc electrode, the current is given by the Levich equation [467]:

$$i_{(\omega)} = 0.62zFAD^{2/3}\upsilon^{-1/6}\omega^{1/2}c. \quad (2:8)$$

Here, A refers to the electrode area, D is the diffusion coefficient of the substrate, υ is the kinematic viscosity of the solvent, ω is the electrode rotation rate, and c is the concentration of the substrate. According to eq. (2:8), the current increases as the square root of the electrode rotation rate. Eventually, the resistance component Ω_{trans} will cease to control the current and, depending on the activity of the enzyme, the linear relationship between the current and $\omega^{1/2}$ breaks down as the rotation rate continues to increase and control passes to the enzyme [467]. Then, the Koutecky-Levich equation

$$\frac{1}{i_{\lim(\omega)}} = \frac{1}{i_{\lim}} + \frac{1}{0.62zFAD^{2/3}\upsilon^{-1/6}\omega^{1/2}c}, \tag{2:9}$$

where $i_{\lim(\omega)}$ is the limiting plateau current at rotation rate ω and $i_{\lim}$ is the maximum limiting current achieved at infinite rotation, describes the relationship between current and rotation rate. Whereas $i_{\lim}$ is normally obtained from the intercept of plotting $1/i_{\lim(\omega)}$ *vs.* $1/\omega^{1/2}$, an approximation can often be obtained by using a rotation rate above which the current and waveform no longer change significantly upon increasing ω [467]. Alternatively, albeit in a more primitive way, the electrolyte solution can be sparged with gas close to the working electrode surface to assist rapid substrate delivery and product removal.

In regards to interfacial electron transfer (Ω_E in Figure 2:3), the relationship between Faradaic current and applied potential is governed by the Butler-Volmer equation, which can be derived as follows [471]. Consider the reversible charge-transfer reaction occurring at the interface between a metal electrode (M, phase α) and the solution phase (β)

$$(M)^{\alpha} \underset{k_c}{\overset{k_a}{\rightleftarrows}} (M^{z+})^{\beta} + z(e^{-})^{\alpha}, \tag{2:10}$$

where k_a and k_c are the rate constants for the anodic (oxidation) and cathodic (reduction) reaction, respectively. At equilibrium, there is no net current flow and the anodic current

density (*i.e.* current per unit of geometric electrode area) j_a, which, per definition, carries a positive sign, is equal to the absolute value of the cathodic current density j_c:

$$j_a = |j_c| = j_0. \tag{2:11}$$

In eq. (2:11), j_0 is defined as the exchange current density, which represents the balanced Faradaic oxidation and reduction currents contributing to the net zero current. In order to drive reaction (2:10) and induce a current, a potential different to E_{eq} needs to be applied. The *overpotential* η is defined as the difference between the applied potential E and the reversible equilibrium potential:

$$\eta = E - E_{eq}. \tag{2:12}$$

The resulting current that flows through the system is characterised by the current density j, which is the sum of j_a and j_c:

$$j = j_a + j_c = j_a - |j_c|. \tag{2:13}$$

Transition State Theory (TST) [472] can be used to derive the rate constants k_a and k_c in eq. (2:10). TST assumes that an activated complex (transition state) is formed prior to formation of the products in a chemical reaction, and that this transition state is in equilibrium with the reagents. The free energy of activation $\Delta G^{\ddagger}$ is described by

$$\Delta G^{\ddagger} = -RT\ln K^{\ddagger}, \tag{2:14}$$

where $K^{\ddagger}$ denotes the equilibrium constant for formation of the activated complex, and

$$k = A_p e^{\frac{-\Delta G^{\ddagger}}{RT}}. \tag{2:15}$$

Here, k is the rate of the reaction and A_p is a constant pre-exponential factor. Using TST and assuming no potential difference between metal and solution in eq. (2:10) (see Figure 2:4, black curve), the following rate constants are obtained:

$$k_a^0 = k_a' e^{\frac{-\Delta G_a^{0\ddagger}}{RT}} \tag{2:16}$$

and

$$k_c^0 = k_c' e^{\frac{-\Delta G_c^{0\ddagger}}{RT}}. \tag{2:17}$$

However, it is important to remember that if, as in eq. (2:10), charged species migrate from one phase into another by overcoming a potential difference, one has to explicitly consider the term $zF\Delta\phi^{\ddagger}$ that describes the electrical work. In Figure 2:4, the gradient of $zF\phi$ between electrode and solution is depicted in blue, using the simplest model of a rigid Helmholtz layer. The sum $G^0 + zF\phi$ is depicted in red.

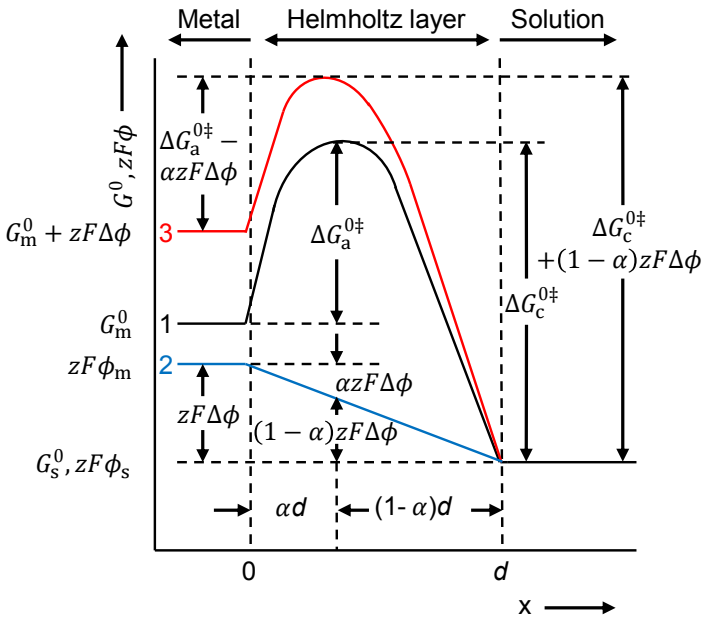


Figure 2:4 Schematic illustration of the activation energies of anodic and cathodic processes in charge-transfer reactions. Figure adapted from reference [471].

Inspection of Figure 2:4 shows that the value of $\Delta G^{0\ddagger} + zF\phi^{\ddagger}$ greatly depends on the location of the activated complex within the Helmholtz layer: at positions close to the outer Helmholtz plane the electric potential has a large influence on the anodic process and only marginally affects the cathodic reaction, and *vice versa* for positions close to the electrode surface. The symmetry of the barrier to electron transfer is reflected in the transfer coefficient α, which can range from 0 to 1. A value close to 0 implies that the transition state closely

resembles the reactants, whereas a value close to 1 represents a transition state similar to the products. In Figure 2:4, α shows after which fraction of the Helmholtz layer the transition state is found, coming from the IHP. For many reactions, α is found to equal 0.5, suggesting that the transition state has intermediate behaviour [470]. Taking into account the electrical term of the activation energy and, as in the derivation of the Nernst equation in Appendix A, expressing the potential difference between metal and solution as $E = \phi_{\mathrm{m}} - \phi_{\mathrm{s}}$, eqs. (2:16) and (2:17) can be rewritten as

$$k_{\mathrm{a}} = k'_{\mathrm{a}} e^{\frac{-(\Delta G_{\mathrm{a}}^{0\ddagger} - \alpha zFE)}{RT}} = k_{\mathrm{a}}^{0} e^{\frac{\alpha zFE}{RT}} \tag{2:18}$$

and

$$k_{\mathrm{c}} = k'_{\mathrm{c}} e^{\frac{-(\Delta G_{\mathrm{c}}^{0\ddagger} + (1-\alpha) zFE)}{RT}} = k_{\mathrm{c}}^{0} e^{\frac{(\alpha-1) zFE}{RT}}. \tag{2:19}$$

The total current density j, defined in eq. (2:13), can be expressed as

$$j = kzF\Gamma. \tag{2:20}$$

Here, Γ refers to the coverage ('area concentration') of the reduced (Red) and oxidised (Ox) species at the inner and outer Helmholtz plane, respectively. Thus, $zF\Gamma$ corresponds to 'charge per area'. Combining eq. (2:20) with eqs. (2:18) and (2:19), the anodic and cathodic current densities are [470]

$$j_{\mathrm{a}} = k_{\mathrm{a}} zF\Gamma_{\mathrm{red}} = k_{\mathrm{a}}^{0} zF\Gamma_{\mathrm{red}} e^{\frac{\alpha zFE}{RT}} \tag{2:21}$$

and

$$j_{\mathrm{c}} = -k_{\mathrm{c}} zF\Gamma_{\mathrm{ox}} = -k_{\mathrm{c}}^{0} zF\Gamma_{\mathrm{ox}} e^{\frac{(\alpha-1) zFE}{RT}}. \tag{2:22}$$

Using the state of electrochemical equilibrium as reference point, eq. (2:11) can be rewritten using eqs. (2:21) and (2:22):

$$j_0 = k_{\mathrm{a}}^{0} zF\Gamma_{\mathrm{red}} e^{\frac{\alpha zFE_{\mathrm{eq}}}{RT}} = k_{\mathrm{c}}^{0} zF\Gamma_{\mathrm{ox}} e^{\frac{(\alpha-1) zFE_{\mathrm{eq}}}{RT}}. \tag{2:23}$$

Combining eqs. (2:21) and (2:22), respectively, with eq. (2:23), and substituting in the overpotential η (defined in eq. (2:12)) leads to

$$j_{\mathrm{a}} = j_0 e^{\frac{\alpha z F \eta}{RT}} \tag{2:24}$$

and

$$j_{\mathrm{c}} = -j_0 e^{\frac{(\alpha-1) z F \eta}{RT}}. \tag{2:25}$$

Substitution of eqs (2:24) and (2:25) into eq. (2:13) gives the Butler-Volmer equation, which describes the current density as a function of overpotential, and lies at the heart of electrochemical kinetics:

$$j = j_0 \left[e^{\frac{\alpha z F \eta}{RT}} - e^{\frac{(\alpha-1) z F \eta}{RT}} \right]. \tag{2:26}$$

Consider again the state of electrochemical equilibrium. Solving eq. (2:23) for the equilibrium potential E_{eq} yields

$$E_{\mathrm{eq}} = -\frac{RT}{zF} \ln \frac{k_{\mathrm{a}}^0}{k_{\mathrm{c}}^0} - \frac{RT}{zF} \ln \frac{\Gamma_{\mathrm{red}}}{\Gamma_{\mathrm{ox}}} \tag{2:27}$$

With $\frac{k_{\mathrm{c}}^0}{k_{\mathrm{a}}^0} = K$ and $\Delta G^0 = -RT \ln K$ (compare eq. (2:14)), conversion of ΔG^0 into E^0 (see eq. (A:15)) leads to

$$E_{\mathrm{eq}} = E^0 + \frac{RT}{zF} \ln \frac{\Gamma_{\mathrm{ox}}}{\Gamma_{\mathrm{red}}}. \tag{2:28}$$

Eq. (2:28) becomes identical to the Nernst equation (eq. (2:7)) by substituting the area concentrations Γ_{red} and Γ_{ox} for the concentrations [Ox] and [Red].

Figure 2:5 depicts the current-voltage behaviour predicted by the Butler-Volmer equation [469]. The solid curve reflects the total current, which is the sum of the anodic and cathodic components (compare eq. 2.13), represented by dashed lines. For large negative overpotentials, the anodic current i_{a} is negligible and the total current equals the cathodic current i_{c}, and *vice versa* for large positive overpotentials. At extreme overpotentials (in

either direction), the current levels off, becoming limited by potential-independent steps, *i.e.* mass-transfer limitations or by the maximum turnover frequency according to eqs. (2:20) – (2:22).

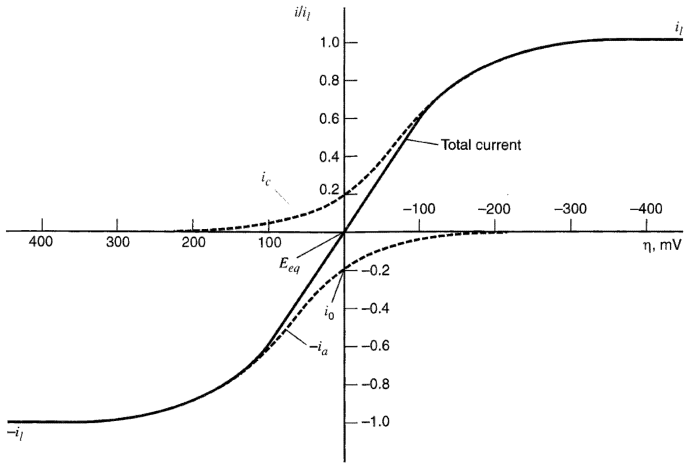


Figure 2:5 Illustration of the Butler-Volmer relationship. The solid curve shows the total current for a system [Ox] + e^- ⇌ [Red] with $\alpha = 0.5$, $T = 298$ K, $i_{l,c} = -i_{l,a} = i_l$ and $i_0/i_l = 0.2$. The anodic and cathodic component currents are shown as dashed lines. Note that cathodic currents carry a positive sign in this Figure. Reprinted with permission from reference [469]. Copyright 2001 John Wiley & Sons, Inc.

2.2.6 Catalytic voltammetry

The reversible catalytic processes displayed by the redox enzymes studied in this thesis (see section 1.6) are characterised, in terms of Butler-Volmer kinetics, by large exchange current densities j_0, meaning that only small overpotentials are required to induce current flow. Their voltammograms generally adhere to the sigmoidal wave shapes predicted by eq. (2:26), in contrast to most synthetic catalysts (see **Figure 1:17** and Figure 1:19 for the case of CO_2 reduction). This discrepancy is illustrated in Figure 2:6, where reversible behaviour, displayed by hydrogenases and CODH, is shown in blue and irreversible reactions are depicted in red.

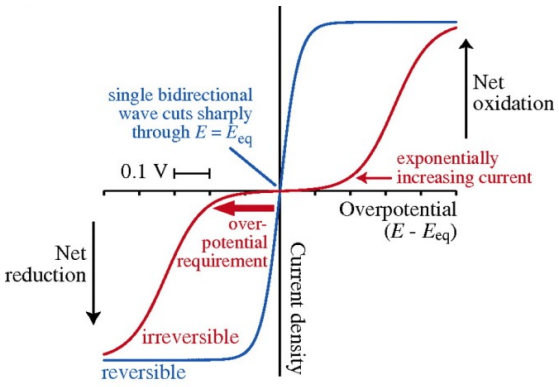


Figure 2:6 Steady-state electrochemical kinetics visualised by cyclic voltammetry. A reversible electrochemical reaction (characterised by a large exchange current density) produces a single sigmoidal wave (blue) that cuts (without inflection) through the zero-current axis at the equilibrium potential (E_{eq}) and achieves a potential-independent limiting current in either direction at relatively low overpotential. If the exchange current density is low, as in most synthetic energy transducing catalysts, the current is negligible around E_{eq} and two sigmoidal waves (red), one for either direction, are separated in potential, emerging from the baseline with an exponential dependence on potential: a substantial overpotential is required to match the current produced by the reversible system. Reprinted with permission from reference [350].

In protein film voltammetry experiments, deviations from the ideal wave shape depicted in Figure 2:6 can arise for example from a distribution of enzyme orientations on the electrode surface [350], resulting in a dispersion of interfacial electron transfer rates. This effect is resembled by a residual slope in the current-voltage curve even at high driving force [473], characteristic for an electron transfer-limited process. The voltammogram of [NiFeSe]-hydrogenase adsorbed on a PGE electrode depicted in Figure 4:3B constitutes an example of catalytic voltammetry limited by interfacial electron transfer. Potential dependent inactivation steps such as the formation of the H_{ox}^{inact} state in [FeFe]-hydrogenases at oxidising potentials can also alter the predicted waveform.

In the absence of such non-idealities and when mass transport is not limiting, the inherent enzyme activity is directly related to the maximum catalytic current, as outlined in the previous section:

$$k_{cat} = i_{lim}/zFA\Gamma. \qquad (2:29)$$

Eq. (2:29) is a variation of eq. (2:20), where k_{cat} denotes the maximum turnover frequency at the limiting current i_{lim}. In order to ascertain k_{cat}, the electroactive coverage Γ needs to be determined. Γ is different to the gross coverage (which is based on how much enzyme is applied to the surface) due to, among other things, the above-mentioned dispersion phenomena [467]. However, in PFE it is rarely possible to ascertain the electroactive coverage of an enzyme as this requires, under non-turnover conditions, the detection and integration of reversible signals (for example, due to FeS redox couples), which are usually vanishingly small. It is the high activity of enzymes that amplifies the current and PFE provides precise and continuous measurement of the *relative* catalytic rates in either direction.

Because of the porosity of the electrode materials used in this thesis and the resulting variation in actual surface area between different experiments, currents i are generally reported instead of current densities j, in conjunction with voltammograms of the respective bare electrode (as is common in PFE).

2.2.7 Chronoamperometry

Among its many different applications, chronoamperometry (CA) is primarily used in this thesis to study and determine the kinetics of enzyme inhibition processes, predominantly in chapter 3. The black trace in Figure 2:7A illustrates the principle: the current is measured as a function of time at a given potential. The potential and time domains are deconvoluted, in contrast to voltammetry experiments. In the particular case of Figure 2:7A, the applied potential is held constant throughout the experiment, but this need not be the case: potential steps can be introduced to induce changes in catalytic activity. However, as described in section 2.2.3, these cause transient non-Faradaic currents that have to be accounted for. In the example of Figure 2:7A, an inhibitor is introduced into the electrochemical cell at $t = 0$,

followed by a decrease in enzyme activity, kinetic analysis of which yields the rate constant of inhibition k_{obs}.

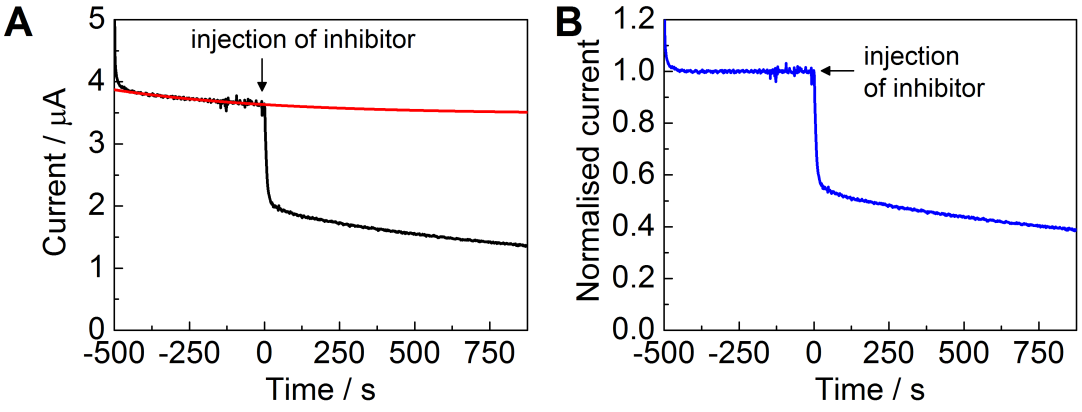


Figure 2:7 (A) Example of a chronoamperometry experiment (H_2 oxidation by *Ca*HydA adsorbed on PGE at 0.05 V *vs.* SHE, pH 6.0), in which an inhibitor (acetaldehyde) is introduced at $t = 0$ (black curve). Underlying film loss is depicted in red. The red curve is obtained by least square analysis of the experimental data using eq. (2:30). (B) Current-time curve obtained after normalisation by dividing the raw data displayed in (A) by the exponential fit.

In the example above, the red curve represents a slow, underlying decay of enzymatic activity that occurs even in the absence of any inhibitor. This process, occurring in every PFE experiment, is commonly known as 'film loss' and arises due to several phenomena including desorption of enzyme from the electrode surface, reorientation of enzyme molecules that results in loss of electronic contact, and denaturation of adsorbed enzyme. The effect of film loss is all the more pronounced when the enzyme-modified electrode is subjected to high overpotentials, high temperatures, and, in rotating disk experiments, high rotation rates. To be able to determine accurate kinetics from chronoamperometry experiments, the experimentalist needs to correct for film loss, which generally follows mono-exponential kinetics:

$$i_{(t)} = (i_0 - i_\infty)e^{\left(\frac{t_0 - t}{\tau}\right)} + i_0. \qquad (2:30)$$

In eq. (2:30), the time dependence of the current (i_t) is defined in terms of the current at the start (t_0) of the data to be fitted (i_0), the time constant of film loss (τ), and the limiting current

of the exponential (i_∞) [474]. Figure 2:7B depicts a normalised current *vs.* time trace, obtained by dividing the experimental data displayed in Figure 2:7A by the exponential fit according to eq. (2:30) (*i.e.* dividing the black curve in Figure 2:7A by the red curve).

To obtain meaningful data from chronoamperometry experiments, the investigator needs to ensure that mass transport and interfacial electron transfer are not limiting (*vide supra*).

2.3 Semiconductor electrochemistry

The modern era of semiconductor electrochemistry started in 1955 with Brattain and Garrett's investigations of the interface between germanium and an aqueous electrolyte [475]. The field emerged rapidly over the following decades, spurred in particular by the 1973 oil crisis and the resulting need to establish ways to convert and utilise renewable sources of energy such as sunlight. Following a decline in the 1980s, triggered, in the U.S., by funding cuts for research into alternative energy sources by the Reagan administration [476], the field came to life again in the 1990s, driven especially by the advent of the dye-sensitised solar cell. Throughout the last decade, research into artificial photosynthesis has been contributing increasingly more. To name but a few, seminal contributions include Fujishima and Honda's demonstration of photoelectrochemical water splitting using TiO_2 [10], Grätzel and O'Regan's DSSC [82], and the Turner water splitting cell, capable of achieving STH efficiencies > 10% [12].

2.3.1 The energy band model

The electronic structure of solids is typically discussed in terms of energy bands, due to the essentially infinite number of atoms that must be considered [340]. Extending the concept of molecular orbitals (MOs), the difference in energy between adjacent MOs is, because of the large number of orbitals, so small that the band can be effectively considered a continuum of energy levels. The highest and lowest energy levels of a band are termed 'band edges' [340].

In contrast to metals, semiconductors have energy gaps between the highest occupied electron band (valence band) and the lowest unoccupied energy band (conduction band) (Figure 2:8). The size of the band gap E_g strongly influences the electrical and optical properties of the material. As illustrated in Figure 2:8, a material is a good conductor of electricity if E_g is small ($E_g << k_BT$) or when the valence and conduction band overlap [469]:

filled and vacant electronic energy levels then exist at virtually the same energy and electrons can move freely from one level to another with only small activation energies being required. Conversely, electrons in a completely filled band have no means for redistributing themselves in response to a field [469].

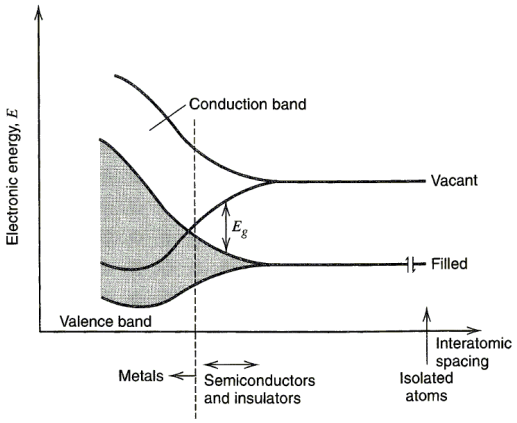


Figure 2:8 Band formation in solids (at the left of the image) by assembly of isolated atoms (characterised by orbitals at the far right) into a lattice. Reprinted with permission from reference [469]. Copyright 2001 John Wiley & Sons, Inc.

If E_g > 1.5 eV, a material is considered an electrical insulator at room temperature [469], but thermal or optical excitation can promote electrons from the valence band to the conduction band, where they can transfer freely among vacant levels within the band, *i.e.* they have electrical mobility. Left behind in the valence band are vacancies, or holes, that also possess mobility, since the valence band electrons can rearrange themselves to shift the spatial location and energy of a vacancy [469]. Electrons and holes exist in a dynamic equilibrium. In an *intrinsic* semiconductor (Figure 2:9A), the carrier densities n_i for conduction band electrons and p_i for valence band holes are equal and can by approximated by the following equation [469,477]:

$$n_i = p_i \approx 2.5\times10^{19} e^{\left(\frac{-E_g}{2kT}\right)} cm^{-3} \text{ (near 25°C).} \quad (2:31)$$

Extrinsic semiconductors are created by doping, *i.e.* substitution of acceptor or donor atoms into the semiconductor lattice. Doping with donor atoms (*e.g.* the introduction of a group V element (*e.g.* phosphorus) into a group IV element semiconductor such as Si) produces *n*-type semiconductors (Figure 2:9B) by creating an energy level E_d just below the conduction band. Most of the donor atoms are ionised at room temperature, each producing a conduction band electron and leaving behind an isolated positive site at the donor atom. Hence, most of the electrical conductivity is due to the conduction band electrons, which are termed majority carriers. Holes are the minority carriers and account for only a small contribution to the conductivity. The opposite situation arises for *p*-type materials (Figure 2:9C) (created by doping with acceptor atoms, *e.g.* introduction of a group III element such as Al into Si), where acceptor levels E_a just above the valence band are created. This results in the formation of mobile holes in the valence band and isolated, negatively charged acceptor sites. In this case holes are majority carriers and electrons are minority carriers.

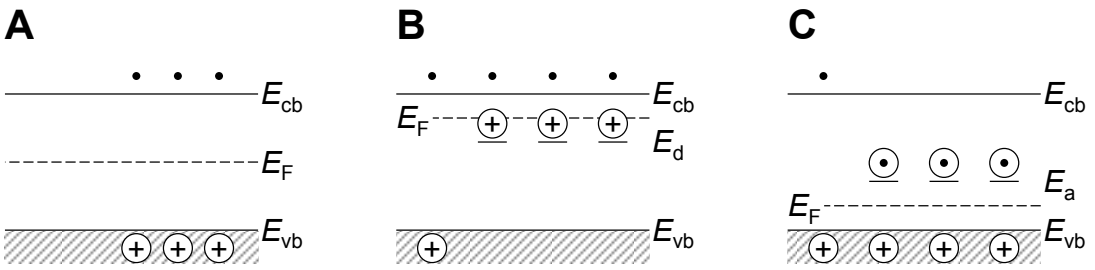


Figure 2:9 Schematic depictions of the energy levels (bands) in (A) intrinsic, (B) *n*-type, and (C) *p*-type semiconductor materials. Adapted from references [340] and [469].

Apart from impurity insertion as a means of doping, non-stoichiometric compound semiconductors also give rise to *n*- or *p*-type behaviour [478]. This phenomenon is exemplified in section 2.3.3.3 using TiO_2 and NiO electrodes.

The Fermi level E_F is defined as the energy at which the probability of electron occupation is 1/2 [478]. In an intrinsic semiconductor at room temperature, E_F lies at the

midpoint of the band gap (Figure 2:9A). Conversely, in extrinsic semiconductors the location of E_F is dependent on the doping level [469]: for moderately to heavily doped *n*-type solids E_F lies slightly below the conduction band edge, and for moderately to heavily doped *p*-type materials the Fermi level is located just above the valence band edge. Thermodynamically, the Fermi level of a phase α can be interpreted as the electrochemical potential of an electron in α [469] (compare eq. (A:2)), *i.e.* the Fermi level corresponds to the electrochemical potential of the electron in the solid [479]:

$$E_F^\alpha = \tilde{\mu}_e^\alpha = \mu_e^\alpha - e\phi^\alpha \text{ (in eV)}. \quad (2:32)$$

The absolute value of E_F depends on the reference state: using zero for a free electron in vacuum, Fermi levels in semiconductors and metals can be determined by measuring the work function (conduction band edge energies can be determined from the electron affinity) [469]. As in metal electrodes, the Fermi level in semiconductors changes upon application of a potential [340].

2.3.2 The semiconductor/solution interface

Consider the formation of a junction that forms between a(n idealised) semiconductor surface and a solution containing a redox-couple Ox/Red upon immersion of the semiconductor into the liquid redox-electrolyte. When thermodynamic equilibrium is attained, the electrochemical potentials $\tilde{\mu}_e$ must be equal in both phases. The redox potential of the electrolyte solution, given by the Nernst equation eq. (2:7), can be identified with the Fermi level in the electrolyte [478].[ii] In other words, the Fermi levels equilibrate under transfer of charges between the semiconductor and the solution phase [469]. If E_F lies above the solution potential, as is typically the case for *n*-type materials at open-circuit [340], electrons will

[ii] In electrochemistry the standard hydrogen electrode is traditionally used as reference scale, whereas it is common in solid-state physics to use the electron energy in vacuum. The SHE electrode lies at approximately −4.5 eV *vs*. the vacuum level [478].

transfer from the semiconductor to the solution, with the former becoming positively charged (depleted) and the latter carrying a negative charge (Figure 2:10A). Charge-transfer equilibration in a doped semiconductor removes carriers from the most easily ionisable sites, *i.e.* dopant atoms [480]. In principle, it could also be the electrochemical potential of the solution that shifts during equilibration. However, in accordance with double layer theory, the side of the interface containing the lower concentration of charge carriers experiences the greater change in potential upon a potential modulation [479], and even with dilute concentrations of redox species (< 10 μM), the number of available states per unit energy in the solution far exceeds the number present in a semiconductor [481]. Hence, there is little negative movement of the electrochemical potential of the solution during equilibration upon formation of a semiconductor/liquid junction, and the Fermi level for both phases in the equilibrium is principally equal to the initial value of the solution redox potential [481].

Unlike in metals, the excess charge in the semiconductor after equilibration does not reside on the surface; it is instead distributed across the so-called *space-charge* region. This region is comparable to the diffuse double layer found at the electrode interface in solution (see section 2.2.3) and extends well into the material, with nominal dimensions of the so-called depletion layer width W typically being in the range of $10-1000$ nm [478]. The corresponding, adjacent Helmholtz layer width, in contrast, is normally in the range of $0.4-0.6$ nm. Therefore, assuming a simple model in which the space-charge region and the Helmholtz layer comprise two capacitors in series, the space-charge region usually determines the total capacity of the interface (in a metal, in contrast, the high electronic conductivity cannot support an electric field within the material; almost all the potential drop at the interface occurs within the Helmholtz layer) [478].

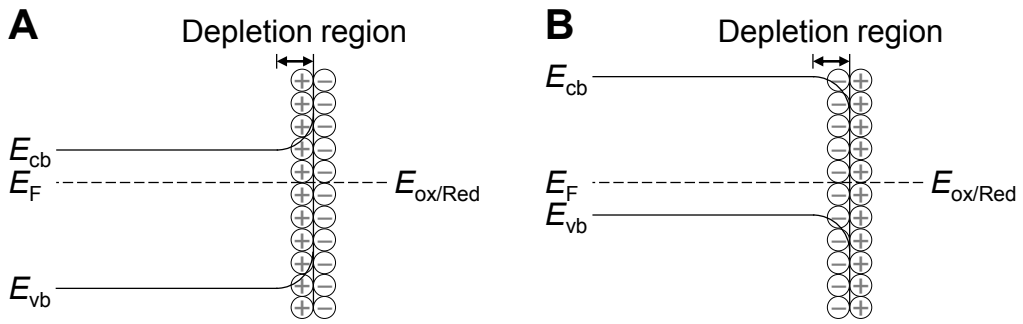


Figure 2:10 The semiconductor solution interface at open-circuit for (A) an *n*-type semiconductor and (B) a *p*-type semiconductor. Adapted from reference [340].

The electric field in the space-charge region affects the electrochemical potentials of electrons, *i.e.* their local energy, and the band energies are different to the field free semiconductor bulk [469]. The band positions at the interface do not change, as almost the entire potential drop between bulk semiconductor and solution occurs across the space-charge region, rather than at the semiconductor/solution interface. The number of charges that need to be transferred is generally far larger than the number of dopant atoms that are present in one atomic layer of the solid [480] (the implication being that the above-mentioned depletion width W is a function of the donor density, N_D).

A positive charge in the space-charge region causes the band energies to become more negative with increasing distance from the surface, until they remain flat in the field free bulk. This effect is termed *band-bending*. In the example of Figure 2:10A, the bands bend upward with respect to the energy levels in the bulk semiconductor. The space-charge region in this case is also referred to as depletion layer, as the majority charge carriers of the semiconductor have been removed from this region [340]. Consistent with the electric field in the depletion layer, excess electrons would move into the semiconductor bulk and holes would migrate towards the surface. The opposite situation arises for *p*-type materials (Figure 2:10B), where, at open-circuit, the Fermi level is generally lower than the redox potential of

the electrolyte [340]. Hence, a negative charge is associated with the space-charge region and the bends bend downward, again forming a depletion layer.

If the Fermi level of the semiconductor and the redox potential of the solution have the same energy even *before* equilibration, there is no net transfer of charge and hence no band-bending [340]. The corresponding potential is termed the flat-band potential $E_{fb.}$ No electric field and no space-charge region exist at $E_{fb.}$ It is worth noting that electrostatic adjustments analogous to the band-bending phenomena at the semiconductor/electrolyte interface described in this section occur whenever two dissimilar phases are in contact, *e.g.* in the case of semiconductor/metal or semiconductor/gas junctions [478].

2.3.3 The semiconductor/electrolyte junction under applied bias

2.3.3.1 Qualitative description of the semiconductor/liquid interface under applied bias

Further to the properties of semiconductor/electrolyte junctions at open circuit, interesting effects arise upon application of an electrostatic potential. As mentioned in the previous section, applying a potential shifts the Fermi level of the semiconductor electrode, similarly to metallic electrodes. The band edges in the interior of the semiconductor (*i.e.* the bulk, away from the space-charge region) undergo a concomitant change in energy [340].

Assuming that all of the applied bias drops across the space-charge region (compare section 2.3.2), only the majority carrier population within the semiconductor at the surface is modulated, not the potential drop across the Helmholtz layer [478]. This means that the band edge positions at the interface (not the Fermi level) are pinned and thus *not* affected by changes in band energies occurring in the field free semiconductor bulk and the space-charge region upon application of a potential. Consequently, the magnitude and direction of band-bending change with applied potential [340].

One can now distinguish between three different scenarios that are all depicted, schematically, in Figure 2:11.[iii] In case of an an *n*-type semiconductor: (i) the applied potential E is equal to the flat-band potential E_{fb}. In this case, band-bending does not occur, as outlined in the previous section, because there is no net transfer of charge at equilibrium and no space-charge region exists. (ii) Formation of an *accumulation* layer. Applying a potential $E < E_{fb}$ to an *n*-type semiconductor shifts its Fermi level upwards, causing the bands to bend downward, since the band edge positions at the interface remain fixed (Figure 2:11B). An excess of majority carriers in the space charge region exists and the material becomes increasingly conductive [340]. The surface becomes degenerate when the Fermi level contacts the conduction band edge and the semiconductor then exhibits metal-like electrochemistry [482]. Making the potential even more negative will cause a potential difference to develop across the Helmholtz layer instead of the electrode. (iii) When $E > E_{fb}$ (Figure 2:11C), a depletion layer is formed, having properties described in section 2.3.2. *p*-Type materials show equivalent behaviour (Figure 2:11D–E): with holes being the majority carries and the Fermi level located close to the valence band, a depletion region arises at potentials negative of E_{fb} and accumulation occurs when the potential is increased with respect to the flat-band potential.

[iii] Formation of 'deep depletion' and 'inversion' layers is not discussed herein as these are not relevant to this thesis.

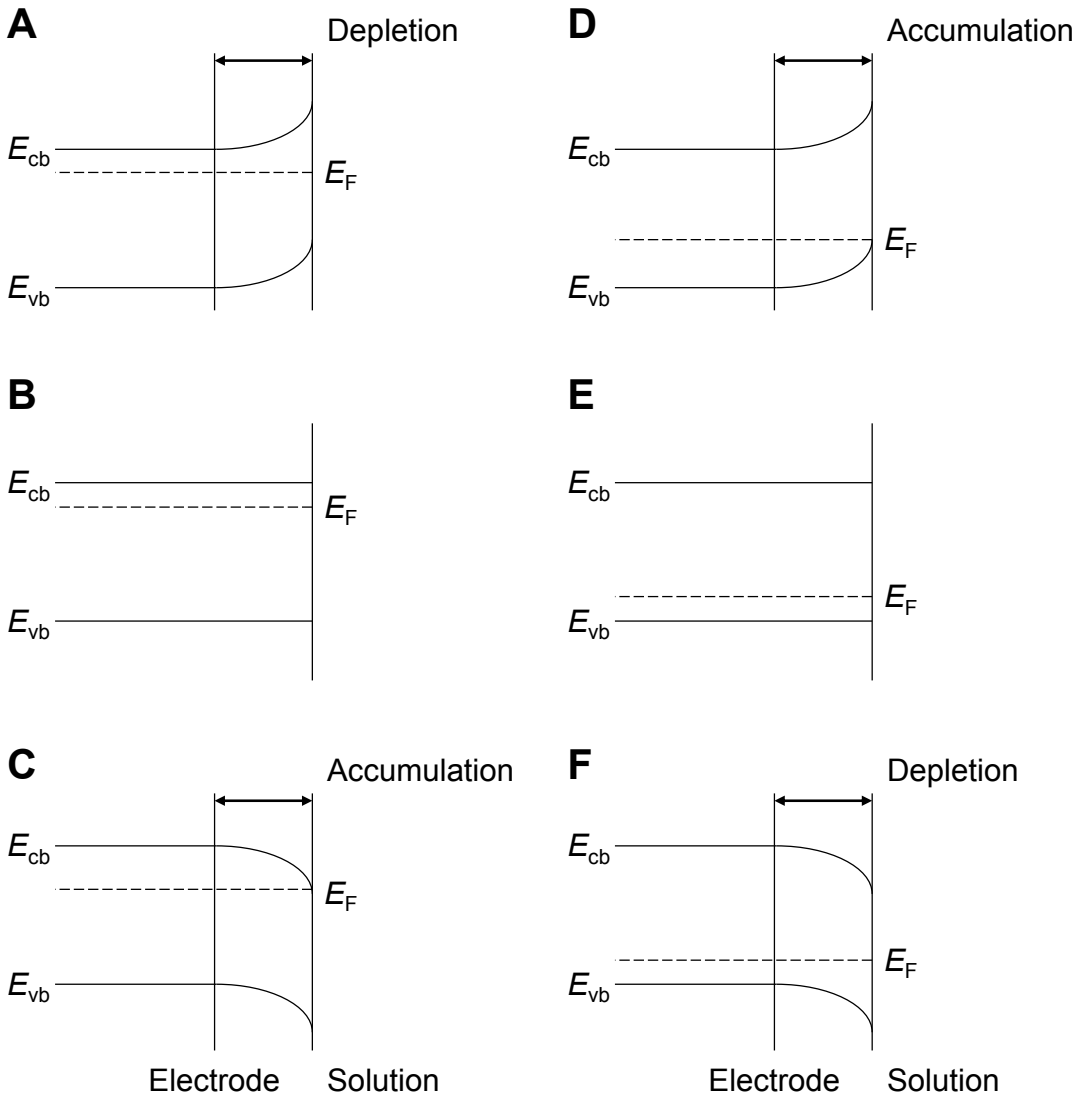


Figure 2:11 Schematic illustration of the semiconductor/electrolyte interface under applied bias, in the case of *n*-type semiconductors (A) – (C), and for *p*-type materials (D) – (F). $E > E_{fb}$ (A),(D); $E = E_{fb}$ (B),(E); $E < E_{fb}$ (C),(F). Adapted from reference [340].

2.3.3.2 Current potential curves of semiconductor electrodes in the dark

In contrast to conducting electrodes such as PGE, electron transfer processes at the semiconductor/electrolyte interface strongly depend on the density of available carriers at the semiconductor surface. In the dark, electron transfer is usually dominated by the majority carriers. Moderately doped *n*-type materials, for instance, can effect reduction reactions but not oxidations [469]. In analogy to eq. (2:20), the cathodic current corresponding to the reduction of a species Ox by an *n*-type semiconductor is given by the following equation:

$$i_c = -zFAk'_c n_{sc}[\mathrm{Ox}], \tag{2:33}$$

where n_{sc} (cm^{-3}) is the concentration of electrons at the interface and k'_c represents the heterogeneous electron transfer rate constant, the units of which are $cm^4\ s^{-1}$, different from a metal electrode, where the high carrier density is included in the rate constant (k_c in $cm\ s^{-1}$) [469]. In other words, the second order kinetics stemming from the two multiplied concentration terms in eq. (2:33), n_{sc} and [Ox] (each comprising a cm^{-3} term), require the $cm^4\ s^{-1}$ dimensions of k'_c [478].

p-Type materials, in turn, generally able to effect oxidation processes in the dark but not reductions, show the following anodic current for the oxidation of a species Red in the redox electrolyte:

$$i_a = zFAk'_a p_{sc}[\mathrm{red}], \tag{2:34}$$

where k'_a is the heterogeneous rate constant for oxidation (of the same dimensions as k'_c) and p_{sc} represents the concentration of holes at the surface (cm^{-3}) [469]. In contrast to conducting electrodes, both the rate constants k'_c and k'_a in eqs. (2:33) and (2:34), and the surface concentrations (n_{sc} and p_{sc}, respectively) depend on the applied potential. The concentrations of majority carriers on the surface respond to potential changes by

$$n_{sc} = N_D e^{\left[\frac{-F(E-E_{fb})}{RT}\right]} \tag{2:35}$$

and

$$p_{sc} = N_A e^{\left[\frac{F(E-E_{fb})}{RT}\right]}. \tag{2:36}$$

In eqs. (2:35) and (2:36), N_D and N_A represent the donor and acceptor densities, respectively, and ($E - E_{fb}$) is the amount of band-bending (also known as ΔE_{sc}) [478]. The potential dependences of k'_c and k'_a in eqs. (2:33) and (2:34) are a result of the potential drop ΔE' across the Helmholtz layer at the semiconductor-electrolyte interface [469]. They follow

Butler-Volmer kinetics and can be described by eqs. (2:18) and (2:19), using ΔE' instead of E.

Eqs. (2:35) and (2:36) allow the quantitative interpretation of the phenomena described in section 2.3.3.1. Under conditions of depletion, *i.e.* at potentials positive of E_{fb} in *n*-type semiconductors and negative of E_{fb} in *p*-type materials, the majority carrier concentrations in each case are lower than the respective density of dopants ($n_{sc} < N_D$ and $p_{sc} < N_A$). Because the potential drop under depletion is distributed across the space-charge region and not the Helmholtz layer, the respective current voltage curves are governed by the carrier concentrations rather than k'_c and k'_a [469]. The currents resulting from applying such a so-called reverse bias are potential independent and remain low, the reason being the lack of minority carriers in the dark [340,478].[iv] Under accumulation (forward bias), *i.e.* $E < E_{fb}$ in *n*-type semiconductors and $E > E_{fb}$ in *p*-type electrodes, the respective currents are exponentially dependent on the potential until the surface becomes degenerate, when the behaviour becomes similar to that of a metallic electrode [340]. The previous section outlined that a further increase in driving force will cause the potential difference to distribute across the Helmholtz layer rather than the electrode and this can now be rationalised as the further change in potential no longer affecting n_{sc} or p_{sc} significantly, but instead causing changes to ΔE' and hence k'_c and k'_a (experimentally verifiable by transfer coefficients α different to those arising under depletion) [469].

2.3.3.3 Case studies: TiO_2 and NiO

This section will reinforce the properties of semiconductor liquid junctions established in the previous two sections by looking at two specific examples: the *n*-type semiconductor TiO_2 and the *p*-type material NiO. Both are non-stoichiometric materials (see section 2.3.1) and

[iv] Dark currents will arise at very high overpotentials due to breakdown phenomena.

wide band gap semiconductors, transparent to visible light ($E_g > 3.0$ eV in both materials). Figure 2:12 depicts a cyclic voltammogram of a TiO_2 film electrode.

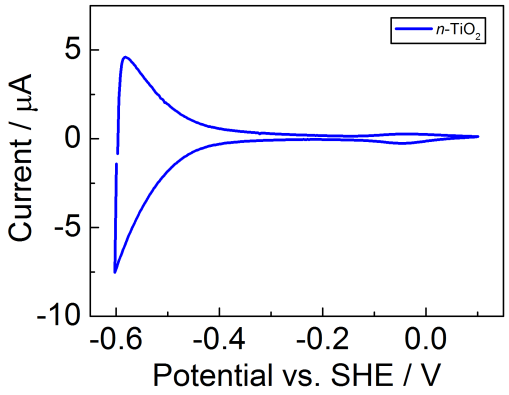


Figure 2:12 Cyclic voltammogram of a TiO_2 electrode. Conditions: 0.2 M MES buffer (pH 6.0); 20 °C; scan rate: 10 mV s^{-1}; N_2 atmosphere.

Due to its inherent non-stoichiometry (oxygen vacancies), TiO_2 is a rather heavily doped *n*-type semiconductor [341]. In Figure 2:12 there is virtually no current at potentials above −0.4 V, in agreement with the theoretical assessment in section 2.3.3.2: the TiO_2 flat-band potential lies at approximately −0.5 V *vs*. SHE at pH 6.0 (measured in section 4.2.3.1) and a depletion layer is formed upon scanning in anodic direction. When E_{fb} is approached in cathodic direction, (trap levels below the conduction band are being populated [483] before) conduction band states become occupied and the current increases exponentially in agreement with eq. (2:35), showing that the carrier concentration n_s is the dominating factor. In chemical terms, the signature 'trumpet shape' of the voltammogram arises from the reversible reduction of Ti(IV) surface centres to Ti(III), which is accompanied by uptake of one proton per site and can be described by the following equation [484]:

$$Ti^{4+}O_2 + e^- + H^+ \rightarrow Ti^{3+}O(OH). \qquad (2:37)$$

These Ti(III) sites are reoxidised when the potential is raised. The minor peak at *ca*. –0.1 V corresponds to the population of surface trap states [485,486] lying about 0.5 eV below the conduction band edge [487].

Figure 2:13 shows a cyclic voltammogram of NiO, which, upon calcination in air, forms a $Ni_{1-x}O$ non-stoichiometry. As expected for a *p*-type semiconductor, the current-voltage curve displays opposite behaviour compared to *n*-TiO_2. The material is essentially an insulator at cathodic potentials and conductivity only commences at positive potentials (the flat-band potential of NiO is approximately 0.61 V *vs.* SHE at pH 6.0 [488]). The increase in current is attributed to the oxidation of surface Ni(II) to Ni(III), coupled with desorption of protons from the surface. It is the presence of these Ni(III) surface sites that is believed to be responsible for the conductivity of NiO [489]. Whereas electron transport in TiO_2 is predominantly conduction band mediated [489], hole conduction in NiO is mainly occurring at the mesoporous NiO/electrolyte interface, most likely by hopping of charges, with holes being present as oxidised Ni(III) atoms [490].

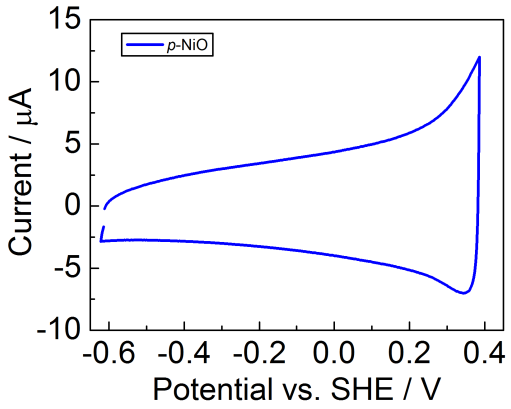


Figure 2:13 Cyclic voltammogram of a NiO electrode. Conditions: 0.2 M MES buffer (pH 6.0); 20 °C; scan rate: 30 mV s^{-1}; N_2 atmosphere.

2.3.4 Photoeffects at the semiconductor/electrolyte interface

We now turn our attention to the semiconductor/liquid junction under illumination (*i.e.* we finally turn the light on[v]). Upon irradiation of sufficient energy to overcome E_g, electrons can be promoted from the semiconductor valence band into the conduction band. If this process occurs within the semiconductor bulk, recombination under release of heat is likely to prevail [340]. However, if excitation takes place in the space-charge region, the electric field can effect *charge-separation*. Consider an *n*-type semiconductor at potentials positive of E_{fb}, where a depletion layer exists and the bands bend upwards (Figure 2:11A). Light-excitation will cause the excited conduction band electron to move into the semiconductor bulk; holes, in contrast, will migrate to the interface, where they are available for oxidative chemistry. Hence, *n*-type semiconductors behave as dark cathodes and photoanodes.

Figure 2:14 illustrates this behaviour by showing an idealised current-voltage curve of an *n*-type semiconductor both in the dark (A) and under irradiation (B). In the dark, a reductive current arises at potentials below $E_{fb,}$ increasing exponentially with driving force as established in section 2.3.3. An accumulation layer forms and the electrode will display metallic-like behaviour once the surface becomes degenerate. At potentials positive of the flat-band potential, no oxidative current can be observed due to the formation of a depletion layer.

[v] The author apologises for this pun.

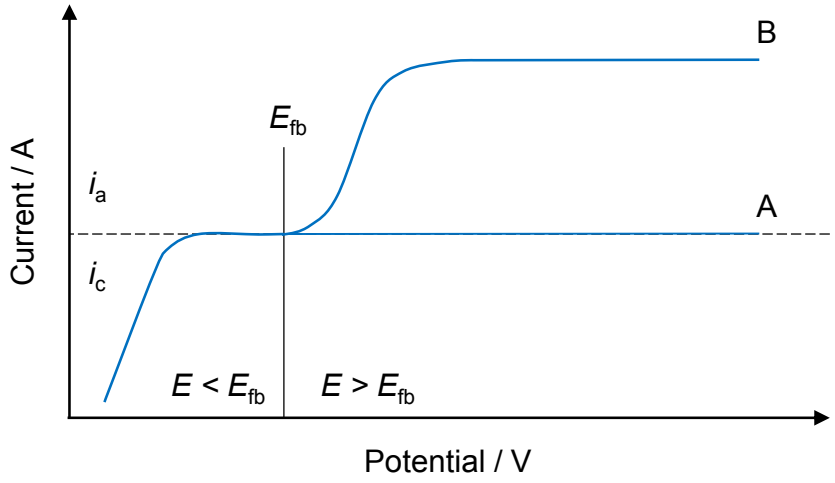


Figure 2:14 Current-voltage curve showing the ideal behaviour of an *n*-type semiconductor in the dark (A) and under irradiation (B). Adapted from reference [340].

Upon irradiation, the behaviour at potentials negative of E_{fb} is virtually indistinguishable from the dark-current. Photoeffects are generally not observed at *n*-type materials under accumulation [469]; with the Fermi level being very close, energetically, to the conduction band, no significant current enhancement can be expected under irradiation. In a doped semiconductor, photoeffects are greatest when the minority carriers dominate the electrode response, due to the enormous disparity in the concentrations of the two types of charge carriers [479]. At potentials positive of E_{fb}, the electric field of the space-charge region in the depletion layer assists charge-separation and a photocurrent is observed. Here, the minority carriers (holes) are driving the oxidative chemistry at the semiconductor/electrolyte junction. It is important to note that the photooxidation of the species Red in the redox-electrolyte will occur at potentials less than those required at an inert metal electrode in the dark [469], due to the additional driving force provided by illumination with light energy. The notion of apparent *underpotentials* in photoelectrochemical reactions is of particular importance for chapter 5 of this thesis. Analogous concepts apply to *p*-type materials, which act as dark anodes and photocathodes.

In quantitative terms, the current-potential curve in Figure 2:14 can be interpreted by simply adding the photocurrent i_{ph} (minority carrier component) to the dark current component (due to majority carriers) given in eqs. (2:33) and (2:34), respectively, noting that the two components are of different sign [478], *i.e.* they represent opposite directions of flow. Assuming the absence of any recombination in the space-charge layer, that all holes generated within or reaching the depletion layer cause photocurrent (which is not true for potentials close to E_{fb}), and, further, the absence of mass transfer or kinetic limitations, the photocurrent density j_{ph} can be expressed by the Gärtner equation [491] as the product of the incident photon flux I_0 (photons per second per area) and the effective quantum yield Φ [479]:

$$j_{ph} = I_0 \Phi = 1 - \frac{e^{-\alpha W}}{1 + \alpha L}. \tag{2:38}$$

In eq. (2:38), j_{ph} depends on the absorption coefficient α, the minority carrier diffusion length L (L_p for holes and L_n for electrons), and the width of the depletion layer, W, introduced in section 2.3.2. In regards to the example in Figure 2:14 of an *n*-type semiconductor under illumination, the fact that eq. (2:33) is offset by eq. (2:38) can be rationalised with the plateau photocurrent being proportional to the photon flux [478]. As long as the depletion layer thickness exceeds the depth of charge carrier generation, the photocurrent quantum efficiencies are independent of the applied potential and the current plateaus. The space-charge layer thickness decreases when the applied potential approaches E_{fb} and recombination rates increase because electrons and holes are no longer being separated by the electric field. The effect is a sharp decrease in photocurrent, which merges with the dark current near E_{fb} [479].

2.3.5 Measurement of the flat-band potential

The flat-band potential is one of the most important parameters in a semiconductor electrode; the concept of E_{fb} is central to chapter 4 of this thesis and also plays an important role in chapters 5 and 6. Knowing E_{fb}, the position of the band edges on the electrochemical scale, the direction of band-bending and, in favourable cases, its magnitude can be derived [479]. The flat-band potential of a semiconductor can be determined by several experimental techniques, most notably by measuring the photocurrent onset potential, the open-circuit photopotential as a function of radiation intensity, or the capacitance of the space-charge region. This section will briefly review the three different methods, emphasising the role of capacitance measurements.

2.3.5.1 Photocurrent onset potential

As established in the previous section using the example of an *n*-type semiconductor, the photocurrent diminishes as E_{fb} is approached. Its total disappearance at the photocurrent onset potential E_{on} should coincide with the flat-band potential [341,492].[vi] However, it should be noted that the absolute values obtained by this method are often shifted (anodically in the case of *n*-type semiconductors and cathodically for *p*-type materials) as recombination becomes practically complete already at potentials with *ca.* 0.1 – 0.3 V from E_{fb} [341]. While E_{on} can be measured relatively easily, the large uncertainty in the measurement and the arbitrariness in deciding at what potentials the photocurrent is perceptible above the dark current constitute significant disadvantages [479].

2.3.5.2 Open-circuit photovoltage

Another simple method to determine E_{fb} is to measure the open-circuit photopotential E_{oc} of the electrochemical cell under radiation of varying intensity [340]. Consider again an *n*-type

[vi] More precisely, E_{fb} is the potential at which the dark current and the current component due to illumination are equal.

semiconductor in contact with a redox-electrolyte. As described in section 2.3.2, the two phases will equilibrate at open-circuit under the formation of a depletion layer in the semiconductor. Upon irradiation with light energy $h\nu > E_g$, photogenerated holes move to the surface (where some of them might be captured by reduced molecules in solution) and excited electrons move into the conduction band bulk where they, once having left he depletion layer, have no possible exit [479]. Consequently, the Fermi level[vii] increases, reflecting the change in conduction band occupancy; it is approaching but not exceeding E_{fb}. Hence, under sufficiently high light intensity, E_{oc} becomes constant, attaining a limiting plateau at E_{fb} [340,341]. Similar to measuring the photocurrent onset potential, a weakness of this method is that surface recombination will decrease the open circuit photovoltage, meaning the experimentally determined flat-band potential is shifted from its true value [479].

2.3.5.3 The Mott-Schottky plot

The third and most important commonly employed method to determine E_{fb} of a semiconductor is the Mott-Schottky measurement. One of its greatest advantages is that it can be performed in the absence of light, a factor that is of particular importance when the semiconductor of interest undergoes photocorrosion processes that alter its surface. Mott-Schottky measurements are based on the capacitance associated with the space-charge layer.

The different regions around the semiconductor/electrolyte interface (*i.e.* the space-charge layer, the Helmholtz layer, and also the diffuse layer) have associated capacitances, as they are considered planes of charge separated by distance [479]. The three capacitances are in series with the smallest one dominating the overall capacitance C_{dl} (dl = double layer), as the latter depends on the reciprocals of the separate contributions:

[vii] More precisely, it is now a quasi-Fermi level, since the system is no longer in thermodynamic equilibrium.

$$\frac{1}{C_{\mathrm{dl}}} = \frac{1}{C_{\mathrm{sc}}} + \frac{1}{C_{\mathrm{H}}} + \frac{1}{C_{\mathrm{diff.}}}. \tag{2:39}$$

We already established in section 2.3.2 that the capacitance of the space-charge layer usually dominates over the capacity of the Helmholtz layer. The capacitance of the diffuse layer $C_{\mathrm{diff.}}$, omitted in section 2.3.2, is generally so large that it can be completely neglected [479]. Thus, the capacitive properties of the space-charge region govern the total double layer capacitance C_{dl}. Under the conditions of a depletion layer, C_{sc} varies with the width of the space-charge region, which in turn is a function of the potential relative to E_{fb}. The Mott-Schottky equation (derived in Appendix B) incorporates these factors into one equation [479]:

$$C_{\mathrm{sc}}^{-2} = \frac{2}{\varepsilon\varepsilon_0 e_0 N_{\mathrm{D}}}\left(E - E_{\mathrm{fb}} - \frac{k_{\mathrm{B}}T}{e_0}\right). \tag{2:40}$$

In eq. (2:40), ε is the dielectric constant in the direction normal to the surface, ε_0 is the permittivity of free space, e_0 is the electron charge, and the other parameters are as defined earlier. In the depletion region, plotting the reciprocal square of the capacitance against the applied potential should yield a straight line, from which the doping level (slope) and the flat-band potential (intercept) can be determined.

Building upon the excellent introduction by Fisher [470], I will now briefly describe how to experimentally measure the capacitance of the space-charge region, and the capacitance of the electrode/solution interface in general (*i.e.* including electrodes of metallic conductivity). The capacitance was defined in eq. (2:4) as the ratio q/E, *i.e.* the charge 'stored' on the capacitor plates upon application of a potential difference E across them. For a simple capacitor where the plates are separated at a fixed distance, the capacitance predicted according to eq. (2:4) is constant. In an electrochemical cell the problem is more complex as the double layer capacity depends upon the applied potential. Therefore, in electrochemical experiments the differential capacitance C_{d} characterises the electrode/solution interface and

is the variable of interest. For a metal/solution interface with an electrolyte of constant composition, C_d is defined as [470]:

$$C_d = \left(\frac{dq}{dE}\right) = \left(\frac{\partial q^m}{\partial \Delta\phi_{m/s}}\right). \quad (2:41)$$

The differential capacitance is measured by the technique of a.c. impedance spectroscopy, where an oscillating, sinusoidal potential $E(t)$ is applied across the cell:

$$E(t) = E_m \sin(\omega t). \quad (2:42)$$

In eq. (2:42), E_m represents the maximum amplitude and ω is the angular frequency in rad s^{-1} ($\omega = 2\pi\nu$, with ν being the (ordinary) frequency in Hz). At first, the response of a simple capacitor to an a.c. voltage will be assessed. This will provide the basis for interpreting real electrode/solution interfaces [470]. No Faradaic d.c. current will pass if the electrode potential is insufficient to cause any electrolysis, but the sinusoidal potential in eq. (2:42) induces an a.c. capacitive current by

$$i(t) = i_m \sin(\omega t + \theta), \quad (2:43)$$

where i_m denotes the maximum current amplitude and θ characterises any phase difference between the applied potential and the detected current. Using eq. (2:6) that relates current and capacitance, the differential capacitance C_d can be substituted into eq. (2:43):

$$\begin{aligned} i(t) = C_d \frac{dE}{dt} = C_d \frac{d(E_m \sin(\omega t))}{dt} = C_d(\omega E_m \cos(\omega t)) \\ = C_d\left(\omega E_m \sin\left(\omega t + \frac{\pi}{2}\right)\right), \end{aligned} \quad (2:44)$$

implicating the phase difference $\theta = \pi/2$.

The *impedance* Z is often used to describe the response of an electrical circuit to an applied a.c. voltage:

$$Z(\omega) = \frac{E(t)}{i(t)}. \quad (2:45)$$

Being similar to Ohm's law (where the resistance $R = E/i$), the impedance provides a measure of how a current is 'impeded' by the circuit, *i.e.* it provides a generalisation of the idea of the 'resistance' of a circuit [470]. As established in eq. (2:44), for a capacitor the phase difference between current and voltage is $\pi/2$. The conduction is indirect and results from the attraction or repulsion of electrons from the plates as their potential changes [470]. Conversely, for a single resistance the voltage and current are in phase ($\theta = 0$), since charge can flow directly through a resistor. For a real, complex circuit the phase difference can take any value and also change with frequency. The impedance as a function of frequency can then be described, mathematically, by

$$Z(\omega) = Z' \sin(\omega t) - Z'' \cos(\omega t), \tag{2:46}$$

where Z' represents the 'real' component of the impedance ('in-phase') and $-Z''$ the imaginary part ('out-of-phase'). The impedance can be conveniently plotted as $-Z''$ (ordinate) *vs.* Z' (abscissa), a form also known as Nyquist plot (typically, Z at each frequency is plotted as a point with coordinates [Z',$-Z''$], and the resulting vector from the origin of the coordinate system to this point represents the impedance, having a magnitude equal to the length of the vector and a phase difference of θ) [470]. In the example of a simple capacitor, the real and imaginary parts of the impedance can be written as

$$Z' = 0 \qquad -Z'' = \frac{1}{\omega C_{\mathrm{d}}}. \tag{2:47}$$

This general description of the basic principles that underlie a.c. impedance spectroscopy allows the interpretation of the more complex impedance response of an electrochemical cell. Consider an *n*-type semiconductor/electrolyte junction in the depletion region, where the semiconductor is employed as working electrode in a conventional three-electrode cell and no electrolysis occurs. The aim is to measure the capacitance of the space-charge layer C_{sc}, so as to be able to determine E_{fb}.

For this cell configuration, a simple *equivalent circuit* can be drawn that represents the different cell components. The circuit contains a capacitor that corresponds to the double layer at the electrode according to eq. (2:39) (in this case the desired variable C_{sc}), connected in series with a resistor that accounts for the solution resistance (Figure 2:15A). The real and imaginary components of the impedance are:

$$Z' = R_s \qquad -Z'' = \frac{1}{\omega C_{sc}}, \tag{2:48}$$

and the capacitance of the space-charge layer can be calculated from the imaginary component of the impedance [340,341]. The Nyquist plot corresponding to this circuit consists of a vertical line offset from the Z'' axis by the solution resistance R_s (Figure 2:15B).

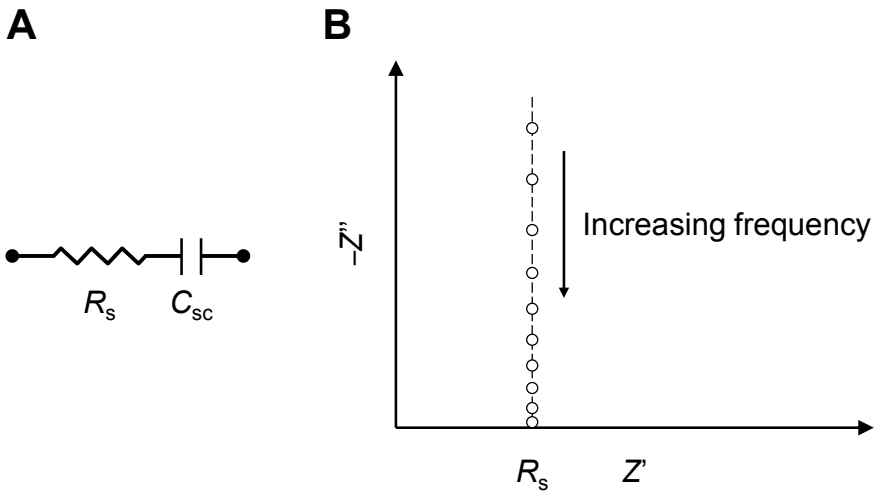


Figure 2:15 Equivalent circuit (A) and Nyquist plot (B) for the semiconductor solution interface.

Experimentally, modern configurations employ an electrochemical cell coupled to a frequency response analyser, allowing impedance plots to be generated over frequencies in the range of $10^{-2} - 10^{5}$ Hz [470]. The potential dependence of the capacitance can be measured at constant, set frequencies, or, alternatively, the impedance can be recorded over a range of frequencies at different potentials. In the latter case, the capacitance can then be calculated at selected frequencies for each potential, or the equivalent circuit model can be

used to fit the experimental data, automatically generating the capacitance values at different frequencies [340]. In this type of analysis, it is common to plot the impedance components against the frequency domain in what is known as a 'Bode plot'.

To give the reader a more complete picture, I will conclude this section by briefly discussing, qualitatively, the impedance of an electrochemical cell under conditions where electron transfer reactions take place. This general description is not limited to the semiconductor/electrolyte interface and also holds for conductive electrodes. Under conditions where an electrolytic reaction takes place at the electrode, the situation is more complex than in the example above and the simple equivalent circuit needs to be expanded to account for the Faradaic charge transfer reaction and also for diffusion. Figure 2:16A depicts an equivalent circuit known as 'Randles' circuit [493] that includes these components.

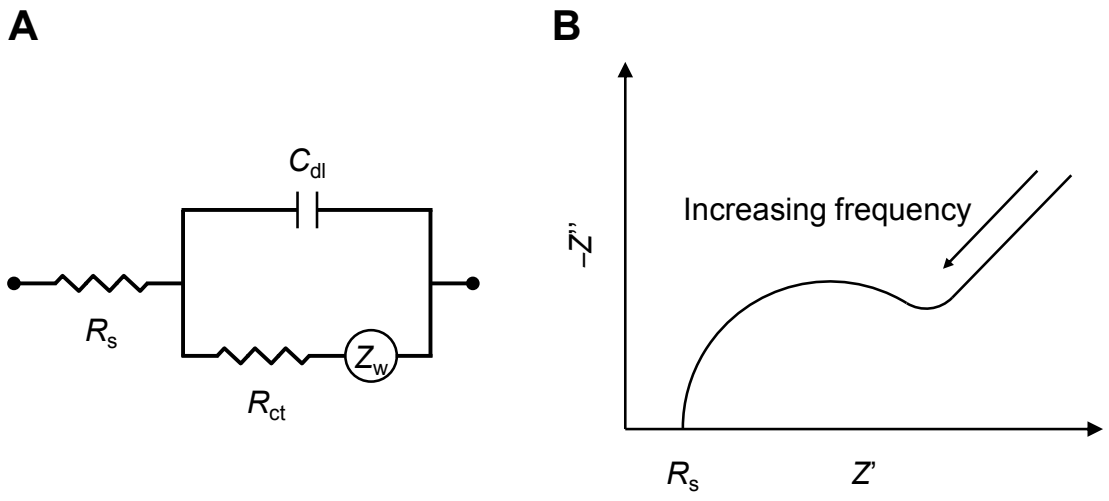


Figure 2:16 (A) Randles circuit and (B) corresponding Nyquist plot.

The charge-transfer resistance R_{ct}, which models Faradaic charge-transfer, is connected in series to the Warburg impedance Z_w, which measures the difficulty of mass transport of the electroactive species [494]. The double layer capacitance C_{dl} (eq. (2:39)) is connected in parallel to these two elements, meaning the current can either pass through the capacitor, the

restive components, or both at the same time. The subset of these three components, in turn, is connected in series to the solution resistance R_s. A typical Nyquist plot corresponding to electrolytic conditions is depicted in Figure 2:16B [470]: at high frequencies, no electrolysis takes place and the impedance plot is dominated by the solution resistance. The double layer (C_{dl}) provides a path of negligible resistance to the current. As the frequency is lowered, R_{ct} and C_{dl} will become dominating, giving rise to the characteristic semi-circular part of the plot. At even lower frequencies, significant concentration changes induced by the a.c. current become increasingly difficult to replenish by diffusion and the impedance shows a large rise, modelled by the Warburg impedance element Z_w [470].

Electrodes of porosity and rugosity give rise to a constant phase element CPE, a non-ideal capacitor that is represented by [494]

$$Z_{\mathrm{cpe}} = \frac{1}{b(i\omega C)^{\alpha}}, \tag{2:49}$$

where b is a proportionality constant, i is the imaginary number, and $0 < \alpha < 1$. In real systems, the CPE is manifested by an impedance spectrum altered from the expected shape, especially in the diffusive part. Typically, $\alpha = 0.5$ for porous electrodes and 1 for a smooth electrode, with rough surfaces giving rise to values between 0.5 and 1 [494].

Before closing this section on semiconductor electrochemistry, it needs to be re-emphasised that all the phenomena discussed in section 2.3 consider the idealised semiconductor/electrolyte interface. Non-idealities can arise due to a number of reasons, notably photodecomposition of the electrode in the depletion region, corrosion (generally oxide layer formation in non-oxide semiconductors [479]), or surface states [340].

2.4 Marcus theory and theoretical treatment of photoinduced electron transfer

Following the review of the underlying principles of PFE and semiconductor electrochemistry, this section will focus on electron transfer theory. Marcus has made seminal contributions to this area and, consequently one might say, was awarded the 1992 Nobel Prize in Chemistry "for his contributions to the theory of electron transfer reactions in chemical systems" [495]. His theories, originally developed for outer-sphere electron transfer problems, are central for understanding electron transfer in biological systems, photosynthesis in particular. Important contributions to the theory of electron transfer reactions were also made by Levich and Dogonadze [496], as well as Hush [497]. This section will briefly convey the key concepts underlying the rate constants and the activation energy requirements of electron transfer reactions (including photoinduced electron transfer), limited to those of relevance to the understanding of this thesis. Instructive, more comprehensive reviews were published by Marcus and Sutin [498-500], as well as Kavarnos [41]. This introductory section broadly follows the structure adopted by the latter.

2.4.1 The electron transfer rate constant

Consider an electron transfer reaction between a donor molecule D and an acceptor A in solution:

$$D + A \xrightarrow{k_{et}} D^{+} + A^{-}. \qquad (2:50)$$

For electron transfer to take place, the two reactant molecules must approach each other closely, forming an *encounter complex*, where they are contained within a solvent cage. We assume the reaction is not diffusion-limited, *i.e.* the rate of the reaction is controlled by the rate constant of electron transfer k_{et}.

The key to understanding electron transfer reactivity lies in separating the rate-determining factors into nuclear and electronic components, *i.e.* nuclear motions and electronic interactions [41]. In doing so, the first-order electron transfer rate constant k_{et} can be written as [500]:

$$k_{et} = \nu_n \kappa_n \kappa_{el}, \tag{2:51}$$

where ν_n is the nuclear frequency, in the range of ~10^{12} – 10^{14} s^{-1}, and κ_n and κ_{el} represent the nuclear and electronic factors, respectively. Both are dimensionless quantities that range from 0 – 1. The nuclear factor contains the activation energy for electron transfer:

$$\kappa_n = e^{\frac{-\Delta G_{et}^{\ddagger}}{RT}}. \tag{2:52}$$

Using eq. (2:52), eq. (2:51) can be expanded to

$$k_{et} = \nu_n \kappa_{el} e^{\frac{-\Delta G_{et}^{\ddagger}}{RT}}. \tag{2:53}$$

Electronic barriers are usually neglected when applying the classical electron transfer theory of Marcus to reactions in solution, *i.e.* $\kappa_{el} \approx 1$ [41]. Such reactions are termed *adiabatic* (see section 2.4.5.1). Quantum mechanical or nonclassical treatments also separate nuclear and electronic factors, but with more emphasis being placed on electronic barriers. The concepts in this section will be established using the classical model and, subsequently, briefly related to the semiclassical expression. First, the different components of eq. (2:53) will be discussed in more detail.

2.4.2 The free energy of activation

Assume donor and acceptor in eq. (2:50) are in contact distance and experience a weak electronic interaction, still retaining their individuality. This corresponds to the weakly adiabatic case [41]: $\kappa_{el} \approx 1$ and the rate-determining factors are assumed to involve nuclear reorganisation. On the kinetic domain, nuclei move much slower than electrons due to their much higher mass (electrons move with frequencies on the order of ~10^{15} s^{-1}; nuclear

vibration occurs at $10^{12} – 10^{14}$ s^{-1} [41]). In line with the Born-Oppenheimer approximation, electronic and nuclear motions can be treated as separate events occurring on different timescales. According to the Franck-Condon principle, the nuclei do not have time to change either their positions or their momenta during instantaneous electron transfer and remain 'frozen'[498].

Importantly, in Marcus theory the encounter complex (precursor state) undergoes a change in nuclear reorganisation *before* electron transfer can take place. Once the transition state is reached, the electron is transferred under conservation of energy. Reorganisation subsequent to electron transfer would violate the first law of thermodynamics (imagine a 'self-exchange' reaction $D + D^+ \rightarrow D^+ + D$ where $\Delta G_{et} = 0$; without nuclear reorganisation prior to electron transfer, vibrationally excited states of $D^+ + D$ would be created before nuclear motions could take place, and their decay would release heat in to the solution [41]). The required activation energy $\Delta G_{\mathrm{et}}^{\ddagger}$ is reached through collisions with solvent molecules. Generally, an electron transfer transition state is determined by the bond changes that take place during its formation and the change in orientations of the surrounding solvent molecules. The free energy of activation can thus be separated into two components:

$$\Delta G_{\mathrm{et}}^{\ddagger} = \Delta G_{\mathrm{i}}^{\ddagger} + \Delta G_{\mathrm{o}}^{\ddagger}. \tag{2:54}$$

In eq. (2:54), the subscripts i (= inner-sphere) and o (= outer-sphere) represent, respectively, bond distortions and solvent changes in the ionic sphere that surrounds the reactants. Further, according to Marcus [501-503] the activation energy for electron transfer can be expressed as

$$\Delta G_{\mathrm{et}}^{\ddagger} = \frac{(\lambda + \Delta_{\mathrm{d}} G_{\mathrm{et}}^{0})^2}{4\lambda}, \tag{2:55}$$

where $\Delta_{\mathrm{d}} G_{\mathrm{et}}^{0}$ represents the standard free energy for the electron transfer process (where the reactants are separated by a distance *d* [500]) and λ denotes the reorganisation energy. This quantity can be separated into two terms:

$$\lambda = \lambda_{\mathrm{i}} + \lambda_{\mathrm{o}}. \tag{2:56}$$

Here, λ_{i} represents the *inner-sphere* reorganisation energy that accounts for the energy required to effect changes in bond lengths and angles. The *outer-sphere* reorganisation energy λ_{o} in turn corresponds to energy changes caused by the rearrangement of the solvent shells surrounding the reactants [41].

2.4.3 Reorganisation

Marcus derived the following equation for bond-reorganisation [498,504]:

$$\lambda_{\mathrm{i}} = \sum_j \frac{f_j^{\mathrm{r}} f_j^{\mathrm{p}}}{f_j^{\mathrm{r}} + f_j^{\mathrm{p}}} \left(\Delta q_j\right)^2, \tag{2:57}$$

where f_j^{r} and f_j^{p} are the force constants for the respective *j*th vibration of the reactant and product state. The fraction thus represents the reduced force constant. Δq_j denotes the change in equilibrium bond distance between the reactant and product state corresponding to the *j*th vibration [41]. Eq. (2:57) is a summation over all vibrational modes, which are treated as harmonic oscillators [498]. In principle, using eq. (2:57) λ_{i} can be determined from changes in bond lengths. However, if short-lived transients such as excited states are involved, these are often difficult to determine experimentally.

Solvent reorganisation is described by eq. (2:58) [498], based on the fairly simple physical picture of two spherical reactants being surrounded by a cage of solvent molecules [41].

$$\lambda_{\mathrm{o}} = (\Delta e_0)^2 \left(\frac{1}{2r_D} + \frac{1}{2r_{\mathrm{A}}} - \frac{1}{d_{\mathrm{cc}}}\right)\left(\frac{1}{\varepsilon_{\mathrm{op}}} - \frac{1}{\varepsilon_{\mathrm{s}}}\right), \tag{2:58}$$

where r_{D} and r_{A} are the (spherical) radii of the donor and acceptor species in eq. (2:50), d_{cc} is the centre-to-centre separation distance, $\varepsilon_{\mathrm{op}}$ is the optical dielectric constant of the solvent

(the square of the refractive index n), and ε_s corresponds to the static dielectric constant, sometimes referred to as the relative permittivity). ε_s varies greatly between polar and nonpolar solvents (for instance, there is a 40-fold difference between water and benzene [505]), the implication being that the reorganisation energy is greater for polar molecules, which must undergo substantial nuclear changes to adjust to a hypothetical charge in the transition state. According to eq. (2:58), the outer-reorganisation energy also depends on the size and separation distance of the reactants. The solvent barrier is greater for small spherical molecules and increases with distance. The latter phenomenon can be rationalised by visualising the two reactants positioned at a contact distance within a nonpolar, ellipsoidal cavity that is immersed in the dielectric continuum [41]: at small separation distances, λ_o should be small as the reactants 'feel' the relatively nonpolar environment of the cavity. With increasing separation, however, the reactants become more sensitive to changes in the more polar dielectric continuum of the solvent

2.4.4 The normal and inverted regions

2.4.4.1 Implications from the Marcus equation

Revisiting eq. (2:55), we note the quadratic dependence between driving force and activation energy. Substituting eq. (2:55) into eq. (2:53) yields a direct link between the free energy of the electron transfer reaction and the kinetic rate constant. With $\kappa_{el} \approx 1$ (section 2.4.1),

$$k_{et} = \nu_n e^{\frac{-\left(\lambda+\Delta_d G_{et}^0\right)^2}{4\lambda RT}}. \tag{2:59}$$

It is well-known that the rate of a chemical reaction generally tends to increase with increasing driving force. The same holds, *initially*, for eq. (2:59). However, this equation also predicts a maximum rate constant, following which a further increase in exergonicity will cause a *decrease* in rate. This behaviour is schematically illustrated in Figure 2:17.

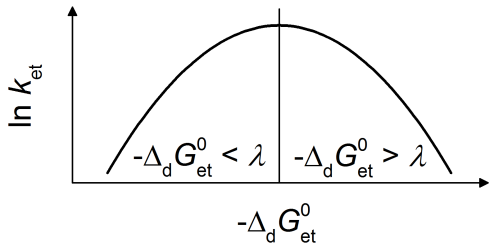


Figure 2:17 The relationship between rate constant and driving force in electron transfer reactions predicted by eq. (2:59).

In agreement with Figure 2:17, two kinetic domains can be distinguished. First, in the *normal region*, where $-\Delta_d G^0_{et} < \lambda$, the electron transfer rate k_{et} increases with increasing driving force until a maximum is reached when $-\Delta_d G^0_{et} = \lambda$. In this case, $\kappa_n = 1$ and the reaction is termed 'barrierless'. Moving further along the abscissa in Figure 2:17, $-\Delta_d G^0_{et}$ will exceed λ and we enter the Marcus *inverted region*. Here, k_{et} decreases with increasing $\Delta_d G^0_{et}$.

2.4.4.2 Pictorial representations of electron transfer processes

The three different scenarios of electron transfer occurring in the normal region, being barrierless, or taking place in the inverted regime can be visualised graphically. In pictorial representations, electron transfer processes are typically represented using potential energy surfaces, which are topological depictions of chemical reactions [41]. The energy of the system is plotted as a function of the reaction coordinate, which is often represented as nuclear motion. To reduce complexity, the resulting multidimensional 'hypersurfaces' are commonly reduced to two-dimensions: often, one particular nuclear deformation can be used to describe a reaction or, in more complicated cases, a mean or composite of all nuclear changes can be represented as a moving point [41]. As noted in section 2.4.3, nuclear vibrations in classical Marcus theory are treated as harmonic oscillators, the behaviour of which is described by symmetrical one-dimensional parabolic functions. Thus, intersecting parabolic curves are used as idealised energy curves to describe the course of electron transfer from the *precursor state*, immediately prior to electron transfer, to the *successor state*

directly following electron transfer [41]. In other words, each of these two supermolecules is described by their own potential energy curve.

Figure 2:18A shows two intersecting parabolic curves representing electron transfer in the normal region. It is worth noting here that the Butler-Volmer model for interfacial electron transfer described in section 2.2.5 is in agreement with the Marcus model, as long as overpotentials are small, *i.e.* for $\eta < \lambda$ in the normal region [467,506,507]. Barrierless electron transfer occurring at maximum rate is depicted in Figure 2:18B, while Figure 2:18C depicts electron transfer in the inverted region.

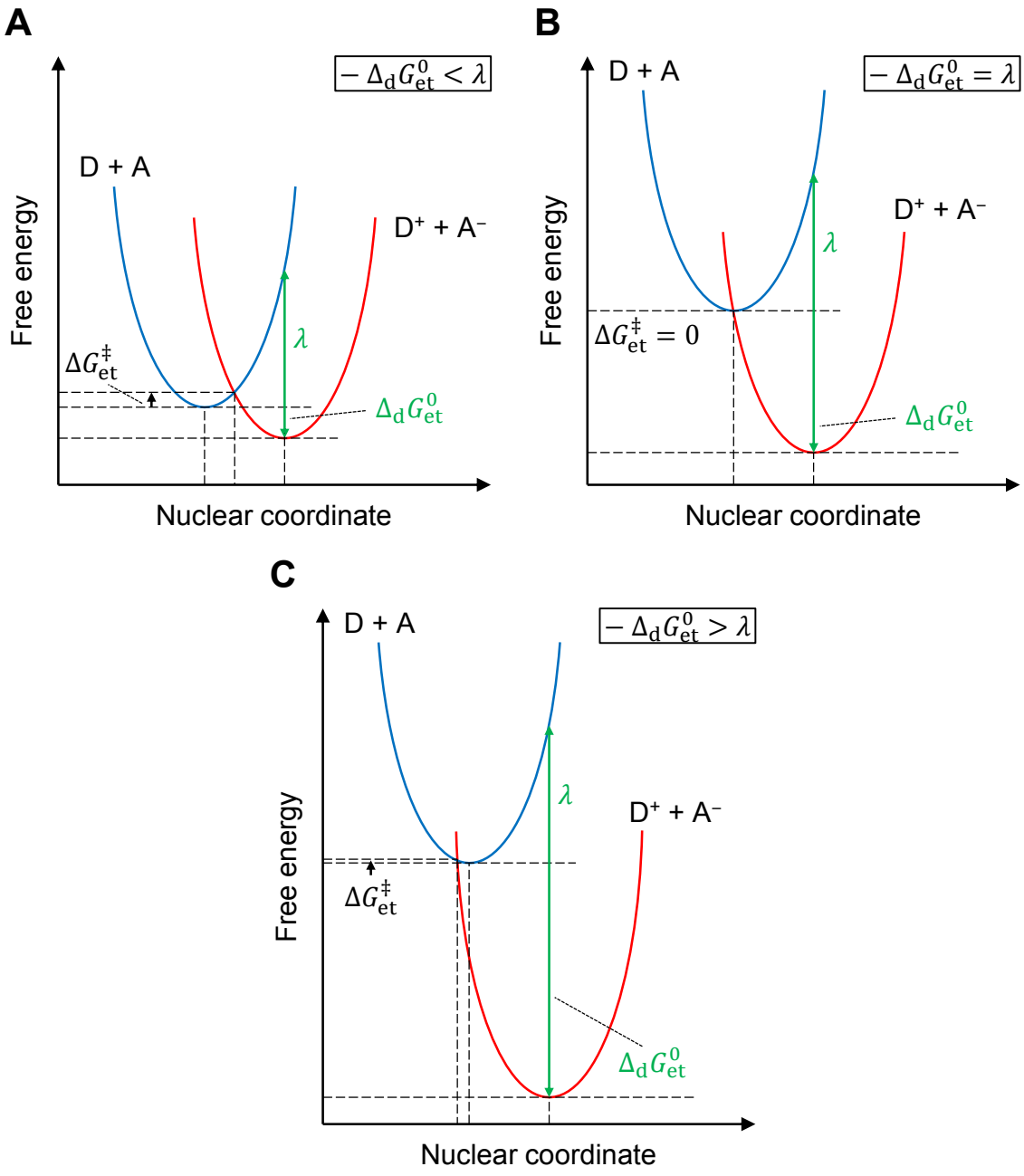


Figure 2:18 Potential energy curves depicting the electron transfer reaction between D and A according to eq. (2:50). The surface representing the reactants is shown in blue; the product curve is depicted in red. (A) Normal region ($-\Delta_d G^0_{et} < \lambda$), (B) barrierless electron transfer ($-\Delta_d G^0_{et} = \lambda$), (C) inverted region ($-\Delta_d G^0_{et} > \lambda$).

Experimentally verifying Marcus' prediction of the inverted region proved to be daunting [41]. For electron transfer experiments in solution, experimental plots of ln k_{et} *vs.* $\Delta_d G^0_{et}$ often show a plateau, one of the reasons being that diffusion becomes rate-limiting at high driving force, 'masking' the electron transfer rate constant k_{et} (second order rate constants for

diffusion are on the order of 10^9 M^{-1} s^{-1} [41]). Concluding evidence for the existence of the inverted region was provided by Miller *et al.* in 1984 [508], almost three decades after Marcus' theoretical prediction. The authors employed pulse radiolysis to study intramolecular electron transfer from a 4-biphenyl electron donor linked to acceptors of different energy *via* a rigid steroid bridge (Figure 2:19).

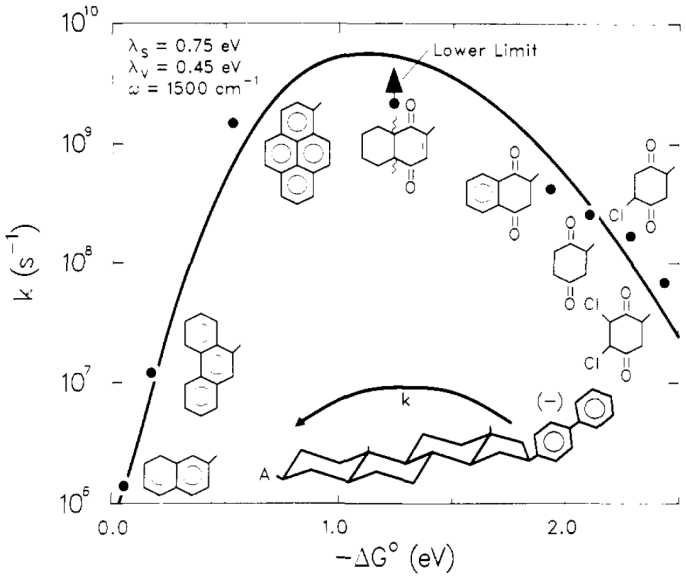


Figure 2:19 Experimental demonstration of the Marcus inverted region: intramolecular electron transfer rate constants recorded in 2-methyltetrahydrofuran for a series of bi-functional 4-biphenyl steroids, plotted as a function of driving force (free energy change). Reprinted with permission from reference [508]. Copyright 1984 American Chemical Society.

The possibility of exploiting the stark differences in electron transfer kinetics depending upon whether a reaction occurs in the normal or the inverted region sounds attractive, not only from a hypothetical perspective: with respect to light-driven electron transfer reactions, particularly those involved in driving the thermodynamically uphill reactions of artificial photosynthesis, it would be advantageous if forward electron transfer rates were occurring at maximum rate (*i.e.* being barrierless), but destructive recombination being kinetically retarded through positioning in the Marcus inverted regime. For reactions in solution, control

can in principle be exerted *via* modifications to the polarity of the solvent, provided λ_o dominates the reorganisation energy [41].[viii]

2.4.4.3 Photoinduced electron transfer

Photoinduced electron transfer events can also be represented by two-dimensional potential energy surfaces, using the principles described in the previous section. In this case eq. (2:50) is modified and written as

$$D + A \xrightarrow{h\nu} D^* + A \xrightarrow{k_{et}} D^+ + A^-, \tag{2:60}$$

where light-excitation ($h\nu$) generates the excited donor D*, which reacts with acceptor A. The corresponding changes in free energy as a function of nuclear motion are depicted in Figure 2:20. According to the Franck-Condon principle, photoexcitation occurs vertically on the reaction coordinate (*i.e.* the nuclei remain frozen), yielding a vibrational level of the optically excited state. This system will then relax into the vibrational ground state of the electronic excited state by thermal equilibration. The next steps are analogous to the events described in the previous section: formation of the precursor complex is followed by electron transfer and subsequent nuclear relaxation to establish the equilibrated product ions of the successor state [41]. Although the latter steps are downhill in energy, the overall reaction (starting with D + A) is endergonic ($\Delta G^0 > 0$); light-energy is stored in the process.

[viii] The reader needs to bear in mind, however, that artificial photosynthesis will ultimately have to be carried out in water.

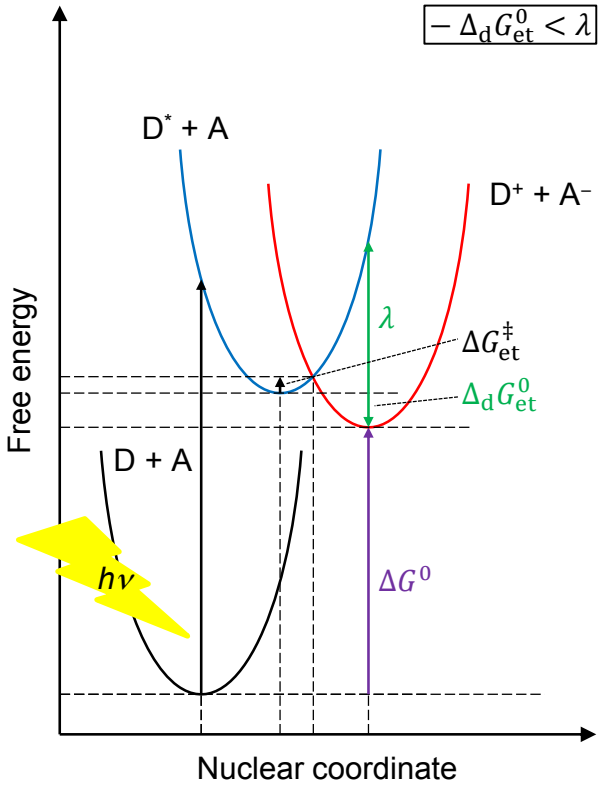


Figure 2:20 Potential energy curves in photoinduced electron transfer according to eq. (2:60). Vertical excitation of D leads to the formation of the excited state D^*, which, following rapid thermal equilibration, undergoes an electron transfer reaction with A analogously to Figure 2:18A. Although the electron transfer step is exothermic, energy is stored in the overall process ($\Delta G^0 > 0$). Adapted from reference [41].

2.4.5 Electronic coupling

2.4.5.1 Adiabatic and nonadiabatic electron transfer

Despite being very instructive and commonly used throughout the literature, the potential energy curves depicted in Figure 2:18 and Figure 2:20 are somewhat misleading. When the two reactants D and A in eq. (2:50) approach one another closely, their frontier orbitals will begin to interact, causing a perturbation of their electronic eigenfunctions and the Hamilton operator, which results in a shift in energies [41]. Graphically, a new set of curves emerges as the intersecting potential energy curves representing the precursor and successor complexes interact under perturbation (Figure 2:21A). The electronic coupling H_{el} between the lower

and upper potential energy curve represents the repulsion between the two traces. The term adiabacity is a measure of the strength of the electronic coupling.

The classical treatment of electron transfer, to which section 2.4 was limited thus far, was developed for weakly adiabatic reactions where $\kappa_{el} \approx 1$ (Figure 2:21B), meaning that the reaction proceeds on a *single* potential energy surface, with a smooth transition from the precursor complex to the successor state (reactions are considered adiabatic if $H_{el} \geq 0.5$ kcal mol^{-1}) [41]. Conversely, non-interacting, intersecting potential energy surfaces, where H_{el} is small, are termed *nonadiabatic* or *diabatic* (Figure 2:21C). Reactants separated by a large distance constitute an example for a diabatic reaction.

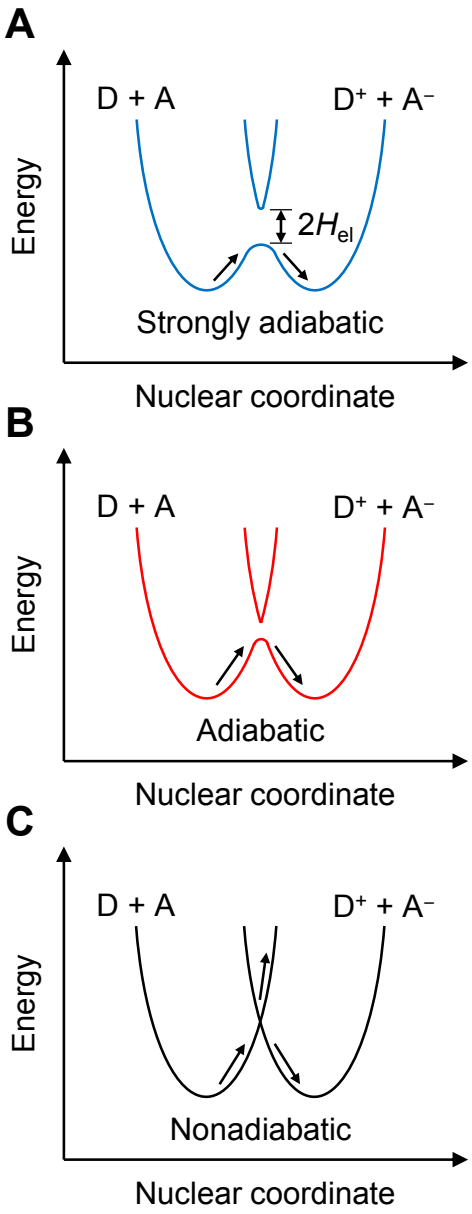


Figure 2:21 Potential energy curves representing adiabatic (A),(B) and nonadiabatic electron transfer (C). In strongly adiabatic electron transfer (A), H_{el} is large enough for the reaction to proceed on one curve. In nonadiabatic electron transfer, the 'moving point' oscillates many times on the reactant curve before electron transfer takes place. Adapted from reference [41].

The shape of the potential energy curve (*i.e.* its steepness) can have a profound influence on the probability of electron transfer [41]: the wavefunction responds more abruptly to nuclear changes in case of a steep slope, rendering electron transfer improbable. Conversely, a smooth transition is allowed if the lower potential energy curve is shallower. The velocity with which reactants and products approach one another also influences the probability of

electron transfer: at high nuclear velocities, one can imagine the nuclear point moving back and force many times on the reaction curve, the little time spent on the crossing point causes the probability of electron transfer to decrease [41].

2.4.5.2 Distance dependence of electron transfer and the semiclassical Marcus equation

The previous section alluded to the fact that H_{el} depends on the separation distance between the reactants. This, by extension, also holds for k_{et} (*vide infra*). In quantum mechanical terms, the distance dependence of the probability of electron transfer through a potential barrier (*i.e.* tunnelling) in a nonadiabatic process is expressed as the square of the electronic coupling matrix element H_{el} [509]:

$$H_{el}^2 = \left(H_{el}^0\right)^2 e^{-\beta(d-d_0)}, \tag{2:61}$$

where d is the separation distance between the two reactants and d_0 represents the separation distance in the case of an encounter complex, determined by the van der Waals radii of the two reactants [41]. H_{el}^0 corresponds to the maximal electronic coupling element when D and A are in contact. An important parameter is the 'damping factor' β, also known as attenuation factor or decay coefficient. Being inversely proportional to the orbital overlap between donor and acceptor orbitals [41], β depends on the medium through which the electron travels [509]. In vacuum, for example, β ranges from 2.8 – 3.5 $Å^{-1}$ [389,390]. Common values for saturated hydrocarbons bridges are much lower, on the order of 0.8 – 1.0 $Å^{-1}$ [448,510,511], and slightly higher decay constants (1.0 – 1.4 $Å^{-1}$) have been measured in proteins [390,512,513]. Remarkably low β-values as low as 0.04 $Å^{-1}$ have been reported for oligomers of *p*-phenylenevinylene: electron transfer rates constants of 10^{11} s^{-1} have been measured for separation distances of 40 Å [514]. Consequently, such systems are termed 'molecular wires' [515].

Provided no parameters other than distance influence k_{et}, the electron transfer rate constant can be written as [498]

$$k_{et} = k_{et}^{0} e^{-\beta(d-d_0)} = 10^{13} e^{-\beta(d-d_0)} s^{-1}, \quad (2:62)$$

where 10^{13} s^{-1} represents the frequency for nuclear motion along the reaction coordinate, implicitly assuming that the reaction is adiabatic at $d = d_0$.

Comparing eqs. (2:59) and (2:62) makes apparent that k_{et} shows two exponential dependences, both *via* the nuclear factor κ_n and the electronic factor κ_{el}. The semiclassical Marcus equation [498] combines the two dependences and can be used to predict both adiabatic and nonadiabatic electron transfer

$$k_{et} = \sqrt{\frac{4\pi^3}{h^2 \lambda k_B T}} H_{el}^2 e^{\frac{-(\lambda + \Delta_d G_{et}^0)^2}{4\lambda k_B T}}. \quad (2:63)$$

2.4.6 Electron transfer in biological systems

Marcus theory has been adopted for electron transfer in biological systems [498]. Several researchers made seminal contributions to this field, with Gray being one of the most notable experimentalists (see, for example, references [448,513,516-518]).

Eq. (2:62) is widely used in the study of biomolecules, where electrons tunnel, often over long distances, between electron transfer relay centres such as the FeS chains in the fuel-forming enzymes that are subject to this thesis. Complex I, the first enzyme of the respiratory chain, constitutes a particular striking example, where the electron transport chain comprises nine iron sulphur clusters that shuttle charges over a distance of more than 80 Å [519]. The FeS clusters in this and other iron sulphur enzymes such as hydrogenases or CODH have in common that their reorganisation energies are low, and the individual centres are arranged in a near linear fashion and spaced apart at distances short enough to allow efficient electron tunnelling at rates well above the limiting turnover rate [389]. Dutton and co-workers

established, empirically, by surveying a wide range of electron transfer proteins with known atomic structure that electrons can travel up to 14 Å between redox centres through the protein medium. Transport over longer distances *always* involves a chain of cofactors [389]. Electron transfer rates on the order of $10^8 – 10^9$ s^{-1} are calculated for the redox enzymes used in this thesis.

Using the principles of electron transfer theory, we can interpret the near-unity efficiency of the initial photosynthetic charge-separation processes described in section 1.2.2.2. Electron transfer from the special pair to the initial pheophytin *a* acceptor is barrierless with a rate constant of *ca.* 10^{12} s^{-1}, the outer-sphere reorganisation energy inside the hydrophobic protein membrane is low, and bond-length changes are negligible in the rigid porphyrin frameworks [41]. Subsequent electron transfer to plastoquinone Q_A is again barrierless, albeit three orders of magnitude slower, at least in part due to the large separation distance. Yet, destructive recombination is kinetically disfavoured, being placed in the Marcus inverted region owing to its large driving force. Recombination between reduced Q_A and the oxidised special pair $P680^+$ is also impeded by strong barriers, notably the poor electronic overlap because of the large separation distance [41].

Long-range electron transfer is still a thriving and actively researched area, and the theoretical concepts described in section 2.4 are powerful tools, not only for describing experimentally observed phenomena, but also for predicting reactivity and hence guiding the experimentalist.

2.5 Electron paramagnetic resonance spectroscopy

2.5.1 The electronic *g* value

This chapter on experimental theory will be concluded with a short, phenomenological discussion of the basic principles behind electron paramagnetic resonance spectroscopy (EPR), focusing on continuous-wave EPR. In a magnetic field B, an electron with spin $S = 1/2$ can have two orientations, either parallel to the magnetic field, where $m_s = +1/2$, or antiparallel with $m_s = -1/2$. It is the latter orientation that is lower in energy. The electronic Zeeman energies are given by [520]

$$E = g\mu_B B m_s, \tag{2:64}$$

where μ_B denotes the Bohr magneton and g is the property of interest in the experiment (*vide infra*). Upon absorption of electromagnetic radiation $h\nu$ equal to the energy difference ΔE in the two orientations, the electron will change orientation according to the resonance condition

$$h\nu = g\mu_B B. \tag{2:65}$$

This process is schematically depicted in Figure 2:22.

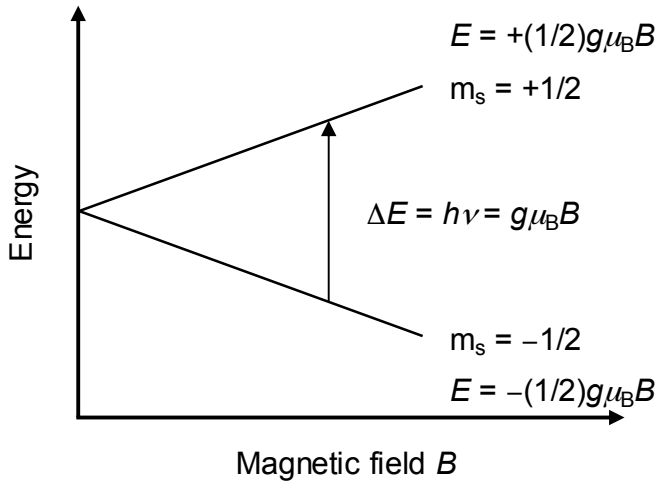


Figure 2:22 Removal of the degeneracy of the electron spin states by a magnetic field. An EPR allowed transition is observed when the resonance condition is fulfilled. Adapted from reference [521].

From eq. (2:65) follows that there are, in principle, two options for detecting EPR absorption: the frequency can be varied at constant field, or the field can be varied at constant frequency until the resonance condition is met. It is the latter case that finds application in continuous-wave EPR spectroscopy: for practical purposes resonant cavities are used to enhance sensitivity, their use dictates a fixed frequency with a corresponding wavelength that fits the resonator dimensions [520].

The g value of a free electron *in vacuo* $g_e = 2.00232$. However, as a result of spin-orbit coupling, an electron orbiting around one or more nuclei (*e.g.* a transition metal ion in a metalloenzyme) will experience a second magnetic field δB. In this case, the resonance condition can expressed as

$$h\nu = g_e \mu_B (B_e + \delta B) \tag{2:66}$$

or, since δB is not known, as

$$h\nu = (g_e + \delta g)\mu_B B. \tag{2:67}$$

The notion of δg lies at the heart of EPR: this quantity not only serves as a 'fingerprint' of a given molecule (as $g = g_e + \delta g$), it also contains information about its electronic structure, as well as the nature of electron-nucleus interactions.

2.5.2 The *g* value is anisotropic

Anisotropy is a key concept in EPR spectroscopy: molecular properties such as δg are angular dependent and thus reflect the three-dimensional structure of a paramagnetic molecule [520]. The principle is illustrated using the following example. Figure 2:23 schematically depicts an oxidised cytochrome *c*-type molecule, having a low-spin ferric haem centre (S = 1/2) embedded in a porphyrin plane, with the axial positions being occupied by a histidine and a methionine ligand, respectively. The molecule is depicted spanning a Cartesian coordinate system, such that the tetrapyrrole plane spans the *x*- and *y*-plane and the axial ligands are aligned with the *z*-axis.

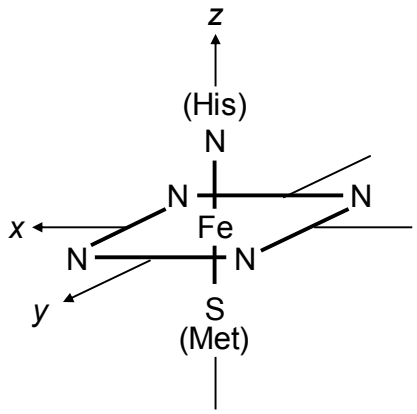


Figure 2:23 Schematic illustration of axial paramagnetic anisotropy using a simplified representation of a cytochrome *c*-type haem porphyrin with histidine and methionine occupying the axial positions. Adapted from reference [520].

Consider this molecule being subjected to an external dipolar magnetic field B with the field vector $\boldsymbol{B}$ along the x axis: δg in eq. (2:67) is largely determined by the heteroatomic electrons of the tetrapyrrole plane [520]. Because of the porphyrin plane being symmetric, no change in

δg will be observed upon rotation around the *z* axis so that the *y* axis is aligned with the magnetic field vector. However, the electronic structure of the His and Met ligands will determine δg if the molecule is rotated so that the *z* axis is aligned with the magnetic field. The example in Figure 2:23 is considered to display axial symmetry, with $B_x = B_y \neq B_z$ and thus $g_x = g_y \neq g_z$. In a sample of randomly oriented cytochrome *c* haems, many more molecules will exist with the ***B*** vector anywhere near the *xy* plane than there will be molecules where ***B*** is parallel to the unique *z* axis. This discrepancy will impact the intensity distribution of the resulting EPR signals, as (qualitatively) depicted in Figure 2:24A. A real EPR spectrum is obtained when this stick spectrum is convoluted with a line shape with finite line width (Figure 2:24B) [520], reflecting the different orientations with respect to the ***B*** vector lying somewhere in between the extreme values that give rise to the sharp, distinct peaks [408]. Figure 2:24C shows the derivative (with respect to the magnetic field) EPR spectrum, which is usually recorded in practice, as standard EPR spectrometers employ field modulation plus phase-sensitive detection to increase sensitivity by filtering out non-resonant noise [520].

Distortion of the axial symmetry (such as in the porphyrin plane in Figure 2:23) leads to the formation of a rhombic spectrum, where $g_x \neq g_y \neq g_z$. An example of a rhombic absorption spectrum is shown in Figure 2:24D and the corresponding derivative spectrum is depicted in Figure 2:24E. The latter shows three different features, the field positions of which correspond closely to the different *g* values g_x, g_y, and g_z.

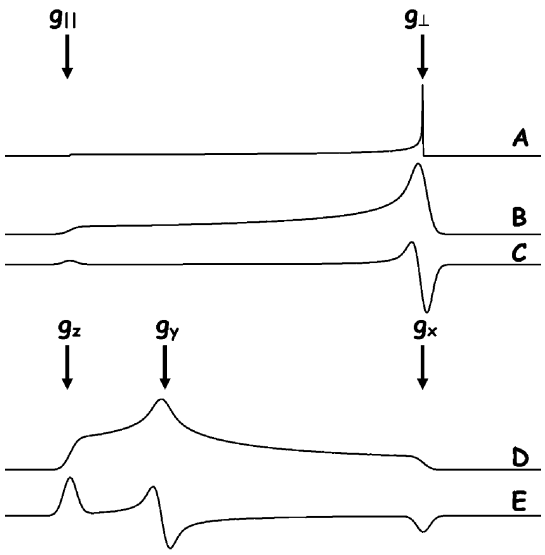


Figure 2:24 Anisotropy in EPR illustrated for absorption and derivative spectra of axial (A) – (C) and rhombic symmetry (D),(E). (A) axial intensity pattern; (B) axial EPR absorption; (C) axial EPR derivative; (D) rhombic EPR absorption; (E) rhombic EPR derivative. Reprinted with permission from reference [520]. Copyright 2006 The Royal Society of Chemistry.

For completeness, in the simplest case, termed isotropic system, $g_x = g_y = g_z$.

2.5.3 Multiple magnetic interactions

Electronic Zeeman interactions in addition to those between the external magnetic field *B* and the electron spin *S* (termed *S***B* interactions) give rise to more complicated EPR spectra than those reported in Figure 2:24. Generically speaking, one can distinguish between electron-electron spin interactions (*S***S* interactions) and interactions between electron spins and nuclear spins (*S***I* interactions).

Although much weaker than the electronic Zeeman (*S***B*) interaction (typically one to several orders of magnitude [520]), *S***I* interactions do cause perturbations to the EPR spectrum, they give rise to hyperfine splitting: each of the basic *S***B* features (see Figure 2:24) will be split into $2I + 1$ lines, with the magnitude of the splitting (*A*) reflecting the strength of the interaction. *A* is an anisotropic quantity, meaning each *g* value may show

hyperfine splitting of different magnitude. In a rhombic system, for instance, this leads to A_x, A_y, and A_z corresponding to the magnitude of the splitting at g_x, g_y, and g_z, respectively.

Hyperfine splitting arising from interaction with metal ion nuclei is referred to as central hyperfine splitting and allows determination of the isotope of the metal with which the electron is associated. Interaction of electron spin with nuclei from (first) coordination sphere ligands is termed ligand hyperfine or superhyperfine splitting. This type of interaction is important for chapter 3 of this thesis. The magnitude of ligand hyperfine splitting is typically an order of magnitude less compared to metal hyperfine splitting [520].

Spin systems comprising more than one unpaired electron ($S > 1/2$), *e.g.* triplet states, give rise to *S***S* interactions and cause what is known as zero-field splitting. Magnetic dipole-dipole interaction between unpaired electrons removes their degeneracy even in the absence of an external field [521].

Nuclear Zeeman interactions (*I***B*) and quadrupolar interactions (*I***I*) are usually too weak to be detected in a standard continuous wave EPR experiment; they are, however, amenable to characterisation by some advanced (pulsed-) EPR techniques, notably electron nuclear double resonance (ENDOR) and electron spin echo envelope modulation (ESEEM) [520].

2.5.4 'Advanced' EPR techniques

The term 'advanced' EPR is rather vague. Generally, it refers to so-called double resonance techniques involving two sources of radiation. The common underlying principle involves the partial or full saturation of an EPR absorption, normally using pulsed excitation, and subsequent transfer of spin energy to a different absorption by means of the second radiation, leading to the detection of the difference signal [522]. Contrary to pulsed NMR spectroscopy, pulses in EPR are often not able to excite the entire spectrum of the electron spin.

Electron-nuclear hyperfine interactions that are too small to be resolved within the natural EPR line width can be studied by ESEEM and ENDOR. ESSEM is typically used in the characterisation of 'more distant', weekly coupled nuclei with $A \leq 10$ MHz [523]. Weakly coupled nuclear spins cause a modulation of the intensity of the spin echo at the nuclear frequencies of the interacting nucleus. From the modulation depth, it is in principle possible to determine the number of equivalent nuclei of a particular type of coupling with the electron spin; an example is presented in chapter 3. ESEEM experiments can be carried out as two- or three-pulse experiments, with the latter usually giving better resolution (in the three-pulse experiment, the nuclear coherence decays with the longer nuclear relaxation time T_1 instead of the shorter spin-spin relaxation time T_2) [524]. Hyperfine sublevel correlation spectroscopy (HYSCORE) is a four-pulse variation of the ESEEM experiment.

ENDOR is complementary to ESEEM and generally used for more strongly coupled, 'closer' nuclei, with A being in the range of $2 - 40$ MHz [523]. The technique probes the nuclear transitions directly, through coupling of the EPR excitation with an NMR radio frequency pulse. Simply speaking, NMR spectroscopy is detected on an EPR spectrometer.

Because of the highly complicated nature of double-resonance techniques, a theoretical treatment of the above-mentioned pulsed-EPR experiments would be beyond the scope of this introduction. The reader is instead referred to the wealth of literature on advanced EPR spectroscopy. Concise introductions for example are given Chasteen and Snetsinger [523], and Roessler [524].

3 The mechanism of [FeFe]-hydrogenases – how aldehydes inhibit H_2 evolution

Part of the work presented in this chapter has been published: Andreas Bachmeier, Julian Esselborn, Suzannah V. Hexter, Tobias Krämer, Kathrin Klein, Thomas Happe, John E. McGrady, William K. Myers, and Fraser A. Armstrong, *J. Am. Chem. Soc.* **2015**, *137*, 5381.

Abstract

This chapter deals with investigations into the mechanism of [FeFe]-hydrogenases, using aldehyde molecules as (partly) reversible inhibitors. Of particular interest is the order of the electron and proton transfer steps that lead to the formation of hydrogen. Building upon the initial discovery of formaldehyde being a reversible inhibitor of [FeFe]-hydrogenases that preferably targets the super-reduced oxidation level of this class of enzymes [400,525], the reaction of [FeFe]-hydrogenases with four different aldehydes of varying steric demand and electrophilicity is studied by protein film electrochemistry techniques. The degree of inhibition seems to correlate with the steric nature of the aldehydes and their reactivities towards nucleophiles. Analysis of the potential dependences and reversibility patterns of inhibition suggests that the smaller aldehydes react directly at the H-cluster, corroborating earlier findings made with formaldehyde [400,525].

To gain structural insight into the binding of aldehydes to the H-cluster, inhibition by formaldehyde, the simplest and (due to its highly electrophilic carbonyl group) most reactive aldehyde inhibitor of the H-cluster, is studied by pulsed-EPR techniques in collaboration with Dr. William Myers (Centre for Advanced Electron Spin Resonance, University of Oxford). ESEEM experiments on deuterated formaldehyde firmly establish that formaldehyde can access the enzyme active site. ENDOR studies using carbon-13-labelled formaldehyde give rise to hyperfine interactions that are in agreement with several binding modes. Complementary density functional theory calculations by Professor John McGrady (Inorganic Chemistry Laboratory, University of Oxford) provide a mechanism that accounts for specific binding of formaldehyde to the distal iron of the H-cluster.

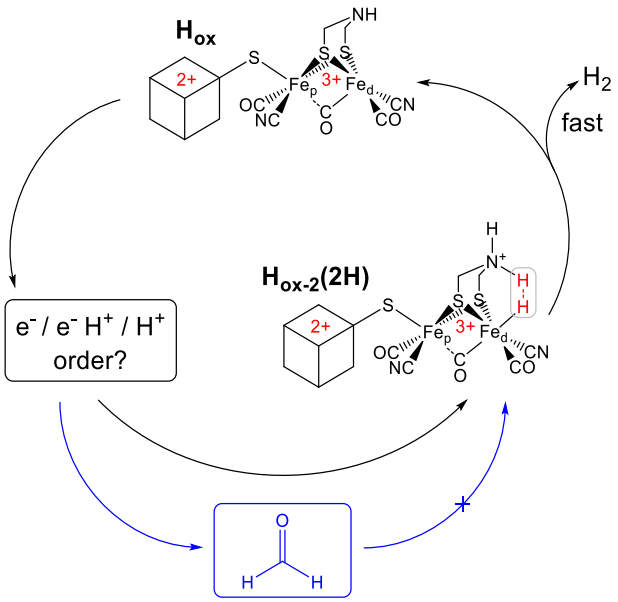
A comparative analysis of the experimental evidence provided by different techniques leads to the proposal of a new mechanism for formaldehyde inhibition with important

implications on the catalytic cycle: unusual for biological systems, protonation of the H-cluster only takes place after the consecutive transfer of two electrons.

3.1 Introduction

As outlined in section 1.6.2.4, the elementary steps by which [FeFe]-hydrogenases evolve hydrogen so efficiently are still unclear. Scheme 3:1 draws attention to an outstanding question concerning their mechanism. Of the two structures shown, H_{ox} is well characterised; the other structure represents a *transient* state, termed $H_{ox\text{-}2}(2H)$, immediately prior to or at the point of H_2 release. To go from H_{ox} to $H_{ox\text{-}2}(2H)$ requires two electrons and two protons but it has not been established in a kinetic study in which order these events occur. In the $H_{ox\text{-}2}(2H)$ transient, the two additional electrons (with respect to H_{ox}) are stored as a terminal hydride bound to Fe_d; therefore, the oxidation numbers of the H-cluster components $[2Fe]_H$ and $[4Fe\text{-}4S]_H$ are already adjusted to the H_{ox} level, which is left behind after H_2 is released from the active site (the individual oxidation numbers of Fe_d and Fe_p (I,II) are not yet established).

Scheme 3:1 Pathway to the transient precursor for catalytic H_2 formation at the H-cluster, formation of which is prevented by formaldehyde. As the individual charges on Fe_p and Fe_d are still under debate, the overall oxidation number of $[2Fe]_H$ is presented, together with the charge of $[4Fe\text{-}4S]_H$. In H_{ox}, $[4Fe\text{-}4S]_H$ is established to have an overall charge of 2+, and both $Fe_p(I)\text{-}Fe_d(II)$ and $Fe_p(II)\text{-}Fe_d(I)$ are possible combinations for $[2Fe]_H$. In $Hox_{\text{-}2}(2H)$, $[4Fe\text{-}4S]_H$ is also formulated as 2+ [412], implicating that $[2Fe]_H$ comprises $Fe_p(I)\text{-}Fe_d(II)$ [210].



The reversible inhibition of [FeFe]-hydrogenases by formaldehyde has recently been established using protein film electrochemistry [400,525]. The combination of PFE and inhibition by aldehydes provides an interesting new probe for the mechanism of H_2 production: aldehydes almost certainly react at the H-cluster, intercepting highly active reduced states.

Importantly, the activity that is lost very rapidly when formaldehyde is injected into the electrochemical cell is recovered *immediately* when formaldehyde is removed (Figure 3:1A). Formaldehyde binds rapidly within seconds, the reaction in the potential region where H_2 production occurs is dominated by a fast component with $\tau = 7.89$ s at –0.56 V *vs*. SHE (Figure 3:1B). Importantly, the enzymatic activity is almost fully recovered when formaldehyde is flushed from the cell after 5 minutes exposure (Figure 3:1A).

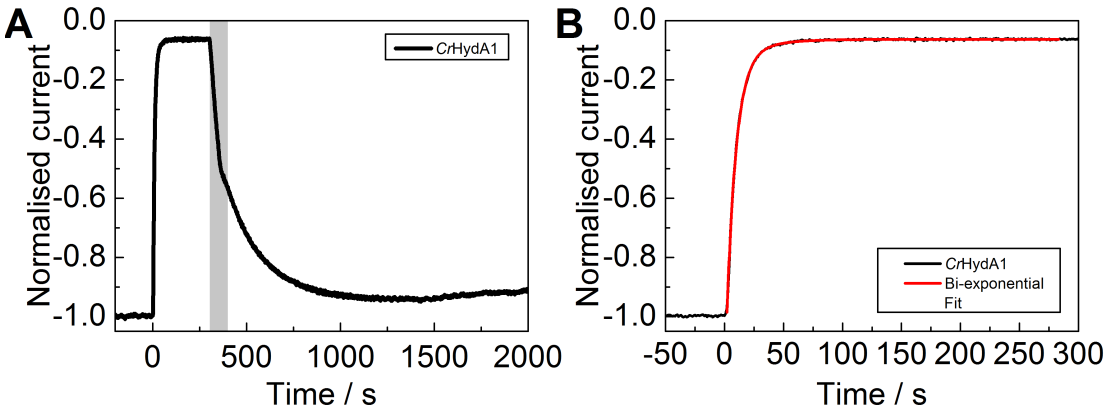


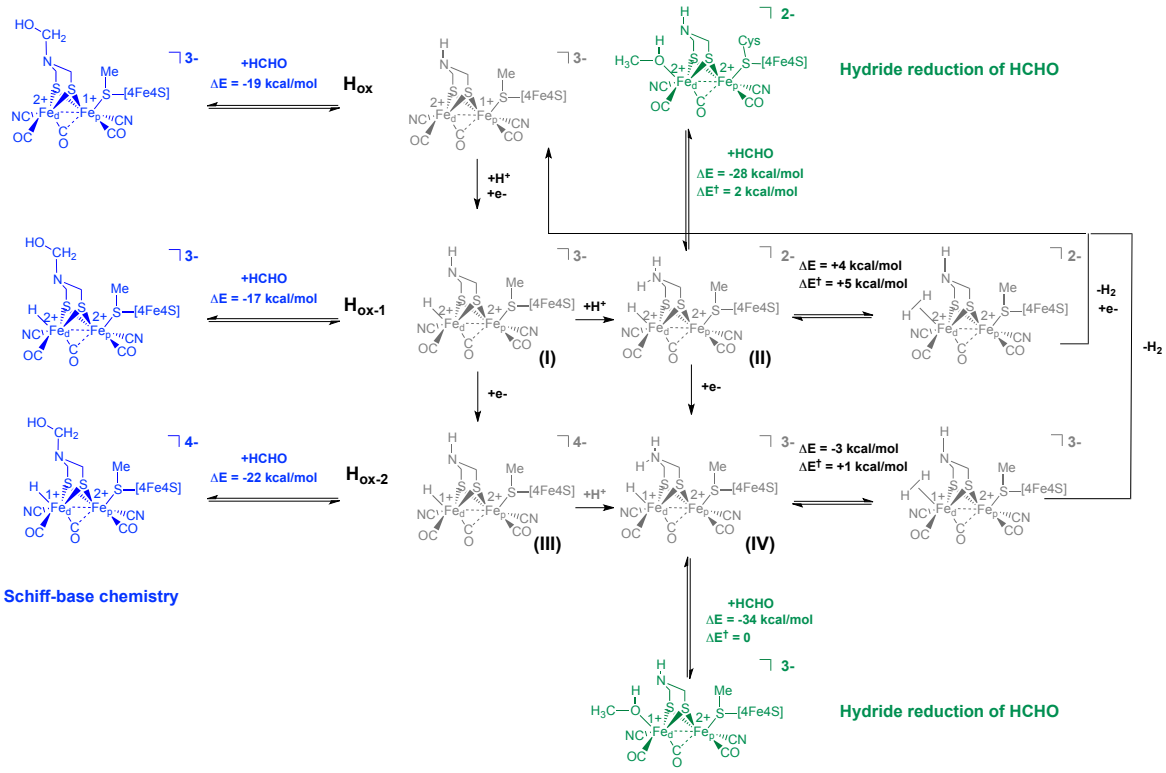
Figure 3:1 Formaldehyde-inhibition of H^+ reduction by *Cr*HydA1, adapted from reference [525]. (A) Formaldehyde was injected at $t = 0$ to give a final concentration of 4.5 mM. After 300 s, the cell was rinsed with 50 mL of phosphate buffer (rinsing took approximately 100 s, grey stripe). Other conditions: electrode potential –0.56 V *vs.* SHE; pH 6.0; 10 °C; 100% H_2; $\omega = 2500$ rpm. (B) represents an expanded section of (A), in which the decay of activity following injection of formaldehyde is fitted to a bi-exponential process by least-square analysis using OriginPro 9.0.

The fraction of the total current attenuation that is due to rapid, *reversible* interaction with HCHO increases as the electrode potential is lowered [525]: a detailed study with the enzyme from *Clostridium acetobutylicum* showed that the potential dependence spans three zones linked by one-electron Nernst transitions and thus termed H_{ox}, $H_{ox\text{-}1}$, and $H_{ox\text{-}2}$. Allowing for

small shifts, the profile complemented that obtained for inhibition by CO, thus implicating the most reduced catalytic intermediate, two electrons below H_{ox} and hence at the level of H_{ox-2}, as the primary target for rapid and reversible inhibition [400]. Formaldehyde thus prevents the formation of the transient species $H_{ox-2}(2H)$ depicted in Scheme 3:1 (blue pathway). A much slower reaction, which is not reversible, is also observed, and becomes dominant as the electrode potential is raised [400,525]. However, the fact that at negative potentials where H_{ox-2} prevails, the rapidly inhibited fraction is almost quantitatively recovered upon formaldehyde removal after 5 minutes (Figure 3:1A) means that the fast binding process offers substantial protection against the slow and irreversible reaction.

Based on earlier evidence from density functional theory (DFT) [412,526,527] that in the H_{sred} state (and likely also H_{red}) Fe_d should carry a hydrido-ligand, it has originally been proposed that HCHO inhibition of the H_{ox-1} and H_{ox-2} levels occurs, mechanistically, through electrophilic attack on the respective hydrido complex to form a bound methanol or methoxide species [400]. This process is thermodynamically favourable and resembles Noyori chemistry (catalytic hydrogenation) (Scheme 3:2).

Scheme 3:2 Theoretical calculations of the mechanism of H_2 formation by the H-cluster (grey). The thermodynamically favourable reaction with formaldehyde is depicted in green. An alternative pathway, Schiff base chemistry at the bridgehead nitrogen atom, is shown in blue. Reprinted with permission from reference [400]. Copyright 2012 American Chemical Society.



However, subsequent efforts to detect any release of methanol have been unsuccessful [400,528], implying that HCHO might bind as a true inhibitor and not as an alternative, slow substrate. Further, results from spectroscopic investigations by different groups have led to the proposal that Fe_d neither carries a hydrido ligand in H_{red} [411,529] ($H_{ox\text{-}1}$ level) nor in the spectroscopically accessible form of H_{sred} ($H_{ox\text{-}2}$ level) [376] – the implication being that H_2 evolution occurs very rapidly following transfer of two protons upon the transition to or at the $H_{ox\text{-}2}$ redox level (compare Scheme 1:1) [210]. These developments place the nature of the reaction with formaldehyde, which contains a potent electrophilic C-atom, in a new context – namely as a probe to investigate *when* the initial H^+ transfer to Fe_d (to form the hydrido complex) occurs during catalysis, as well as the subsequent second protonation of the adt-moiety. The results also convey additional structural information, because known complexes

of metals with formaldehyde do not bind only through a single metal-C bond, but involve secondary stabilisation through *di*-hapto (η-C,O) coordination [530-532], a notable example being $Fe(\eta^2\text{-}CH_2O)(CO)_2(P(OMe)_3)_2$ reported by Berke *et al.* [533].

This chapter expands the concept of using the combination of PFE and formaldehyde as probe for the mechanism of H_2 production to longer chain aldehydes, *i.e.* trifluoroacetaldehyde, acetaldehyde, butyraldehyde, and isovaleraldehyde. Having different electronic and steric properties, these molecules might allow a distinction between different postulated reaction pathways at the H-cluster. Moreover, in addition to intercepting and trapping reactive intermediates such as the super-reduced state H_{sred}, extended alkyl chains provide the equivalent of a 'trail of string' marking the route taken to and from the active site. These inhibitors could hence shed more light on the gas channels that allow diffusion through the protein towards the active site.

Separately, using the algal enzyme *Cr*HydA1, pulsed-EPR spectroscopy experiments with isotopically enriched formaldehyde (DCDO and $H^{13}CHO$) were undertaken in collaboration with Dr. William Myers (Centre for Advanced Electron Spin Resonance, University of Oxford) to gain insight into the binding mode of formaldehyde (the simplest and most reactive aldehyde inhibitor) to the H-cluster. Use of EPR allows the species formed upon rapid and reversible reaction with formaldehyde to be studied over long periods in frozen samples, avoiding the irreversible degradation that would inevitably result if using techniques such as IR that normally require ambient temperatures. Furthermore, DFT calculations were carried out by Professor John McGrady (Inorganic Chemistry Laboratory, University of Oxford) to provide mechanistic support. *Taken together,* the results have important implications for the mechanism of [FeFe]-hydrogenases.

3.2 Protein film electrochemistry investigations

Aiming at establishing whether aldehydes can react with the $H_{ox\text{-}2}$ redox level and, further, discriminating between the two originally postulated reaction pathways Schiff-base chemistry and hydridic carbonyl reduction [400] (see Scheme 3:2), the concept of using formaldehyde as probe for the mechanism of H_2 production was expanded to longer chain aldehydes of different steric demand and electrophilicity. Through chronoamperometry experiments, the potential dependences of the inhibition of *Ca*HydA by four different aldehydes have been determined: (i) trifluoroacetaldehyde (CF_3CHO), (ii) acetaldehyde (MeCHO), (iii) butyraldehyde (PrCHO), and (iv) isovaleraldehyde (*i*-BuCHO) (Figure 3:2).

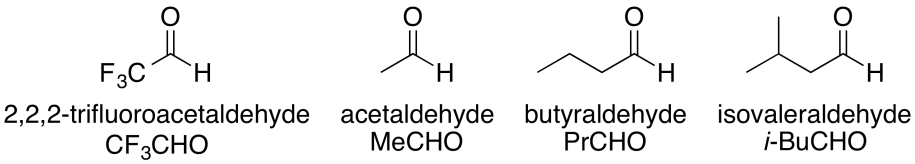


Figure 3:2 Structures of the different aldehyde molecules studied as inhibitors of [FeFe]-hydrogenases.

To illustrate the general principle, two typical experiments using MeCHO are depicted in Figure 3:3. In the red trace, the electrode is poised at a low potential in the hydrogen production regime (–0.6 V). Acetaldehyde inhibitor is injected at $t = 0$. The *inhibition kinetics* can be obtained by subsequent monitoring of the decrease in catalytic current. After 300 s, the cell solution is rinsed with fresh, temperature- and gas-equilibrated buffer (ten times the original cell volume, grey area), while maintaining electrical connectivity. The activity that is restored after the rinse determines the *extent of reversibility* the inhibition process displays. Note the initial increase of normalised current immediately after the start of the rinsing process ('current overshoot'); this can most likely be attributed to a slightly higher temperature in the fresh buffer solution, giving higher activity [525]. The black current *vs.* time trace in Figure 3:3 shows MeCHO inhibition of hydrogen oxidation by *Ca*HydA. Here,

the extent of inhibition is higher than in the red trace. However, the process at +0.05 V is less reversible.

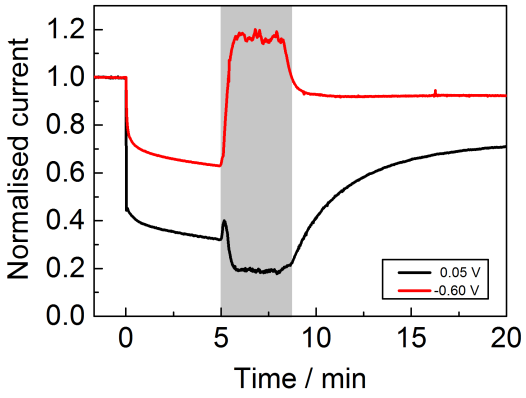


Figure 3:3 Current *vs.* time traces depicting the decrease of hydrogen oxidation (black) and hydrogen evolution (red) activity of *Ca*HydA following injection of 168 μM MeCHO at $t = 0$. The currents are normalised for film loss according to eq. (2:30) The grey area shows Δt in which the buffer solution is exchanged to establish whether activity can be restored after removal of the inhibitor. Experimental conditions: pH 6.0 phosphate buffer; $\omega = 3000$ rpm, dark, 5 ºC, 100% H_2. Due to the volatility of MeCHO (bp 20 ºC) H_2 flow was briefly interrupted during inhibition and restored after buffer exchange (see section 3.2.3).

3.2.1 Inhibition by formaldehyde

For comparison, the potential dependence of inhibition of *Ca*HydA by formaldehyde, which serves as 'benchmark', is shown in Figure 3:4. The dependence was established by Foster *et al.* [400] through chronoamperometry experiments analogous to those shown in Figure 3:3. The reactivity of formaldehyde towards the enzyme increases as the potential is lowered. The potential dependence follows two one-electron Nernst transitions and maximum inhibition occurs at the $H_{ox\text{-}2}$ redox level. Kinetic analysis (see Figure 3:1 for a sample trace recorded in the H_2 production region) shows that inhibition at low potentials essentially follows a single-exponential time-course. Conversely, at high potentials where formaldehyde inhibition of *Ca*HydA is marginal, the kinetics are biphasic, with the slower component being the dominating kinetic process. It needs to be mentioned that formaldehyde is believed to enter the enzyme in its gaseous form, *i.e.* as free, non-hydrated HCHO [525]. The equilibrium constant for hydration, K_{eq}, is approximately 2000 at 25 °C [534,535].

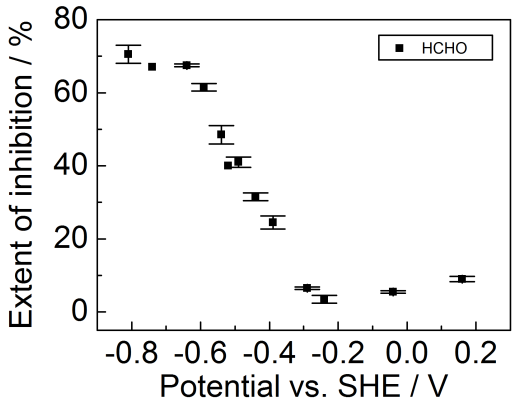


Figure 3:4 Potential dependence of inhibition of *Ca*HydA by formaldehyde. Data taken from reference [400]. The extent of inhibition was measured after 100 s of exposure to 4.5 mM HCHO in 100% H_2, which corresponds to 2.25 μM non-hydrated HCHO. Conditions: pH 6.0 phosphate buffer, $\omega = 2500$ rpm, 20 °C, dark (blacked-out) cell. Error bars represent one standard deviation.

3.2.2 Inhibition by trifluoroacetaldehyde

The potential dependence of CF_3CHO inhibition of *Ca*HydA is depicted in Figure 3:5. Due to the high K_{eq} for hydrate formation of $\sim 2.9\times10^4$ [536] (one order of magnitude larger than $K_{eq,HCHO}$), the maximum concentration that could be employed in these measurements (restricted by a maximum electrochemical cell volume of 5.0 mL) was 182 mM CF_3CHO, which corresponds to 6.3 μM non-hydrated aldehyde (compared to 2.25 μM HCHO in section 3.2.1). Generally, inhibition studies could not be carried out in the 'intermediate' potential region close to the equilibrium potential for H^+/H_2 interconversion (*i.e.* between −0.4 V and −0.15 V, see Figure 1:33), due to the relatively low catalytic currents in this region that are lowered even further by the exponential 'film loss' processes that underlie every experiment (see section 2.2.7).

As shown in Figure 3:5, in the potential region where hydrogen formation takes place, the extent of CF_3CHO inhibition follows a similar potential dependence profile to that of HCHO inhibition (Figure 3:4). Even though the magnitude of the extent of inhibition cannot be directly compared, since different concentrations of aldehydes had to be employed, it

becomes immediately apparent that CF_3CHO inhibits hydrogen production activity of *Ca*HydA to a much lesser extent than formaldehyde. Interestingly, CF_3CHO shows higher inhibition of H_2 oxidation than proton reduction, which stands in contrast to *Ca*HydA inhibition by formaldehyde, where H_2 oxidation inhibition is marginal.

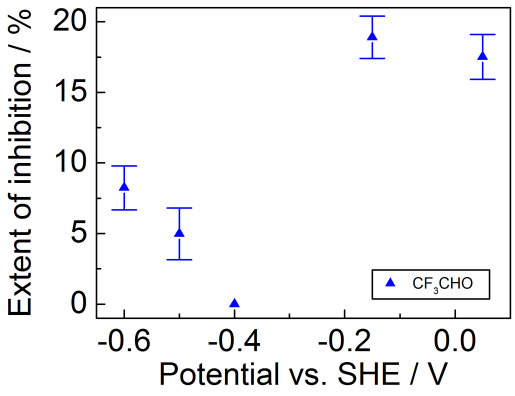


Figure 3:5 Percentage inhibition of *Ca*HydA by CF_3CHO after 100 s of exposure. Conditions: 100% H_2, 6.3 µM (non-hydrated) CF_3CHO, 20 °C, $\omega = 3000$ rpm, pH 6.0, dark. Error bars represent one standard deviation; all measurements were carried out in triplicate.

The kinetics of CF_3CHO inhibition are shown in Figure 3:6. Similar to formaldehyde inhibition of *Ca*HydA, CF_3CHO inhibition follows bi-exponential kinetics. The rate constants of the fast and slow components of the reaction are depicted in red and blue, respectively. Both increase as the potential is raised, with k_{fast} being about one order of magnitude larger than k_{slow}. In formaldehyde inhibition of *Ca*HydA, the rate constant of the fast component also increases as the potential is increased, but k_{slow} is potential independent [528]. In agreement with the faster overall reactivity displayed by HCHO, both the fast and the slow process of HCHO inhibition [528] occur on much faster timescales than CF_3CHO inhibition – $k_{fast,HCHO} \sim 10^6 \times k_{fast,CF3CHO}$; $k_{slow,HCHO} \sim 10^4 \times k_{slow,CF3CHO}$.

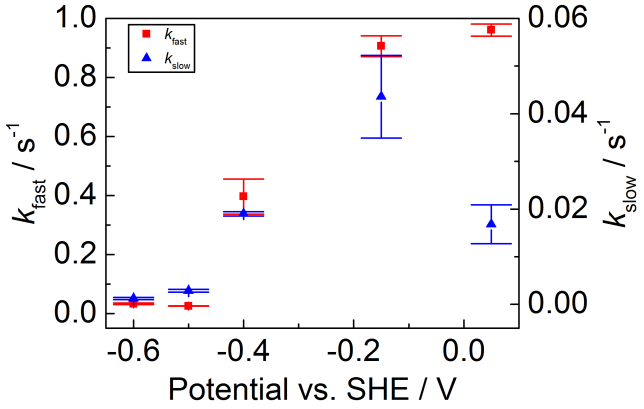


Figure 3:6 Potential dependences of the average rate constants of the fast (red) and slow (blue) phase of the biphasic reaction of CF_3CHO with *Ca*HydA. Error bars represent one standard deviation of propagated errors from least-square analysis of the inhibition kinetics. All measurements were carried out in triplicate.

Figure 3:7 shows the portions of the fast and slow process of the total inhibition (red, blue), compared to the overall reversibility of the inhibition at different potentials (depicted in black). Although caution in interpreting these data has to be taken because of the significant errors, the general trend is that the proportion of the fast phase increases as the potential is raised. This stands in contrast to formaldehyde inhibition, which follows the opposite behaviour [528]. Inhibition of hydrogen oxidation by CF_3CHO shows higher reversibility than inhibition of hydrogen formation and the former is enhanced compared to high potential inhibition by HCHO. Although the amount of fast phase shows the opposite trend with potential depending upon whether HCHO or CF_3CHO is used, in both cases a higher proportion of the fast inhibition process leads to more reversibility.

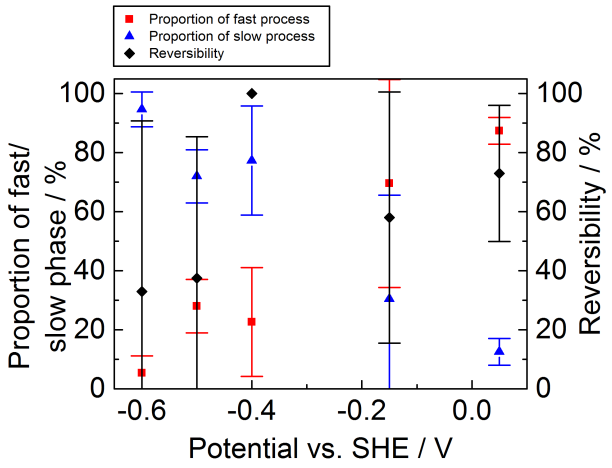


Figure 3:7 Comparisons of the potential dependences of the proportions of CF_3CHO inhibition that are due to the fast (red) and slow (blue) process with the average overall reversibility of the inhibition reaction (black). Error bars represent one standard deviation; all measurements were carried out in triplicate.

3.2.3 Inhibition by acetaldehyde

The potential dependence of MeCHO inhibition of *Ca*HydA is depicted in Figure 3:8. In the hydrogen production region at potentials below –0.4 V, MeCHO inhibition shows a trend similar to both HCHO and CF_3CHO inhibition, *i.e.* increasing inhibition with decreasing potential. Because of the high volatility of MeCHO (bp 20 ºC), experiments were performed at a lower temperature (5 °C) compared to all other aldehydes used in this work (20 °C) and the gas flow was interrupted simultaneously to aldehyde injection, until the end of the buffer exchange (rinsing step). The effect of H_2 consumption at high potential during the 5 min of MeCHO exposure was determined in control experiments where buffer was injected in place of aldehyde: less than 5% of activity was lost in these experiments (see Appendix C). Therefore, the impact of the substrate depletion on the activity of *Ca*HydA is negligible compared to actual inhibition be acetaldehyde. A relatively high concentration of acetaldehyde was required for significant inhibition to be observable, 168 µM non-hydrated MeCHO was used compared to 2.25 µM non-hydrated formaldehyde and 6.3 µM CF_3CHO.

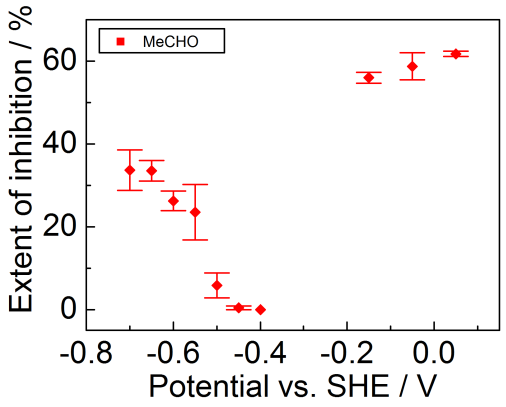


Figure 3:8 Percentage inhibition of *Ca*HydA by acetaldehyde after 100 s of exposure. Conditions: 336 µM MeCHO solution, 5 °C, dark, $\omega = 3000$ rpm, pH 6.0 phosphate buffer, 100% H_2 (interrupted during 5 min exposure to MeCHO). MeCHO has an equilibrium constant of 1, *i.e.* 336 µM MeCHO corresponds to 168 µM of non-hydrated aldehyde. Error bars represent one standard deviation; all measurements were carried out in triplicate.

Although inhibition increases as the potential is lowered, the total extent of inhibition is much lower than for HCHO. Similar to CF_3CHO, but in contrast to HCHO, MeCHO shows higher degrees of inhibition of hydrogen oxidation than proton reduction. The extent of MeCHO inhibition is approximately twice as great as that of CF_3CHO inhibition, although more than 50 times more MeCHO was used. Assuming scalability, this indicates greater reactivity of CF_3CHO compared to MeCHO, in agreement with the former's more electrophilic C=O group.

Although acetaldehyde inhibition is at least partially reversible both in the H_2 oxidation and in the H_2 evolution regime (see Figure 3:3), no clear trend in reversibility was observed across the potential window studied. The kinetics of the inhibition could not be determined due to the relatively large errors of the experiments, particularly at low potential, which are due to the complex experimental conditions that had to be employed with MeCHO. Although the interrupted H_2 flow had only marginal effects on H_2 consumption over the course of the experiments (*vide supra*), simultaneous aldehyde injection and removal of the H_2 gas inlet caused the initial decay in activity to differ slightly between repeats.

3.2.4 Inhibition by butyraldehyde

Butyraldehyde is significantly less soluble in water than the C1 and C2 analogues described in the previous sections. The maximum aldehyde concentration that could be employed in the experimental set-up was 30 mM. The potential dependence of the inhibition of *Ca*HydA by PrCHO is shown in Figure 3:9. At potentials below –0.4 V, it is qualitatively similar to the dependences recorded for MeCHO and CF_3CHO, but PrCHO shows much less inhibition.

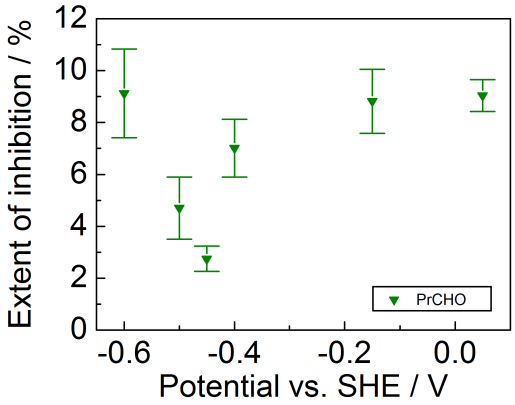


Figure 3:9 Percentage inhibition of PrCHO after 100 s of exposure. Conditions: *Ca*HydA, 100% H_2, 30 mM PrCHO, 20 °C, ω = 3000 rpm, pH 6.0 phosphate buffer, dark. Error bars represent one standard deviation; all measurements were carried out in triplicate.

In the hydrogen production region (below –0.4 V) in Figure 3:9 the reactivity increases when the potential is lowered. At intermediate and high potentials, no clear trend is apparent. This is also the case for the kinetic rate constants (Figure 3:10). Two separate processes occur across the whole potential range. The fast process (k_{fast}), is generally approximately 10 times faster then the slow process (k_{slow}), but no correlation between potential and rate constants can be drawn.

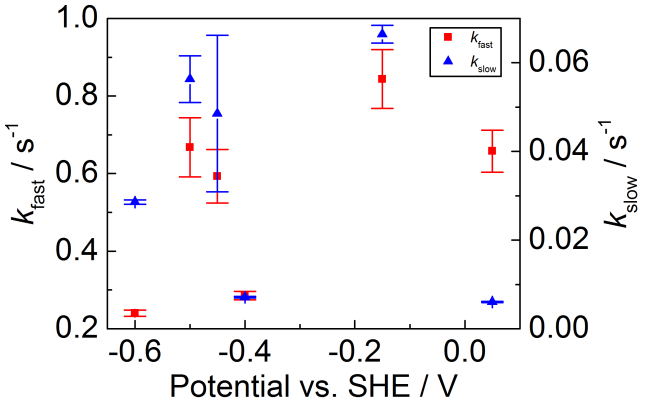


Figure 3:10 Potential dependences of the average rates constants of the fast (red) and slow (blue) phase of the biphasic reaction of PrCHO with *Ca*HydA. Error bars represent one standard deviation of propagated errors from least-square analysis of the inhibition kinetics. All measurements were carried out in triplicate.

Figure 3:11 shows that inhibition by PrCHO is partially reversible, but no clear tendency can be observed across the potential window studied.

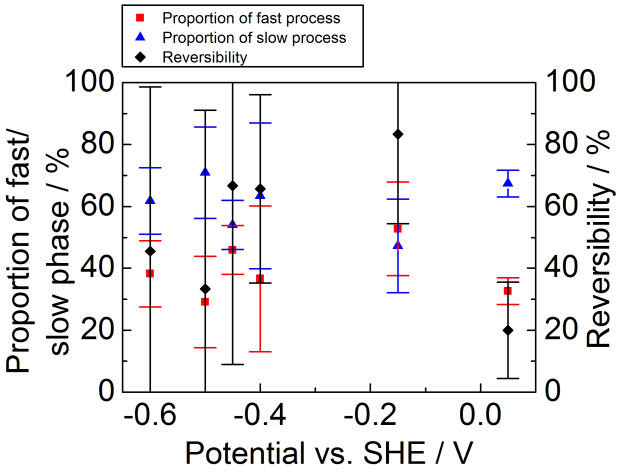


Figure 3:11 Comparisons of the potential dependences of the proportions of PrCHO inhibition that are due to the fast (red) and slow (blue) process with the average overall reversibility of the inhibition reaction (black). Error bars represent one standard deviation; all measurements were carried out in triplicate.

3.2.5 Inhibition by isovaleraldehyde

The branched aldehyde *i*–BuCHO is the least water-soluble aldehyde used in this work. Its reactivity towards *Ca*HydA is intrinsically low, even at the maximum concentration of 30 mM that could be used in the electrochemical cell. The potential dependence of the extent

of inhibition of *Ca*HydA by *i*-BuCHO is depicted in Figure 3:12. Isovaleraldehyde clearly shows the least inhibition of all the different aldehydes studied.

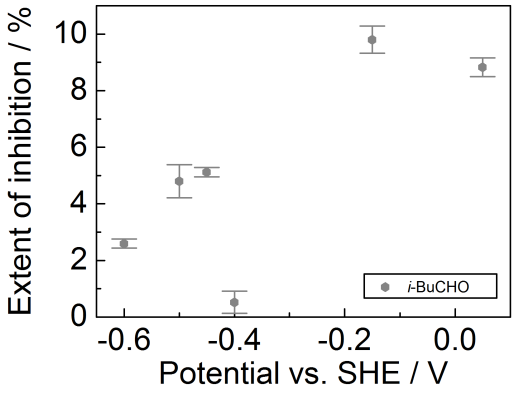


Figure 3:12 Percentage inhibition of *i*-BuCHO after 100 s of exposure. Conditions: *Ca*HydA, 100% H_2, 30 mM *i*-BuCHO, 20 °C, ω = 3000 rpm, pH 6.0 phosphate buffer, dark. Error bars represent one standard deviation; all measurements were carried out in triplicate.

All recorded current *vs*. time traces follow bi-exponential decomposition pathways. Similar to inhibition by PrCHO, the obtained rate constants do not follow any trend (Figure 3:13).

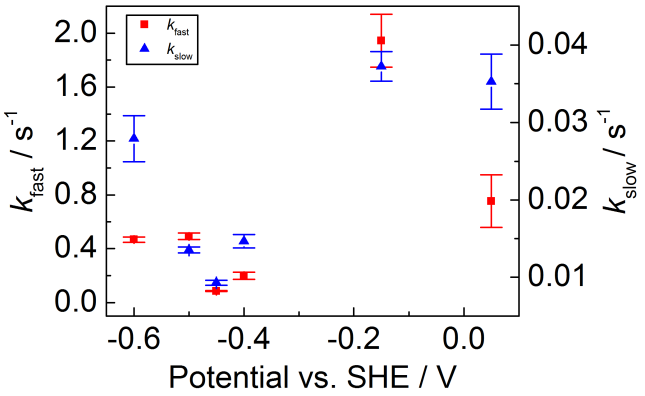


Figure 3:13 Potential dependences of the average rate constants of the fast (red) and slow (blue) phase of the biphasic reaction of *i*-BuCHO with *Ca*HydA. Error bars represent one standard deviation of propagated errors from least-square analysis of the inhibition kinetics. All measurements were carried out in triplicate.

As depicted in Figure 3:14, the proportion of the fast phase increases as the potential is raised (for potentials > –0.4 V). The inhibition at low potential is irreversible, indicating *i*-BuCHO might not be able to reach the active site of the enzyme.

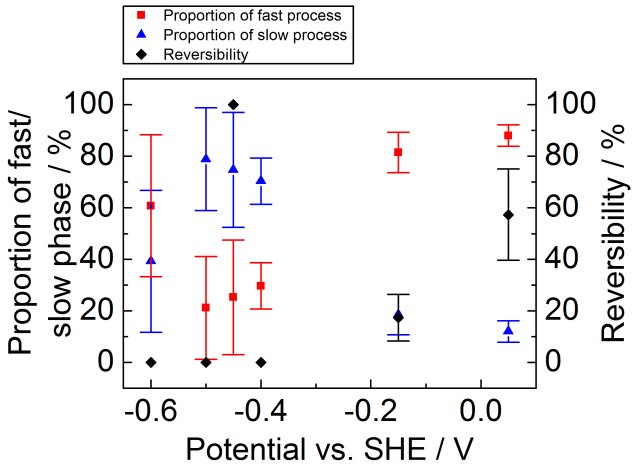


Figure 3:14 Comparisons of the potential dependences of the proportions of *i*-BuCHO inhibition that are due to the fast (red) and slow (blue) process with the average overall reversibility of the inhibition reaction (black). Error bars represent one standard deviation; all measurements were carried out in triplicate.

3.3 Discussion

3.3.1 Discussion of the different aldehyde reactivities

If aldehyde inhibition of [FeFe]-hydrogenases takes place at the active site, either at the Fe_d atom or at the pendant amine group (adt-N), the size and electrophilicity of the aldehyde should have a strong influence on its reactivity towards the enzyme. All aldehydes apart from the 'bulky' *i*-BuCHO show at least partial reversibility over the entire potential region studied, indicating that these molecules can penetrate into the enzyme, and reaction pathways at the H-cluster similar to those proposed for formaldehyde are feasible.

Both CF_3CHO and MeCHO are similar in steric demand, but the former possesses a more electrophilic C=O group. In the H_2 production regime, both show increased inhibition as the potential is lowered, in agreement with postulated reactivity towards the $H_{ox\text{-}2}$ level of the H-cluster. However, both aldehydes also show reversible inhibition at high potential, in contrast to HCHO. Concentrations significantly higher than those used for experiments involving HCHO had to be employed to observe measurable inhibition. At low potential, the potential dependence of inhibition by PrCHO is qualitatively similar to CF_3CHO and MeCHO, but PrCHO shows much less reactivity. *i*-BuCHO shows the least inhibition of all aldehydes employed in this work and reacts irreversibly with *Ca*HydA at low potentials.

Figure 3:15 shows a comparison between the normalised potential dependences of all four aldehydes, revealing orders of magnitude differences in (concentration corrected) reactivity. One has to be cautious and avoid a quantitative interpretation of this comparison, due to normalisation over a large concentration range, but qualitative trends become apparent: the order of reactivity HCHO > CF_3CHO > MeCHO > PrCHO > *i*-BuCHO suggests that the less electrophilic and sterically accessible the carbonyl C-atom (the former

because of positive inductive effects of the different alkyl substituents and the latter due to increasing steric hindrance caused by the alkyl groups), the lower the reactivity at low potentials where the H_{ox-2} level prevails and the enzyme is most active for H_2 formation. The correlation suggests that these aforementioned properties of the aldehydes modulate their reactivities at the enzyme active site, corroborating the hypothesis of aldehyde inhibition occurring at the H-cluster, preferably targeting the H_{ox-2} level, as proposed for HCHO [400].

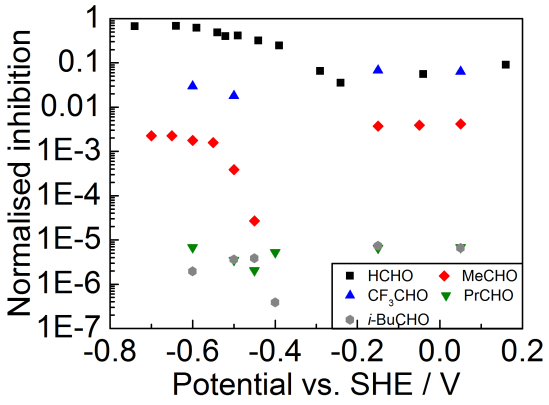
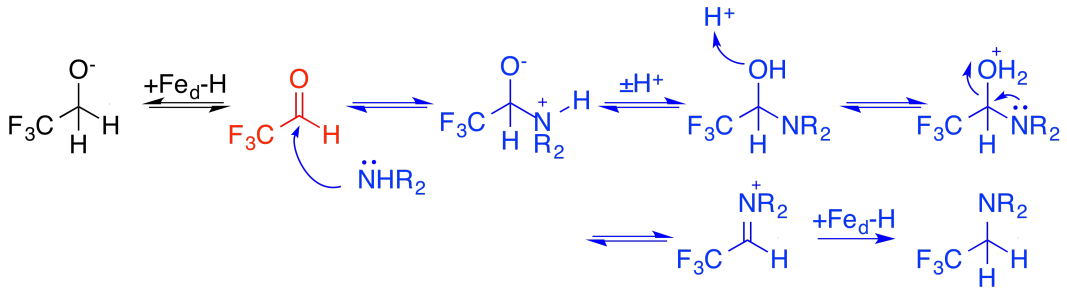


Figure 3:15 Comparison of the normalised (*i.e.* concentration corrected) extent of inhibition as a function of potential for the four different aldehydes studied in this work, measured after 100 s of exposure. Data for formaldehyde inhibition were taken from reference [400].

Kinetic analyses of the inhibition reactions of the different aldehydes were carried out with the aim of gaining more insight into the possible reaction pathways. All aldehydes display biphasic inhibition kinetics, but no direct correlations between fast/slow reaction and reversibility (as is the case for HCHO [400,525,528,537]) could be determined. Instead, the picture is more complex. Whereas formaldehyde shows relatively 'clean' reactivity, with the proportion of the dominating, fully reversible rapid reaction increasing as the potential is lowered, aldehydes of larger size are more likely to react with nucleophilic groups at the protein periphery or in the gas channels (blocking substrate delivery and product removal to and from the active site) since access to the H-cluster is likely to be restricted. Furthermore, different reactivities towards the adt-N moiety of the H-cluster have to be taken into account.

For example, HCHO and CF_3CHO cannot form enamines due to the lack of α-carbonyl protons. Although formation of enamines is theoretically a reversible reaction, these are expected to be thermodynamically (*meta*-) stable products. Possible reaction pathways of CF_3CHO and the H-cluster are depicted in Scheme 3:3, specifically reduction by Fe_d-hydrido species (black) and nucleophilic attack by adt-N (blue). Since α-protons in CF_3CHO are replaced with fluorine substituents, the only likely fate of an iminium ion formed by Schiff base chemistry, other than the reverse reaction, is irreversible reduction with an iron hydride to form a fluorinated alkylamine.

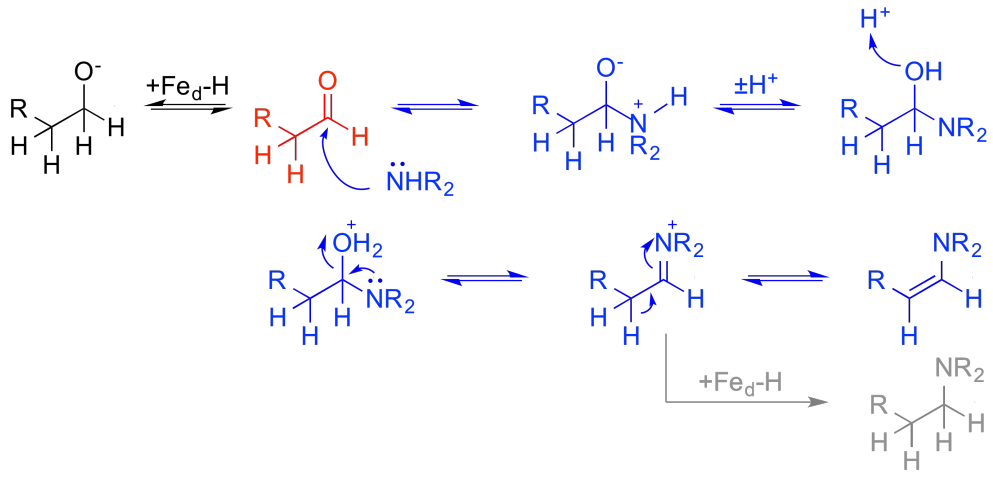
Scheme 3:3 Possible reactions of CF_3CHO (red) with the H-cluster. Alkoxide formation through hydride transfer from Fe_d is depicted in black. Iminium chemistry is shown in blue.



The higher irreversibility of CF_3CHO inhibition at low potentials compared to HCHO (see **Figure 3:7**) can in principle be rationalised by equilibration to the iminium ion and its subsequent reduction (blue pathway in Scheme 3:3) being the dominant pathway over direct Fe_d-H reduction of the carbonyl bond. This would be in agreement with the more bulky nature of CF_3CHO compared to HCHO; greater sterical demand might likely favour reaction at the more easily accessible adt-N. The greater reversibility of the inhibition at high potentials could be explained by the fact that Schiff base chemistry cannot proceed beyond reversible equilibration to the iminium ion, since neither highly reducing metal-hydrido species nor α-protons required for enamine formation are available.

In contrast to CF_3CHO, MeCHO, PrCHO, and *i*-BuCHO do possess α-protons, and reversible enamine formation is possible, in addition to the interception of Fe-H species that occur transiently at the H-cluster. The different reaction pathways are outlined in Scheme 3:4. For acetaldehyde, direct reduction of the carbonyl carbon by a metal-hydrido bond formed in a reduced H-cluster state (black pathway) would be in agreement with the observed potential dependence (Figure 3:8), since the reactivity of the H-cluster increases as the potential is lowered. Electrophilic attack of MeCHO on adt-N is projected to yield, initially, the iminium ion (*via* the aminol). Subsequently, two different routes have to be considered: irreversible hydride transfer to form a tertiary amine (grey pathway) and reversible enamine formation (depicted in blue). Although iminium ions are considerably easier to reduce than carbonyl bonds, under strong reducing conditions (*i.e.* low potentials), direct reaction with the aldehyde is still expected to be the kinetically dominant pathway, since the former species are only accessible through a multistep equilibrium.

Scheme 3:4 Possible reaction pathways of MeCHO, PrCHO, and *i*-BuCHO with the H-cluster. Hydride transfer to the carbonyl bond is depicted in black, Schiff base chemistry at the bridgehead N atom of the H-cluster is shown in blue, and formation of formation of a tertiary amine is shown in grey. R = -H (MeCHO), $-CH_2CH_3$ (PrCHO), or $-CH(CH_3)_2$ (*i*-BuCHO).



Acetaldehyde inhibition at potentials where *Ca*HydA catalyses H_2 oxidation (> –0.3 V) displays a different potential dependence to inhibition by formaldehyde. *Ca*HydA shows very

little formaldehyde inhibition (< 15%, irrespective of the applied potential in this region; Figure 3:4), whereas ~60% of activity is inhibited by acetaldehyde (Figure 3:8). Since inhibition of H_2 oxidation at high potentials is, due to the absence of reducing species such as metal-hydrides, less likely to stem from direct hydride transfer, the potential independent iminium chemistry can be expected to prevail, leading to enamine formation. Conversely, formaldehyde *cannot* form enamines due to the lack of α-protons, a fact that might contribute to the observed difference in reactivity between these two aldehydes. The greater extent of acetaldehyde inhibition at high potentials compared to formaldehyde indicates that nucleophilic attack by the adt-N moiety might be more favoured for acetaldehyde. This may be related to the greater steric demand of acetaldehyde, possibly limiting access to Fe_d compared to the pendant amine group.

Nucleophilic attack by adt-N on the carbonyl carbon proceeds *via* the hemiaminal (Scheme 3:3 and Scheme 3:4). Although it is an intermediate in the equilibrium towards formation of the iminium ion (and further products), the hemiaminal *itself* can be stabilised through secondary ligation (by its $-O^-$ group) to Fe_d, which has a vacant coordination site in the H_{ox} state. Figure 3:16 depicts the resulting species, which can, principally, account for reversible inhibition of the H-cluster (by all four aldehydes studied in this work) at oxidising potentials.

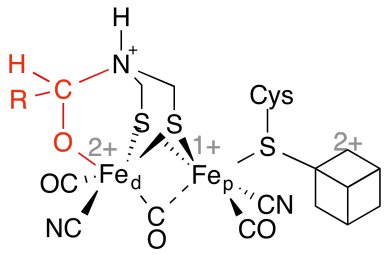


Figure 3:16 Possible aldehyde adduct to the H-cluster in the H_{ox} state, formed upon hemiaminal formation following electrophilic attack of the aldehyde carbonyl-C on adt-N of the enzyme active site. R = -H (HCHO), $-CH_3$ (MeCHO), $-CF_3$ (CF_3CHO), $-(CH_2)_2CH_3$ (PrCHO), or $-CH_2CH(CH_3)_2$ (*i*-BuCHO).

In principle, both PrCHO and *i*-BuCHO should follow the same reaction pathways as acetaldehyde (Scheme 3:4 or Figure 3:16). In PrCHO, even though free rotation is allowed in the two additional σ-bonds compared to MeCHO/CF_3CHO, the increased chain length seems to have a profound effect on the extent of inhibition, which is significantly lower compared to its smaller analogues. The increase in inhibition with added driving force in the hydrogen production region shown in Figure 3:9 (between−0.45 and −0.6 V) might indicate that this aldehyde can, to some extent, reach and react with the H-cluster. However, inhibition is only partially reversible, no coherent reactivity pattern is observable at intermediate to high potentials, and there is no correlation between potentials, rate constants, and reversibility (Figure 3:10 and Figure 3:11). Thus, processes other than reaction at the active site must be taken into account, including reaction at nucleophilic residues surrounding the active site or at the periphery of the protein, possibly blocking H_2 binding sites or disturbing the proton transfer chain.

The low inhibition observed with *i*-BuCHO suggests that this relatively bulky molecule can hardly, if at all, reach the enzyme active site (Figure 3:12). Inhibition in the hydrogen oxidation region could stem from reaction at the periphery of the protein (*vide supra*). These reactions have not been explicitly taken into account for the other aldehydes apart from PrCHO, as they do not explain the potential dependences observed for these molecules. The the fact that inhibition by *i*-BuCHO at low potential is irreversible (Figure 3:13) supports the hypothesis that this branched aldehyde cannot reach the active site.

In general, the observed reactivity trends of the four different aldehydes investigated by PFE (Figure 3:15) seem to support previous mechanistic hypotheses [400] and suggest that aldehydes can target and inhibit the active site of [FeFe]-hydrogenases. However, the complex kinetic patterns the different aldehydes displayed over the examined potential

window stand in stark contrast to inhibition by formaldehyde, where a fast, fully reversible process dominates inhibition of H_2 formation and a slower, potential independent process is responsible for (marginal) inhibition of H_2 oxidation [528,537]. Further, the fact that only partial reversibility was observed for these 'longer chain' aldehydes strongly suggests a more complex picture than with formaldehyde, *i.e.* additional, different processes occur. Aldehydes are highly reactive electrophiles that can target many nucleophilic residues and positions in the complex and intricate structures of [FeFe]-hydrogenases.

An inherent disadvantage of PFE is that it does not provide any structural information. Hence, the mechanistic proposals put forward in this chapter, as attractive or unattractive as they may be, have in common that they lack structural evidence and therefore remain speculative. In order to determine the *mode* of binding and the *mechanism* of inhibition, one has to utilise other, structure-specific techniques, such as EPR spectroscopy. Implications from investigations of HCHO inhibition by advanced EPR-techniques, supported by density functional theory, are presented in the following sections.

3.3.2 Implications from the investigation of formaldehyde inhibition of the H-cluster by pulsed-EPR techniques

3.3.2.1 Formaldehyde inhibition of the H-cluster detected by ENDOR and ESEEM

Pulsed-EPR experiments were undertaken with the aim of directly determining the binding mode of formaldehyde to the H-cluster, using the enzyme *Cr*HydA1 (instead of *Ca*HydA) because of its lack of F-clusters, which would give rise to complicated EPR-signatures. The experiments where conducted in collaboration with Dr. William Myers (Centre for Advanced Electron Spin Resonance, Oxford), who developed the mathematical model for analysis of the pulsed-EPR spectra, analysed and simulated the data, and prepared the figures presented in this section.

Figure 3:17 shows the integrated free-induction decay (FID) X-band EPR spectrum of H_2-reduced *Cr*HydA1 in the presence of HCHO. I equilibrated the sample in an anaerobic glove box under H_2 flow for 3.5 h before injecting formaldehyde into the enzyme solution to give a final concentration of free, (*i.e.* non-hydrated) HCHO equal to the concentration of *Cr*HydA1 (see section 8.2.4). The spectrum features a rhombic system consistent with a reduced cubane cluster ($[4Fe\text{-}4S]^{1+}$) [538], meaning that the great majority of spin density resides on $[4Fe\text{-}4S]_H$. EPR simulation yields g values of 2.074, 1.946, and 1.886, in agreement with those observed previously for $H_{ox\text{-}2}$ [376,399]. The minor signal at $g = 2.025$ most likely corresponds to a slowly formed decay product following HCHO inhibition of *Cr*HydA1. This observation is consistent with PFE results, where small proportions of slow, irreversible inhibition are observed when *Cr*HydA1 is subjected to HCHO at negative potentials (even though fast, reversible inhibition is the dominant pathway) [528]. For comparison, the derivative continuous-wave (CW) spectrum of the same sample, also obtained at X-band, is shown in Appendix D.

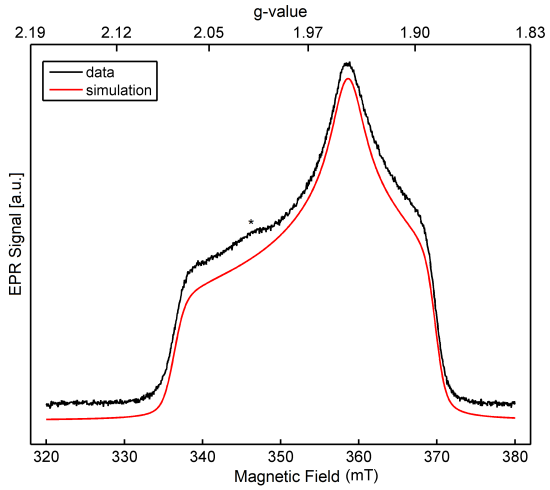


Figure 3:17 X-band FID-detected EPR spectrum, recorded at 10 K (black), and a simulation (red) of formaldehyde-inhibited *Cr*HydA1, at a spin concentration of 830 μM. The π/2 pulse length was 320 ns. Simulation values were $g_x = 2.074$, $g_y = 1.946$, $g_z = 1.886$. A degradation product at $g = 2.025$ is indicated (*).

To characterise the interaction of formaldehyde with the H-cluster in the $H_{ox\text{-}2}$ level, pulsed-ENDOR spectra of ^{13}C-labelled HCHO were recorded at Q-band[i] for several *g* values, as shown in Figure 3:18 (at the extreme *g* values, the single-crystal-like spectra provide the highest resolution of different classes of ^{13}C [523]). The observed ENDOR frequencies for the hyperfine interaction (*A*) of *A*/2 less than the nuclear Larmor frequency are

$$\nu^{\pm}_{\mathrm{ENDOR}}(^{13}C) = \nu(^{13}C) \pm |A(^{13}C)|/2. \tag{3:1}$$

Here, $\nu(^{13}\mathrm{C})$ is the nuclear Larmor frequency and $A(^{13}\mathrm{C})$ corresponds to the hyperfine interaction value for an arbitrary orientation of the electron-nucleus vector in the magnetic field. The ENDOR data were analysed using the following equation:

$$\boldsymbol{A} = a_{\mathrm{iso}}\mathbf{1} + \boldsymbol{gT}/g_{\mathrm{e}}, \tag{3:2}$$

where $\boldsymbol{A}$ is the full hyperfine tensor, a_{iso} is the isotropic value of $\boldsymbol{A}$, defined as its mean, **1** is the identity matrix, and $\boldsymbol{T}$ is the dipolar component for the nucleus which is scaled by the effective *g* value, $\boldsymbol{g}/g_{\mathrm{e}}$. In the principle axis of a point-dipole interaction $\boldsymbol{T}$ is defined as

$$\boldsymbol{T} = \frac{\mu_0}{4\pi h}\frac{g_{\mathrm{e}}\mu_{\mathrm{B}}g_{\mathrm{n}}\mu_{\mathrm{n}}}{r^3}\rho_{\mathrm{Fe}}[-1 \quad -1 \quad 2] = [-T \quad -T \quad 2T]. \tag{3:3}$$

Importantly, eq. (3:3) shows that the dipolar interaction is proportional to the spin density of the Fe centre, ρ_{Fe} (but also dependent on the distance, *r*), and this could be appropriate for coordination at the distal Fe, more than 8 Å away from the spin-bearing $[4Fe\text{-}4S]_H^{1+}$ subdomain. However, since for a mixed-valence metal cluster *T* is a summation of dipolar interactions of *all* spin densities with a given nucleus, an approximate local spin model was developed (by Dr. William Myers) that is sufficiently accurate to test trial locations for the coordination of HCHO in the presence of the $[4Fe\text{-}4S]_H^{1+}$ and $[2Fe]_H$ domains of the H-cluster [539]. In addition to Fe_d, other sites that are able to undergo nucleophilic attack at the HCHO carbonyl carbon also constitute points of interest, including adt-N and the bridging

[i] ENDOR measurements performed at Q-band afford increased orientation selection and separate the ^{13}C Larmor frequency from overlapping ^{14}N frequencies that are of concern at X-band.

CO position between Fe_p and Fe_d, which has recently been suggested to be occupied by a μ-hydrido ligand in the H_{ox-2} level, most likely separate from the catalytic H_{sred} state (*vide infra*) [529].

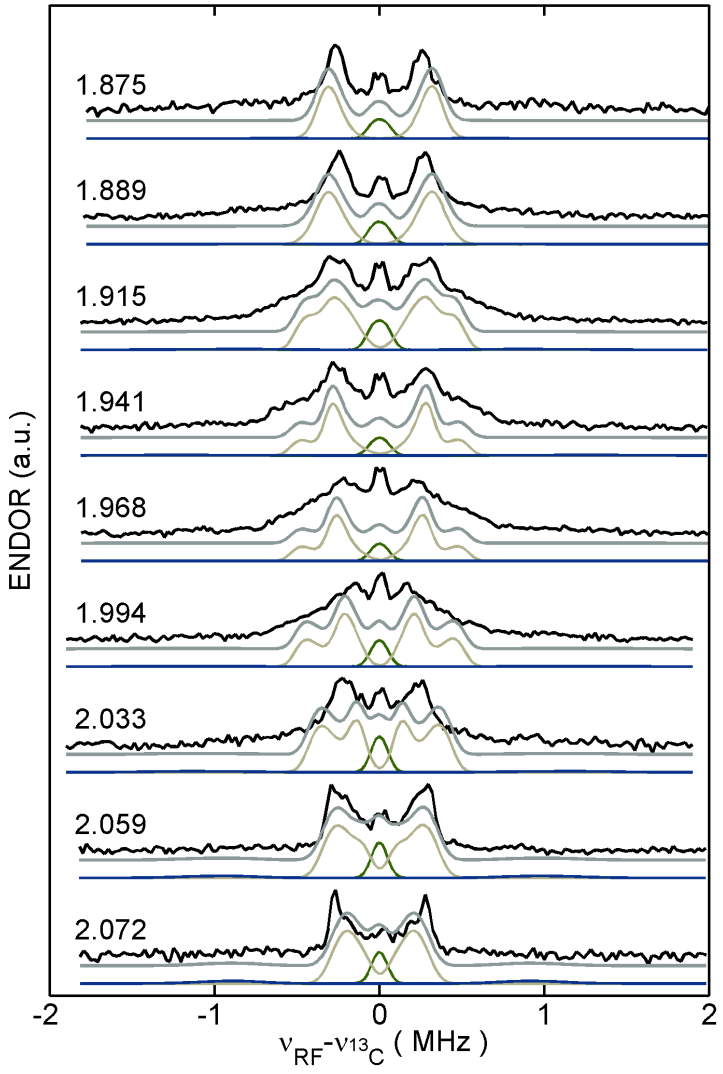


Figure 3:18 Q-band Mims ENDOR spectra (black) and simulations of $H^{13}CHO$ inhibited *Cr*HydA1 recorded at several *g* values, as indicated. For all traces the temperature was 8 K, with a τ value of 250 ns, π(RF) = 80 μs, repetition time of 20.4 ms; the microwave frequency was 33.7704 GHz [539].

In Figure 3:18, ^{13}C hyperfine interaction with formaldehyde that is remote from Fe_d is seen in the centre of the spectrum as a small peak that is somewhat suppressed (with a τ value of 250 ns). This signal does not stem from naturally occurring ^{13}C atoms in the protein close to the active site (as, for example, observed in ^{13}C ENDOR studies on CO inhibited nitrogenase

[540]), as ENDOR experiments using unlabelled $H^{12}CHO$ show no such signal contributions (Appendix E).

The splitting of about 0.6 MHz at both extreme *g* values in Figure 3:18 changes over the EPR envelope, to approximately 1.2 MHz in width for broad shoulders, with the maximum intensity narrowing to 0.3 MHz at intermediate fields. These variations suggest that the dipolar component is larger than the isotropic component [539]. Simulation using $A_{iso} = 0.12$, and $T = 0.55$ represents the field dependent pattern, but cannot account for the orientational distributions that give rise to the low resolution shoulders in Figure 3:18. Simulations using the approximate local spin model show that dipolar components required to fit the shoulders in intermediate fields in Figure 3:18 (*i.e.* $A_{max} \approx 1.2$ MHz) could arise only through positions of formaldehyde that either bisect the azadithiolate bridge or positions lying on the side of adt-bridge closer to the $[4Fe\text{-}4S]_H^{1+}$ subcluster [539].

A third class of ^{13}C contributes to the ENDOR data in Figure 3:18 with very low intensity as shoulders at ±0.5 MHz at $g = 2.072$ and as slight peaks near ±0.9 MHz at $g = 1.8752$. X-band HYSCORE data recorded on the same $H^{13}CHO$-inhibited *Cr*HydA1 sample suggest these signals are largely isotropic rather than dipolar in character, but the intensity is insufficient for detailed analysis [539]. In short, while ^{13}C hyperfine interactions detected in ENDOR experiments on $H^{13}CHO$-inhibited *Cr*HydA1, poised in the $H_{ox\text{-}2}$ level, unambiguously show that formaldehyde can access the H-cluster, the complicated nature of these interactions also reveals a complex picture where binding takes place in multiple orientations.

As it is possible to determine the number of equivalent nuclei of a particular type of coupling with the electron spin from the ESEEM modulation depth (section 2.5.4), 3-pulse ESEEM experiments were carried out (using deuterated formaldehyde, DCDO) to gain

insight into the relative amounts of the different formaldehyde-bound species suggested by the aforementioned ENDOR experiments. The modulation depth in the ESEEM data presented in Figure 3:19A is primarily due to weakly coupled formaldehyde [541] and simulations suggest *six* weak ^{2}H hyperfine interactions that are randomly oriented [539].

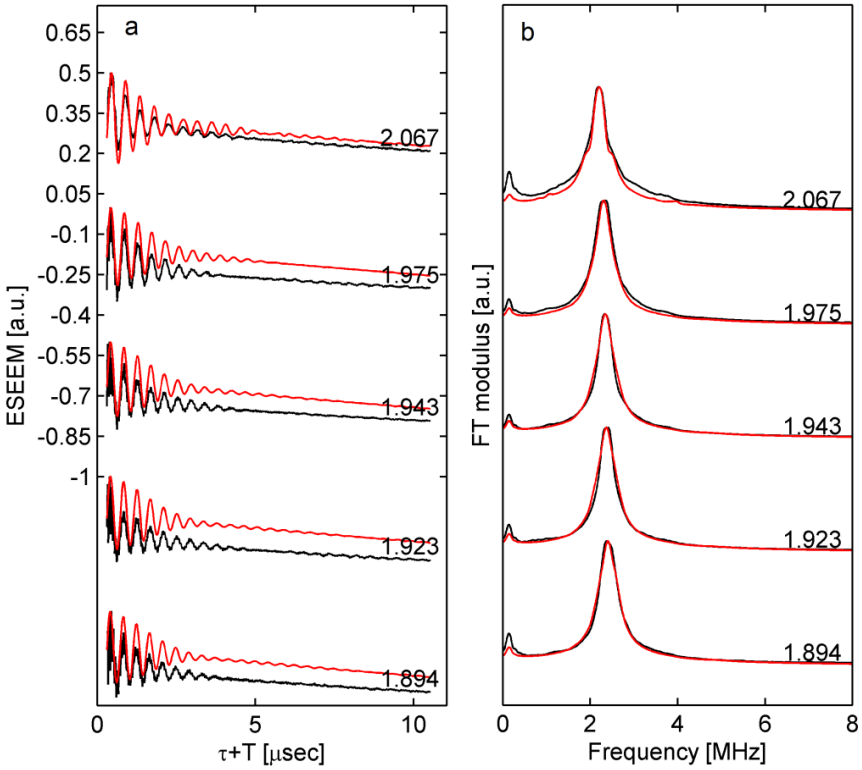


Figure 3:19 X-band 3-pulse ESEEM of DCDO inhibited *Cr*HyA1 (black) and simulations (red) at several *g* values as listed for (A) time domain and (B) frequency domain. The temperature was 12 K, microwave frequency of 9.7491 GHz, at a field of 337.2 mT. For ESEEM, $\tau = 212$ ns, with an initial T of 100 ns, a time step of 20 ns, and a shot repetition time of 1.36 ms [539].

3.3.2.2 Implications

The pulsed-EPR experiments presented above establish that formaldehyde can access the active site of the H-cluster and simulations indicate *several* possible binding sites. When evaluating these from a mechanistic perspective, one needs to take into account a recent study that suggests, based on observations by site-selective XAE spectroscopy, a bridging μ-hydrido ligand between Fe_p and Fe_d might be formed and accumulate in the $H_{ox\text{-}2}$ level under conditions similar to the way EPR samples were prepared in this work, *i.e.* under H_2

flow without the presence of an external redox partner [529]. Although the ENDOR results cannot rule out the existence of such a species, it is unlikely that it can be a catalytic intermediate of *mechanistic* relevance, given the recently established requirement for the organic bridging ligand to be adt [406,407,542], an observation that is rationalised by the bridgehead N-atom acting as the pendant base, lying in close proximity to Fe_d to cleave H_2 in the manner of a frustrated Lewis pair mechanism (Scheme 1:1). Further, although it would be thermodynamically more stable than its terminal analogue, formation of a bridging hydride seems to be kinetically hindered, as it would require rearrangement of surrounding amino acids at a significant energetic cost. In the [FeFe]-hydrogenase from *Clostridium pasteurianum* the salt bridge that holds Lys358 in place (Lys358 is conserved in other [FeFe]-hydrogenases) to form a hydrogen bond to the Fe_d ligated CN^- is stabilised by a binding energy of 99 kcal mol^{-1} [410].

To help understand how formaldehyde inhibits the *mechanism* of hydrogen formation by [FeFe]-hydrogenases, *i.e.* the catalytic cycle, the EPR results presented above need to be evaluated in the context of other experimental and theoretical observations, thus placing realistic chemical constraints on possible binding modes. PFE experiments [400,525] established that the *rapid* binding of formaldehyde under catalytic turnover occurs with $\tau = 7.89$ s at −0.56 V (Figure 3:1) and is *fully reversible*, and the formaldehyde-inhibited state is fully recovered after 300 s, a timescale similar to the EPR sample preparations. Further, as depicted in Figure 3:4, this reversible process exhibits a strong potential dependence, with the most reduced level $H_{ox\text{-}2}$ showing the highest degree of inhibition. Taken together with the EPR results that firmly establish the presence of formaldehyde in the vicinity of the H-cluster, these observations strongly suggest that HCHO reacts at a mechanistically important site in the H-cluster, *i.e.* Fe_d, the likely the site of H_2 binding, as inferred from CO inhibition studies [401]. If formaldehyde were to react with a hydrido-ligand bound to Fe_d (or

bridging between Fe_d and Fe_p) as originally proposed (Scheme 3:2) [400], a methoxide species would be formed. However, release of methanol is not detected [528], and it has recently been suggested that hydride formation only occurs upon reduction of $H_{ox\text{-}1}$ [210,376], indicating that formaldehyde is very likely to intercept the H-cluster *before* formation of a Fe-hydride in the most reduced state of the enzyme. In light of these arguments, DFT calculations were conducted by Professor John McGrady (Inorganic Chemistry Laboratory, University of Oxford) on a likely candidate that may form during turnover and is consistent with the aforementioned restraints.

3.3.3 Insight from density functional theory

Scheme 3:1 highlighted the fact that the precise order of protonation and electronation steps that ultimately lead to release of H_2 is uncertain. The combination of the EPR results presented in the previous section and the lack of methanol detection [400,528] suggests that formaldehyde might intercept the $H_{ox\text{-}2}$ level *before* hydride formation at Fe_d rather than afterwards, as assumed previously [400], since hydride transfer to the carbonyl-C should produce methoxide. Based on DFT calculations, Bruschi and colleagues proposed a number of possible intermediates that link H_{ox} and hydrido-forms of the $H_{ox\text{-}2}$ level including one, '$H_{ox\text{-}2}(H^-)$' (denoted H_{sred}-H^- in Scheme 1:1), where Fe_d carries a terminal hydride and adt-N is unprotonated. This species bears a strong consistency with one of the species responsible for the ^{13}C ENDOR signal and the strong potential dependence of inhibition observed in PFE experiments. $H_{ox\text{-}2}(H^-)$ is in the $H_{ox\text{-}2}$ electronation level and Fe_d is coordinatively saturated, with a small amount of spin density delocalised onto Fe_d [412]. Density functional theory was therefore used to explore potential modes for formaldehyde binding to Fe_d in the $H_{ox\text{-}2}$ level *in place* of a proton. The computational protocol followed closely that established by Bruschi *et al.* [412] in that the protein active site from the H-cluster of *Desulfovibrio desulfuricans* was taken and truncated as shown in Figure 3:20, with four methyl carbons frozen at their

crystallographic positions. Total energies and Mulliken spin densities for the various stationary points are summarised in Table 3:1.

Table 3:1 Total energies and Mulliken spin densities for the formaldehyde adducts I and II depicted in Figure 3:20 [539].

	HCHO (I)	**$^{-}CH_2OH$ (II)**	
Functional	BP86	BP86	B3LYP
Energy / au	−12501.3804	−12501.9462	−12500.4320
$<S^2>$	6.53	6.68	8.01
$\rho(Fe_1)$	3.16	3.11	3.51
ρ(Fe2)	3.12	3.05	3.60
ρ(Fe3)	−2.97	−3.04	−3.44
ρ(Fe4)	−2.69	−2.69	−3.28
$\rho(Fe_p)$	0.02	0.23	0.03
$\rho(Fe_d)$	0.01	0.09	0.01
$\rho(S_{br})$	0.05	0.01	0.04

Introduction of a HCHO molecule in the vicinity of Fe_d yields a rather weakly bound intermediate **I** with Fe-C and Fe-O distances of 2.86 Å and 3.56 Å, respectively (**I** in Figure 3:20 and Table 3:1). In **I**, formaldehyde is stabilised by a hydrogen bond to the proton on adt-N, but is otherwise not strongly bound. The spin density on $[2Fe]_H$ is negligible in **I** (< 0.03 electrons in total) which, consistent with the spectroscopically characterised (H_{sred}) form of H_{ox-2} [376], is formulated as a $[4Fe\text{-}4S]^{1+}$ species. The net spin densities and values of $<S^2>$ suggest that the electronic structure of **I** is well described as an exchange-coupled $[4Fe\text{-}4S]^{1+}$ cluster.

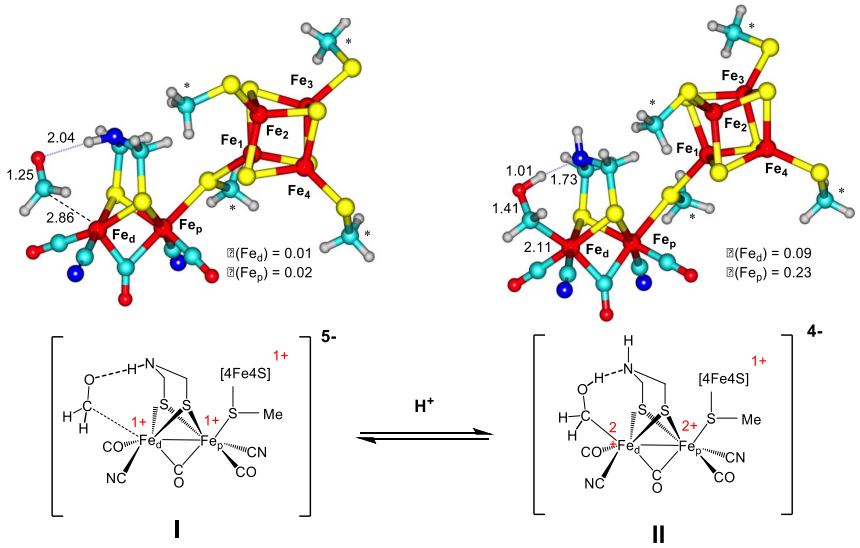


Figure 3:20 DFT-computed structures for possible adducts of $H_{ox\text{-}2}$ and HCHO. Asterisks indicate methyl carbons that are frozen during the geometry optimisation process [539].

Protonation of adt-N, *i.e.* addition of a proton to the system, leads to formation of a *direct Fe–C covalent bond* (Fe–C = 2.11 Å), accompanied by transfer of a proton from adt-N to the O atom of HCHO (structure **II** in Figure 3:20 – note the 'mirror image'-like similarity to the proposed H_{ox} adduct depicted in Figure 3:16). This formation of an Fe_d–C bond, following (the first) protonation of adt-N, leads to a formal 2-electron oxidation of the $[2Fe]_H$ subdomain. The result is the accumulation of a small amount of spin density on Fe_d, consistent with the ENDOR results. The precise value of this spin density however is extremely dependent on the computational details, and in particular on the exchange functional (Table 3:1). A larger spin moment on the high-spin Fe centres of the cubane together with a concomitant decrease at the $[2Fe]_H$ subsite is obtained upon switching from the BP86 functional to the hybrid B3LYP [539]. While the uncertainty in the absolute magnitude of the spin density precluded a study of the hyperfine coupling, the computational investigation establishes that binding of HCHO *via* a *covalent Fe–C bond is favourable* at the highly reduced oxidation levels of interest in this system, but only when a proton is also present at adt-N.

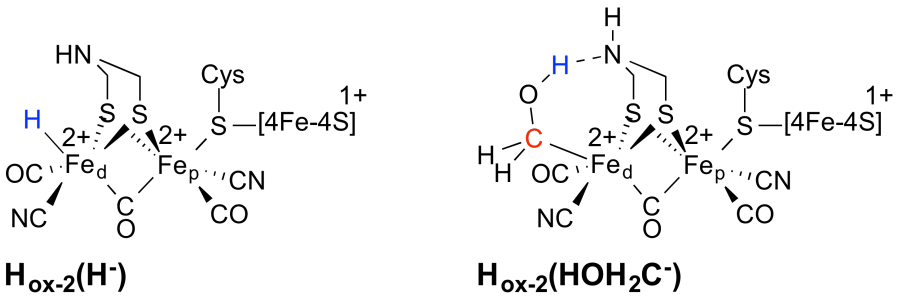
3.3.4 Comparative analysis and discussion

Taking into consideration all the observations and data obtained on the formaldehyde inhibition reaction, along with evidence from investigations of others, a new hypothesis can be proposed to arrive at a consistent model. Comparing the structural information obtained from the X-band ^{2}D ESEEM experiments (Figure 3:19) to the ^{13}C ENDOR results depicted in Figure 3:18, it becomes apparent that although there is a *specific* interaction of formaldehyde with the H-cluster that is responsible for the isotropic component of the hyperfine interaction and can, amongst other possibilities, be attributed to direct Fe-C coordination, the whole picture is more complex. The large ^{2}D ESEEM modulation depth suggests that much more 'matrix' formaldehyde is present in the vicinity of the active site than is specifically bound. This is not surprising: anhydrous HCHO molecules, being neutral and of similar size to other small molecules such as CO or O_2 that are known to diffuse freely into hydrogenases [393], should be able to occupy many different sites within the protein.

Structure **I** can be interpreted as being the 'limiting case' of a single 'matrix' HCHO, *i.e.* a single formaldehyde molecule approaching Fe_d closely, but not yet being bound. As depicted in Figure 3:20, protonation of adt-N is required to shift the equilibrium towards **II**. The precise values of the spin density at Fe_d in **II** are to some extent dependent on the details of computational methodology, but lie in the range of $0 - 0.10$ electron (Table 3:1), consistent with the EPR data that require the great majority of spins to be localised on $[4Fe\text{-}4S]_H$ (Figure 3:17). The results reported by Bruschi *et al*. for the hydrido complex $H_{ox\text{-}2}(H^-)$ show very similar trends and very similar absolute values of $\rho(Fe_{p/d})$ [412]. The computational results presented in section 3.3.3 therefore give rise to the hypothesis that HCHO coordination to *un*protonated Fe_d is favourable provided it is accompanied by protonation at the bridgehead adt-N (the first proton transfer, in this case). The results suggest

that binding of HCHO as in structure **II** results in a state that is equivalent to the hydrido complex $H_{ox\text{-}2}(H^-)$ that exists just before H–H bond formation (Scheme 3:5).

Scheme 3:5 Comparison of the hydrido species $H_{ox\text{-}2}(H^-)$ [412] with the formaldehyde adduct II.



In essence, HCHO has intercepted the catalytic cycle at the point of the first H^+ transfer from adt-N to Fe_d. This proton, transferring from quaternised adt-N, is abstracted instead by HCHO during formation of the covalent Fe_d–C bond. Structure **II** is best expressed as a carbanionic complex $H_{ox\text{-}2}(HOH_2C^-)$, in which HOH_2C^- is a hydride analogue. The stable adduct may also offer protection against more permanent inactivation, if the latter involved attack by formaldehyde on the bridgehead amine-N.

There are the strong links to existing models for the catalytic cycle where a bridging [529] or, most-likely, terminal hydride (at Fe_d) [410] is formed upon reduction of $H_{ox\text{-}1}$ and transfer of the first proton required for H_2 formation from the bridgehead adt-N [210,412]: the subsequent second protonation of adt-N leads to electron transfer from $[4Fe\text{-}4S]_H$ to $[2Fe]_H$. This through-bond reoxidation of $[4Fe\text{-}4S]_H^{1+}$ [412] results in the formation of $H_{ox\text{-}2}(2H)$ (Scheme 3:1), which is immediately followed by facile formation and release of H_2. Structure **II**, which requires only minimal reorganisation of the H-cluster, accounts for the rapid and reversible inhibition by formaldehyde. The main mechanistic difference between formaldehyde inhibition and H_2 formation is that the second protonation of **II** at adt-N is not achievable, as the amine group is stabilised through hydrogen bonding with the

adjacent hydroxyl group. This aspect explains why in **II**, similar to $H_{ox\text{-}2}(H^-)$ but in contrast to $H_{ox\text{-}2}(2H)$, the majority of unpaired electron density still resides on $[4Fe\text{-}4S]_H$ [412].

In Figure 3:20 all that is required to release HCHO from the active site is the transfer of the hydroxyl proton back to the bridgehead adt-N. This proposed mode of inhibition accounts not only for the PFE results but also the subsequent failure to detect any release of methanol. Moreover, direct reaction with unprotonated Fe_d in $H_{ox\text{-}2}$, *i.e.* Fe_d having a vacant coordination site (as opposed to hydride transfer from $H_{ox\text{-}2}(H^-)$[400]), is also fully consistent with recent experimental evidence for $H_{ox\text{-}1}$ being unprotonated at Fe_d [411,529].

Previous PFE experiments carried out under turnover conditions established that formaldehyde shows a weak affinity for the $H_{ox\text{-}1}$ level and a much stronger affinity for $H_{ox\text{-}2}$ (Figure 3:4). This observation strongly indicates that, while the second electronation step to form $H_{ox\text{-}2}$ might not be necessary for some minor degree of HCHO inhibition to occur (*e.g.* through formation of an $H_{ox\text{-}1}$ analogue of **I**), significant inhibition by Fe–C bond formation occurs only in the $H_{ox\text{-}2}$ level. A large population of the $H_{ox\text{-}1}$ level can be excluded since the EPR-sample preparation method that I employed, *i.e.* prolonged H_2 incubation, produces clean $H_{ox\text{-}2}$ samples, as established by Lubitz and co-workers using FTIR spectroscopy [376].

The possibility that the *state* on the $H_{ox\text{-}2}$ overall redox level that is inhibited by formaldehyde (leading to structure **II**) measured by EPR differs from the transient state on the same redox level that is formed under catalytic turnover (inhibition of which has been demonstrated by PFE experiments [400,525]) cannot be excluded. However, while this general restriction applies to all spectroscopic states identified and characterised by various methods (see references [376,399,529] for the $H_{ox\text{-}2}$ level), the combination of experimental and theoretical evidence presented in this chapter provides compelling evidence that, under

catalytic turnover, formaldehyde inhibits H_2 formation by binding to a highly reduced H-cluster having a vacant coordination site at Fe_d.

To summarise, the combination of results supports a model in which Fe–C bond formation in the most reduced state of the H-cluster can only occur if a Fe–H bond has not yet formed, a conclusion that has important mechanistic implications. The requirement for secondary stabilisation through interaction with the O atom, as seen in simple formaldehyde complexes [530-533], is satisfied by use of the pendant adt-N···H. A new link, both structural and conceptual, is now made between the pendant adt-N and the catalytic Fe_d. Whereas free formaldehyde is a proton mimic, the *bound* protonated formaldehyde anion, as illustrated in Scheme 3:5, mimics a terminal hydride just before the point at which a second proton binds to adt-N, ultimately transferring to form H_2.

3.4 Conclusions and perspectives

Using protein film electrochemistry, the kinetics of the (partially reversible) inhibition of the [FeFe]-hydrogenase *Ca*HydA by different aldehyde molecules with varying steric and electronic properties have been determined (section 3.2). Despite these new findings, evidence for the *mechanism* of inhibition of the H-cluster could not be provided. In agreement with the observed potential dependences, the initial working hypothesis was that reversible aldehyde inhibition occurs, mechanistically, by electrophilic attack on a reducing Fe_d-hydrido species (Scheme 3:2). However, previous attempts to ascertain the methanol/methoxide product of formaldehyde inhibition *via* NMR spectroscopy have been unsuccessful [528] and recent studies [376,529] suggest hydride formation *only* takes place when the enzyme is in the super-reduced oxidation level. On the basis of these findings, which indicate that formaldehyde might react *before* a metal-hydrido species is formed, pulsed-EPR and DFT calculations have been conducted to gain *structural insight* into the binding mode. The EPR observations firmly establish that formaldehyde can access the H-cluster, but reveal a complex picture. The relatively large modulation depth observed in ^{2}D ESSEM experiments (Figure 3:19) suggests that several aldehyde molecules surround the H-cluster, and Q-Band ENDOR spectra of *Cr*HydA1 inhibited by $H^{13}CHO$ can be fitted with the ^{13}C nucleus being in several positions in the vicinity of the enzyme active site [539]. Further, the protonation state of the spectroscopically accessible 'resting-form' of H_{ox-2} is yet to be definitively established. Whereas earlier studies suggested the $[2Fe]_H$ subdomain is unprotonated [210,376], recent XAE observations suggest the existence of a bridging hydride between Fe_p and Fe_d [529]. The presence/absence of such a hydrido complex has a profound impact on the possible reaction pathways of the H-cluster with formaldehyde.

However, despite this complex picture obtained under 'static' (frozen) equilibrium conditions, formaldehyde inhibition under catalytic turnover, *i.e. in operando*, is likely very different. While not giving structural insight, formaldehyde inhibition measured by PFE not only shows a strong potential dependence, inhibition is rapid, fully reversible, and dominated by a single-exponential process, indicating that a single reaction pathway prevails (Figure 3:1). Based on the above-mentioned observations, DFT calculations show that formaldehyde, acting as a proton-mimic, is likely to intercept the reduced H-cluster before formation of a Fe_d-hydride can take place, with bound formaldehyde acting as a hydride-mimic (Scheme 3:5).

While the experiments discussed in section 3.3.2 seem to have reached the limit in terms of the information EPR spectroscopy can provide on the reaction of formaldehyde with the H-cluster, other physical techniques might yield more conclusive structural evidence. Co-crystallisation of [FeFe]-hydrogenase in the presence of formaldehyde is one possibility: following the principles established by Dobbek and colleagues in the co-crystallisation of CODH with *n*-butyl isocyanide [450], crystals of [FeFe]-hydrogenase would have to be chemically reduced to the $H_{ox\text{-}2}$ level and then exposed to formaldehyde. However, the highly reactive electrophile is likely to cause irreversible degradation of the enzyme upon prolonged exposure. Despite this limitation, preliminary experiments are currently being carried out in the laboratory of Professor Thomas Happe at the Ruhr-Universität Bochum, Germany.

A recently developed technique known as protein film infrared electrochemistry (PFIRE) [429] has the potential to provide structural information under catalytic conditions: here, protein film electrochemistry is coupled to infrared spectroscopy, allowing the investigator to simultaneously gain information from both techniques. PFIRE has thus far only been applied to [NiFe]-hydrogenases [429,430], but could become a valuable tool for

elucidating the remaining ambiguities concerning the mechanism of [FeFe]-hydrogenases, Nature's most proficient hydrogen cycling catalysts.

4 The direct electrochemistry of fuel-forming enzymes on semiconducting electrodes: how light-harvesting semiconductors can alter the bias of reversible electrocatalysts in favour of H_2 production and CO_2 reduction

Part of the work presented in this chapter has been published: Andreas Bachmeier, Vincent C.-C. Wang, Thomas W. Woolerton, Sophie Bell, Juan C. Fontecilla-Camps, Mehmet Can, Stephen W. Ragsdale, Yatendra S. Chaudhary, and Fraser A. Armstrong, *J. Am. Chem. Soc.* **2013**, *135*, 15026.

Abstract

This chapter describes the direct electrochemistry of the fuel-forming enzymes [NiFeSe]-hydrogenase (section 1.6.3) and carbon monoxide dehydrogenase (CODH, section 1.6.4) immobilised on porous *n*-type semiconductor electrode materials. Being reversible electrocatalysts for CO_2/CO and H^+/H_2 interconversion, these enzymes show high activities for both oxidation and reduction when attached to metallic-like graphite electrodes (PGE). Yet, whereas the most efficient catalysts for the formation of solar fuels should, in addition to operating close to reversible potentials, possess a catalytic bias for the *fuel-forming direction*, both [NiFeSe]-hydrogenase and CODH possess an *inherent* catalytic bias that favours the oxidation over the reduction half-reaction.

When [NiFeSe]-hydrogenase and CODH are adsorbed on *n*-type semiconductor electrodes constructed from CdS and TiO_2 nanoparticles, a marked shift in bias is observed, now favouring CO_2 or H^+ reduction. The fuel-forming reaction is efficiently catalysed at minimal overpotentials (both in the dark and under illumination), while the, in this case destructive oxidation reaction is greatly suppressed. This chapter describes how the electronic state of the electrode can strongly bias the direction of electrocatalysis of both CO_2 and H_2 cycling. Electrical impedance spectroscopy (EIS) experiments shed light on the binding mode of these enzymes on porous surfaces and indicate possible rate-limiting parameters in photocatalytic CO_2 or H^+ reduction by metalloenzymes adsorbed on semiconductor nanoparticles.

4.1 Introduction

In artificial photosynthesis, both the fuel- and O_2-forming catalysts can be regarded as electrocatalysts, as they catalyse the respective electrochemical half-cell reaction. Ideal artificial photosynthetic catalysts exhibit high activities and do not rely on large, wasteful overpotentials to drive the reaction; a minimal overpotential requirement corresponds most closely to reversibility. However, it is beneficial to render the reaction as unidirectional as possible, thus trapping the electrons or holes and opposing recombination [543]. Under the condition of very low overpotential that is beneficial for efficiency, it is interesting and important to consider how the relative rates of catalysis for the forward and reverse reactions can be biased in favour of the desired direction. Photocatalytic fuel-formation by enzymes immobilised on semiconductor particles is now well established (section 1.5.3.4), but the processes at the enzyme-semiconductor interface that are likely to govern efficiencies are still relatively poorly understood. Protein film electrochemistry techniques are valuable tools that can be of help in improving the understanding of the enzyme-semiconductor interface.

To briefly recapitulate, electrochemical kinetics at semiconductors depend on the density of charge carriers in the space-charge region adjacent to the solution interface (see section 2.3) [340,482]. In principle, control over the relative rates of oxidation and reduction catalysis can be provided if the carrier density of the semiconductor material changes greatly in a potential region close to the reduction potential of the reaction of interest. A useful physical characteristic of a semiconductor, unrestricted by its chemical nature, but of general relevance, is the flat-band potential (E_{fb}). For an *n*-type semiconductor, the electron density at the surface increases as the applied potential becomes more negative than E_{fb}, giving rise to an accumulation layer. The conduction and valence bands bend downward and the semiconductor approaches metallic-like electrochemistry when the Fermi level contacts the

conduction band edge at the semiconductor-catalyst/-electrolyte interface [482]. Conversely, when the applied potential is increased relative to E_{fb}, a depletion layer forms and the bands bend upwards, resulting in a barrier for electron transfer from the catalyst/electrolyte to the semiconductor. At E_{fb} there is no band-bending. The space-charge region can extend well into the material, with values in the range from 10 nm to 1 μm being reported [340].

Several reports have described the electrochemistry of proteins on semiconductor electrodes. Durrant *et al.* reported a series of studies dealing with the electrochemistry of cytochrome *c* and haemoglobin immobilised on TiO_2 film electrodes [544,545]. The authors found irreversible reduction of the proteins' active sites at potentials substantially more negative than the solution-based redox potentials, similar to observations with simple redox couples such as potassium ferricyanide $K_3[Fe(CN)_6]$ [545]. The TiO_2 electrode thus exerts a rectifying effect. However, these electrochemical reductions are not catalytic.

This chapter explores the directionality that can be imposed on electrocatalytic behaviour when certain enzymes (*i.e.* [NiFeSe]-hydrogenase and CODH) and, by extension, any *reversible* electrocatalyst, are attached to a semiconductor. Although materials will differ considerably in their chemical properties, the concept of E_{fb} provides the means to explore some generalisations because changes in carrier density ought to be particularly influential in biasing the direction if they occur in the potential region of the reduction potential for the redox reaction being catalysed. Therefore, the reversibility of H^+/H_2 and CO_2/CO interconversion by [NiFeSe]-hydrogenase (see section 1.6.3) and CODH (section 1.6.4) is compared at a metallic-like graphite electrode (PGE) and at TiO_2 and CdS electrodes (both *n*-type semiconductors) by analysing the electrocatalytic voltammograms recorded under H_2 or CO_2/CO mixtures.

Both types of FeS enzymes are excellent examples of reversible electrocatalysts when attached to a metallic electrode (including 'semi-metallic' PGE) [211,215,350,546,547]. Voltammograms recorded with the enzyme-modified electrode being immersed in a solution containing both oxidised and reduced forms of the substrate (*i.e.* the redox-active molecules in solution) intersect the zero current axis at the equilibrium potential with little or no inflection.

The *n*-type semiconductors CdS and TiO_2 (anatase) have conduction band potentials (E_{cb} at pH 6.0 *ca.* −0.87 and *ca.* −0.52 V *vs.* SHE, respectively [279]) more negative than the equilibrium potentials for H^+/H_2 (−0.36 V *vs.* SHE) and CO_2/CO (−0.46 V), and nanoparticles of CdS and dye-sensitised TiO_2 (anatase or P25, a commercially available mixed rutile-anatase phase) modified with hydrogenases or CODH are excellent model-systems for photoreducing H_2O and CO_2 [377-381] (compare section 1.5.3.4).

4.2 Results

4.2.1 Characteristics of porous CdS and TiO_2 electrodes and enzyme immobilisation

Protein film electrochemistry has been pioneered using PGE electrodes [548]. The roughness of the 'edge' plane (see SEM image depicted in Figure 4:1A) compared to the basal plane, as well as its hydrophilicity and richness in acidic oxides [549] make it particularly suitable for electroactive enzyme immobilisation – it enables the irregularly shaped macromolecules to make multiple polar contacts with the electrode [548]. Dispersion of interfacial electron transfer kinetics, a result of protein molecules adopting a distribution of orientations on the electrode, is minimised, as the rough surface allows for efficient electron transfer with a multitude of different enzyme orientations. Protein film electrochemistry on semiconductor electrodes in turn is not well established yet and, to my knowledge, only few preliminary studies exist [377,550,551], none of which having the focus on the underlying principles of enzyme semiconductor interaction. In a broader context, little is known about electron transfer between semiconductors and *reversible* electrocatalysts.

Figure 4:1 also depicts SEM images of porous TiO_2 (B, prepared from Degussa P25) and CdS electrode films (C). The TiO_2 thin film exhibits porous structures consisting of nanoparticles (on the order of 20 nm, the average particle diameter of P25) which have formed aggregates, as expected upon calcination at 450 °C (see section 8.3.2.1). The CdS film consists of a highly porous 3-dimensional network of CdS nanoflakes/sheets. These nanosheets are typically 20 ± 5 nm in width and the pore size of CdS varies from 700 nm to approximately 1 μm. The porous nature of these two electrode materials somewhat resembles

the surface characteristics of PGE and should therefore allow electroactive enzyme immobilisation.

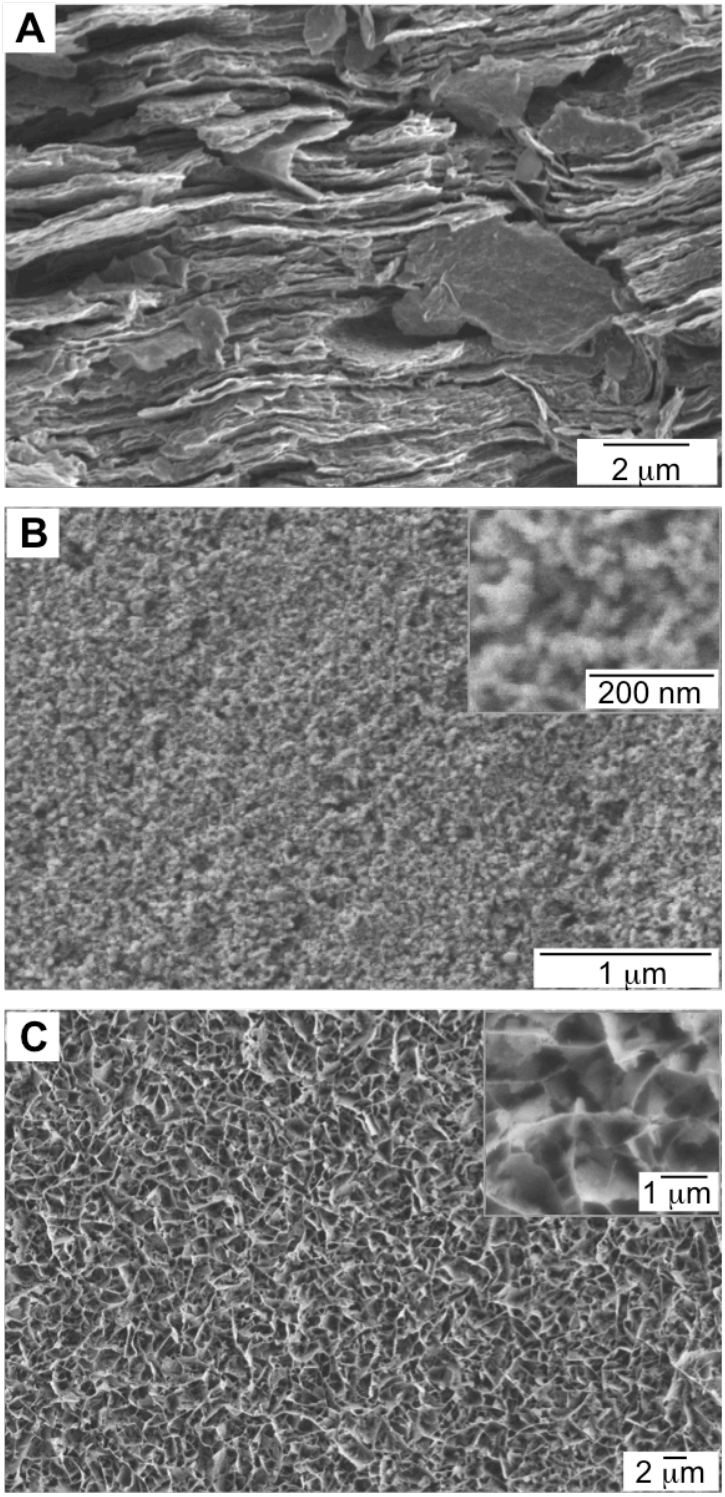


Figure 4:1 SEM images of (A) PGE, (B) TiO_2, and (C) CdS film electrodes used in this thesis.

The surface charge of a semiconductor is an important quantity that can be used to facilitate 'directed' enzyme adsorption by exploiting attractive electrostatic interactions. The point of zero charge (PZC) of P25 TiO_2 is 6.2 [552]. With the isoelectric points of CODH being 5.5 [463] and of [NiFeSe]-hydrogenase being 5.4 [378], stable attachment of both enzymes at TiO_2 nanoparticles has been achieved for photocatalytic CO_2 and H^+ reduction at pH 6, where the net surface charge of the enzymes is negative and TiO_2 is positively charged [377-379]. In the case of [NiFeSe]-hydrogenase, the presence of a negatively charged surface patch around the distal FeS cluster indicates that the interaction between enzyme(s) and TiO_2 particles is likely to be controlled by localised polar interactions between side-chain carboxylates and a number of Ti-O(H) sites rather than by overall electrostatic interactions [378,544]. In aqueous solution, CdS has a PZC of 7.5 [553]. Hence, attractive electrostatic interactions similar to those observed with TiO_2 and CODH or [NiFeSe]-hydrogenase can be expected. Indeed, CODH immobilised on CdS nanocrystals shows activity towards light-driven CO_2 reduction in aqueous media at pH 6 [381].

To assess the stability of both enzymes for electrochemical CO_2/H^+ reduction, chronoamperometry experiments of CODH-TiO_2, CODH-CdS, [NiFeSe]-TiO_2, and [NiFeSe]-CdS were performed over a period of 4 h (Figure 4:2). The enzymes show excellent stability on both TiO_2 and CdS; catalytic currents persist up to the 4 h mark (cyclic voltammograms were recorded after these experiments to verify the catalytic nature of the current *vs.* time curves and confirm that the enzymes had remained intact throughout the experiments). For CODH this stability is indeed remarkable: this enzyme is relatively unstable on PGE electrodes, where the presence of poly-ionic co-adsorbates such as the cationic polymyxin B sulphate are normally required to allow PFE experiments to be carried out [444,554] (particularly for rotating disk experiments).

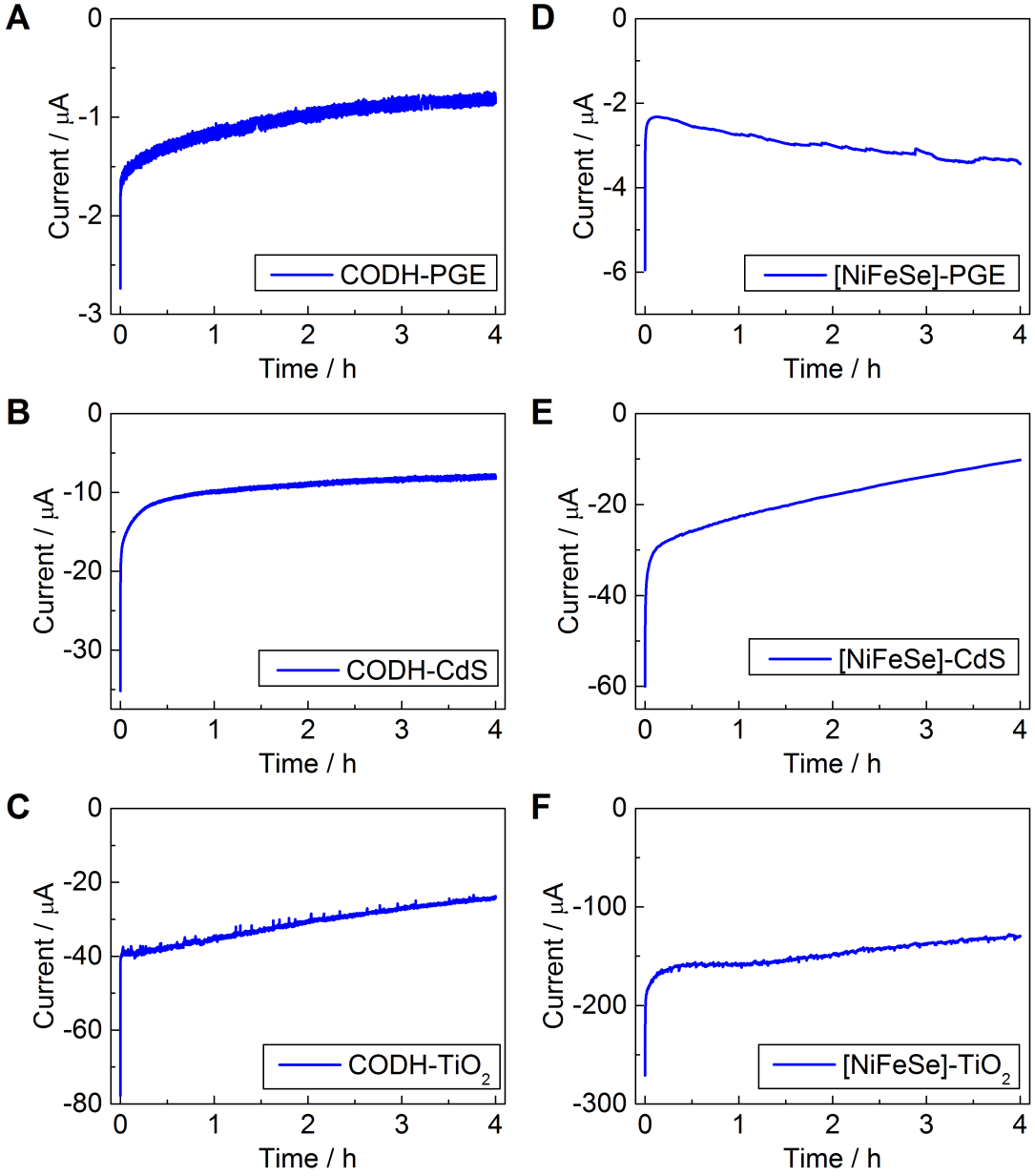


Figure 4:2 Chronoamperometry experiments recorded at −0.65 V *vs.* SHE on PGE, CdS and TiO_2 electrodes modified with CODH (left panel, recorded under 100% CO_2 flow) or [NiFeSe]-hydrogenase (right panel, recorded under 100% N_2 flow). In all experiments the buffer solution was 0.2 M MES (pH 6.0), 20 °C, and the cell solutions were sparged with the respective gas close to the stationary working electrode surface throughout the experiment.

4.2.2 Direct electrochemistry of CODH and [NiFeSe]-hydrogenase on TiO_2 and CdS

Panel A of Figure 4:3 shows cyclic voltammograms of CODH attached to PGE (CODH-PGE), CdS (CODH-CdS), and TiO_2 (CODH-TiO_2) electrodes in separate experiments with 100% CO_2 or a mixture of 50% CO_2/50% CO gently bubbling through the cell solution. Protein film electrochemistry provides precise and continuous measurement of the relative catalytic rates in either direction. The shapes of the cyclic voltammograms on PGE in the presence of both oxidised and reduced substrates reveal the inherent catalytic bias of the enzymes to function more effectively in one particular direction, and reaffirm that on metallic-like electrodes, catalysis is controlled by the redox properties of the enzyme [213,555]. A dominant factor in determining the bias of an enzyme is the reduction potential ($E^0_{Ox/Red}$) of the relay centre that serves as the electron entry/exit point for transfer to the buried catalytic centre [213,556].

In contrast to CODH adsorbed on PGE, the voltammograms recorded on CODH-CdS and CODH-TiO_2 are dominated by CO_2 reduction, *i.e*. the bias appears *reversed* (with respect to the bias observed at PGE) to favour instead the formation of CO. In fact, CO oxidation is negligible at CdS and extremely sluggish at TiO_2. The effect is all the more pronounced if one considers that CO is a natural inhibitor of CO_2 reduction by CODH (a phenomenon known as product inhibition) [554], *i.e.* the exponentially increasing reductive current is suppressed when both oxidised and reduced substrate are present (red traces in Figure 4:3A). Voltammograms recorded under 100% CO_2 (blue traces) reveal the further increase in current that is obtained when CO is not introduced.

Panel B of Figure 4:3 shows analogous experiments for [NiFeSe]-hydrogenase immobilised on PGE, CdS, and TiO_2 carried out under H_2 flow through the cell solution.

Once again, the effect of product inhibition is clearly visible in the case of [NiFeSe]-PGE [215]. Electrocatalysis in the reduction direction is strongly inhibited by H_2 and cyclic voltammograms recorded in the absence of H_2 reveal the higher rate of H^+ reduction by uninhibited enzyme. As with CODH, comparison with PGE shows that the H_2 oxidation currents at CdS or TiO_2 are greatly suppressed relative to the rates of H^+ reduction.

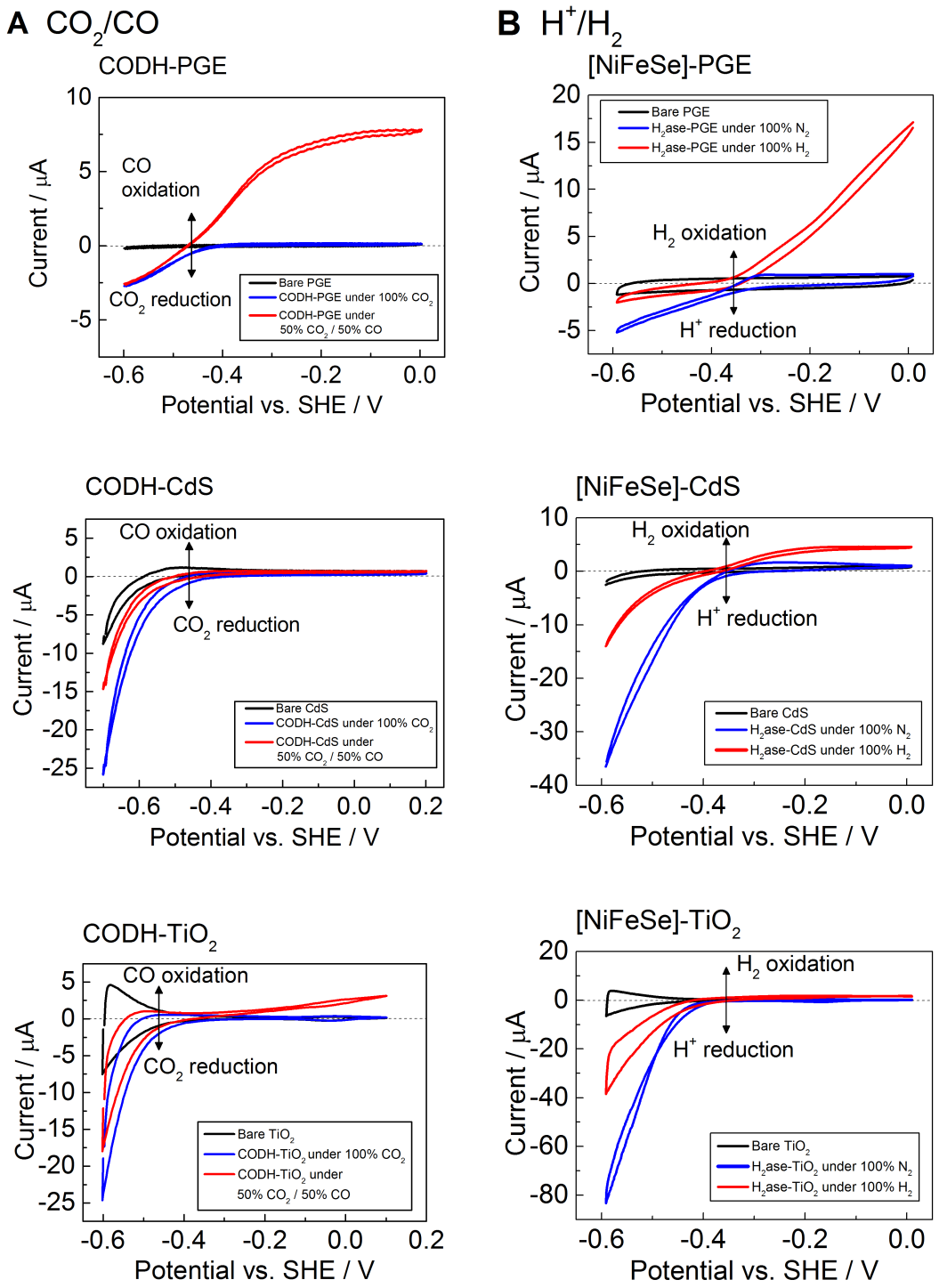


Figure 4:3 Cyclic voltammograms (10 mV s^{-1}) of unmodified (black) and enzyme-modified electrodes (red, blue), recorded in 0.2 M MES, pH 6.0, at 20 °C. Voltammograms recorded under 100% CO_2 (CODH-PGE, CODH-CdS, and CODH-TiO_2) or 100% N_2 ([NiFeSe]-PGE, [NiFeSe]-CdS, and [NiFeSe]-TiO_2) are depicted in blue. Experiments with a 50% CO_2/50% CO gas mixture (CODH-PGE, CODH-CdS, and CODH-TiO_2) or with 100% H_2 ([NiFeSe]-PGE, [NiFeSe]-CdS, and [NiFeSe]-TiO_2) bubbling through the cell are shown in red.

With regard to the voltammetric reduction waves observed on CODH-CdS and CODH-TiO_2 (panel A of Figure 4:3), experimental verification for these to correspond to catalytic conversion of CO_2 into CO was needed. In previous work by our laboratory on photocatalytic CO_2 reduction using CODH-TiO_2 and CODH-CdS nano-assemblies, catalytic CO_2 reduction was monitored by gas chromatography [379,380]. This approach is not feasible herein because of the minute quantities of enzyme used in protein film electrochemistry experiments (on the order of pmol). A selective inhibitor of CODH was used instead to prove that the reduction currents at each semiconductor electrode correspond to CO_2 reduction to CO. Cyanate (NCO^-), which is isoelectronic to the substrate CO_2, targets the active site of CODH and selectively blocks CO_2 reduction by intercepting the reduced C_{red2} level of the enzyme [554]. NCO^- is released as the potential is raised and does not significantly inhibit CO oxidation.

The selective inhibition of CO_2 reduction on CODH-modified TiO_2 and CdS electrodes after addition of KOCN is depicted in Figure 4:4. Quantitative inhibition was achieved with a final concentration of 20 mM KOCN in the case of CODH-TiO_2 (Figure 4:4A) and 60 mM KOCN at CODH-CdS (Figure 4:4B). Upon KOCN injection (red current-voltage curves), the portions of the cathodic currents due to CO_2 reduction before introducing the inhibitor (blue traces) are quenched. Instead, the voltammogram for CODH-TiO_2 resembles the characteristic shape of a TiO_2 electrode at low potential (see section 2.3.3.3). In the CODH-CdS system, the voltammogram also closely resembles the shape of the bare electrode after introduction of the inhibitor. Thus, it is established that the reductive catalytic currents stem specifically from CO_2 reduction.

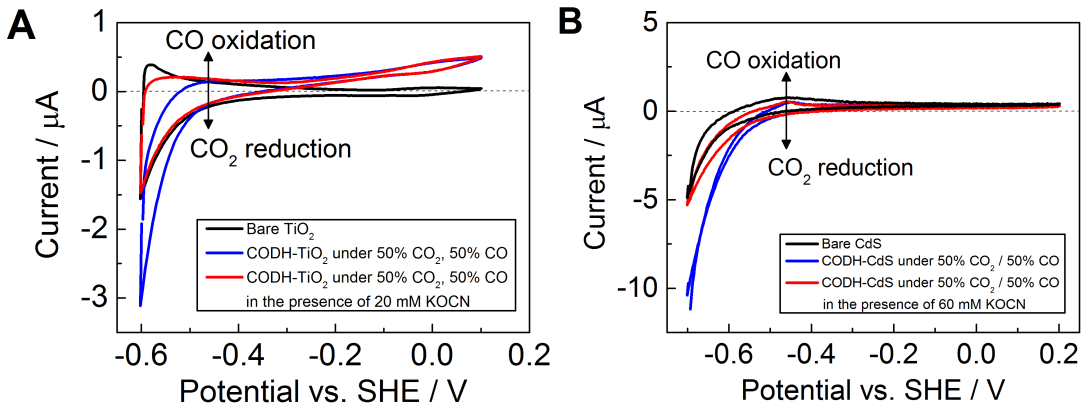


Figure 4:4 Cyclic voltammograms showing selective inhibition of CO_2 reduction on CODH-modified TiO_2 (A) and CdS (B) electrodes in the presence of 20 mM and 60 mM KOCN, respectively, under a mixture of 50% CO_2/50% CO bubbling through the cell. The solutions contained 0.2 M MES (pH 6.0) buffer; temperature: 20 °C; scan rate: 10 mV s^{-1}.

The potential dependences of the low-level CO and H_2 oxidation currents at CdS and TiO_2 depicted in Figure 4:3 vary slightly between different experiments and residual oxidation currents differ in magnitude at both electrodes. These non-idealities can be ascribed to several complex phenomena including direct contact between some enzyme molecules and the conducting oxide support (due to pinholes in the semiconductor film), dispersion in enzyme orientation on the semiconductor surface and variations in semiconductor film thickness, electron tunnelling through the interfacial potential barrier (depletion region) near the surface (mainly *via* surface states/semiconductor defects), and electrons surmounting this barrier.

These non-idealities however do not change the general effect of catalytic rectification, which becomes even more prominent when 'background-subtracted' voltammograms are taken into account. When first observing the effect of catalytic rectification in preliminary experiments on CODH-modified TiO_2 electrodes, Woolerton [551] suggested comparing the ratios of background-corrected reduction/oxidation currents at a fixed value either side of the equilibrium potential for CO_2 reduction. Figure 4:5 depicts typical ratios of reduction *vs*. oxidation currents at ±0.15 V either side of the thermodynamic potential for CO_2/CO and H^+/H_2 interconversion, clearly revealing the changes in catalytic

bias for each enzyme. For [NiFeSe]-hydrogenase, the background-corrected current ratio (H_2 oxidation/H^+ reduction) drops from 8.1 on PGE, to 0.81 on CdS and 0.11 on TiO_2, *i.e.* attenuation factors of approximately 10- and 80-fold, respectively. For CODH the current ratio (CO oxidation/CO_2 reduction) drops from 2.2 on PGE to 0.04 on CdS and 0.05 on TiO_2, *i.e.* an attenuation factor of approximately 50-fold in each case. These results demonstrate that although the residual oxidising currents for both enzymes differ at TiO_2 and CdS, the fuel-forming reactions are essentially rendered irreversible.

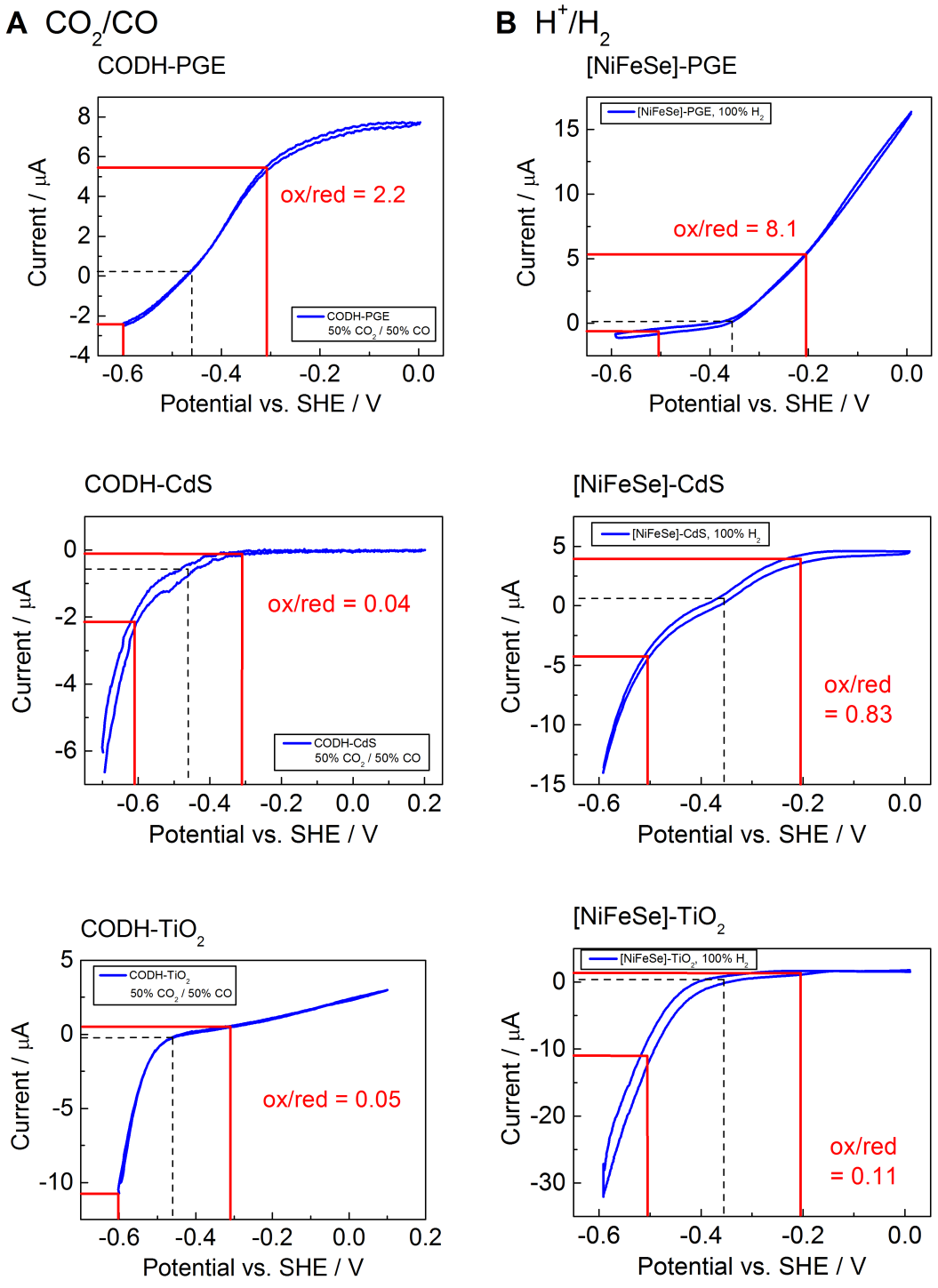


Figure 4:5 'Background-corrected' current-voltage curves, obtained after subtracting the current *vs.* voltage traces of the bare electrodes of the voltammograms depicted in Figure 4:3 (*i.e.* red traces minus black traces). Vertical dotted lines mark the thermodynamic equilibrium potentials for CO_2/CO and H^+/H_2 interconversion at pH 6.0; horizontal red lines mark the current recorded 150 mV either side of the equilibrium potential, from which the ratio of oxidation current to reduction current ('ox/red') is calculated (using the arithmetic average of the respective forward and backward scan).

4.2.3 Mott-Schottky measurements

4.2.3.1 The flat-band potential of TiO_2 and CdS electrodes

In the case of enzyme-modified TiO_2 electrodes (Figure 4:3 and Figure 4:4A), the exponential increase in reductive current for both H^+ and CO_2 reduction coincides closely with the characteristic increase in capacitive current of the bare TiO_2 electrode [557,558]. In chemical terms, the reversible reduction Ti(IV) sites (accompanied by uptake of one proton per centre) is responsible for this effect, increasing the carrier density as the potential is lowered (see 2.3.3.3) [557]. An analogous observation is not immediately apparent for CdS, apart from reduction and stripping of Cd(II) centres at potentials below *ca.* –0.65 V *vs.* SHE [559].

Electrical impedance spectroscopy (EIS, section 2.3.5.3) is a suite of techniques that can help resolve the effects that conductivity changes near the flat-band potential impose on the properties of immobilised catalysts, and probe interfacial interactions between enzyme and electrode. The initial task at hand was to measure how the capacitance of TiO_2 and CdS electrodes changes with applied potential, as it allows extracting the respective E_{fb} through Mott-Schottky analysis according to eq. (2:40):

$$C_{sc}^{-2} = \frac{2}{\varepsilon\varepsilon_0 e_0 N_D}\left(E - E_{fb} - \frac{k_B T}{e_0}\right).$$

Linear extrapolation of the 1 kHz plots depicted in Figure 4:6 yields flat-band potentials of approximately –0.50 V *vs.* SHE for TiO_2 and *ca.* –0.61 V *vs.* SHE for CdS; both values were obtained in 0.2 M MES buffer (2-(*N*-morpholino)ethanesulfonic acid) at pH 6.0 at 20 °C.

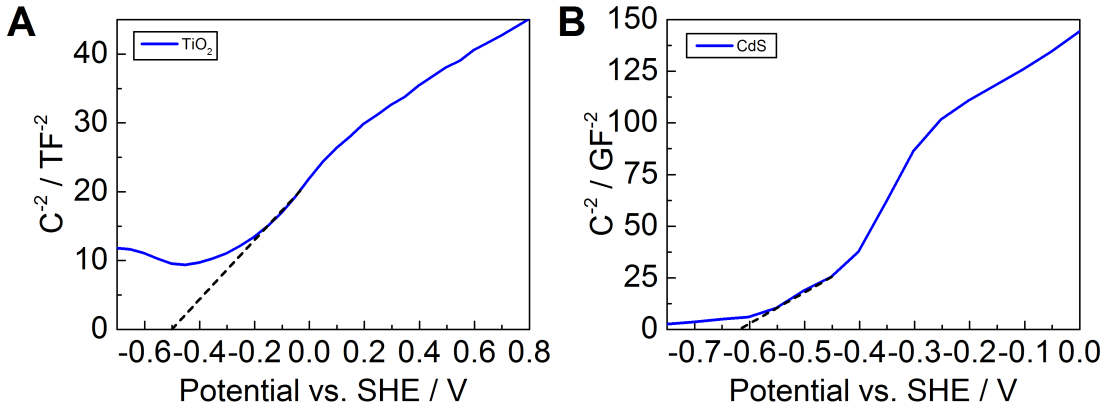


Figure 4:6 Mott-Schottky plots ($1/C^2$ *vs.* E) recorded in the presence of CO_2 at 20 °C, 1 kHz for (A) TiO_2 and (B) CdS. The cell buffer solution was 0.2 M MES (pH 6.0) in both cases.

It must be noted that the electrodes prepared in this work are made up of particles that are interconnected and partly fused together, making the materials thick enough to support a space-charge region (see SEM images in Figure 4:1), in contrast to semiconductor nanoparticles where formation of a space-charge layer is improbable because of the very small crystallite sizes [341] and the concepts of band-bending and formation of accumulation and depletion layers do no longer apply. Investigations by others on TiO_2 electrodes similar in structure to those used in this thesis [560] further suggest that the aggregates exhibit bulk properties to some extent rather than being completely dominated by the individual particles. Thin 'compact' TiO_2 films behave similarly to conventional macroscopic semiconductor electrodes, formation of a space-charge layer is feasible, and the Schottky-formalism can be applied to measure E_{fb} [341].

The E_{fb} value of *ca.* −0.50 V measured for TiO_2 at pH 6.0/20 °C agrees well with the value of −0.52 V *vs.* SHE predicted by a model for nanostructured TiO_2 electrodes in aqueous solution developed by Fitzmaurice [561] (using the correction 0.2445 V for the conversion of SCE to SHE at 20 °C [469]):

$$E_{fb}\,(\mathrm{V, SCE}) = -0.40 - (0.06 \times \mathrm{pH}), \qquad (4{:}1)$$

The relationship described by eq. (4:1) has also been observed experimentally [562].

In principle, E_{fb} should be independent of the applied frequency. However, the impedance response of the probed systems often contains non-idealities such as back contact capacitance (from the transparent conducting oxide), sample resistance, electrolyte resistance, and capacitance and resistance of Helmholtz layer and surface states [341]. These effects show different contributions depending on the applied frequency. In the particular case of TiO_2 adsorbed on ITO, similar E_{fb} values have reproducibly been obtained in different studies using frequencies in the range of 0.1 – 2 kHz [341,562,563]. Hence, impedance studies in this thesis were carried out in this low-to-mid frequency range.

Mott-Schottky measurements on TiO_2 electrodes carried out in a different protic electrolyte ($LiClO_4$, Figure 4:7) confirm that the flat-band potential is independent of the electrolyte [561], *i.e.* the capacitance of the Helmholtz layer C_H at the semiconductor-electrolyte interface is negligible compared to the capacitance of the space-charge region C_{SC} [341] (compare section 2.3.2).

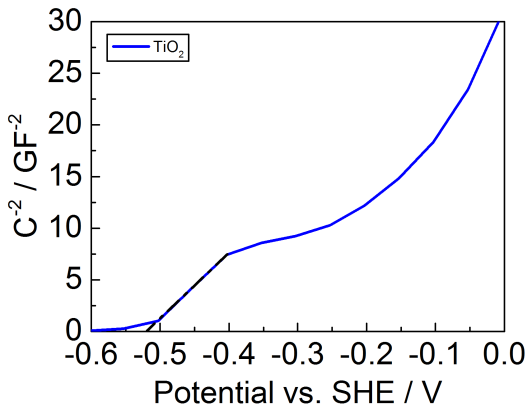


Figure 4:7 Mott-Schottky plot ($1/C^2$ *vs.* E) recorded for a TiO_2 electrode at 0.5 kHz, 20 °C, under an atmosphere of N_2. The cell buffer solution was 0.1 M $LiClO_4$ (pH 6.0).

4.2.3.2 The flat-band potential of CODH-TiO_2 in the absence of substrate

Having measured the flat-band potentials of TiO_2 and CdS electrodes, I sought to investigate the influence of CODH. In contrast to [NiFeSe]-hydrogenase, where the solvent (buffer) constitutes the substrate (protons) for the fuel-forming reaction, surface-immobilised CODH can be studied both under turnover (in the presence of CO_2/CO) and non-turnover conditions (under an inert atmosphere). Figure 4:8 shows a Mott-Schottky experiment carried out with CODH immobilised on TiO_2 under 100% N_2 without the presence of substrate (an analogous experiment on CODH-CdS is depicted in Appendix F). Importantly, when CODH was employed in impedance spectroscopy experiments, cyclic voltammograms were recorded prior to and after every impedance measurement to ensure that the catalytic activity of the enzyme had remained steady throughout the experiment.

The experiment depicted in Figure 4:8 shows that the presence of enzyme alone has a considerable effect on the shape of the Mott-Schottky plots. Independent of the applied frequency, each trace is characterised by an unfeatured shape and sensible E_{fb} values can no longer be extrapolated because of the absence of defined linear gradients.

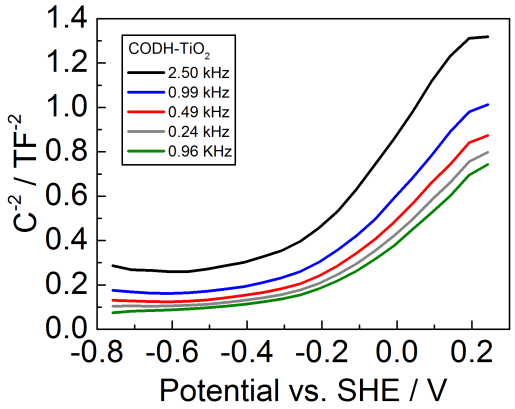


Figure 4:8 Mott-Schottky plots ($1/C^2$ *vs.* E) recorded at 20 °C for CODH-TiO_2. Each experiment was performed under 100% N_2 in a 0.2 M MES (pH 6.0) cell buffer solution.

Although the SEM images in Figure 4:1 show the pores in the TiO_2 and CdS films to be of approximately the same size as the dimensions of CODH (approximately 88 × 63 × 60 Å), these observations suggest the enzyme adsorbs mainly on the outer (geometric) surfaces and acts mostly as a 'resistive' film, blocking the inner surface area created by the porous electrode structure from contact with the solution. This effect can be rationalised by the relatively short enzyme adsorption times employed in PFE experiments, where minute quantities of protein (μL volumes) are spotted onto the respective electrode and dried within minutes. A study by Durrant and co-workers supports this hypothesis; it was measured that haemoglobin takes up to 15 days to fully penetrate into nanostructured pores of TiO_2 electrodes similar to those employed in this work [544].[i]

The aforementioned hypothesis was investigated in more detail using well established TiO_2 electrodes as test-system. First, Mott-Schottky experiments were carried out on electrodes where CODH was only applied to half of the exposed geometric TiO_2 surface area, creating a system that comprises both 'bare' and CODH-modified zones on the solution-exposed TiO_2 surface. The C^{-2} *vs.* potential traces in Figure 4:9 are similar to the capacitive behaviour exhibited by unmodified TiO_2 (shown in Figure 4:6A) and comparable E_{fb} values can be obtained through extrapolation in the frequency range of 0.5 – 2 kHz. This observation implies that sites on the unmodified part of the TiO_2 electrode dominate the capacitance of the surface. As indicated by the porosity of the TiO_2 electrodes (Figure 4:1B), the intrinsic (*i.e.* real) surface area is much greater then the 'outer' geometric area. Leaving half of the latter uncovered allows the electrolyte to access the larger inner surface.

[i] This approach is entirely impractical in PFE experiments with hydrogenase or CODH enzymes due to the low yields of the enzyme preparations, where typically only μL of enzyme are obtained from 10+ L batches.

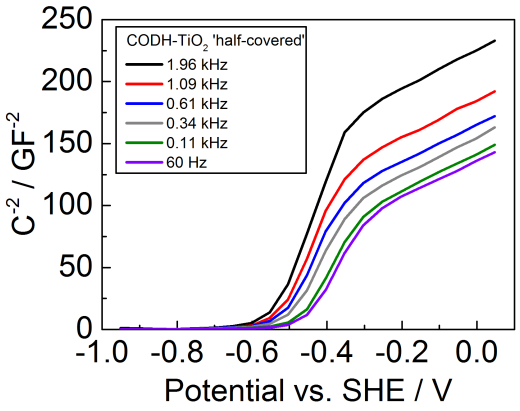


Figure 4:9 Mott-Schottky experiments (C^{-2} *vs.* potential) for a TiO_2 electrode half-covered with CODH, recorded at various frequencies as indicated. Experimental conditions: 100% N_2, 0.2 M MES buffer (pH 6.0), 20 °C.

Second, a series of dilution experiments was conducted in which each TiO_2 electrode was modified with the same volume of CODH solution (4 µL), but with different concentrations being employed. Figure 4:10 shows flat-band potential measurements carried out using (A) 15 µM CODH, *i.e.* $1/10^{th}$ the concentration of the normally employed enzyme 'stock' solution of 0.15 mM; (B) 30 µM, *i.e.* $1/5^{th}$ the concentration of the original stock solution; and (C) 75 µM, *i.e.* 1/2 the initial CODH concentration. The stock solution was diluted to the respective concentration using 0.2 M MES buffer (pH 6.0) before the enzyme was applied to the TiO_2 electrodes of 0.25 cm^{-2} geometric surface area each. Assuming all enzyme molecules bind to the surface, 0.15 mM CODH corresponds to a 'geometric surface concentration' of 1.44×10^{15} molecules cm^{-2}.

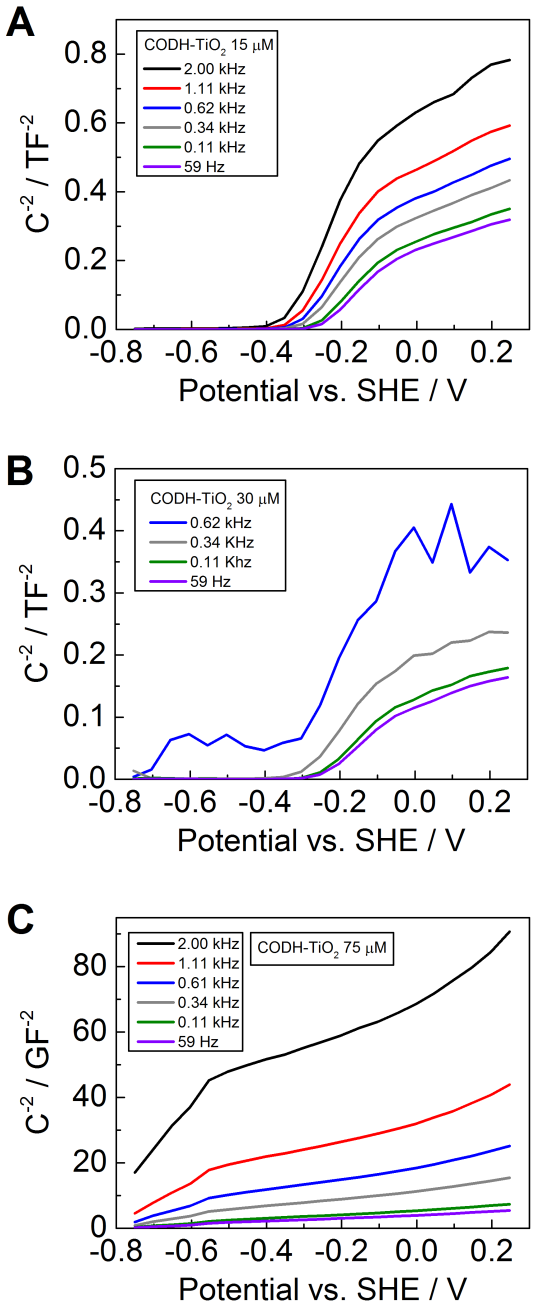


Figure 4:10 Mott-Schottky measurements on TiO_2 electrodes modified with (A) 4 µL of 15 µM CODH solution, (B) 4 µL of 30 µM CODH, and (C) 4 µL of 75 µM CODH. All experiments were carried out under a 100% N_2 atmosphere at 20 °C in 0.2 M MES buffer (pH 6.0). In (B), frequencies above 0.6 kHz are omitted because no defined gradients were observed.

In Figure 4:10, properties consistent with TiO_2 dominating the capacitance are observed with diluted CODH concentrations of 15 µM (A, 1.44×10^{14} molecules cm^{-2}) and, at lower frequencies, 30 µM (B, 2.89×10^{14} molecules cm^{-2}). In contrast, Figure 4:10C suggests that at a concentration increased to 75 µM ($7.22 \cdot 10^{14}$ CODH molecules cm^{-2}) enough surface sites

are covered so that, independent of the applied frequency, the measured capacitance is no longer dominated by TiO_2 and an extrapolation to yield E_{fb} can no longer be made. The effects shown in Figure 4:9 and Figure 4:10 both seem to corroborate the hypothesis that CODH mainly adsorbs as a dense film when immobilised on TiO_2 electrodes, blocking charge-transfer between electrode and solution.

4.2.3.3 The flat-band potential of CODH-modified TiO_2 under turnover conditions.

Compared to the observations made with CODH-TiO_2 electrodes under non-turnover conditions, an interesting effect is revealed when substrate is added: a much sharper plot is obtained in the presence of CO_2 (Figure 4:11), but becomes 'flattened' as the frequency is raised. This finding suggests that when CO_2 is introduced, a charge-transport pathway becomes available and E_{fb} can be measured at frequencies low enough for interfacial electron transfer to occur between the semiconductor surface and CODH. At higher frequencies, in contrast, charge-transfer seems to be slower than the potential modulation applied in the experiment and E_{fb} can no longer be obtained.

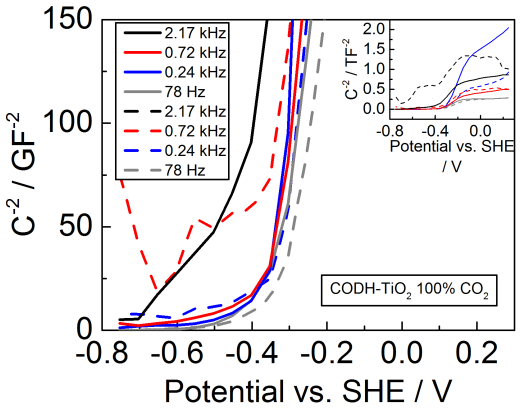


Figure 4:11 Mott-Schottky plots ($1/C^2$ *vs.* potential) recorded on CODH-TiO_2 under 100 % CO_2 at 20 °C in 0.2 M MES buffer, (pH 6.0). Two sets of experiments carried out at several frequencies are shown. The main figure shows a magnification to highlight the linear gradients from which E_{fb} can be obtained; the inset depicts a larger C^{-2} range, showing the change in curvature when the frequency is increased to 2.17 kHz.

4.2.4 Photoelectrochemistry

Visible-light-driven photoelectrochemical H_2 production at the [NiFeSe]-hydrogenase-CdS electrode was also studied (Figure 4:12). Cadmium sulphide, having a band gap of around 2.3 eV (540 nm), allows for visible-light excitation. Cyclic voltammograms were first recorded on an unmodified (bare CdS) electrode, both in the dark and under illumination ($\lambda > 420$ nm, 16 mW cm^{-2}). To eliminate heating effects, the water bath temperature was monitored throughout the experiments; no light-dependent variation was noted. Upon irradiation, the unmodified CdS electrode exhibits an anodic photocurrent at potentials above –0.4 V (as expected for an *n*-type semiconductor at a potential positive of E_{fb}; Figure 4:12A). In the presence of [NiFeSe]-hydrogenase, the anodic photocurrent is of the same magnitude as that of the bare CdS electrode. Because of the transparency of ITO toward visible-light irradiation, possible direct contact of enzyme and the underlying transparent conducting oxide support-layer (mediated by pinholes in the semiconductor surface) does not contribute to the observed photooxidation current under light exposure.

Regarding the cathodic currents, no difference can be observed for the bare CdS electrode in the dark and under illumination, as expected for an *n*-type semiconductor with high majority carrier density at potentials close to E_{fb}. Conversely, when [NiFeSe]-hydrogenase is introduced, catalytic H_2 reduction can be observed in the dark, analogous to the experiments described in section 4.2.2. When the [NiFeSe]-CdS electrode is illuminated with visible-light, a two-fold enhancement of H_2 evolution current is observed, accompanied by a small but noticeable shift in onset potential towards less cathodic potentials. This cathodic photocurrent remains steady over prolonged light exposure, illustrated in the chronoamperometry experiment depicted in Figure 4:12B. These observations, unusual for an *n*-type semiconductor, will be discussed in the following section.

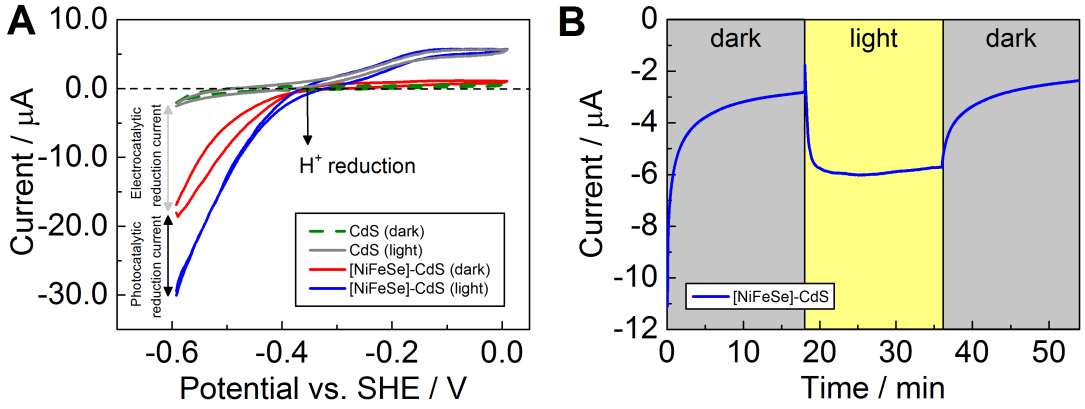


Figure 4:12 (A) Cyclic voltammograms recorded both under dark conditions and under visible-light irradiation for an unmodified CdS electrode, and following modification with [NiFeSe]-hydrogenase. Scan rate: 10 mV s^{-1}. (B) Chronoamperometry experiments comparing the catalytic H_2 evolution current of [NiFeSe]-CdS at −0.65 V *vs.* SHE in the dark and under irradiation. Both experiments were carried out under an inert atmosphere in 0.2 M MES solution (pH 6.0) at 20 °C. Visible-light irradiation was carried out with $\lambda > 420$ nm at 16 mW cm^{-2}.

4.3 Discussion

When measured at TiO_2 and CdS electrodes instead of PGE, the cyclic voltammograms depicted in Figure 4:3 clearly display a pronounced rectification of the otherwise reversible electrocatalysis of H^+/H_2 and CO_2/CO interconversion by [NiFeSe]-hydrogenase and CODH enzymes. According to established models, the surface concentration of electrons (the majority carriers for an *n*-type semiconductor) increases exponentially as the potential is scanned towards more negative values: according to eq. (2:35) it is controlled, through a Boltzmann-like relationship, by the difference between E_{FB} and the applied potential [277]. As the electrode potential is lowered beyond E_{fb} there is a transformation to metallic-like character as an accumulation layer forms (Figure 4:13). The increase in electron density at the semiconductor-catalyst interface favours efficient electron transfer from the semiconductor to the enzyme to drive fuel-formation.

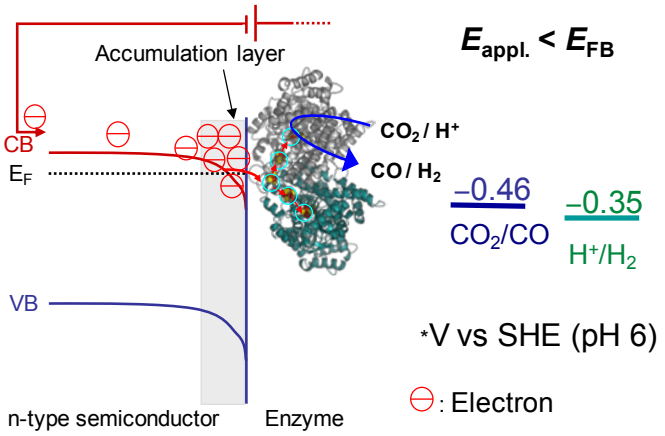


Figure 4:13 Schematic representation of the formation of an accumulation layer at the surface of CdS or TiO_2 electrodes due to the increased electron density at the semiconductor surface when E is lowered relative to E_{fb}. The increased electron density and subsequent downward band-bending facilitate efficient electron transfer to the enzyme active site *via* FeS clusters to catalyse H_2 production or CO_2 reduction.

In contrast, raising the applied potential E above E_{fb} results in the formation of a depletion layer that poses a barrier for electron transfer from the enzyme to the semiconductor. This reasoning explains the resistive effect observed for the oxidation reactions when each enzyme

is coupled to CdS and TiO_2 surfaces. The E_{fb} values broadly lie within 0.25 V of the reduction potentials for CO_2/CO and H^+/H_2 under the experimental conditions used: this is important because the catalysts are operating in a nearly reversible manner and the respective currents change direction (oxidation ↔ reduction) across the same limited potential region. The apparent catalytic bias of each enzyme is thus shifted to favour fuel-formation when coupled to CdS and TiO_2 electrode surfaces, which is catalysed, efficiently, at very low overpotentials. The destructive back reaction (oxidation) in turn is greatly suppressed.

Investigations by EIS have revealed some insight into the binding of CODH on TiO_2 electrodes. Although these electrodes possess pore sizes large enough to accommodate enzyme molecules, these are now rationalised to adsorb mainly on the outer geometric surface, presumably at least partly due to the short adsorption times employed in PFE experiments. Mott-Schottky experiments on CODH-TiO_2 carried out under an inert atmosphere show that the properties greatly depend on the surface concentration of enzyme: behaviour consistent with bare TiO_2 surfaces (albeit with small shifts of the intercepts of the linear gradients to more positive values) is observed only when part of the geometric area is left uncovered or when diluted CODH solutions are employed. Taken together, these results imply that CODH adsorbs as a 'resistive' film, blocking charge-transfer between semiconductor and electrolyte. This description is corroborated by the change in shape of the Mott-Schottky traces upon introduction of substrate (CO_2) and the observed frequency dependence (compare Figure 4:11 to Figure 4:8), suggesting that a charge-transfer pathway becomes available only in the presence of CO_2.

Although these phenomena are far from being fully understood, there are implications on systems for photocatalytic CO_2 reduction that use CODH as catalyst [379-381]. In cases where small ruthenium polypyridyl dye molecules are employed as visible-light sensitisers, these are thought to penetrate more deeply into TiO_2 films/aggregates, generating excited

conduction band electrons throughout the TiO_2 electrode film/particle aggregate. These electrons must migrate to the outer surface, at which interfacial electron injection into CODH occurs. The limited carrier mobility and lifetime of the transient conduction band electrons in TiO_2 thus favour charge recombination even *before* interfacial electron transfer can occur. This notion is one explanation for the turnover frequencies of photocatalytic CO_2 reduction catalysed by CODH (the record being 1.23 s^{-1} [381]) being orders of magnitude lower than values obtained from PFE experiments conducted under controlled potentials or from conventional solution assays.

The photoelectrochemistry experiments on [NiFeSe]-hydrogenase-modified CdS electrodes are interesting and unusual in that a two-fold enhancement of H^+ reduction current is observed under illumination of [NiFeSe]-CdS as a result of an only modest increase in free carrier concentration. For an *n*-type semiconductor at potentials close to E_{fb}, illumination should only have a marginal effect on the magnitude of the reductive current due to the already high density of free carriers. Typically, E_F lies within 50 mV of the conduction band edge [482], consistent with the only small shift in onset potential observed for [NiFeSe]-CdS under irradiation (Figure 4:12A). Yet, H_2 evolution is significantly enhanced by photoexcitation of electrons from the CdS valence band into the conduction band, from where they transfer to the hydrogenase enzyme. This significant amplification in catalytic current highlights the importance of the enzyme as a reversible catalyst: the enzyme is so proficient that the current is controlled more by the charge carrier availability in the semiconductor than by the properties of the hydrogenase, and the availability (concentration) of electrons can be at least as important as the overpotential driving the reaction.

However, the results in depicted in Figure 4:12 also underline that electrode assemblies such as [NiFeSe]-CdS are not ideal photoelectrodes in a classical sense: generally, a photoelectrode should be able to lift the thermodynamic restrictions that apply to dark

reactions to potentials well above the thermodynamic equilibrium. However, as *minority* carriers drive the reactions in a typical photoelectrode, an *n*-type semiconductor would be employed to drive photooxidation reactions. Still, different geometries can be used as light-absorbing and charge-separating units in artificial photosynthesis. In PV-PEC configurations for instance, the minority carriers recombine in buried junctions inside the materials, whereas the majority carriers are injected into the catalysts [277]. Demonstrating visible-light enhanced fuel-forming catalysis carried out by reversible catalysts that are driven by majority carriers, as observed in Figure 4:12, is thus very important.

4.4 Conclusions and perspectives

Although the enzymes used in this thesis are wholly unsuited for long-term, large-scale systems, the results presented in this chapter provide valuable insight for developing integrated artificial systems where getting as close as possible to reversible catalysis is important for efficiency. Semiconducting electrodes can be used to impose directionality on reversible catalysts that operate in the region of the semiconductor flat-band potential: the catalytic direction shifts in response to the exponential increase in surface electron concentration as the applied potential approaches E_{fb}. In the *n*-type semiconductors studied in this chapter, the reduction reaction is then favoured over (destructive) oxidation.

The fact that in impedance spectroscopy experiments a frequency-dependent charge-transfer pathway becomes available when substrate is introduced (Figure 4:11) suggests that the kinetics of electron transfer between semiconductor and enzyme could in principle be determined from the frequency dependence of the changes in capacitance *vs.* applied potential. However, more detailed impedance experiments and further analysis are needed to characterise the complex behaviour of the enzyme-electrode assemblies used in this thesis and construct appropriate equivalent circuits in order to fit the respective Bode and Nyquist plots (section 2.3.5.3). Preliminary experiments conducted in our laboratory by Katherine Lee suggest that uniform electrodes (particularly in terms of semiconductor film-thickness) are needed to be able to determine reproducible equivalent circuits across the applied potential range. These cannot be obtained *via* the 'Doctor blading' method [564] by which TiO_2 electrodes are prepared in our laboratory (*i.e.* by spreading a TiO_2 slurry on the underlying transparent conducting oxide substrate using a microscope glass slide, see section 8.3.2). Instead, more elaborate deposition techniques such as spin coating are required.

The photoelectrochemistry results are intriguing and important in that they establish that even under limited carrier-enhancement, significantly amplified catalysis (*i.e.* by a factor of two) can be observed, highlighting the proficiency of the enzyme. In reduction catalysis, *p*-type materials would be required to maximise the enhancement of free carrier generation by illumination and achieve catalysis at significant *under*potentials. Accordingly, having established the principles of PFE on semiconductor electrodes in this chapter, the next chapter deals with the construction of a true, 'minority carrier utilising' photocathode for light-driven fuel-formation.

5 Selective visible-light-driven CO_2 reduction on a *p*-type dye-sensitised NiO photocathode

Part of the work presented in this chapter has been published: Andreas Bachmeier, Samuel Hall, Stephen W. Ragsdale, and Fraser A. Armstrong, *J. Am. Chem. Soc.* **2014**, *136*, 13518.

Abstract

Building on the principles of protein film electrochemistry on semiconductor electrodes established in chapter 4, a photocathode assembly for the visible-light-driven, selective reduction of CO_2 to CO at potentials below the thermodynamic equilibrium in the dark is presented in this chapter. The photoelectrode comprises a porous *p*-type semiconducting NiO electrode modified with the visible-light responsive organic dye P1 and CODH as reversible CO_2 cycling enzyme. The direct electrochemistry of the enzymatic electrocatalyst on NiO shows that in the dark the electrocatalytic behaviour is rectified towards CO oxidation, with the reactivity being governed by the carrier availability on the semiconductor/catalyst interface.

5.1 Introduction

As a general rule, fuels derived from artificial photosynthesis fuels can either be H_2, the immediate product of water splitting, or carbon-based compounds such as methanol. Most obviously, carbon fuels can be formed indirectly by 'hydrogenation' of CO_2, similar to the processes occurring in photosynthetic dark reactions. However, direct reduction of CO_2 is also an attractive possibility that could lead to CO_2 replacing petrochemicals as the feedstock for value-added organic chemicals. Like natural photosynthesis, artificial photosynthesis can be broken down into four essential processes: harvesting of visible-light, charge (electron-hole) separation, fuel formation, and water oxidation to O_2. The last two processes require an efficient and selective catalyst (see section 1.2). It is difficult to integrate all of these processes, so researchers have streamlined efforts by focusing on individual aspects.

This chapter addresses the direct reduction of CO_2 to CO using a photoelectrochemical cell comprising a dye-sensitised *p*-type NiO photocathode functionalised by spontaneous adsorption of CODH (Figure 5:1). Reductive CO_2 activation is a fundamentally challenging process and only CODH and formate dehydrogenase are known to selectively and reversibly achieve synchronous, proton-coupled two-electron reduction of CO_2 to CO or formate, avoiding the highly unfavourable one-electron reduced intermediate $CO_2^{\bullet-}$ (eq. (1:4)).

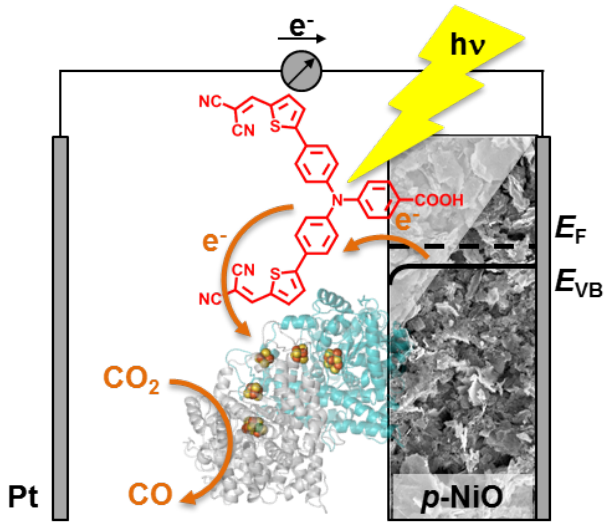


Figure 5:1 Schematic representation of a photoelectrochemical cell for the selective reduction of CO_2 to CO at *p*-type NiO. Light-absorption by the organic dye P1 (red) is followed by electron transfer to CODH, which is co-adsorbed on the NiO surface and carries out CO_2 reduction, while hole injection into the NiO valence band regenerates the P1 ground state. The porous nature of the NiO surface is indicated by the SEM image (full image in Figure 5:2). The Fermi level and valence band potentials of NiO are denoted as E_F and E_{vb}.

Despite its low majority carrier (*i.e.* hole) mobility, values between 10^{-8} and 10^{-9} $cm^2 S^{-1}$ have been reported – two orders of magnitude lower than the electron diffusion coefficient in *n*-TiO_2 [565], NiO is the most widely studied semiconductor material in *p*-type DSSCs [489,566]. Having a band gap of 3.55 eV [567], NiO is transparent to visible light (apart from a phenomenon known as 'parasitic absorption', *vide infra*) and requires sensitisation to extend the absorbance into the visible region of the electromagnetic spectrum. To this end, Sun and co-workers developed the organic pigment P1 (Figure 5:1) as photosensitiser for *p*-type dye-sensitised solar cells [383]. Being one of the most efficient sensitisers to date (maximum IPCE = 63%, open-circuit voltage V_{oc} = 84 mV, short-circuit current density j_{sc} = 5.48 mA cm^{-2}, fill factor *ff* = 33%, resulting in a photoconversion efficiency of 0.15% [565]), this 'push-pull' dye uses a triphenylamine moiety as electron donor component and two malononitrile groups as acceptors. The different components are connected by a conjugated chain comprising a thiophene unit. Light excitation is associated with spatial intramolecular charge separation through electron transfer from the donor part of the dye to

the acceptor [383]. Being partly localised on the triphenylamine unit and hence close to the –COOH anchoring group/NiO surface and having its energy level (1.38 V *vs.* NHE) below the valence band of NiO, the HOMO of P1 allows for efficient hole injection into NiO. The LUMO, in turn, is spatially separated from the HOMO and localised on the acceptor (*i.e.* malononitrile) moieties.

Recently, Sun *et al.* achieved light-driven H_2 evolution by co-adsorbing P1 and a molecular cobalt cobaloxime catalyst on NiO [188]. Taking their lead, the work described in this chapter adapted the concept for light-driven CO_2 reduction. The mechanistic principle being exploited is that each excitation of P1 results in an electron being transferred to its co-adsorbed partner CODH, passing through a relay of FeS clusters to the [Ni4Fe-4S]-active site at which CO_2 is converted to CO in a proton-coupled two-electron reaction according to Scheme 1:4. Unlike simple molecular catalysts, the additional FeS centres enable redox enzymes such as CODH to capture irreversibly [310] all the electrons required to complete the catalytic cycle when supplied to a highly efficient active site. The P1 ground state is regenerated through hole injection into the NiO valence band. The relevant electrochemical potentials of the individual components are given in Table 5:1.

Table 5:1 Reduction potentials of the individual components of the CO_2 reducing photocathode assembly depicted in Figure 5:1. All values in V *vs.* SHE at pH 6.0.

	$E(CO_2/CO)$	$E(P1/P1^-)$	E_{vb}, E_{cb}
CODH	–0.46 [218]		
P1		–1.13 [383,568]	
NiO			0.60, –3.00 [488]

5.2 Results and discussion

5.2.1 Electrocatalytic activity of carbon monoxide dehydrogenase adsorbed on a *p*-type NiO electrode

First, the dark electrocatalytic activity of CODH adsorbed on a *p*-type NiO electrode was studied using PFE. Figure 5:2 depicts an SEM image of a typical NiO film electrode used in this work. Being similar in porosity to the TiO_2 and CdS films depicted in Figure 4:3, the surface possesses sites for electroactive enzyme adsorption in a variety of orientations. With the point of zero charge between 8.3 – 8.5, depending on the experimental method employed in its determination [569], at pH 6.0 the NiO surface gives rise to attractive electrostatic interactions with CODH similar to those observed for TiO_2 and CdS (section 4.2.1).

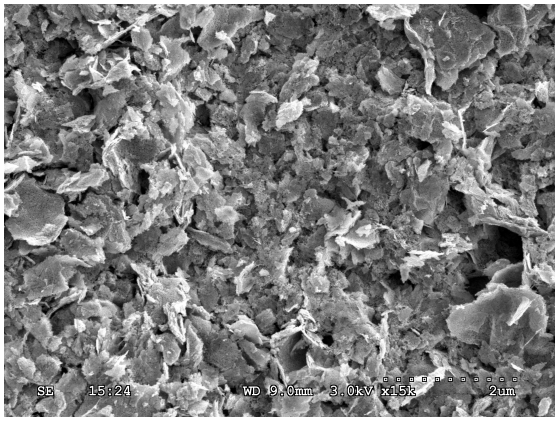


Figure 5:2 SEM image of a NiO film deposited on ITO.

To remind the reader, CODH displays catalytic activity for both CO_2 reduction and CO oxidation when adsorbed on a PGE electrode and both CO_2 and CO are present in the solution, as shown in Figure 5:3A (which displays the same data as Figure 4:3A). Importantly, the voltammogram cuts sharply through the zero-current axis at the thermodynamic potential and catalysis is controlled by the inherent properties of the enzyme [213,555,570]. The catalytic bias prevails, and it is largely controlled by the potential of the

electron entry/exit point of the enzyme [213,556]. As described in section 1.6.4.2, the active site of CODH alternates between the two catalytically active states C_{red1} and C_{red2}, separated by two electrons (Scheme 1:4), with C_{int} as an intermediate formed during long-range electron transfers from the FeS clusters.

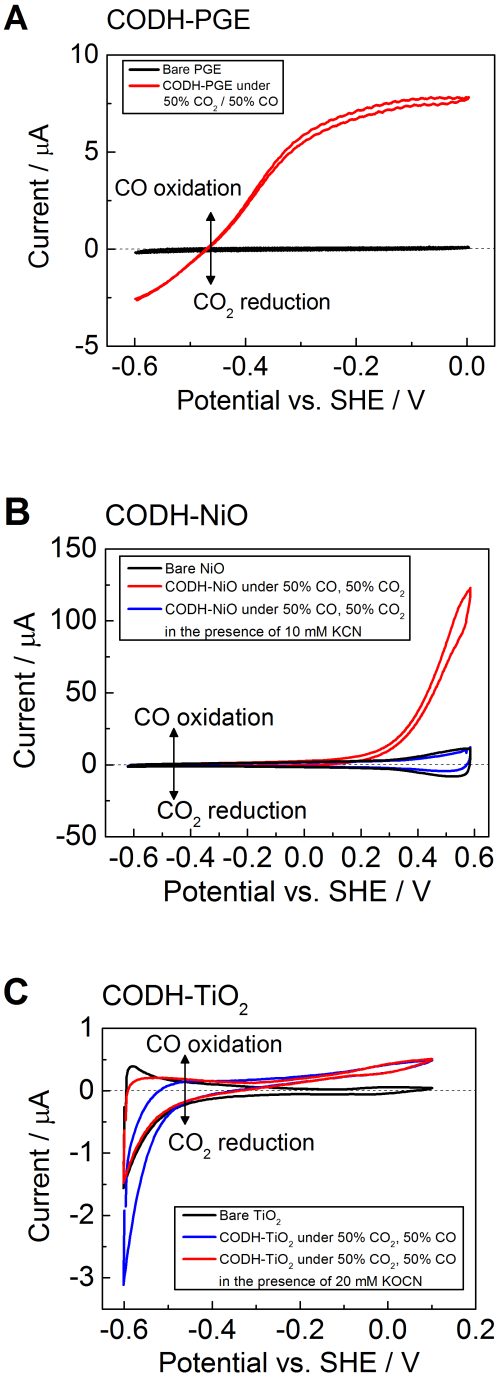
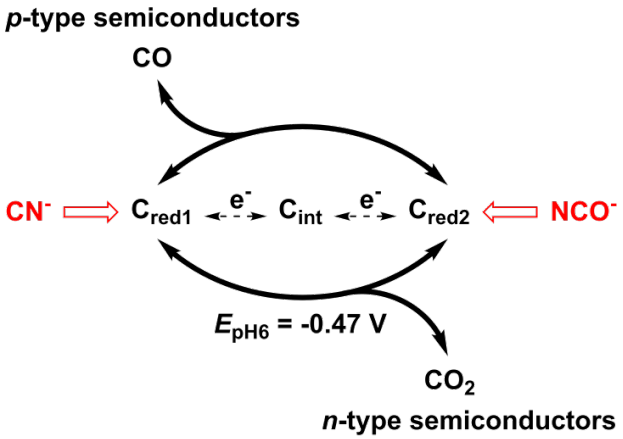


Figure 5:3 Cyclic voltammograms of CODH adsorbed on (A) PGE, (B) NiO, and (C) TiO_2 electrodes. Current-voltage curves of the bare electrodes are depicted in black, experiments with adsorbed CODH (recorded in a 50% CO/50% CO_2 gas mixture bubbling through the cell) are shown in red. The blue CVs in B and C were recorded in the presence of 10 mM KCN (B) and 20 mM KOCN (C). Other conditions: 20 °C, 0.2 M MES buffer (pH 6.0), scan rate: 10 mV s^{-1}. A and C adapted from Figure 4:3.

In contrast to the reversible catalytic interconversion of CO_2 and CO observed on the metallic-type PGE electrode, CODH behaves as a *unidirectional* CO oxidiser when attached

to NiO (Figure 5:3B, red trace); in other words, the otherwise bidirectional catalysis is rectified. A catalytic oxidation current in Figure 5:3B is observed only upon applying an overpotential of approximately 0.6 V (oxidising conditions under which CODH converts slowly to the inactive C_{ox} state [554]). To prove that the oxidation current indeed stems from catalytic turnover, KCN was injected into the electrochemical cell (to a final concentration of 10 mM; blue voltammogram in Figure 5:3B). Being isoelectronic with CO, cyanide targets the C_{red1} state of CODH (Scheme 5:1), thereby selectively inhibiting CO oxidation [554]. The voltammogram thus obtained resembles the baseline (bare NiO). These results mirror the observations with CODH adsorbed on the *n*-type materials TiO_2 and CdS described in section 4.2.2 [570]. Figure 5:3C (adapted from Figure 4:3A) illustrates this effect for TiO_2 and shows cyclic voltammograms of CODH adsorbed on TiO_2 recorded under identical conditions to the voltammograms displayed in Figure 5:3A,B. In contrast to *p*-NiO, CO oxidation at *n*-TiO_2 is barely detectable whereas a strong reduction current is observed, which is established to be CO_2 reduction by introducing cyanate (NCO^-, isoelectronic with CO_2) which targets the C_{red2} state and blocks CO_2 reduction (see Scheme 5:1 and blue trace in Figure 5:3C).

Scheme 5:1 Redox states involved in catalytic CO_2 interconversion at the active site of CODH and how *p*-type and *n*-type semiconductors rectify catalytic electron flow. The small molecule inhibitors CN^- and NCO^- selectively intercept the C_{red1} and C_{red2} states and inhibit CO oxidation (CN^-) and CO_2 reduction (NCO^-) [554].



The results presented in this section highlight that, when attached to semiconducting electrodes such as TiO_2, CdS, and NiO, the activity of an electrocatalyst depends greatly on the properties of the semiconductor, in particular the carrier availability at the semiconductor/enzyme interface. The resulting rectification in either direction, depending on the choice of semiconductor, is evident only when an electrocatalyst that otherwise behaves reversibly is used [570]. According to eqs. (2:35) and (2:36), the surface concentration of majority carriers in a semiconductor depends exponentially on the difference between the applied potential E and the flat-band potential E_{fb} [469]. The catalytic directionality enforced on *n*-type TiO_2 (*i.e.* the inversion of the apparent catalytic bias) coincides with a change in carrier availability around the flat-band potential of the semiconductor (E_{fb} (TiO_2) ≈ –0.50 V *vs.* SHE at pH 6.0; see section 4.2.3.1). In chemical terms, some Ti^{4+} sites are reduced to Ti^{3+}. In contrast, *p*-type NiO (E_{fb} (NiO) ≈ 0.61 V *vs.* SHE at pH 6.0 [488]) forms a depletion layer at potentials negative of E_{fb}, which acts as a barrier for electron transfer from the semiconductor to the catalyst, blocking CO_2 reduction. As E_{fb} is approached, the conductivity of NiO increases exponentially, allowing CO oxidation catalysis to occur. In chemical terms, some Ni^{2+} sites are oxidised to Ni^{3+} (see section 2.3.3.3). This effect is reflected in a steep increase in the catalytic oxidation current in Figure 5:3B positive of *ca.* 0.3 V *vs.* SHE, *i.e.* relatively close to E_{fb}.

5.2.2 Photoelectrocatalytic CO_2 reduction

Having established the electroactivity of CODH on NiO, the semiconductor electrodes have been sensitised with the visible-light-absorbing dye P1 [383] (Figure 5:1), by soaking the electrodes in a 300 mM solution of P1 in ethanol overnight. Figure 5:4 shows linear sweep voltammograms recorded under chopped illumination in CO_2-saturated buffer (cyclic

voltammograms of NiO–P1 are depicted in Figure 5:5).[i] Bare NiO shows very little photocurrent because of its large band gap of 3.55 eV [567] (black current-potential curve). It has to be noted that despite its large band gap, non-stoichiometric NiO is a material of dark colour. Whereas ideal, stoichiometric NiO is pale-green (owing its colour to intra-3d transitions in octahedral Ni^{2+} sites [571]), calcination in air yields a dark-coloured material. Originally, this dark hue in mesoporous NiO films has been ascribed to the presence of Ni^{3+} species at the surface, which are produced as some Ni^{2+} is oxidised during the heat treatment in air [572]. These species give rise to brown or black coloration, and, importantly, excitation of which does not result in photocurrent [490,567]. However, this explanation now seems to be oversimplistic because Renaud *et al.* recently established that black elemental Ni is also formed in the calcination process, and is a major source of the dark colour [571]. The Ni(0) impurities do also not contribute to the photocurrent. Commonly, these phenomena of 'non-current-producing' absorption are known as 'parasitic optical absorption' [573]. Upon sensitisation with P1, the photocurrent increases since P1 is capable of absorbing visible light (λ_{max} = 550 nm in solution and 500 nm when adsorbed on NiO [383]).

[i] Current densities, normalised to the respective geometric surface area, are reported in photoelectrochemistry experiments where this seems advantageous from a viewpoint of allowing general comparability across different (literature) systems. However, the reader should bear in mind that the intrinsic surface areas of porous semiconductor electrodes are much greater than the outer, geometric values suggest.

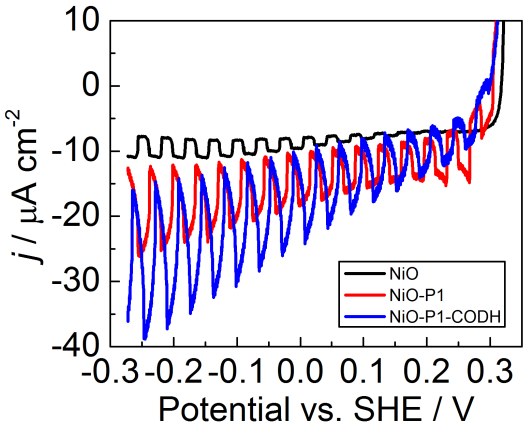


Figure 5:4 Linear sweep voltammograms of NiO (black), NiO–P1 (red), and NiO–P1–CODH (blue) recorded under chopped illumination (0.5 Hz, 45 mW cm^{-2}) and CO_2 flow. Conditions: 0.2 M MES buffer (pH 6.0), T = 32 °C, scan rate = 10 mV s^{-1}.

Modification with CODH results in a further photocurrent enhancement, which can be ascribed to the light-driven reduction of CO_2. Photoexcited P1 provides sufficient driving force to effect CO_2 reduction catalysed by CODH (see Table 5:1) but does not reduce CO_2 itself. The LUMO of P1 lies approximately 0.7 V lower in energy than the $CO_2/CO_2^{\bullet-}$ redox couple: importantly, as a single-electron transfer dye that is not capable of accumulating a second electron, P1 cannot undergo the PCET reactions that are required to lower the activation barrier for CO_2 activation, in contrast to CODH (which easily accumulates the two electrons needed).

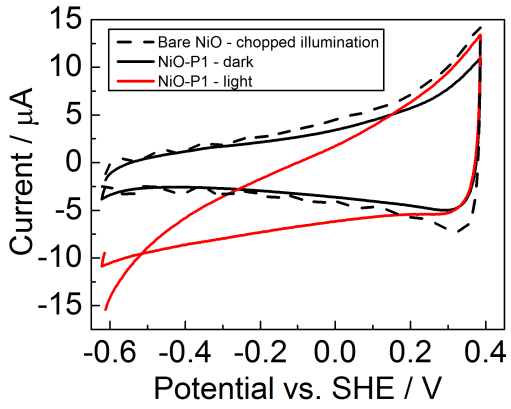


Figure 5:5 Cyclic voltammograms of a bare NiO electrode (dashed line) and NiO–P1 in the dark (black) and under illumination (45 mW cm^{-2}, red). Scan rate: 30 mV s^{-1}, 0.2 M MES buffer (pH 6.0), 25 °C.

The hypothesis that the photocurrent enhancement observed upon adsorption of CODH on NiO–P1 is due to catalytic conversion of CO_2 to CO had to be verified experimentally. Once again NCO^- was used as a selective inhibitor of CO_2 reduction, as even prolonged illumination over several hours did not produce enough CO to allow detection by gas chromatography (Figure 5:6). This was due to the minute quantities of enzymes on the electrode surface (nmol) – in contrast to the much larger amounts of substance used in the photocatalysis experiments our laboratory has carried out previously [379-381].

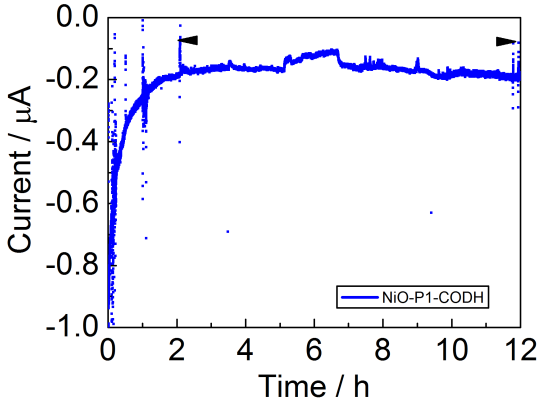


Figure 5:6 Typical long-term chronoamperometry experiment of NiO–P1–CODH under illumination (45 mW cm^{-2}) at –0.3 V *vs.* SHE; 0.2 M MES buffer (pH 6.0), 10 °C. The cell solution (7.5 mL buffer) and headspace were saturated with a mixture of 98% CO_2 and 2% CH_4 prior to the experiment (CH_4 served as internal standard in post-experimental gas chromatographic analysis). The black arrows indicate the capacitive dark current. No CO could be detected after the experiment. A total charge of 5.05 mC (after subtraction of the electrode capacitance) was passed through the system, which would, assuming 100% Faradaic efficiency for CO_2 reduction as the upper limit, correspond to the formation of a maximum of 26.2 nmol CO. Such a small amount could not be detected by GC, as it would still be dissolved in the cell solution and furthermore lie below the detection limit of the employed gas chromatograph.

Figure 5:7 depicts transient photocurrents of NiO–P1–CODH recorded at –0.27 V *vs.* SHE (pH 6.0), which represents a 0.2 V *under*potential with respect to CO_2 reduction in the dark.

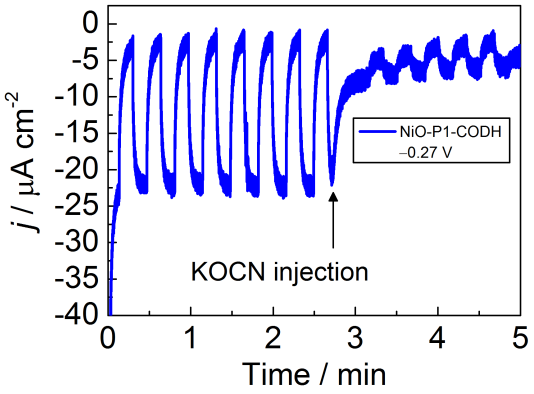


Figure 5:7 Chronoamperometry experiment showing transient photocurrents under chopped illumination of NiO–P1–CODH under a flow of CO_2 with the potential being held at –0.27 V *vs.* SHE. NCO^- was injected to a final concentration of 60 mM as indicated. Experimental conditions: white-light illumination (45 mW cm^{-2}); 0.2 M MES buffer (pH 6.0), T = 32 °C.

The photocurrent decreases significantly upon introduction of 60 mM KOCN, which establishes that the major proportion of the observed photocurrent stems from CO_2 reduction.

Control experiments in the absence of CODH, *i.e.* NiO-P1 only, show that injecting KOCN has no effect on the photocurrent (Figure 5:8).

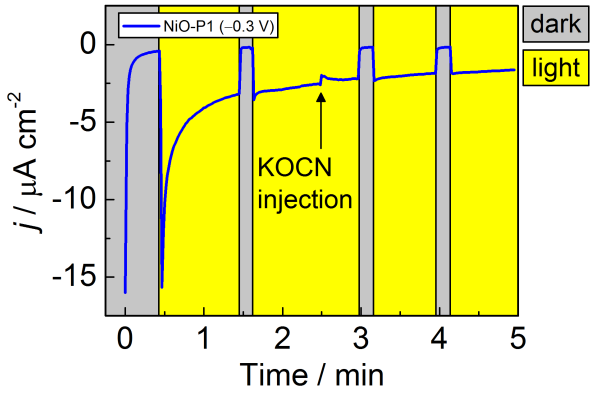


Figure 5:8 Chronoamperometry experiment of NiO–P1 (control experiment *without* CODH) under illumination (45 mW cm^{-2}) at –0.3 V *vs.* SHE; 0.2 M MES buffer (pH 6.0), 25 °C, 50 scc/min CO_2 flow. At $t = 2.5$ min KOCN solution was injected into the cell to a final concentration of 60 mM. KOCN did not affect the photocurrent, in contrast to NiO–P1–CODH shown in Figure 5:7.

Having identified the nature of the photocurrent, the stability of CO_2 reduction was assessed. Figure 5:9 depicts the temporal behaviour of the catalytic current produced by NiO–P1–CODH during prolonged illumination. The assembly shows good stability until cyanate is injected, analogous to the experiment depicted in Figure 5:7, again demonstrating the catalytic turnover of the photocathode-catalyst system. Both Figure 5:4 and Figure 5:7 strongly support a mechanism similar to that described by Sun and co-workers for H_2 production [188]. In the system described in this work, P1 acts as a visible-light-responsive sensitiser that generates excited-state electrons, transfers these to CODH for catalysis, and is regenerated *via* hole injection into NiO.

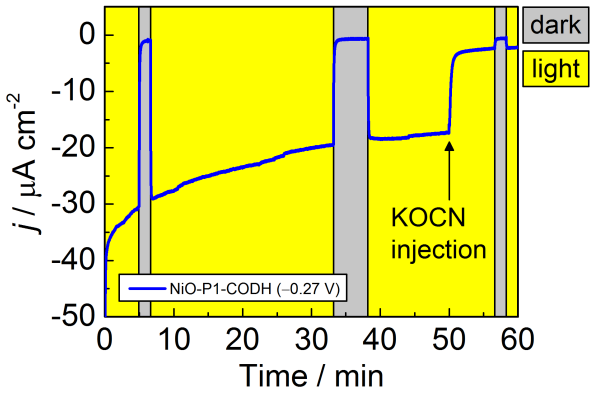


Figure 5:9 Continuous illumination of NiO–P1–CODH to assess the stability of the photocathode-assembly under turnover conditions. Experimental conditions: white-light illumination (45 mW cm^{-2}); E = –0.27 V *vs.* SHE; CO_2 flow; 0.2 M MES buffer (pH 6.0); T = 32 °C. NCO^- was injected to a final concentration of 60 mM at t = 50 min.

Concerning the kinetic order of the elementary steps, the current understanding of these complex multi-site photoinduced reactions is scant. Hole injection into the NiO valence band is usually fast (ps-timescale), but, in contrast to dye-sensitised *n*-type TiO_2, geminate recombination is also a very fast process (ns-regime) [565]. Reasons for the fast back electron transfer processes are not fully understood, but it has recently been shown that, in contrast to most TiO_2-based DSSCs that have a large driving force for recombination [574], for NiO this reaction lies in the normal Marcus regime, as experimentally verified for a series of perylene imide sensitisers attached to NiO surfaces [575]. Rapid recombination in dye-NiO assemblies may arise, in part, due to the Ni(III) sites being located on the semiconductor surface (in contrast to the behaviour of TiO_2, see section 2.3.3.3), in close proximity to the photoreduced dye [489]. Hence, efficient charge-separation *within* the dye, as for example in push-pull architectures such as P1, is crucial to suppress geminate recombination.

Among the few examples in the literature, Hammarström and co-workers recently showed that electron injection from an excited dye immobilised on NiO into a co-adsorbed H^+ reduction catalyst significantly retards destructive geminate recombination between NiO

and the dye, in their case coumarin [384]. Based on these observations, it is plausible to assume a mechanism in which visible-light excitation of P1 is followed, kinetically, by hole injection into the NiO valence band, forming the P1 anion. Then, electron transfer from the LUMO of P1 to CODH (presumably to the D-cluster) takes place. Time-resolved studies of photoinduced electron transfer by transient absorption spectroscopy would, in principle, be insightful and might establish the charge transfer kinetics. However, a major problem is that electron injection into FeS enzymes such as CODH is not accompanied by a distinct change in absorbance, due to the broad absorption bands of FeS clusters [310].

5.3 Conclusions and perspectives

In conclusion, catalytic electron flow through the CO_2-reducing enzyme CODH, which behaves as a reversible catalyst on a metallic-like electrode, is rectified when CODH is attached to *n*-type or *p*-type semiconductors, leading to unidirectional CO_2 reduction and CO oxidation, respectively. When NiO is sensitised with the visible-light sensitiser P1, a photocathode is produced that selectively reduces CO_2 to CO under visible-light illumination and application of a mildly reducing potential. To the best of my knowledge, these results provide the first demonstration of visible-light-driven clean and efficient CO_2 reduction at a *p*-type photocathode – a reaction intrinsically more difficult than proton reduction. While the photocurrent densities observed are too small to allow for scale-up, they are of the same magnitude as similar systems for H_2 evolution [188,291]. Both CODH and P1 are co-adsorbed on NiO without specific coupling, similar to work by Hammarström [384], Mozer [291], and Sun [188]. Specific covalent linkage of CODH and P1 would be an attractive strategy to improve the efficiency of electron transfer, but is not straightforward as it requires genetic modification of the enzyme to introduce binding sites for the sensitiser.

The assembly depicted in Figure 5:1 shows good stability under turnover conditions, indicating that it could, in principle, be coupled with a photoanode for water oxidation in a tandem-photoelectrochemical cell in order to close the photosynthetic cycle. Preliminary experiments have been carried out based on a procedure employed by Mozer *et al.* [291]. A wired photoelectrochemical tandem cell (similar to the schematic in Figure 1:21) was created by connecting the NiO-P1-CODH electrode as working electrode to a W–$BiVO_4$ photoanode serving as counter electrode [85] (see section 6.2.3) for light-driven unassisted CO_2 reduction coupled to water oxidation. The two electrodes were placed in different compartments of an electrochemical cell separated by a Nafion 117 membrane and illuminated separately, using

two visible-light sources. Figure 5:10 depicts a typical experiment under no externally applied bias. Although illumination does generate a photocurrent, this cannot be attributed to CO_2 reduction as injection of KOCN does not result in photocurrent attenuation. The temporal behaviour of the photocurrent after KOCN was introduced was similar to the control experiment carried out in the absence of CODH depicted in Figure 5:8.

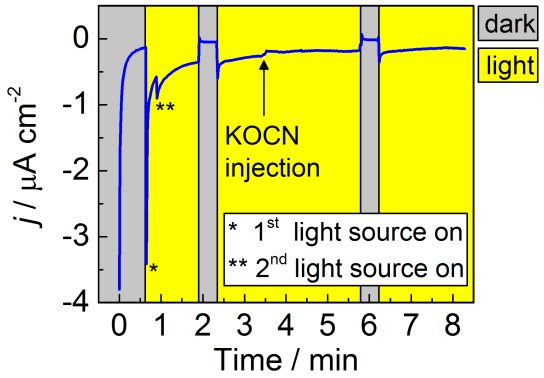


Figure 5:10 Photocurrent profile of a photoelectrochemical cell comprising a NiO–P1–CODH photocathode (working electrode) and a W–$BiVO_4$ photoanode (counter electrode). The electrodes were placed in two compartments of an electrochemical cell, separated by a Nafion 117 membrane, and illuminated separately with P_{in} = 45 mW cm^{-2} in each case. The cell solution was 0.1 M potassium phosphate buffer (pH 6.0 at 25 °C, see section 8.5.1.1) in both compartments. The CE compartment was purged with Ar (50 scc min^{-1}) and the WE was sparged with CO_2 over the course of the experiment (50 scc min^{-1}). At t = 45 s, the CE compartment was illuminated (*) through the ITO back contact, illumination of the WE compartment commenced shortly afterwards at t = 60 s (**). KOCN was injected to a final concentration of 60 mM at t = 210 s, to no effect on the photocurrent.

Although these initial attempts were unsuccessful, they serve to illustrate the importance of the different components not only being active individually, but also when coupled to form an integrated device. Possible reasons for the inactivity of this 'integrated system' include instability of the NiO–P1–CODH electrode under the experimental conditions used (for example, P1 desorption in phosphate buffer [188]), as well as enhanced carrier recombination *before* catalysis can occur [131], due to the transient nature of the charge carriers when no external bias is applied (in contrast to the potential-controlled experiments depicted in Figure 5:7 and Figure 5:9). Other limiting factors of the NiO-P1-CODH cathode-component are the

intrinsically low conductivity of NiO, fast geminate charge recombination within the cathode-assembly, and the low surface concentration of CODH due to its large 'footprint'.

Based on the limited knowledge that is available on the electron transfer kinetics in dye-sensitised NiO films, a mechanism of light-driven photoelectrocatalytic CO_2 reduction by NiO-P1-CODH is proposed, but the precise order of electron transfer steps still remain unclear. The next chapter deals with solar-to-chemical conversion using flavocytochrome c_3, an enzyme containing an electron transfer relay which comprises four coloured haem moieties with distinct absorption bands that change upon oxidation/reduction [576]. Thus, this enzyme should be amenable to future time-resolved optical studies.

Although they are not suitable for large-scale applications, this chapter again highlights that reversible and highly selective electrocatalysts such as CODH are valuable model catalysts for artificial photosynthesis. Only using a catalyst that is otherwise reversible reveals rectification of catalytic electron transport at a semiconductor. Multi-centred enzymes, which have well-defined and stable active sites, have a special ability to accumulate electrons, a property that is less likely for simple catalysts but likely to be very important in competing with recombination.

6 A multi-haem flavoenzyme as a solar conversion catalyst

Part of the work presented in this chapter has been published: Andreas Bachmeier, Bonnie J. Murphy, and Fraser A. Armstrong, *J. Am. Chem. Soc.* **2014**, *136*, 12876.

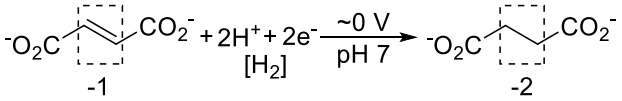
Abstract

The enzyme flavocytochrome c_3 (fcc_3), which catalyses hydrogenation across a C=C double bond (fumarate to succinate), is used to carry out the fuel-forming reaction in an artificial photosynthetic system. When immobilised on dye-sensitised TiO_2 nanoparticles, fcc_3 catalyses visible-light-driven succinate production in aqueous suspension. Solar-to-chemical conversion using neutral water as the oxidant is achieved with a photoelectrochemical cell comprising an fcc_3-modified indium tin oxide cathode linked to a $BiVO_4$ photoanode coated with a cobalt phosphate surface electrocatalyst. The results reinforce new directions in the area of artificial photosynthesis, in particular for solar-energy-driven synthesis of organic chemicals and commodities, moving away from simple fuels as target molecules.

6.1 Introduction

Artificial photosynthesis seeks to convert sunlight to storable chemical energy, *i.e.* fuels. Such 'solar-fuels' have the potential to address both the world's growing energy demand and reduce greenhouse gas emissions caused by the combustion of fossil fuels [3]. Building on the principles of natural photosynthesis, light harvesting and charge separation are coupled by electron transfers to fuel formation and O_2 evolution at efficient and specific catalysts. For ultimate commercial viability and scale-up, an artificial photosynthetic system must not only be intrinsically simpler in design than the complex photosynthetic enzymes, but should also be efficient, stable, and comprise earth-abundant, inexpensive materials. Despite major research efforts and significant progress being made [12,15-17,295,306] (compare section 1.3), the search for 'champions' is slow and major scientific breakthroughs are needed to fulfil all the above-mentioned criteria. Currently, artificial photosynthesis research is focused on H_2 production or reduction of CO_2, but the low-value products have little immediate opportunity to compete with fossil fuels. One way to bridge the gap is to identify reactions that could be driven by an artificial photosynthetic system, especially the synthesis of high-value organic chemicals [577-581]. Such a diversion from conventional paths is intellectually desirable and could attract more immediate commercial interest.

This chapter concerns initial experiments to expand the repertoire of fuel-forming reactions to include reductions of organic molecules. To this end, an enzyme-based photocatalytic system is presented that helps to level the aforementioned hurdles at the bench scale. Catalytic reduction of fumarate to succinate (eq. (6:1)) is equivalent to hydrogenation across a C=C bond, with each olefinic carbon changing oxidation number from −1 to −2. Used in an artificial photosynthetic system, it exemplifies direct conversion of hydrogen into storable organic molecules, not unlike photosynthetic hydrogen fixation as NADPH [26].



(6:1)

This reaction is catalysed by flavocytochrome c_3 (fcc_3) from *Shewanella frigidimarina* NCIMB400 (Figure 6:1). Although succinate itself is not a high-value chemical, a demonstration of its 'photo-synthesis' may stimulate new directions and possibilities for enzymes in the light-driven transformation of organic chemicals. Enzymes are highly selective catalysts, which are already used in the chemical industry; vast libraries are available, and the development of suitable examples for artificial photosynthesis may further increase their commercial usage.

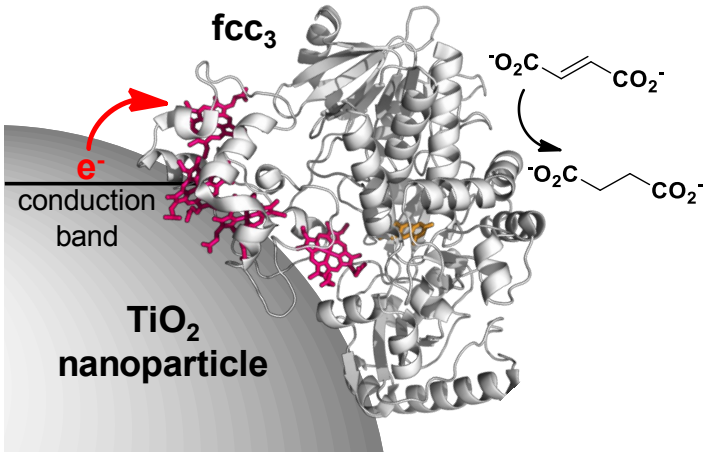


Figure 6:1 Cartoon showing flavocytochrome c_3 (PDB structure 1QJD [582]) adsorbed onto a TiO_2 surface. Intramolecular electron transfer to and from the flavin active site (orange) occurs over a distance of up to *ca.* 40 Å *via* four visible-light absorbing haem groups (pink) that are close to the enzyme surface.

Figure 6:1 shows a pictorial depiction of fcc_3 adsorbed on a TiO_2 surface. The enzyme has four haem groups that collect and relay electrons to the flavin (FAD) active site. A further important feature of fcc_3 is that both FAD and the haem centres strongly absorb visible light [576]: the kinetics of the entire electron transfer process, from the excited light-absorber to catalytic conversion at active site, are thus amenable to time-resolved optical techniques.

6.2 Results and discussion

6.2.1 Protein film electrochemistry

To establish if fcc_3 can be incorporated into an artificial photosynthetic system, the initial task at hand was to study its electroactivity when immobilised on electrodes and light-harvesting components. The interaction of fcc_3 with different electrodes was explored using protein film electrochemistry. Figure 6:2 compares the electrocatalytic reduction of fumarate by fcc_3 adsorbed on the *n*-type semiconductor electrodes TiO_2 and CdS with results obtained using PGE and mesoporous indium tin oxide (*meso*-ITO, 10% Sn(IV)-doped In_2O_3 [352,583]). Cyclic voltammograms recorded on a rotating-disc PGE electrode and a stationary ITO electrode are shown in Figure 6:2A,B, where the peak-like Faradaic current observed for the latter is due to substrate depletion, as expected under these conditions. The two catalytic reduction waves display a similar onset potential (ca. −0.05 V *vs.* SHE at pH 7.0) reflecting the fact that this parameter is controlled by the redox properties of the enzyme, provided the electrode behaves like a metal [213,555,570]. The results for PGE agree well with previous reports [584].

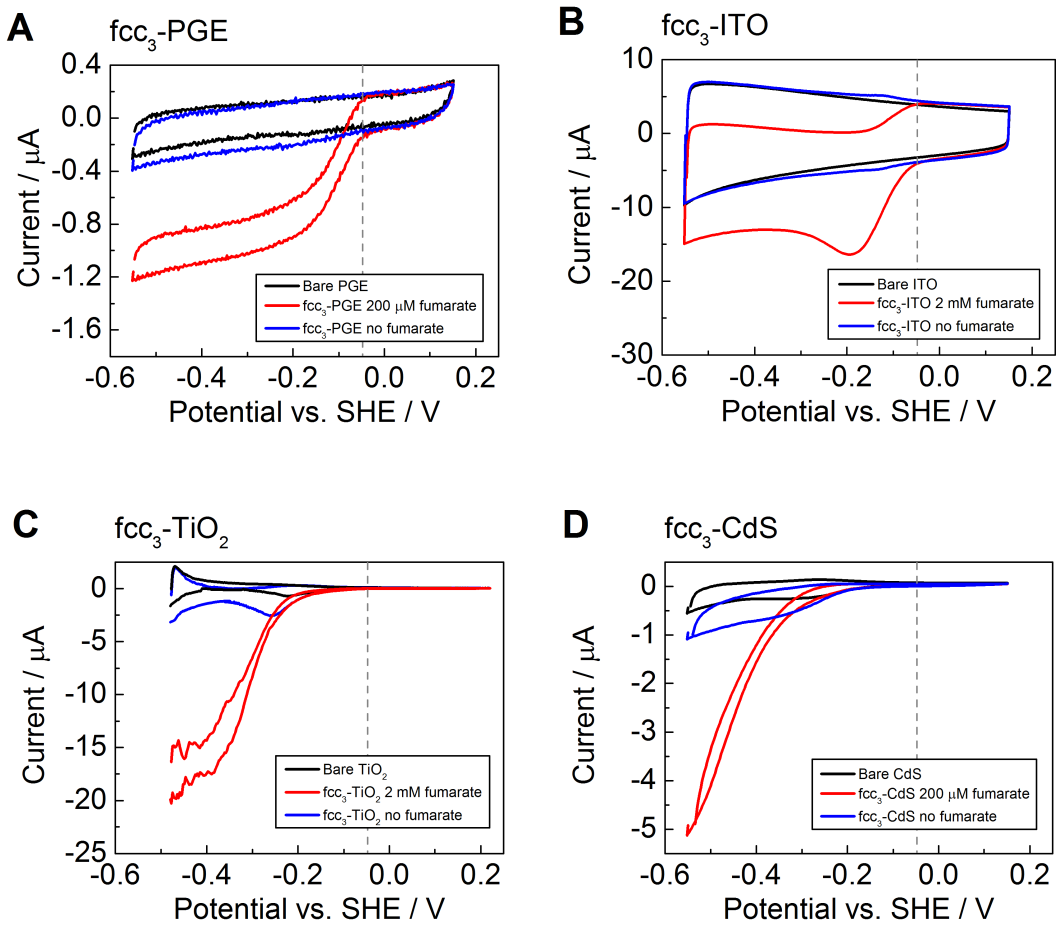


Figure 6:2 (A) – (D) Cyclic voltammograms (20 mV s^{-1}) of unmodified (black, recorded in the presence of fumarate) and fcc_3-modified electrodes (red, blue) in a mixed buffer system (pH 7.0) at 5 °C in the presence of fumarate (red), and after removal of substrate (blue), recorded (A) under rotation (ω = 2500 rpm) and (B) – (D) with a stationary electrode with no gas flow (A), (B) and sparging of the solution with argon close to the working electrode surface (C), (D). The dashed grey lines indicate the onset potential for fumarate reduction on PGE and ITO.

The electrocatalytic behaviour of fcc_3 on TiO_2 and CdS electrodes is shown in Figure 6:2C,D. In contrast to PGE and ITO, the onset of the catalytic current commences at much higher overpotentials on both semiconductor materials. The negative shift in onset potential reflects the limited surface electron availability at the semiconductor/catalyst interface when the applied potential is well away from the semiconductor flat-band potential E_{fb}. The majority carrier (*i.e.* electron in *n*-type semiconductors) availability increases exponentially according to eq. (2:35) as E_{fb} is approached [277]. Figure 6:3 makes this feature even more prominent

by directly comparing the normalised background-subtracted cyclic voltammograms obtained on all four electrodes at pH 7.0.

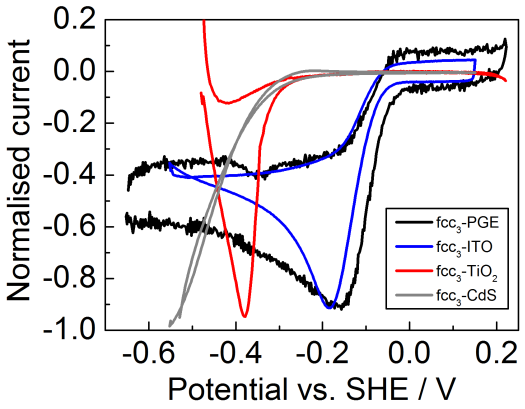


Figure 6:3 A comparison of the onset potentials of fumarate reduction on different electrode materials. These current-voltage curves correspond to normalised, background-subtracted traces of the voltammograms shown in Figure 6:2.

The catalytic onset potentials for fumarate reduction on TiO_2 and CdS are similar, which can be ascribed, at least in part, to their relatively similar E_{fb} [570] (see section 4.2.3.1). These observations reaffirm that the carrier availability and E_{fb} have a profound impact on electrocatalytic activity, effects that are discussed in chapters 4 and 5 for [NiFeSe]-hydrogenase and CODH adsorbed on TiO_2, CdS, and NiO [570,585].

6.2.2 Photocatalytic fumarate formation

Having established the electroactivity of fcc_3 on the semiconducting electrode materials CdS and TiO_2, a photocatalytic system to check for visible-light-driven fumarate reduction based on dye-sensitised TiO_2 nanoparticles was assembled. The enzyme shows good stability when adsorbed on TiO_2 electrodes: cyclic voltammograms recorded 24 h after enzyme immobilisation are shown in Figure 6:4.

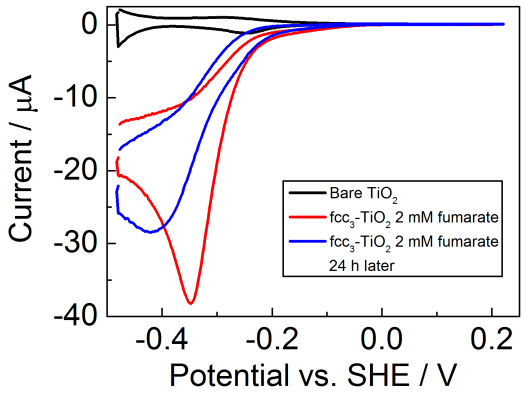


Figure 6:4 Stability of fcc_3 adsorbed on a stationary TiO_2 electrode. The blue voltammogram was recorded approximately 24 h after the current-voltage curve displayed in red. Conditions: 20 mV s^{-1}, mixed buffer (pH 7.0), 5 °C, Ar flow. In the time between the two experiments, the electrode was stored in buffer solution at 5 °C.

The TiO_2 nanoparticles (anatase, 15 nm) were modified with fcc_3 and then sensitised with the visible-light-absorbing chromophore RuP ($[Ru^{II}(bpy)_2(4,4'\text{-}(PO_3H_2)_2bpy)]Br_2$; bpy = 2,2'-bipyridine) as used in previous studies [377,379] to assemble the complete photocatalytic system. Uptake of both RuP and enzyme on the TiO_2 nanoparticles was quantified by analysing the supernatant of the particle suspension by UV/vis spectroscopy after centrifugation. Quantitative adsorption was obtained for 56 nmol RuP and 1.95 nmol fcc_3 on 5 mg TiO_2, corresponding to a surface coverage of up to 86% fcc_3 (depending on enzyme orientation, see section 8.5.5.1) and 25% RuP. Figure 6:5A shows a photograph of TiO_2 nanoparticles modified with fcc_3; the pink colour of the enzyme is clearly observable. UV/vis spectra of an fcc_3 solution taken before and after adsorption on TiO_2 are presented in Figure 6:5B. No features due to fcc_3 are observed after 20 min stirring with TiO_2, confirming quantitative uptake. More details are provided in section 8.5.5.

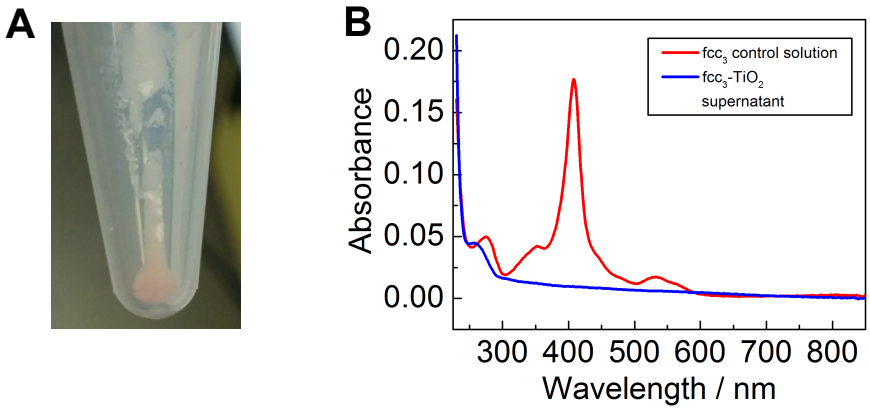


Figure 6:5 (A) Photograph of fcc_3-modified TiO_2 nanoparticles after centrifugation. The pink colour is due to immobilised fcc_3. (B) Absorption spectra recorded before and after modification of TiO_2 with fcc_3 show quantitative enzyme adsorption.

Photochemical fumarate reduction was carried out as follows: 1.95 nmol fcc_3 and 56 nmol RuP were co-adsorbed on 5 mg TiO_2, which was suspended in 5 mL of deuterated 0.2 M pH 6.0 MES buffer containing 6 mM disodium fumarate. MES also acts as sacrificial electron donor. The stirred suspension was irradiated by a W-halogen lamp fitted with a 420 nm UV-filter (P_{in} = 45 mW cm^{-2}). Catalytic turnover was monitored by ^{1}H NMR spectroscopy. Spectra recorded after visible-light illumination of TiO_2 nanoparticles modified with RuP and fcc_3 are shown in Figure 6:6 (NMR spectra were recorded after centrifuging the reaction mixture). Succinate formation was confirmed by the ^{1}H NMR signal at 2.33 ppm, which increased when more succinate was added (see Figure 6:6B inset). The succinate/fumarate ratio calculated after 4 h of irradiation (Figure 6:6A) corresponds to a TON of 5800 and an average TOF of 0.4 s^{-1} (both on a per enzyme basis). The derivation of these values is presented in section 8.5.5

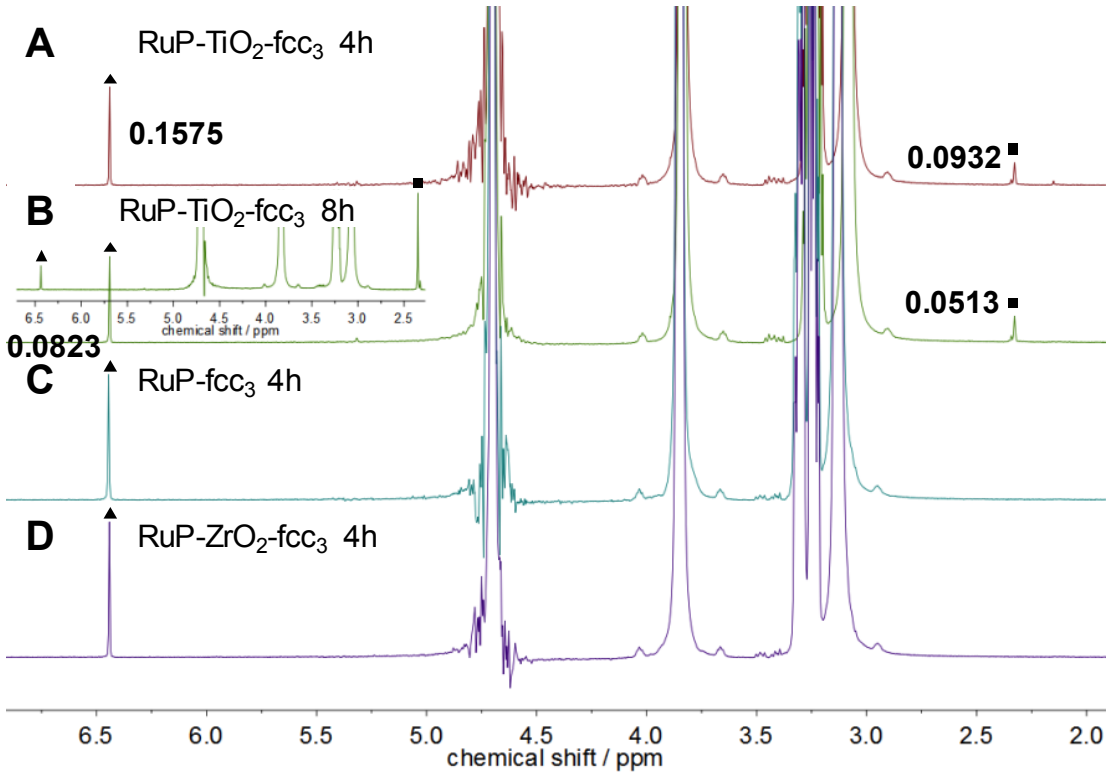


Figure 6:6 (A) – (B) ^{1}H NMR spectra showing visible-light-driven photocatalytic conversion of fumarate to succinate. The olefinic fumarate protons are highlighted by black triangles and give rise to a singlet at 6.44 ppm. The aliphatic succinate protons (indicated by black squares) resonate at 2.33 ppm. The product conversion is calculated from the ratio of the fumarate/succinate integrals provided in A,B. The H_2O signal appears at 4.70 ppm, and the signals at 3.85, 3.29, 3.26, and 3.13 ppm stem from MES buffer. The inset in (B) shows a spectrum recorded after adding additional succinate. Photochemistry experiments in the absence of TiO_2 (C) or with ZrO_2 instead of TiO_2 (D) show no signals corresponding to succinate formation. The original NMR spectra are presented in section 8.5.5.

Illumination over 8 h (Figure 6:6B) gave no significant enhancement in fumarate reduction, indicating that the maximum TON had already been reached after approximately 4 h. The average TOF of 0.4 s^{-1} is therefore a lower limit for what must be achievable under these reaction conditions. Under catalytic turnover, the reaction mixture changed colour from colourless to orange, indicating dissociation of the non-covalently bound flavin active site and/or the haem moieties (see Figure 6:7 and Figure 6:8). This instability is discussed below.

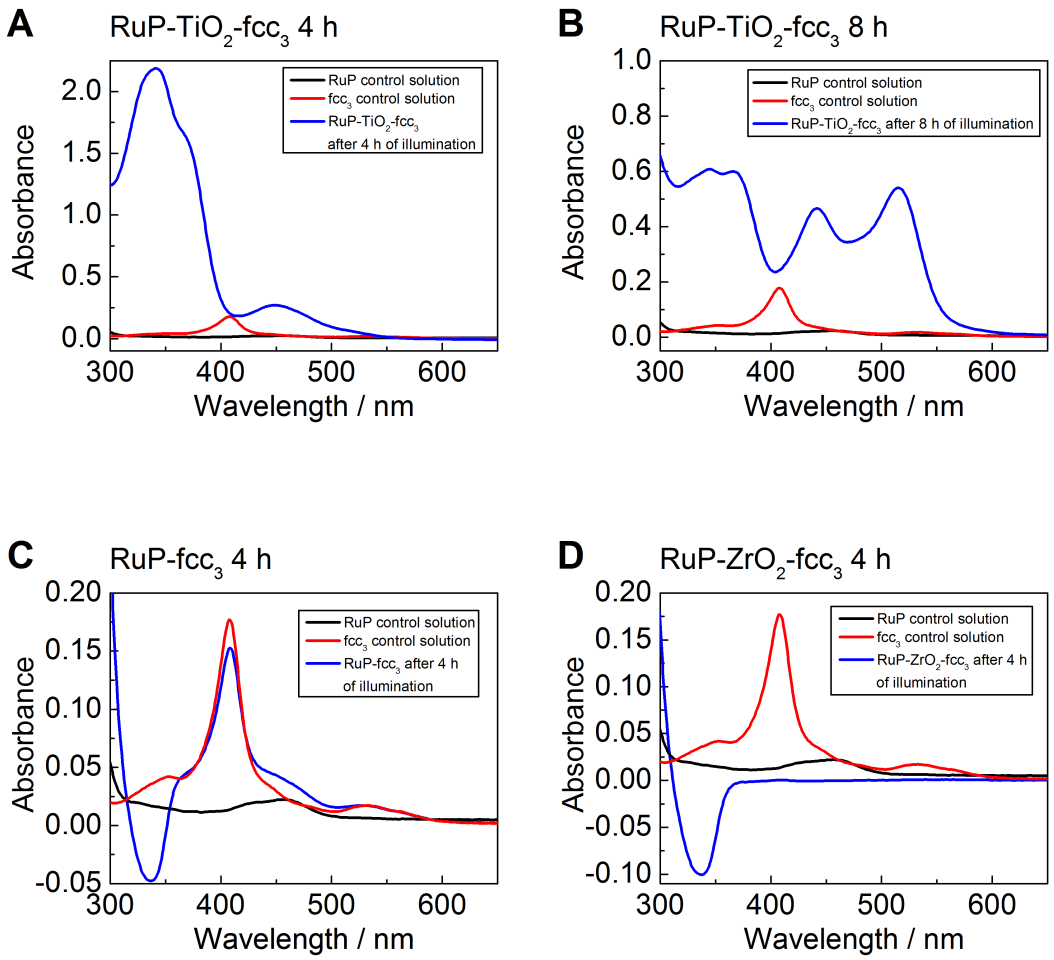


Figure 6:7 UV/vis spectra of the supernatants of the reaction mixtures recorded after centrifugation following photocatalytic fumarate reduction on RuP–TiO_2–fcc_3 (A),(B), and 'control' experiments using RuP–fcc_3 (C) and RuP–ZrO_2–fcc_3 (D).

Mechanistically, visible-light excitation of RuP (giving RuP*) injects electrons into the TiO_2 conduction band; these CB-electrons can then transfer to fcc_3. This 'through-particle' pathway [184] was established by the following experiments. No succinate was formed after illumination for 4 h in the absence of TiO_2, *i.e.* RuP and fcc_3 co-dissolved in MES/fumarate buffer (Figure 6:6C). A bimolecular reaction pathway between RuP* and fcc_3 in solution is thus ruled out. Illumination of RuP and fcc_3 co-adsorbed on ZrO_2 nanoparticles instead of TiO_2 also yielded no detectable amounts of succinate after 4 h (see Figure 6:6D). The conduction band energy of colloidal ZrO_2 in water is about 0.4 V negative of the value for

colloidal TiO_2 [586] and therefore too negative to accept electrons from RuP* [184]. Instead, this experimental configuration would only allow direct electron transfer from surface-bound RuP^* to co-adsorbed fcc_3, which evidently does not occur. The reaction mixtures remained colourless in both types of 'control' experiments and the sensitised ZrO_2 particles retained their pink colour after illumination, indicating that fcc_3 remained undamaged (see Figure 6:7 – Figure 6:9).

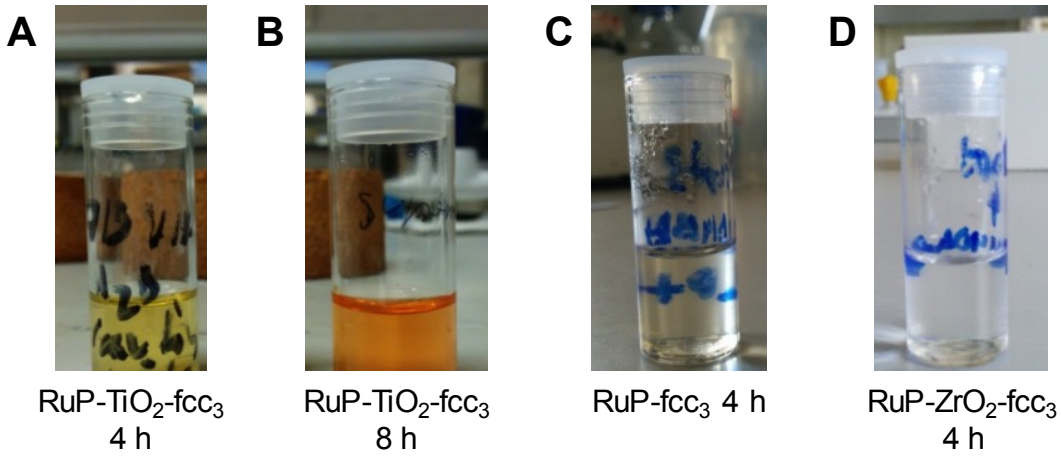


Figure 6:8 Photographs of the supernatants of the reaction mixtures recorded after photocatalytic fumarate reduction by RuP–TiO_2–fcc_3 (A), (B), and 'control' experiments using RuP–fcc_3 (C) and RuP–ZrO_2–fcc_3 (D).

Taken together, these observations suggest strongly that enzyme degradation occurs only under photochemical turnover. A possible degradation route involves the powerfully oxidising species RuP^+ ($E = 1.26$ V *vs.* NHE [587]), formation of which requires TiO_2 as support. RuP^+ is not formed when RuP is adsorbed on ZrO_2.



Figure 6:9 Photograph of fcc_3 adsorbed on ZrO_2 nanopowder, recorded after centrifugation.

6.2.3 Closing the photosynthetic cycle

A full photosynthetic cycle using water as the electron donor was achieved using a photoelectrochemical cell in which a visible-light-responsive *n*-type W–$BiVO_4$ photoanode [85] was used as counter electrode in a two-electrode configuration (Figure 6:10). The $BiVO_4$ conduction band potential (–0.39 V *vs.* SHE at pH 7.0 [87]) provides sufficient driving force to reduce fumarate at neutral pH without an externally applied bias.

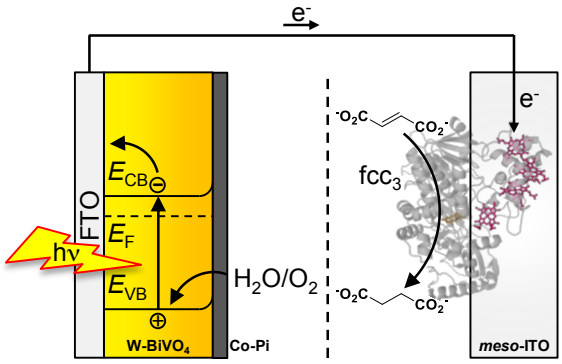


Figure 6:10 Schematic of a photoelectrochemical cell comprising an fcc_3-modified *meso*-ITO cathode (working electrode) and a Co-Pi-modified W–$BiVO_4$ photoanode (counter electrode) in a two-electrode configuration, separated by a porous frit.

To enhance the water oxidation rate, the electrode was coated with a cobalt phosphate (Co-Pi) surface electrocatalyst [134] *via* bias-assisted photodeposition [143] (see Figure 6:11, and section 1.3.2 for an introduction of the Co-Pi catalyst). In a separate cell compartment

(separated by a porous frit), a *meso*-ITO electrode modified with fcc_3 was used as the working electrode as the reductive chemistry constitutes the reaction of interest here (analogous experiments with inverse connections, *i.e.* Co-Pi-modified W–$BiVO_4$ as the working electrode and fcc_3–ITO as counter are depicted in Appendix G). The photoanode was irradiated through the FTO support (back illumination), meaning the charge carriers are generated close to the transparent conducting oxide back contact, since previous studies have shown that 'regular' front illumination (through the electrolyte, where electron-hole separation occurs close the semiconductor/electrolyte interface) gives lower photocurrents, implying that electron transport is the performance-limiting factor in bismuth vanadate photoelectrodes [148,588,589]. Various strategies of tungsten (gradient-) doping have shown to alleviate the problem of poor electron conductivity in this material [148,295,296].

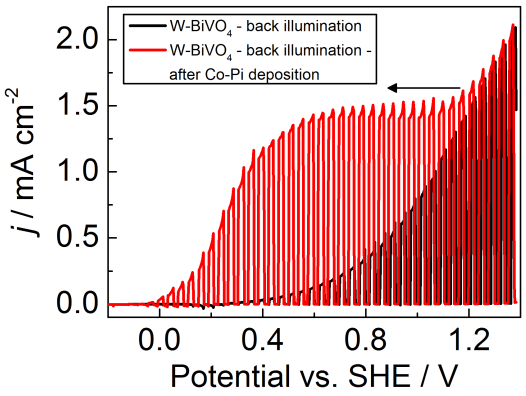


Figure 6:11 Linear sweep voltammograms of a W–$BiVO_4$ electrode before (black) and after photoassisted Co-Pi electrodeposition (red). Scan rate: 10 mV s^{-1}, chopped irradiation (back illumination, 0.5 Hz), 25 °C, 0.1 M KPi buffer (pH 7.0). The black arrow indicates the scan direction.

Figure 6:11 depicts current-voltage curves recorded under chopped illumination for the bare W–$BiVO_4$ photoanode (black) and following surface-modification with the cobaltate electrocatalyst film (red). The effect of Co-Pi becomes immediately apparent: in agreement with the extensive literature available on this catalyst (compare section 1.3.2), there is a significant cathodic shift in onset for the water oxidation photocurrent, *i.e.* the overpotential

requirement for this process is lowered considerably. It is worth noting that this effect has very recently been attributed to Co-Pi not playing a catalytic role when immobilised on $BiVO_4$, but, rather, providing a means to retard destructive electron-hole recombination within the semiconductor [590], not unlike the effects proposed for Co-Pi modified haematite [591] but in contrast to the dark electrocatalysis observed on conducting substrates. While further studies are needed to clarify the precise role of Co-Pi when immobilised on semiconductor surfaces, the important aspect for this work is that, independent of the particular physico-chemical mechanism involved, the desired effect of overpotential-relief is achieved.

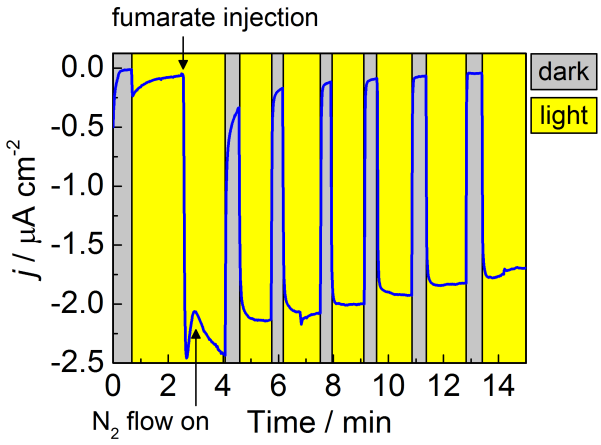


Figure 6:12 Photocurrent profile for visible-light-driven fumarate reduction in the photoelectrochemical cell illustrated in Figure 6:10. The cell solution was 0.1 M potassium phosphate (pH 7.0) at 25 °C. The working electrode compartment was sparged with N_2, but the gas flow was briefly stopped during injection of fumarate (to a final concentration of 2 mM) at $t = 2.5$ min.

Figure 6:12 shows the photocurrent profile for the integrated system illustrated in Figure 6:10, at neutral pH under zero external bias. In the absence of fumarate, only a small, rapidly decaying photocurrent is observed ($\Delta t = 0.7 - 2.5$ min; note that the assembly does not provide enough driving force for H^+ reduction), not unlike the bare ITO electrode (Figure 6:13; the enzyme-modified ITO electrode in Figure 6:12 has a capacitance different to the bare ITO surface, compare chapter 4). Injection of fumarate into the working electrode

compartment at $t = 2.5$ min in Figure 6:12 (final concentration 2 mM) causes an immediate steep increase in photocurrent as the charge-transport pathway becomes available and fumarate reduction takes place.

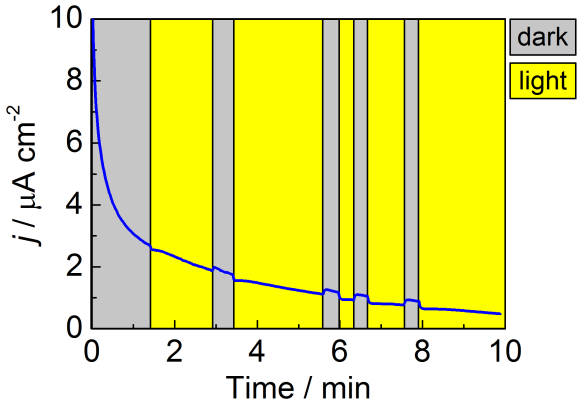


Figure 6:13 Chronoamperometry experiment showing the temporal behaviour of a *meso*-ITO electrode (WE) connected to a Co-Pi modified W-$BiVO_4$ photoelectrode (CE) in a two-compartment photoelectrochemical cell at zero external bias. Conditions: no gas flow, 25 °C, 0.1 M KPi buffer (pH 7.0).

Importantly, as shown in Figure 6:14, voltammograms of each electrode were recorded (separately) after the experiment depicted in Figure 6:12 to verify the activities of the individual components.

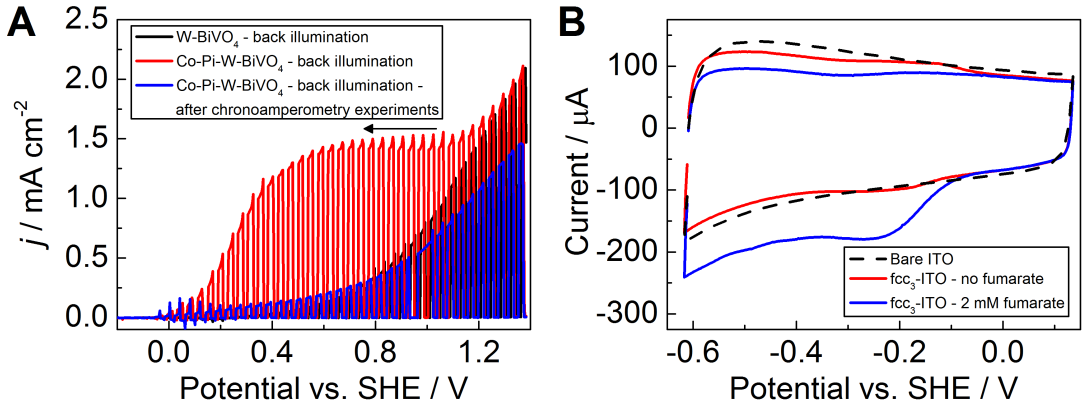


Figure 6:14 (A) Linear sweep voltammogram of a Co-Pi-W–$BiVO_4$ electrode recorded after the chronoamperometry experiments depicted in Figure 6:12 and Figure 6:13 (blue trace). The voltammogram indicates detachment of the Co-Pi catalyst from the electrode surface (compared with the red trace) and resembles the current-voltage curve of the bare W–$BiVO_4$ electrode (black curve). Experimental conditions: 10 mV s^{-1}, chopped illumination (0.5 Hz, back illumination), 25 °C, 0.1 M KPi buffer (pH 7.0). The black arrow indicates the scan direction. (B) Cyclic voltammogram of fcc_3–ITO recorded after the chronoamperometry experiment depicted in Figure 6:12; 30 mV s^{-1}, 25 °C, 0.1 M KPi buffer (pH 7.0), N_2 flow. The trace corresponding to the bare ITO electrode was measured before the chronoamperometry experiment was carried out. The blue trace, recorded after introducing fumarate to the solution (to a final concentration of 2 mM), shows that the enzyme retained catalytic activity for fumarate reduction.

The overall 'solar-to-succinate' efficiency (η_{STS}) can be determined according to eq. (6:2), which is based on eq. (2:2) [464] that describes the efficiency of H_2O photoelectrolysis:

$$\eta_{STS} = j_{ph}\ \eta_F\ 0.79\ \text{V}\ P_{in}^{-1} \qquad (6:2)$$

To remind the reader, in eq. (6:2) j_{ph} is the photocurrent density, η_F is the Faradaic efficiency for fumarate reduction, 0.79 V is the potential that is theoretically required to achieve both fumarate reduction and water oxidation (at pH 7.0, the fumarate/succinate potential is +0.03 V *vs.* SHE [584] and the H_2O/O_2 potential is +0.82 V), and $P_{in} = 45$ mW cm^{-2} refers to the incident light intensity. With $\eta_F = 100\%$ for fcc_3-catalysed fumarate reduction as the upper limit (no significant photocurrent could be observed before introducing fumarate), $\eta_{STS} = 0.03‰$ at $t = 15$ min. The estimated TOF per enzyme molecule is 0.01 s^{-1} (see section 8.5.6.3 for the derivation of this value), one order of magnitude lower than the value obtained in photocatalytic conversion with RuP–TiO_2, where a sacrificial electron donor was used to drive the reaction.

Efficiency limitations in these proof-of-principle experiments include irradiation with only the visible spectral region and delamination of the Co-Pi catalyst from the W–$BiVO_4$ surface (Figure 6:14A), similar to observations made by Sivula and co-workers [298]: under no external bias, the Co-Pi layer detaches within minutes from the photoanode surface, fundamentally limiting the performance of the system. Most likely, it is the 'bare' W–$BiVO_4$ surface that drives water oxidation during much of the chronoamperometry experiments for overall solar-to-succinate conversion using water as the oxidant depicted in Figure 6:12.

Comparing the photoelectrochemical cell presented in this section to a similar $BiVO_4$-based system for H_2 evolution developed by Kudo *et al.* (η_{STH} = 0.014‰) [592] shows that photoconversion efficiencies are similarly low (these authors apply an external bias of 0.8 V, meaning that both their system and the photoelectrochemical cell described herein provide a comparable driving force for the respective overall reaction). This observation and the order of magnitude decrease in turnover frequency observed when going from photocatalytic fumarate reduction driven by a sacrificial electron donor to photoelectrochemical conditions under no applied bias again highlight that the transient nature of charge carriers and resulting destructive, thermodynamically preferred recombination processes remain a grand challenge to artificial photosynthesis research. Yet, despite the low overall efficiency in photoelectrochemical succinate formation, the proof of principle is established, and there is large scope for improvement.

6.3 Conclusions and perspectives

In conclusion, this chapter describes the use of an enzyme that catalyses C=C bond hydrogenation in two types of artificial photosynthetic systems, the implication being that artificial photosynthesis building upon water oxidation can be extended to other enzymes/catalysts performing reductive transformations having greater value than bulk fuel-formation.

Photocatalytic experiments with fcc_3 adsorbed on RuP-sensitised anatase nanoparticles show efficient solar-to-succinate conversion with an average per-enzyme turnover frequency of 0.4 s^{-1} over 4 h, using MES as a sacrificial electron donor. Further, an integrated artificial photosynthetic system is presented, where fumarate reduction is coupled to water oxidation by a Co-Pi-modified W–$BiVO_4$ photoanode in a photoelectrochemical cell. An estimated TOF for fumarate reduction of 0.01 s^{-1} per molecule of fcc_3 was achieved in this architecture. The one order of magnitude drop in TOF is not unexpected when moving to an integrated system without using an externally applied bias. The performance of the photoanode seems, to a great extent, responsible for the low overall efficiency η_{STS} of 0.03‰. Recently developed nanoporous $BiVO_4$ photoanodes modified with dual-layer (FeOOH/NiOOH) oxygen evolving catalysts that show high stability under low external bias [155] are one possible route to increase both stability and efficiency.

From a mechanistic perspective, an important factor is that enzymes like fcc_3, possessing intense chromophores, may be exploited to elucidate electron transfer kinetics by time-resolved optical spectroscopy. The results presented in this chapter help highlight new directions for artificial photosynthesis, away from the traditional solar-to-fuels paradigm to more advanced solar-to-chemical conversions, also using water as the electron source.

7 Conclusions and perspectives

7.1 Conclusions

The work presented in this thesis spans a wide range, from the mechanism of H_2 formation at the H-cluster, the superbly efficient H_2 evolution catalyst, to the interaction between fuel-forming enzymes with semiconductor surfaces, and, finally, towards an integrated model system for solar-to-chemical conversion. To briefly recapitulate:

Chapter 3 describes how aldehydes of different steric nature and electrophilicity react with [FeFe]-hydrogenases. Using advanced EPR techniques, possible binding modes of formaldehyde at the H-cluster were determined. DFT calculations suggest that under catalytic turnover, HCHO coordinates to Fe_d by forming an Fe–C bond that can only occur before Fe–H bond formation, suggesting adt-N protonation and terminal hydride formation only occur at the super-reduced redox level of the enzyme. In short, chapter 3 highlights the importance of precisely tuning electron and proton transfer steps in multi-electron catalysis.

Chapter 4 dealt with the direct electrochemistry of [NiFeSe]-hydrogenase and CODH on the *n*-type semiconductor materials TiO_2 and CdS. Compared to the behaviour on metallic-like PGE electrodes, catalytic rectification arises on the semiconductor electrodes, favouring the fuel-forming reaction over oxidation. The results demonstrate that semiconducting electrodes can be used to impose directionality on reversible catalysts that operate in the region of the semiconductor flat-band potential. Photoelectrochemistry experiments show that the enzymes are so proficient that the current is controlled more by the charge carrier availability in the semiconductor than by properties of the catalyst.

Chapter 5 reaffirms the principles established in chapter 4 by demonstrating that catalysis is also rectified when CODH is attached to a *p*-type semiconductor: catalytic rectification turns the enzyme into a unidirectional CO oxidiser when immobilised on NiO.

When CODH-modified NiO is sensitised with the visible-light-absorbing dye P1, a photocathode-assembly is produced that selectively reduces CO_2 to CO under visible-light illumination and application of a mildly reducing potential that is lower than the thermodynamic potential in the dark, a further evolutionary step compared to photocatalytic reduction in aqueous suspension.

Chapter 6 describes enzyme (fcc_3) catalysed C=C bond hydrogenation in two types of artificial photosynthetic systems, photocatalytic reduction using fcc_3 immobilised on dye-sensitised TiO_2 nanoparticles, and photoelectrocatalytic hydrogenation coupled to water oxidation in a photoelectrochemical cell. The results represent a significant advance in the development of artificial photosynthesis [593] and open up the door to a new research area: the solar-driven, enzyme catalysed synthesis of organic chemicals of greater value than bulk fuel formation, ideally coupled to water oxidation.

7.2 Perspectives

Throughout this thesis, we learned that fuel-forming enzymes such as [FeFe]-hydrogenase, [NiFeSe]-hydrogenase, and CODH are excellent model catalysts for artificial photosynthesis. Enzymes set the benchmark for both light-driven H_2 formation and CO_2 reduction: on a per-site basis, the activities for photocatalytic fuel-formation portrayed in Table 1:1 in the introduction of this thesis are unmatched by even the most efficient synthetic catalysts [214]. Despite the considerable 'footprint' of the individual protein molecules, enzyme systems also appear remarkably lean, compared with the substantial molar quantities of catalysts used in the purely inorganic world, such as the Rh compounds that are deposited on (oxy)nitride photocatalyst particles developed by Domen and co-workers [327].

Yet, an equally relevant point is that the photo- and photoelectrocatalytic enzyme rates fall far short of those measured in other types of kinetic studies, where TOFs for enzyme-catalysed H_2 and CO evolution exceed 10^3 per second. This observation holds in particular for CO_2 reduction, where the highest photocatalytic TOF obtained so far (on a per catalytic unit basis) stems from using CODH adsorbed on CdS nanorods [381]: the value of only 1.23 s^{-1} (three orders of magnitude slower than the theoretical maximum) emphasises the need for improvement in photodriven CO_2 reduction and to understand why there is such a difference compared to electrocatalytic rates.

Reduction of CO_2 to CO is thermodynamically more demanding than H^+ reduction. Further to the obvious problem of only a small driving force being available at semiconductor nanoparticles including TiO_2 (which provides a marginal overpotential with E_{cb} (anatase) at *ca.* −0.52 V *vs.* SHE at pH 6.0) and CdS (where the driving force is shallow, E_{cb} being approximately −0.35 V more negative than that of TiO_2 [343]), this work has provided some insight. Chapter 4 showed that the best catalysts will ultimately be limited by electron

availability (Figure 4:12). This problem is much more severe when electrons are available only transiently, as in the integrated artificial system depicted in Figure 6:12, because there is unfavourable competition with destructive charge carrier recombination. Mott-Schottky experiments in section 4.2.3 indicate that, although enzyme molecules could be accommodated within the sizeable pores of TiO_2 (and other porous materials; CdS and NiO possess similar pore sizes), they mainly adsorb instead on the outer surface, suggesting that due to the limited carrier mobility and lifetime of the transient conduction band electrons in TiO_2 and, by extension, other systems studied throughout this thesis, destructive charge recombination is likely to take place even *before* interfacial electron injection into the enzyme can occur.

Little is known about the actual charge-transfer *dynamics* between excited semiconductor conductions band electrons and fuel-forming enzymes. An assembly comprising the [FeFe]-hydrogenase *Ca*HydA immobilised on CdS nanorods (Figure 7:1) constitutes one of the few examples where the elementary kinetic processes of light-driven hydrogen evolution have been investigated. Initial findings revealed that H_2 generation rates scale linearly with light intensity, consistent with the system being limited by availability of photogenerated electrons rather than catalysis [371].

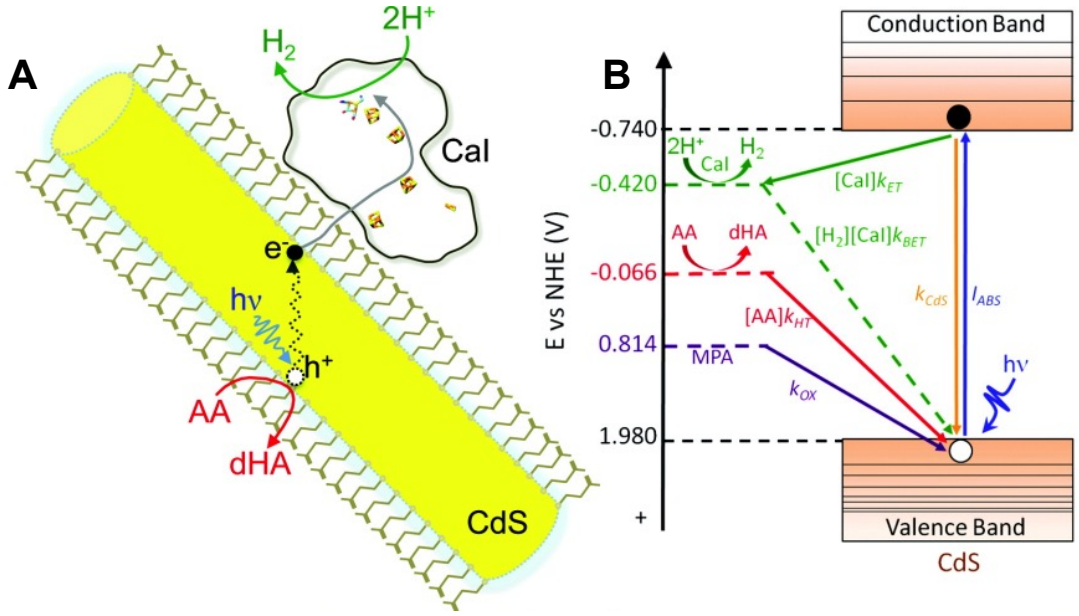


Figure 7:1 (A) Cartoon showing a *Ca*HydA–CdS nanorod assembly for photocatalyic H_2 formation (*Ca*HydA is referred to as CaI in this figure). (B) Energy diagram of *Ca*HydA–CdS and photochemical processes. Reprinted with permission from reference [371]. Copyright 2012 American Chemical Society.

In a follow-up paper, King and Dukovic then investigated the interfacial electron transfer kinetics of the *Ca*HydA–CdS system using transient absorption spectroscopy [310]. The decay of the absorbance of the excited semiconductor conduction band electron should coincide exactly with the arrival of the electron in the enzyme. However, because *Ca*HydA does not have absorptive features with intensities comparable to the strength of the CdS band gap absorption [594], no transient features corresponding to excited electrons in the enzyme are found in transient absorption spectra recorded on *Ca*HydA–CdS [310]. The broad absorption bands of the FeS clusters in the electron transfer relay do not give rise to sharp, distinct changes upon excitation.

Electron injection from CdS to *Ca*HydA (involving the distal [4Fe-4S] cluster as the first acceptor site, well ahead of catalysis itself), occurs with $k_{et} \approx 10^7\ s^{-1}$, similar to the excited state decay rate constant for CdS, but very slow when compared with electron transfer to platinum deposited on CdS ($k_{et} > 10^{11}\ s^{-1}$). The fraction of photoexcited electrons

available for catalysis is therefore much higher in Pt–CdS than in *Ca*HydA–CdS. However, the quantum yields for H_2 formation are much higher in the enzymatic system (20%) than with Pt (1 – 4%), an observation that highlights the proficiency of the enzyme. Given that a limiting factor seems to be slow interfacial electron transfer *to* enzymes, the question is thus raised – how good is an enzyme at trapping electrons once they are transferred?

The properties of the electron transfer relay provide insight. First, electron transfer rates within the enzyme are fast, on the order of $10^8 – 10^9$ s^{-1} through the chain of FeS clusters – a distance of nearly 30 Å. Hence, once transferred to the enzyme, electrons move efficiently, under a small driving force, away from the CdS surface and accumulate to feed the catalytic process at the active site. The large spatial separation distance retards back electron transfer. Second, buried FeS clusters have low reorganisation energies, and counterproductive electron transfer into the semiconductor valence band (driving force ~1.5 eV) probably falls well into the Marcus inverted region, making it kinetically disfavoured. The situation is similar to the initial charge-separation events occurring in PSII in biological photosynthesis [41]. In Pt–CdS assemblies, in contrast, the bare catalytic sites cannot provide such a trap: the catalyst is located at the nanocrystal surface and reorganisation energies are higher. Therefore, recombination with a valence band hole is potentially more likely. Similar restrictions may hold generally for small molecular catalysts [185].

In short, electron injection into the enzyme seems to be the rate-limiting step. However, it is essentially irreversibly because FeS enzymes such as hydrogenase and CODH enzymes are very efficient in charge separation and transport, shuttling electrons away from the interface into the enzyme and placing destructive recombination in the Marcus inverted

regime. The work by Dukovic *et al.* highlights how enzymes employed in artificial photosynthetic systems outperform even the best available synthetic catalysts.

Other spectroscopic techniques have yet to be developed for use with enzymes. Time-resolved infrared measurements could potentially be employed to monitor catalysis under steady-state conditions. The CO and CN^- ligands of the H-cluster, for instance, show very characteristic IR bands. A general advantage of IR spectroscopy over optical techniques is its structure-specificity, *i.e.* signals corresponding to transient species can be correlated with distinct chemical groups. Another potentially useful technique is time resolved X-ray absorption spectroscopy (XAS). Transient XAS may be able to give precise information about bond-length and oxidation state changes during the catalytic cycle, while leading to less radiation damage than crystallography.

7.3 New directions in artificial photosynthesis – where do we go from here and how enzymes may lead the way

Current artificial photosynthesis research is focused on H_2 production or reduction of CO_2, but the low-value products have little immediate opportunity to compete with fossil fuels. One way to break this deadlock is to identify other reactions that could be driven by artificial photosynthesis, especially the synthesis of high-value organic chemicals [595]. Here lie possibilities for enzymes that can perform highly selective redox transformations.

Solar-driven asymmetric reduction of acetophenones, using a commercially available alcohol dehydrogenase [596], establishes this new direction, but relies on multistep NADPH regeneration. Asymmetric, enzymatic C=C bond reduction (ketoisophorone to (*R*)-levodione) by an 'old yellow enzyme' homologue has been coupled with photocatalytic water oxidation by Au:TiO_2 nanoparticles [597]. However, this system also relies on cofactor regeneration. Conversely, an intrinsically simpler system that couples light-driven water oxidation with enzymatic C=C reduction in a photoelectrochemical cell was presented in chapter 6. Building on these few examples, enzymes may lead the way towards new directions in artificial photosynthesis research, away from simple solar-fuels to more advanced solar-chemicals. Synthetic biology provides the platform to engineer enzymes to perform myriad transformations that may ultimately be driven by sunlight.

For the conversion of sunlight to fuels, the reader needs to bear in mind that although some enzymatic artificial photosynthetic systems show remarkable stability under illumination [214], the fuel-forming enzymes used therein are wholly unsuited for long-term, large-scale systems. Nonetheless, the redox enzymes used in this thesis provide valuable insight for developing integrated artificial systems where both rates and efficiency are essential. Enzymes are relatively easy to deposit on materials (albeit not necessarily with

ideal connections) and, as opposed to molecular catalysts, their active site structures remain unperturbed by the support-surface and therefore intact during catalysis. The benchmark per-active site efficiencies for both H_2 evolution and CO_2 reduction achieved by hydrogenases and CODH show that artificial photosynthesis based on highly abundant first-row transition metals has a future. Ultimately, integrated, commercially viable artificial photosynthetic devices need to be based upon robust materials and scalable, earth-abundant, and inexpensive components. Therefore, one of the major scientific challenges in artificial photosynthesis research is 'how can we design synthetic materials to make them work like enzymes?'

8 Experimental section

8.1 General considerations

Unless otherwise noted, all protein film electrochemistry experiments presented in this thesis were carried out inside an anaerobic glove box (Belle Technologies, $O_2 < 3$ ppm, or MBraun, $O_2 < 1$ ppm). Precise gas mixtures (BOC gases) were created using mass flow controllers (Sierra Instruments), and the headspace of the electrochemical cell was, unless otherwise mentioned, constantly purged with the gas mixture throughout the experiments. Pyrolytic graphite edge electrodes of geometric surface area 0.03 cm^2 were constructed in house as described previously [598]. The electrodes were abraded using P400 Tufbak Durite sandpaper and sonicated to remove carbon debris before attachment of enzyme. Unless otherwise noted, the direction of scan in CV experiments was from negative to positive potentials, linear sweep voltammetry experiments were carried out with the potential being swept in cathodic direction.

8.2 The mechanism of [FeFe]-hydrogenases – how aldehydes inhibit H_2 evolution

8.2.1 General considerations

All chemicals were used as purchased without further purification. Phosphate buffer was made up of NaCl, NaH_2PO_4 and Na_2HPO_4 (all analytical reagent grade, Sigma-Aldrich) and titrated to pH 6.0 with HCl or NaOH (both Sigma-Aldrich). For EPR measurements, 10% (v/v) glycerol was added to the phosphate buffer. All aldehydes used in this work were purchased from Sigma-Aldrich: formaldehyde (ACS reagent, 37 wt % in H_2O), acetaldehyde (ACS reagent, ≥99.5%), trifluoroacetaldehyde monohydrate (technical, ~75% in H_2O), butyraldehyde (≥98%), isovaleraldehyde (≥97%), and, for EPR experiments, formaldehyde-d_2 solution (~20 wt % in D_2O, 98 atom % D) and formaldehyde-^{13}C solution (20 wt % in H_2O, 99 atom % ^{13}C).

8.2.2 Enzyme preparation

Electrochemistry experiments were carried out using the [FeFe]-hydrogenase *Ca*HydA from the fermentive, strictly anaerobic bacterium *Clostridium acetobutylicum* [599]. EPR experiments were conducted on *Cr*HydA1 from the green alga *Chlamydomonas reinhardtii* [210,600]. Both enzymes were prepared and provided by Julian Esselborn (laboratory of Professor Thomas Happe, Ruhr-Universität Bochum, Germany). *Ca*HydA was isolated as described previously [413] and showed a hydrogen evolution activity of 130 μmol H_2 min^{-1} mg^{-1}. *Cr*HydA1 was isolated as apo-protein lacking the $[2Fe]_H$ subcluster *via* strep-tactin affinity chromatography from heterologous expression in *E. coli* as described previously [413,601,602]. The protein was maturated *in vitro* with the complex $[Fe_2(\mu\text{-}SCH_2)_2NH(CN)_2(CO)_4]^{2-}$ and subsequently purified using a NAP™ 5 gel filtration

column (GE Healthcare) and concentrated using Amicon Ultra centrifugal 10 K filters (Millipore) as shown before [407]. The total protein concentration (2.4 mM) was estimated spectroscopically using the method of Bradford [603], with bovine serum albumin (Sigma-Aldrich) as the protein standard; protein purity was assessed by SDS-PAGE. The H_2 evolution activity of *Cr*HydA1 was determined to be 1.37 mmol H_2 min^{-1} mg^{-1} in a well established assay with methyl viologen as electron mediator and detection of H_2 via GC [604]. Isolation, handling and storage of both enzymes were conducted under strictly anaerobic conditions. Protein samples were stored at −80 °C before use in protein film electrochemistry experiments or preparation for EPR.

8.2.3 Protein film electrochemistry

In PFE experiments, aliquots of enzyme samples (~1.5 μL of 0.1 g L^{-1} *Ca*HydA) were drop cast onto the PGE electrode and left for one minute until partially dry. The electrode was then connected to an electrode rotator (EcoChemie) and fitted into a gastight electrochemical cell similar to the one shown in Figure 2:1. The cell was covered with electrical tape to prevent light-induced deactivation of the enzyme ('self-cannibalisation' [605,606]) and the temperature was controlled *via* a water jacket surrounding the main cell compartment. Unless otherwise noted, all experiments were carried out at 20 °C. A platinum wire, placed in the main compartment, was used as counter electrode. The saturated calomel reference electrode (SCE) was placed in a side-arm containing 100 mM NaCl electrolyte that was connected to the main cell *via* a Luggin capillary. All potentials are quoted *vs.* the standard hydrogen electrode (SHE) using the correction $E_{SHE} = E_{SCE} + 242$ mV at 20 °C [469]. The electrolyte was 50 mM phosphate buffer containing 100 mM NaCl in purified water (Millipore, 18 MΩ cm). Electrochemical measurements were made with an Autolab potentiostat (PGSTAT30) controlled by Nova software (EcoChemie). To ensure non-rate-limiting

substrate supply, rapid removal of product, and fast gas-solution equilibration, the electrode was rotated at a constant high rate (> 2500 rpm) in all experiments. Chronoamperometry experiments were normalised for film loss according to eq. (2:30). In aldehyde inhibition experiments, 1 mL of the respective aldehyde inhibitor solution was injected into the electrochemical cell containing 4 mL buffer solution. The inhibition kinetics, *i.e.* the current decay over time following injection of the inhibitor, were determined over 300 s. Generally, inhibition studies could not be carried out in the 'intermediate' potential region close to the equilibrium potential for H^+/H_2 interconversion (between −0.4 V and −0.15 V) due to the relatively low current densities in this region, which are further lowered by the exponential 'film loss' processes that underlie every experiment. Rate constants for inhibition k_{obs} and corresponding errors were obtained by 'least square fits' of current *vs*. time traces recorded at different potentials. Fits were attained using OriginPro 9 software. Average values represent the mean value of three different experiments.

8.2.4 Electron paramagnetic resonance

All EPR samples were prepared in an anaerobic glove box (O_2 < 3 ppm) in 50 mM phosphate buffer containing 0.1 M NaCl and 10% (v/v) glycerol, adjusted to pH 6.0 at 20 °C. All samples were prepared in 3.0 mm high-precision EPR tubes (Wilmad 706-PQ-9.50) to ensure accurate spin quantification. EPR-samples were prepared by reducing approximately 70 μL of as-isolated enzyme using 100% H_2 at 20 °C under zero-current flow until the potential of the solution equilibrated, typically after 3.5 h. Formaldehyde (DCDO or $H^{13}CHO$) was then injected to give a final concentration of free, non-hydrated aldehyde (the equilibrium constant for hydration $K_{eq} \approx 2000$ at 25 °C [534,535]) equal to the concentration of *Cr*HydA1. Aliquots (*ca*. 70 – 90 μL) of the resulting solution were transferred as quickly as possible to Wilmad EPR tubes and frozen in liquid nitrogen, *i.e.* within 5 min after injection, a timescale

after which almost all enzymatic activity was noted to be recovered in PFE experiments (Figure 3:1A). Spin quantification was carried out using copper perchlorate samples (50 μM $CuSO_4$ in 2 M $NaClO_4$ (aq) adjusted to pH 1.22 with HCl) measured under non-saturating conditions [524].

Continuous wave EPR experiments were performed using an X-band (*ca.* 9.4 GHz) Bruker EMX^{micro} Premium spectrometer (Bruker BioSpin GmbH, Germany) with an X-band SHQE-W cylindrical TE_{011}-mode resonator (Bruker). Background spectra of the empty resonator were recorded under identical conditions and subtracted from the EPR spectrum of the enzyme sample. Pulse measurements were carried out on an X-/W-band Bruker Elexsys 680 spectrometer and a Q-band Bruker Elexsys 580 spectrometer.

Spectroscopic simulations were performed by Dr. William Myers (Centre for Advanced Electron Spin Resonance, Oxford) in MATLAB 2013a with the EasySpin 4.5 toolbox [607]. Simulation of the FID-detected EPR signal employed matrix diagonalisation with the *pepper* function using a *g*-strain model for linewidth, as is characteristic for simulations of FeS cluster EPR signals. The EPR fit was then converted to an equivalent linewidth defined by hyperfine broadening, 'H-Strain', and this set of EPR simulation parameter values acted as a basis for Mims ENDOR simulations making use of the *saffron* function with explicit use of the experimental parameter values.

8.2.5 Density functional theory

All DFT calculations presented in chapter 4 were performed by Professor John McGrady (Inorganic Chemistry Laboratory, University of Oxford), using the Gaussian09 suite. The basic structure of the H-cluster was extracted from the reported crystal structure of *Desulfovibrio desulfuricans* (PDB code 1HFE [387]) following the procedure set out by Bruschi *et al.* [412]. The active site was extracted from the protein matrix, and the oxygen

atom originally assigned in the bridging position was replaced with a CO unit. The H-cluster is attached to the protein *via* four cysteine units (cys179, cys234, cys378 and cys382); all four were modelled as CH_3S units, with the carbon atoms frozen at the positions found in the matrix. All other structural parameters were freely optimised. Given the uncertainty in the position of the bridging CO ligand, optimisations were initialised from a number of starting geometries where the CO is bridging, semi-bridging, or terminal. In all cases the CO reverts to the bridging position in the optimised structure. At the $H_{ox\text{-}2}$ oxidation level the total charge on the cluster is −5, decreasing to −4 when the system is protonated, as in the $[tH\text{-}dtma]^{4-}$ structure reported by Bruschi *et al.* [412]. The stabilising influence of the wider protein matrix was introduced through a polarised continuum model with dielectric constant $\varepsilon = 4.0$. The majority of the calculations were performed with the BP86 functional [608,609] along with a triple-ζ quality basis set (Ahlrich's TZVP [610]) on all atoms. The dependence of the spin density distribution on methodology was also explored, using the B3LYP [611] functional. These latter calculations were done as single points using the geometries optimised at the BP86/TZVP level. The exchange coupling within the $[4Fe\text{-}4S]_H$ cluster (and also, in principle, within the $[2Fe]_H$ subdomain) was treated using the broken-symmetry approach, wherein opposing spin moments are imposed on the initial (guess) spin density, such that the system converges to a predominantly antiferromagnetic state. In all cases here, the antiferromagnetic species has an $M_S = ½$ ground state, which can be formulated to a first approximation in terms of a reduced $[4Fe\text{-}4S]^{1+}$ cluster. Appropriately spin-polarised initial guesses were constructed using the 'guess=fragment' keyword available in Gaussian 09 [612]. Calculations were initialised using a wide range of initial spin densities corresponding to ferro/antiferromagnetic coupling within the $[4Fe\text{-}4S]_H$ cubane and also to ferro/antiferromagnetic coupling of the spin densities on the $[2Fe]_H$ unit. A range of initial guesses was constructed in which the extra electron starts (a) on the $[4Fe\text{-}4S]_H$ unit and (b) on

the $[2Fe]_H$ subdomain. The converged wavefunction for the one-electron oxidised case (where the oxidation states are unambiguous) was also used as an initial guess. In no case did the initial guess have a significant impact on the converged results; the self-consistent density is essentially identical. Moreover, no evidence for antiferromagnetic coupling (*i.e*. opposing spin densities) on the $[2Fe]_H$ subsite in the converged self-consistent solution was found: Mulliken spin densities on Fe_d and Fe_p are always small (< 0.25 electrons) and of the same sign.

8.3 The direct electrochemistry of fuel-forming enzymes on semiconducting electrodes

8.3.1 General considerations

All chemicals were of the highest available quality and used as received without any further purification. Cadmium acetate, thiourea and ammonia solution (28 – 30%) for the synthesis of CdS thin film electrodes were procured from Sigma-Aldrich. For the preparation of TiO_2 thin film electrodes, nitric acid was purchased from Fisher Scientific, and the TiO_2 particles were Degussa P25 (80% anatase, 20% rutile, average diameter 21 nm). Indium tin oxide coated glass slides (1.1 mm thick, 8 – 12 Ω), used as substrates for the semiconductor thin films, were purchased from SPI Supplies, USA. 2-(*N*-morpholino)ethanesulfonic acid (MES) was obtained from Melford, and aqueous buffer solutions containing MES were titrated to the correct pH using NaOH (Sigma-Aldrich). KOCN was obtained from Sigma-Aldrich. In experiments under gas flow, the electrochemical cell was constantly purged with the respective gas mixture throughout the experiments.

8.3.2 Semiconductor electrodes

8.3.2.1 Synthesis of semiconductor thin films

CdS: ITO slides of approximate dimensions 1 × 2 cm^2 were cleaned by sonication for 15 min each in ethanol, followed by acetone, and deionised H_2O. The cleaned and degreased slides were activated in a solution containing 1.9 mg $KMnO_4$ (Sigma-Aldrich ACS reagent, ≥99%), 30 μL butanol (Alfa Aesar, 99%) and 20 mL water for 30 min at 93 °C. These activated substrates were washed thoroughly with H_2O and dried. To grow CdS thin films, 0.66 g cadmium acetate was dissolved in 2.5 mL deionised H_2O. Subsequently, ammonia solution

was added dropwise until a clear solution was obtained. An aqueous solution (2.5 mL) containing 0.19 g thiourea was then added to the cadmium acetate containing reaction mixture. The activated ITO substrate was placed in a vial containing the reaction mixture, ensuring that a portion of the substrate remained out of solution, and this mixture was then heated at *ca.* 90 °C for 30 min. Upon heating, thiourea releases sulphide ions which then form CdS by metathesis with the hydrolysed Cd(II) species. The overall reaction of CdS formation from cadmium acetate and thiourea is described by the following equation [613]:

$$\begin{aligned} Cd(CH_3COO)_2\,(aq) + (NH_2)_2CS\,(aq) + 2OH^- \rightarrow \\ CdS + H_2CN_2 + 2H_2O + 2CH_3COO^- \end{aligned} \qquad (8{:}1)$$

Following CdS deposition, the thin film was washed thoroughly with deionised H_2O to remove unadsorbed CdS particles, and dried at room temperature. The appearance of diffraction peaks [(002), (102), (110), (112) and (201)] in the XRD pattern indicates predominant formation of the hexagonal phase of CdS (Figure 8:1 lower). However, few peaks corresponding to $Cd(OH)_2$ were also observed.

TiO_2: A suspension was prepared by dispersing 50 mg TiO_2 (P25) in 70 µL of 0.1 M HNO_3, followed by sonication for 30 min. The ITO substrate was cleaned by sonication for 15 min each in acetone, ethanol, and water. TiO_2 thin films were then deposited onto a cleaned conducting glass substrate by the 'Doctor blading' technique [564]. An area of approximately 10 mm × 10 mm was covered, with the TiO_2 film thickness being controlled by a layer of Scotch tape. The TiO_2 films were then subjected to heat treatment at 450 °C for 30 min (ramp rate 5 °C min^{-1}). The TiO_2 XRD pattern, recorded after calcination, shows the presence of both rutile and anatase phases (Figure 8:1 upper).

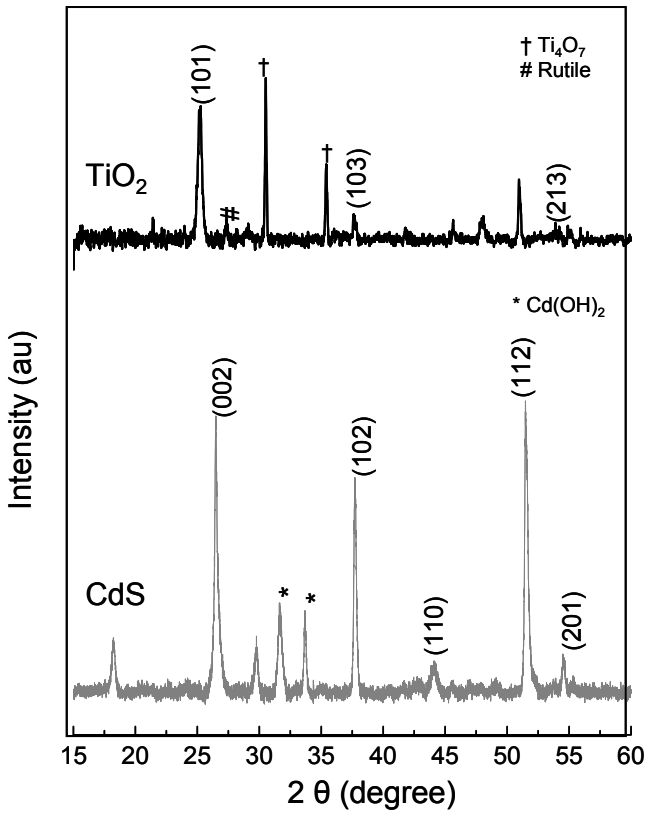


Figure 8:1 X-ray diffraction patterns of TiO_2 (top) and CdS (bottom) deposited on ITO substrates.

8.3.2.2 Electrode fabrication

The semiconductor films deposited on ITO were converted into electrodes by making ohmic contact with copper wire using silver paint (Agar Scientific G3691) at an uncoated area of the transparent conducting oxide [464]. The copper wire was insulated with a glass tube, which was connected to the electrode assembly by epoxy resin (Loctite Hysol 9462). The contact edges of the films were then also covered by Hysol epoxy, leaving only parts of the thin semiconductor films exposed. Typical geometric surface areas were 0.1 – 0.4 cm^2.

8.3.3 Enzyme preparation

Isolation, purification and activity measurements of CODH I from *Carboxydothermus hydrogenoformans* were carried out by Dr. Mehmet Can (laboratory of Professor Stephen Ragsdale, University of Michigan, USA) according to previously described procedures [462]. The activity for CO oxidation was 1.30 mmol min^{-1} mg^{-1} at 20 °C. The [NiFeSe]-hydrogenase

sample from *Desulfomicrobium baculatum*, provided by Professor Juan Fontecilla-Camps (CEA/CNRS Grenoble, France), was obtained according to previously published methods [215,614]. The specific H_2 oxidation activity of [NiFeSe]-hydrogenase was determined as 1.70 mmol min^{-1} mg^{-1}, using conventional room temperature assays after a few minutes under H_2 to fully activate the enzyme.

8.3.4 Protein film electrochemistry

To study the electrocatalytic behaviour of the enzymes on CdS, TiO_2 and PGE, aliquots of enzyme samples (either CODH or H_2ase, < 100 pmol) were drop cast onto the electrode and left for a few minutes until partially dry. The electrode was then placed in an electrochemical cell and connected as the working electrode in conjunction with an Ag/AgCl (1 M KCl) reference electrode and a Pt wire as counter. All potentials are quoted *vs*. the standard hydrogen electrode (SHE) using the conversion $E_{SHE} = E_{Ag/AgCl} + 234$ mV at 20 °C. The electrolyte was 0.2 M MES at pH 6.0, and all solutions were prepared using purified water (Millipore, 18 MΩ cm). Electrochemical measurements were made with an Autolab potentiostat (PGSTAT30) controlled by Nova software (EcoChemie). Impedance measurements were conducted using an Ivium Technologies COMPACTSTAT.e portable electrochemical interface & impedance analyser, controlled by IviumSoft software. Cyclic voltammograms were recorded prior to and after impedance and chronoamperometry experiments with enzyme-modified electrodes, in order to ensure that the catalytic activity of the enzyme had remained steady throughout the measurements.

A Kodak light source (Kodak Carousel S-AV 1010 projector) fitted with a 250 W tungsten-halogen bulb and a 420 nm long-pass filter (UQG Optics) was used in the photoelectrochemistry experiments. At the position of the electrochemical cell, the light

intensity was 16 mW cm^{-2}, measured using a Melles Griot Broadband Power/Energy Meter (13PEM001). All electrochemistry experiments were repeated at least twice.

8.4 Selective visible-light-driven CO_2 reduction on a *p*-type dye-sensitised NiO photocathode

8.4.1 General considerations

All chemicals were of the highest available quality and used as received without any further purification. All PFE experiments were carried out in 0.2 M MES buffer (pH 6.0 at 20 °C), which was prepared by dissolving 2-(*N*-morpholino)ethanesulfonic acid (Melford) in purified H_2O (Milli-Q, 18 MΩ cm). The pH was adjusted to the correct value using NaOH (Sigma-Aldrich). In experiments under gas flow, the electrochemical cell was constantly purged with the respective gas mixture throughout the experiments.

8.4.2 Fabrication of NiO electrodes

8.4.2.1 Synthesis of NiO particles

Nanocrystalline NiO particles were synthesised according to a previously published procedure [573]. Solutions of 4 mM oxalic acid (Sigma-Aldrich, 99+%), 20 mM hexamethylenetetramine (Sigma-Aldrich, ACS reagent, ≥99%) and 20 mM $Ni(NO_3)_2$ (BDH Laboratory Supplies) were mixed and refluxed at 100 °C for 5 hours. The resulting green precipitate was then filtered and washed with ethanol and water before being dried under vacuum overnight and heated to 400 °C for 2 hours. The powder XRD pattern obtained after heating in air is depicted in Figure 8:2.

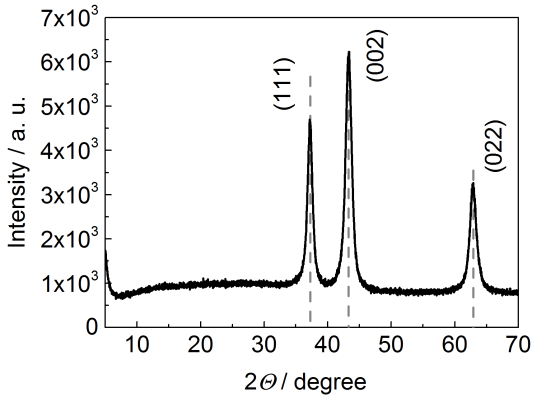


Figure 8:2 X-ray diffraction pattern of synthesised NiO powder.

8.4.2.2 Fabrication of electrodes from NiO particles

First, ITO slides (see section 8.3.2) were degreased and activated as described in section 8.3.2.1-'CdS'. In parallel, NiO powder (2.0 g) was suspended in a mixture of 10 μL acetylacetone (Sigma-Aldrich, ReagentPlus, ≥99%), 25 μL Triton X100 surfactant (Fisher Scientific), and 12 mL H_2O. The suspension was sonicated for 30 min and then centrifuged for 20 s at 4000 rpm to create an aggregate-free NiO suspension. This suspension was applied to the activated ITO sheets by the Doctor's blade technique [564], with the electrode film thickness being controlled by a layer of Scotch tape (compare section 8.3.2.1-'TiO_2'). The resulting films were then calcined at 550 °C for 10 min (an SEM image recorded after calcination is depicted in Figure 5:2). The synthesised NiO films were converted into electrodes according to the procedure described in section 8.3.2.2. Typical geometric surface areas were 0.1 – 0.4 cm^2. Surface areas were determined with the freely available program 'Image J' by counting the number of pixels on a digital picture of the electrode, which included a ruler to set the scale [464].

8.4.2.3 Synthesis of P1 and sensitisation of NiO electrodes

4-[Bis(4-{5-[2,2-dicyanovinyl]-thiophene-2-yl}phenyl)amino]benzoic acid (P1) was synthesised by Samuel Hall under my supervision as previously described by Qin *et al.* [383]

and characterised accordingly. ^{1}H NMR and ^{13}C NMR spectra of P1 are shown in Figure 8:3 and Figure 8:4, respectively. NiO electrodes were sensitised with P1 by soaking the electrodes in a 300 μM solution of P1 in ethanol overnight.

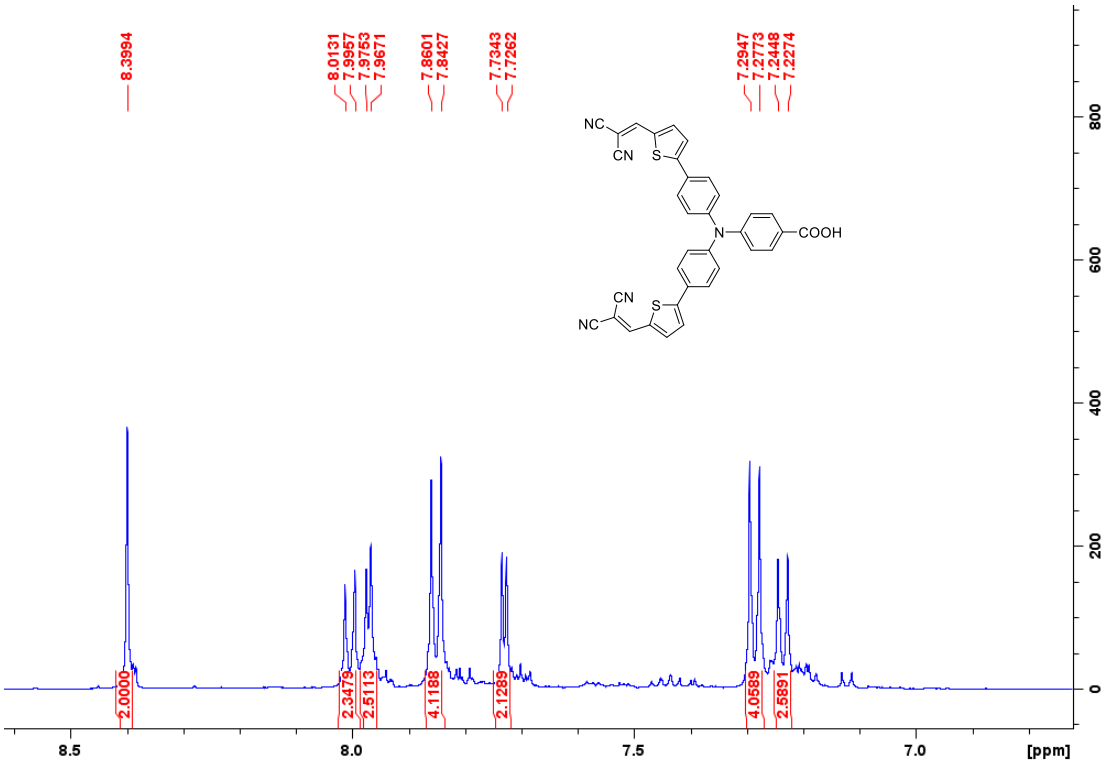


Figure 8:3 ^{1}H NMR spectrum of P1. δ_H (500 MHz, acetone-d_6) 7.23 (2H, d, J 8.72), 7.28 (4H, d, J 8.71), 7.73 (2H, d, J 4.10), 7.85 (4H, d, J 8.69), 7.97 (2H, d, J 4.10), 8.00 (2H, d, 8.70), 8.40 (2H, s).

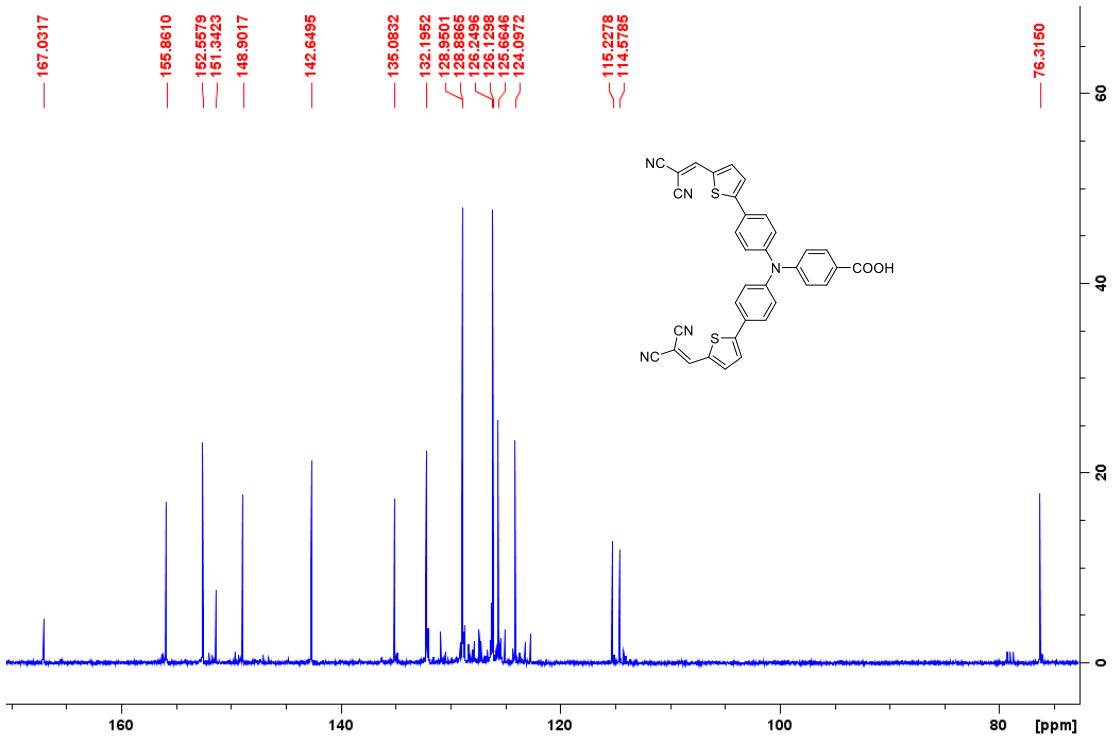


Figure 8:4 ^{13}C NMR spectrum of P1. δ_C (125 MHz, acetone-d_6) 76.3, 114.6, 115.2, 124.1, 125.7, 126.1, 126.2, 128.9, 129.0, 132.2, 135.1, 142.6, 148.9, 151.3, 152.6, 155.9, 167.0.

8.4.3 Enzyme preparation

Preparation and activity parameters of CODH I from *Carboxydothermus hydrogenoformans* are described in section 8.3.3.

8.4.4 Protein film electrochemistry

To study the electrochemistry of CODH on PGE, aliquots of enzyme (< 100 pmol) were drop cast onto the electrode and left for a few minutes until partially dry. In the case of NiO and NiO–P1 electrodes, in a typical experiment, 4 μL of 0.12 mM enzyme was applied to a NiO electrode of 0.4 cm^2 geometric surface area. The total coverage is therefore 1.2 nmol cm^{-2}. The electrodes prepared according to the above mentioned protocols were used as working electrodes in a single-compartment electrochemical cell, with a Pt (wire) counter electrode and a Ag/AgCl 3.5 M KCL reference electrode. All potentials in chapter 5 are quoted *vs.* the standard hydrogen electrode (SHE) using the conversion $E_{SHE} = E_{Ag/AgCl} + 205$ mV at 25 °C.

The electrolyte was 0.2 M MES at pH 6.0, and all solutions were prepared using purified water (Millipore, 18 MΩ cm). Electrochemical measurements were made with an Autolab potentiostat (PGSTAT30) controlled by Nova software (EcoChemie). The Kodak light source and the 420 nm long-pass filter described in section 8.3.4 were used in the photoelectrochemistry experiments. At the position of the electrochemical cell, the light intensity was 45 mW cm^{-2}. An optical chopper, built in-house, was used to measure transient photocurrents.

Inhibition experiments to establish the activity of CODH for CO_2 and CO reduction using the selective inhibitors KOCN (Sigma-Aldrich) and KCN (Fisher-Scientific) were conducted as follows: 1.0 mL of a stock solution of the respective inhibitor (dissolved in 0.2 M MES buffer, pH 6.0, and pre-saturated with the gas-mixture present in the electrochemical cell) was injected into the electrochemical cell containing 9.0 mL buffer.

8.5 A multi-haem flavoenzyme as a solar conversion catalyst

8.5.1 General considerations

All chemicals were of the highest available quality and were used as received without further purification.

8.5.1.1 Buffer solutions

All electrochemistry experiments were carried in one of the following buffer solutions, which were prepared using purified H_2O (Millipore, 18 MΩ cm):

- 0.2 M MES buffer (pH 6.0 at 20 °C), which was prepared by dissolving MES (Melford > 99.5%) in purified H_2O;
- 'Mixed buffer system' (pH 7.0 at 20 °C) containing 50 mM TAPS (3-[[tris(hydroxymethyl)methyl]amino]propanesulfonic acid, Melford > 99.5%), HEPES (*N*-(2-hydroxy-ethyl)piperazine-*N*′-2-ethanesulfonic acid, Melford > 99.5%), MES, PIPES (1,4-piperazinediethanesulfonic acid, Sigma-Aldrich > 99%), and an additional supporting electrolyte of 0.1 M NaCl (Fisher Scientific, 99.9+%);
- 0.1 M Potassium phosphate buffer, 'KPi', (pH 7.0 at 25 °C), made up of K_2HPO_4 and KH_2PO_4 (both Fisher Scientific, 99+%).

Sodium fumarate dibasic (Sigma-Aldrich, ≥99%) was dissolved in or injected into the buffer at various concentrations, depending on the experiment. For each buffer solution, the pH was adjusted to the desired value at the working temperature for the experiment in question using NaOH or HCl (Sigma-Aldrich).

8.5.1.2 RuP synthesis

$[Ru(bpy)_2(4,4'\text{-}(PO3H_2)_2bpy)]Br_2$ (RuP), prepared as reported previously [615], was kindly provided by Dr. Thomas Woolerton.

8.5.2 Protein purification

Samples of flavocytochrome c_3 from *Shewanella frigidimarina* NCIMB400 were provided by Professors Graeme A. Reid (Institute of Cell and Molecular Biology, University of Edinburgh) and Stephen K. Chapman (Department of Chemistry, University of Edinburgh) and purified as described previously [616]. The total protein concentration (4.13 mg mL^{-1}) was estimated spectroscopically using the method of Bradford [603], with bovine serum albumin (Sigma-Aldrich) as the protein standard.

8.5.3 Preparation of thin film electrodes

8.5.3.1 Cadmium sulphide and titanium dioxide

Thin films of CdS and TiO_2 on ITO slides (SPI Supplies USA, 1.1 mm thick, 8 – 12 Ω) were synthesised and characterised as described in section 8.3.2.1.

8.5.3.2 meso-Indium tin oxide

meso-ITO was prepared according to the procedure reported by Kato *et al.* [352] using indium tin oxide nanopowder (Sigma-Aldrich): 1×2 cm^2 ITO slides were sonicated for 20 min each in *iso*-propanol and then acetone. Subsequently, the cleaned and degreased sheets were dried in air. A dispersion of ITO was created by sonicating a mixture of ITO nanopowder (20 wt %) in 5 M acetic acid solution in ethanol. The mixture was applied onto the ITO sheets using the Doctor's blade technique [564], following a 30 min calcination step at 450 °C (ramp rate 4 °C min^{-1}).

8.5.3.3 Tungsten-doped bismuth vanadate

W–$BiVO_4$ electrodes were deposited on FTO slides (Sigma-Aldrich, 2.2 mm thickness, ~7 Ω/sq, 80% transmittance) according to a method described by Bard and co-workers [85]. A premixed solution of $Bi(NO_3)_3 \cdot 5H_2O$, VCl_3 (both Sigma-Aldrich), and $(NH_4)_{10}(H_2W_{12}O_{42}) \cdot 4H_2O$ (Alfa Aesar) in ethylene glycol (Sigma-Aldrich) with a molar ratio of Bi:V:W = 4.5:5:0.5 at 10 mM concentration (total of the three elements) was pipetted onto the FTO substrates followed by annealing at 500 °C for 3 h (ramp rate 1 °C min^{-1}).

8.5.3.4 Electrode fabrication

Semiconductor and *meso*-ITO films were converted into electrodes using the procedure described in section 8.3.2.2. Geometric surface areas were again determined using the program 'Image J' [464], geometric areas were 0.1 – 0.4 cm^2.

8.5.4 Protein film electrochemistry experiments

To study the (photo-)electrochemistry of fcc_3 on PGE, TiO_2, CdS, and *meso*-ITO electrodes, aliquots of enzyme (< 1 nmol) were pipetted onto the respective electrode and left for a few minutes until partially dry. Electrochemistry experiments were carried out as described in section 8.4.4, using an Ag/AgCl 3.5 M KCl reference electrode the conversion factor (to SHE) of which is $E_{SHE} = E_{Ag/AgCl} + 205$ mV at 25 °C. In experiments with PGE electrodes, the working electrode was controlled by an electrode rotator (EcoChemie or EG&G) and rotated at a constant speed. All electrochemistry experiments were repeated at least twice.

8.5.5 Photocatalysis experiments

8.5.5.1 Adsorption of fcc_3 on TiO_2 nanoparticles

5 mg TiO_2 nanoparticles (anatase, average particle diameter 15 nm) were dispersed at room temperature in 5 mL MES buffer (0.2 M, pH 6.0). Following sonication for 20 min,

1.95 nmol fcc_3 (as a 30 μL stock solution) was added to the suspension and the mixture was stirred for 20 min. After centrifugation (8,000 rpm for 12 min), a UV/Vis spectrum of the supernatant was recorded (Figure 6:5B).

The unit cell dimensions of fcc_3 are $a = 77.7$ Å, $b = 86.7$ Å, $c = 211.2$ Å [584], resulting in a maximum 'footprint' per enzyme molecule of $b \times c = 1.83\times10^{-16}$ m^2. With the surface area of anatase nanoparticles being 50 m^2 g^{-1}, the total surface area of 5 mg TiO_2 particles is 0.25 m^2. The upper limit for monolayer coverage of fcc_3 = 0.25 m^2 / 1.83×10^{-16} m^2 $molecule^{-1}$ = 1.37×10^{15} molecules, which equal 2.27 nmol. Hence, 1.95 nmol fcc_3 cover up to 86% of the TiO_2 surface.

8.5.5.2 Adsorption of RuP on TiO_2 nanoparticles

Verification of RuP adsorption on TiO_2 was carried out previously, similarly to adsorption of fcc_3. It was established that 213 nmol RuP is required to completely cover the surface of 5 mg nanoparticle [551]. Thus, 56 nmol is expected to cover approximately 25% of the TiO_2 surface.

8.5.5.3 Photocatalysis by RuP–TiO_2–fcc_3

Photocatalytic fumarate conversion was carried out as follows. In an anaerobic glove box, 5 mg TiO_2 nanoparticles were suspended in 5 mL of 0.2 M MES buffer solution (pH 6.0, D_2O, containing 6.0 mM fumarate) by sonication in a pyrex pressure vessel at room temperature for 20 min. Then, 1.95 nmol of fcc_3 (as a solution of 30 μL) was added to the nanoparticles and the suspension was stirred for 20 min to allow adsorption. Next, attachment of RuP was carried out by adding 100 μL of 0.56 mM RuP (56 nmol) in 0.2 M MES (pH 6.0, D_2O) to the suspension, and stirring the mixture for 20 min. The pressure vessel was tightly sealed with a rubber septum, removed from the glove box, and clamped in a water bath connected to a thermostated water circulator with the temperature maintained at 5 ºC, and

exposed to visible light ($\lambda > 420$ nm) provided by a Kodak Carousel S-AV 1010 projector fitted with a 250 W tungsten-halogen bulb and a 420 nm long-pass filter ($P_{in} = 45$ mW cm^{-2} at the position of the reaction vessel, see section 8.3.4). After illumination, the reaction mixture was centrifuged for 12 min at 8,000 rpm and analysed by ^{1}H NMR and UV/vis spectroscopy. NMR spectra of typical experiments, recorded after 4 h and 8 h of illumination, are depicted in Figure 6:6 (comparison) and Figure 8:5 and Figure 8:6 (original spectra). In Figure 6:6, the olefinic fumarate protons are highlighted by black triangles and give rise to a singlet at 6.44 ppm. The aliphatic succinate protons (indicated by black squares) resonate at 2.33 ppm. This peak increased after addition of further succinate, providing additional evidence for the nature of the product (see Figure 6:6 inlay, original NMR spectrum depicted in Figure 8:7). The product conversion can be calculated from the ratio of the integrals of the fumarate and succinate peaks (see Figure 6:6). It is important to note that, as the experiments were carried out in D_2O, each succinate molecule that is produced contains two aliphatic protons (from the original fumarate molecule) and two aliphatic deuterons (from D_2O) in the central unit, *i.e.* CH(D)-CH(D).

The fumarate/succinate ratio of 0.6 in Figure 6:6A corresponds to a succinate concentration of 2.25 mM, indicating 37.5% conversion of the initial fumarate concentration of 6 mM after 4 h of illumination. With $n_{fcc3} = 1.95$ nmol, this gives a TON of 5800 and an average TOF of 0.4 s^{-1} per enzyme molecule, assuming all enzyme contributed to catalytic turnover. After 8 h of illumination (Figure 6:6B), the fumarate/succinate ratio was 0.62, corresponding to a slightly higher TON of 5900 and an average TOF of 0.2 s^{-1}.

Figure 6:7 depicts UV/vis spectra recorded after 4 h and 8 h of illumination and shows the photodegradation of the enzyme under turnover conditions. The different peaks in Figure

6:7A,B indicate multiple decomposition pathways. Photographs of the solutions corresponding to the UV/vis spectra depicted in Figure 6:7 are shown in Figure 6:8.

8.5.5.4 Photochemistry experiment – RuP–fcc$_3$ in solution

This type of experiment was carried out analogously to the RuP–TiO_2–fcc_3 experiment, but without TiO_2 being added to the reaction mixture. 1.95 nmol fcc_3 and 56 nmol RuP were dissolved in 5 mL 0.2 M MES buffer (pH 6.0, D_2O) containing 6.0 mM fumarate. The pressure vessel was sealed and illuminated at 5 °C as described above. No fumarate was formed after 4 h of illumination (Figure 6:6C and Figure 8:8). UV/vis spectra and a photograph of the reaction mixture taken after the experiment are depicted in Figure 6:7C and Figure 6:8C.

8.5.5.5 Photochemistry experiment – RuP–ZrO_2–fcc$_3$

This experiment was carried out analogously to the RuP–TiO_2–fcc_3 experiment, except that ZrO_2 was used instead of TiO_2. 5 mg ZrO_2 nanopowder (Sigma-Aldrich) were dispersed in 5 mL 0.2 M MES buffer (pH 6.0, D_2O) containing 6.0 mM fumarate, and sonicated for 20 min. 1.95 nmol fcc_3 and 56 nmol RuP were added to the reaction mixture and stirred for 20 min. The reaction vessel was sealed and illuminated at 5 °C as described above. No fumarate was formed after 4 h of illumination (Figure 6:6D and Figure 8:9). UV/vis spectra and a photograph of the supernatant taken after post-experimental centrifugation are depicted in Figure 6:7D and Figure 6:8D. A photograph of the precipitate taken after centrifugation, *i.e.* fcc_3 adsorbed on ZrO_2 nanopowder, is shown in Figure 6:9.

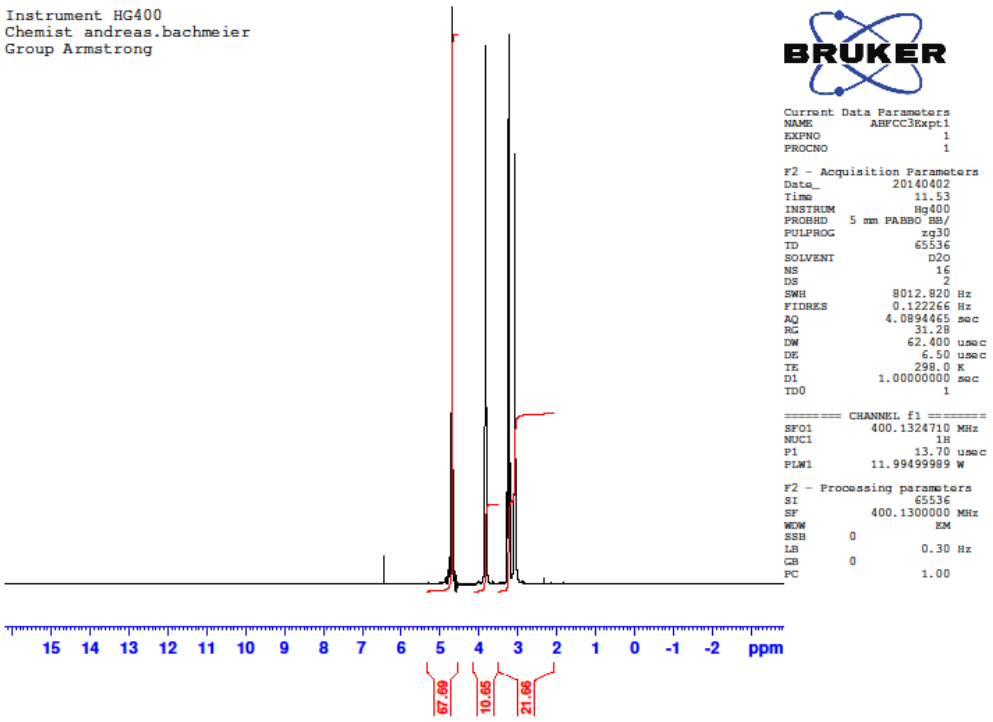


Figure 8:5 ^{1}H NMR spectrum recorded after 4 h of illumination of RuP–TiO_2–fcc_3 in the presence of 6 mM fumarate.

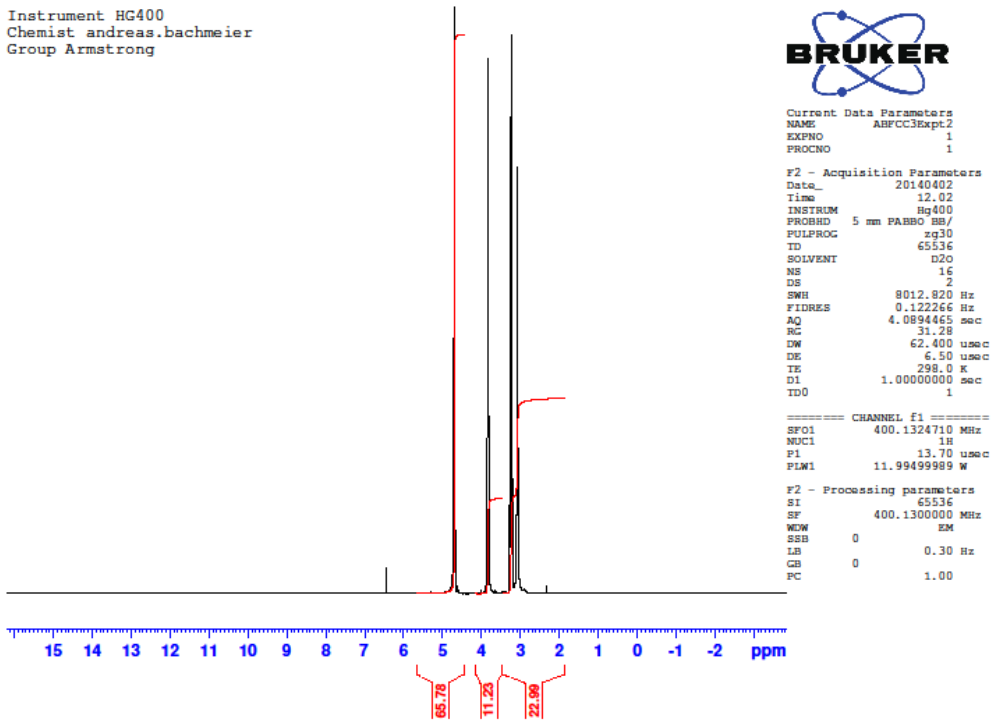


Figure 8:6 ^{1}H NMR spectrum recorded after 8 h of illumination of RuP–TiO_2–fcc_3 in the presence of 6 mM fumarate.

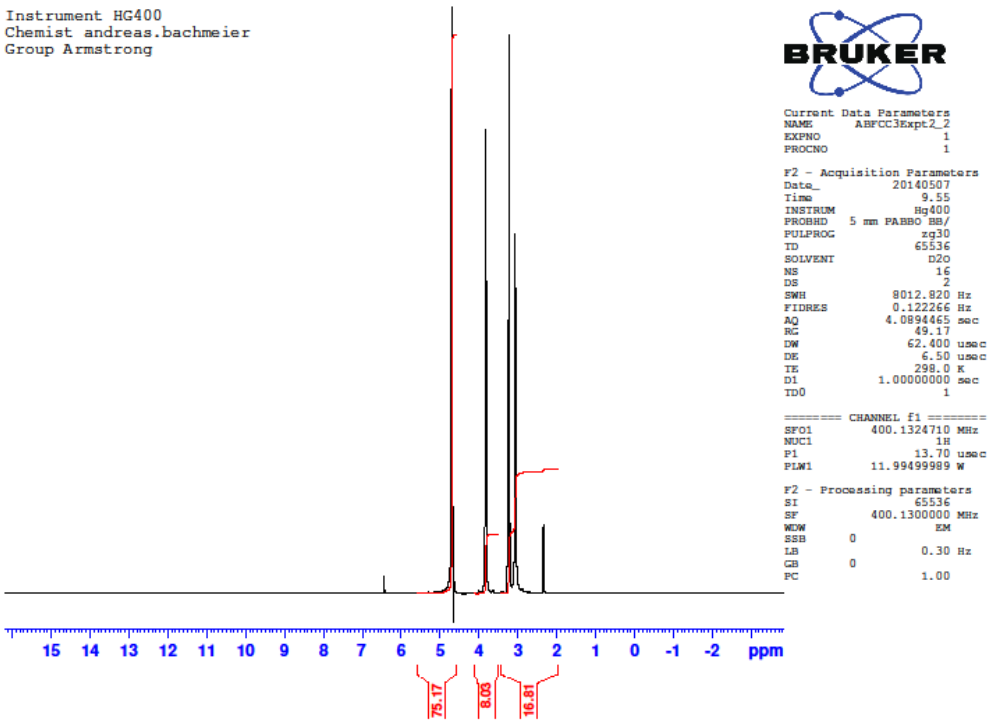


Figure 8:7 ^{1}H NMR spectrum recorded after 8 h of illumination of RuP–TiO_2–fcc_3 in the presence of 6 mM fumarate. 0.5 mL of 6 mM disodium succinate was added to 0.5 mL of the centrifuged reaction mixture, leading to a change in fumarate/succinate ratio compared to Figure 8:6.

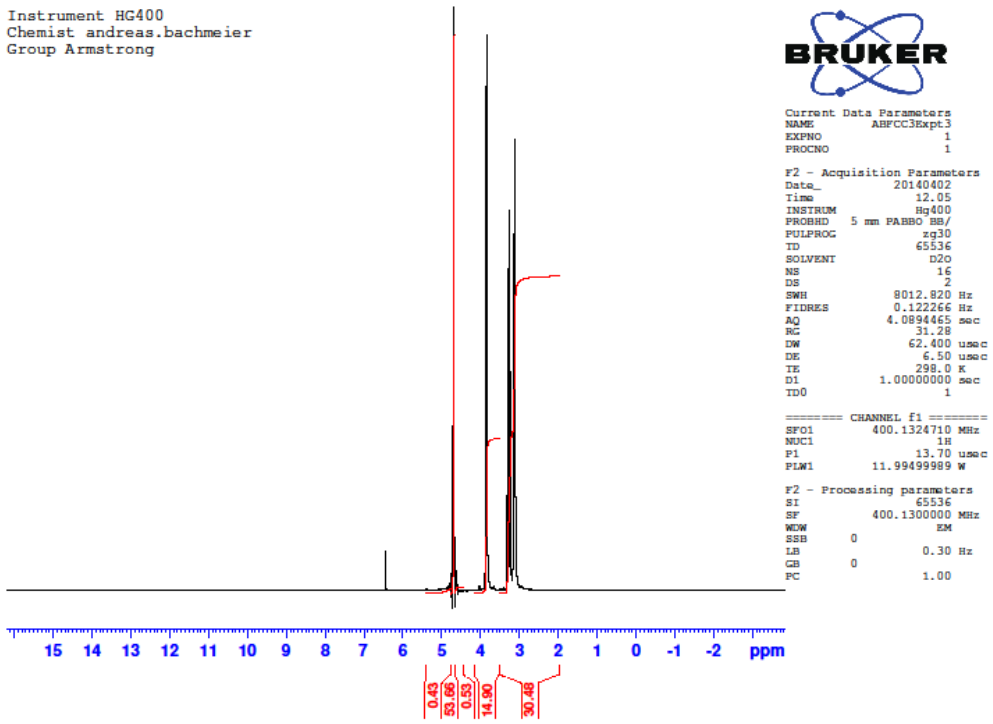


Figure 8:8 ^{1}H NMR spectrum recorded after 4 h of illumination of RuP−fcc$_3$ in the presence of 6 mM fumarate.

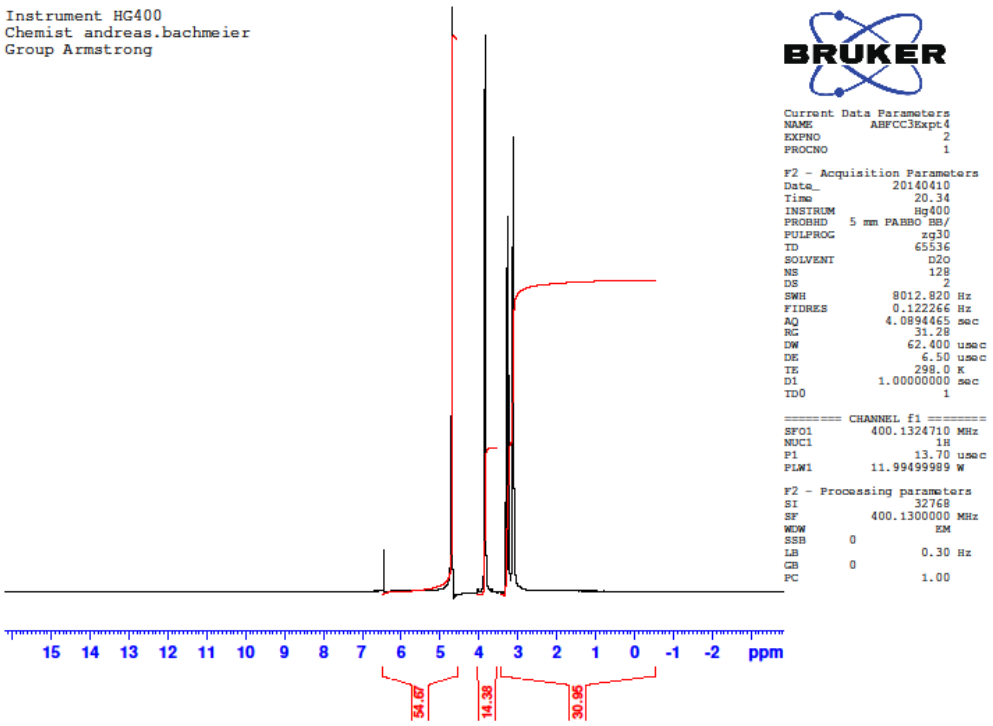


Figure 8:9 ^{1}H NMR spectrum recorded after 4 h of illumination of RuP–ZrO_2–fcc_3 in the presence of 6 mM fumarate.

8.5.6 Photoelectrochemistry experiments

8.5.6.1 Experimental procedures

Generally, photoelectrochemistry experiments were carried out as described in section 8.5.4, either in a thermostated one-compartment electrochemistry cell, or a two-compartment cell, separated by a porous glass frit. The Kodak light source was employed as described above, using a 420 nm long-pass UV filter. An optical chopper, built in house, was used to measure transient photocurrents. For two-electrode measurements, the reference electrode lead of the potentiostat was connected to the counter electrode. Current densities were calculated with respect to the geometric surface area of the working electrode.

8.5.6.2 Catalyst deposition on W–$BiVO_4$ electrodes

The Co-Pi electrocatalyst was photodeposited (bias-assisted) on W–$BiVO_4$ from a solution of 0.5 mM $Co(NO_3)_2$ (Sigma-Aldrich, ACS reagent) dissolved in 0.1 M KPi buffer (pH 7.0) according to a method by Zhong *et al.* [143]. The catalyst film was deposited over a period of 5 min at 0.24 V *vs.* RHE under constant illumination through the FTO support (back illumination). Figure 6:11 depicts a comparison of the current-voltage curves obtained before and after Co-Pi deposition.

8.5.6.3 Photoelectrocatalysis experiments

Figure 6:13 shows the temporal behaviour of a bare *meso*-ITO electrode (WE) connected to a Co-Pi modified W–$BiVO_4$ photoelectrode (CE) in a two-compartment photoelectrochemical cell at zero external bias. The systems displays a rapidly decaying capacitive current and the current shows little response to illumination, as the energy levels of the illuminated Co-Pi-W–$BiVO_4$ electrode do not permit overall water splitting.

Photoelectrocatalysis experiments including fcc_3 were carried out in the same two-electrode configuration, with the electrode compartment containing the fcc_3–*meso*-ITO working electrode being sparged with N_2 to allow rapid substrate/product transport to and from the electrode. During the experiments, 1.0 mL 20 mM fumarate solution (in pH 7.0 KPi buffer) was injected into 9.0 mL buffer solution to a final concentration of 2.0 mM. Gas flow was briefly interrupted during the introduction of fumarate.

An *estimate* of the turnover frequency on a per enzyme basis was obtained from the overall charge passed through the photoelectrochemical cell under catalytic turnover. In the experiment depicted in Figure 6:12, a total charge of 6.3×10^{-4} C was passed through the system between $\Delta t = 153 - 900$ s (*i.e.* after fumarate was injected into the solution). The capacitive charge during this period, estimated from the dark currents, was 1.7×10^{-5} C. With

$F = 96485$ C mol^{-1}, the 'turnover'-charge (*i.e.* the total charge minus the capacitive charge) corresponds to 6.4 nmol electrons. Assuming $\eta_F = 100\%$ as the upper limit, 3.2 nmol succinate was formed over the course of the reaction, since 2 e^- are required to reduce one equivalent of fumarate, corresponding to 5.6 pmol s^{-1} (under illumination). Assuming all fcc_3 molecules immobilised on *meso*-ITO (0.4 nmol) were adsorbed in an electroactive configuration, a TOF (on a per enzyme basis) of 0.01_4 s^{-1} is obtained. An analogous photoelectrocatalysis experiment carried out with reversed connections, *i.e.* Co-Pi-W–$BiVO_4$ employed as WE and fcc_3–ITO as the counter is depicted in Appendix G.

Bibliography

[1] Lewis, N.; Crabtree, G.; Nozik, A.; Wasielewski, M.; Alivisatos, P. *Basic research needs for solar energy utilization*; US Department of Energy: Washington, DC, **2005**.
[2] Hoffert, M. I.; Caldeira, K.; Jain, A. K.; Haites, E. F.; Harvey, L. D. D.; Potter, S. D.; Schlesinger, M. E.; Schneider, S. H.; Watts, R. G.; Wigley, T. M. L.; Wuebbles, D. J. *Nature* **1998**, *395*, 881.
[3] Lewis, N. S.; Nocera, D. G. *Proc. Natl. Acad. Sci. U. S. A.* **2006**, *103*, 15729.
[4] Thomas, J. M. *ChemSusChem* **2014**, *7*, 1801.
[5] May, R. M. *Phil. Trans. R. Soc. A* **2007**, *365*, 879.
[6] *International Energy Agency: Key World Energy Statistics 2014* Paris, 2014.
[7] Oreskes, N. *Science* **2004**, *306*, 1686.
[8] John, C.; Dana, N.; Sarah, A. G.; Mark, R.; Bärbel, W.; Rob, P.; Robert, W.; Peter, J.; Andrew, S. *Environ. Res. Lett.* **2013**, *8*, 024024.
[9] Green, M. A.; Emery, K.; Hishikawa, Y.; Warta, W.; Dunlop, E. D. *Prog. Photovolt: Res. Appl.* **2014**, *22*, 701.
[10] Fujishima, A.; Honda, K. *Nature* **1972**, *238*, 37.
[11] Rocheleau, R. E.; Miller, E. L.; Misra, A. *Energy & Fuels* **1998**, *12*, 3.
[12] Khaselev, O.; Turner, J. A. *Science* **1998**, *280*, 425.
[13] Khaselev, O.; Bansal, A.; Turner, J. A. *Int. J. Hydrogen Energy* **2001**, *26*, 127.
[14] Peharz, G.; Dimroth, F.; Wittstadt, U. *Int. J. Hydrogen Energy* **2007**, *32*, 3248.
[15] Jacobsson, T. J.; Fjallstrom, V.; Sahlberg, M.; Edoff, M.; Edvinsson, T. *Energy Environ. Sci.* **2013**, *6*, 3676.
[16] Luo, J.; Im, J.-H.; Mayer, M. T.; Schreier, M.; Nazeeruddin, M. K.; Park, N.-G.; Tilley, S. D.; Fan, H. J.; Grätzel, M. *Science* **2014**, *345*, 1593.
[17] Cox, C. R.; Lee, J. Z.; Nocera, D. G.; Buonassisi, T. *Proc. Natl. Acad. Sci. U. S. A.* **2014**, *111*, 14057.
[18] Bockris, J. O. *Science* **1972**, *176*, 1323.
[19] Edwards, P. P.; Kuznetsov, V. L.; David, W. I. F.; Brandon, N. P. *Energy Policy* **2008**, *36*, 4356.
[20] Wells, S. A.; Sartbaeva, A.; Kuznetsov, V. L.; Edwards, P. P. In *Encyclopedia of Inorganic Chemistry*; John Wiley & Sons, Ltd: 2006.
[21] Olah, G. A.; Goeppert, A.; Prakash, G. K. S. *Beyond Oil and Gas: The Methanol Economy*; 2 ed.; Wiley-VCH, 2009.
[22] Barber, J. *Chem. Soc. Rev.* **2009**, *38*, 185.
[23] Barber, J. *Phil. Trans. R. Soc. A* **2007**, *365*, 1007.
[24] Janssen, P. J. D.; Lambreva, M. D.; Plumeré, N.; Bartolucci, C.; Antonacci, A.; Buonasera, K.; Frese, R. N.; Scognamiglio, V.; Rea, G. *Front. Chem.* **2014**, *2*.
[25] Barber, J. In *Energy : Beyond Oil*; Armstrong, F., Blundell, K., Eds.; Oxford University Press: Oxford, 2007, p 137.
[26] Archer, M. D.; Barber, J. In *Molecular to Global Photosynthesis*; Archer, M. D., Barber, J., Eds.; Imperial College Press: London, 2004, p 1.
[27] Fleming, G. R.; Schlau-Cohen, G. S.; Amarnath, K.; Zaks, J. *Farad. Discuss.* **2012**, *155*, 27.
[28] Herek, J. L.; Wohlleben, W.; Cogdell, R. J.; Zeidler, D.; Motzkus, M. *Nature* **2002**, *417*, 533.
[29] Blankenship, R. E. *Molecular Mechanisms of Photosynthesis*; 2 ed.; Wiley-Blackwell, 2014.

[30] Edwards, G. E.; Walker, D. A. In *Molecular to Global Photosynthesis*; Archer, M. D., Barber, J., Eds.; Imperial College Press: London, 2004, p 189.
[31] Nocera, D. G. *Acc. Chem. Res.* **2012**, *45*, 767.
[32] Blankenship, R. E.; Tiede, D. M.; Barber, J.; Brudvig, G. W.; Fleming, G.; Ghirardi, M.; Gunner, M. R.; Junge, W.; Kramer, D. M.; Melis, A.; Moore, T. A.; Moser, C. C.; Nocera, D. G.; Nozik, A. J.; Ort, D. R.; Parson, W. W.; Prince, R. C.; Sayre, R. T. *Science* **2011**, *332*, 805.
[33] Rappaport, F.; Diner, B. A. *Coord. Chem. Rev.* **2008**, *252*, 259.
[34] Dau, H.; Zaharieva, I. *Acc. Chem. Res.* **2009**, *42*, 1861.
[35] Kothe, T.; Plumeré, N.; Badura, A.; Nowaczyk, M. M.; Guschin, D. A.; Rögner, M.; Schuhmann, W. *Angew. Chem. Int. Ed.* **2013**, *52*, 14233.
[36] Vinyard, D. J.; Ananyev, G. M.; Charles Dismukes, G. *Annu. Rev. Biochem.* **2013**, *82*, 577.
[37] Dau, H.; Zaharieva, I.; Haumann, M. *Curr. Opin. Chem. Biol.* **2012**, *16*, 3.
[38] Umena, Y.; Kawakami, K.; Shen, J.-R.; Kamiya, N. *Nature* **2011**, *473*, 55.
[39] Vogt, L.; Vinyard, D. J.; Khan, S.; Brudvig, G. W. *Curr. Opin. Chem. Biol.* **2015**, *25*, 152.
[40] Ferreira, K. N.; Iverson, T. M.; Maghlaoui, K.; Barber, J.; Iwata, S. *Science* **2004**, *303*, 1831.
[41] Kavarnos, G. J. *Fundamentals of Photoinduced Electron Transfer*; Wiley-VCH: Weinheim, 1993.
[42] Cardona, T.; Sedoud, A.; Cox, N.; Rutherford, A. W. *BBA-Bioenergetics* **2012**, *1817*, 26.
[43] Woodbury, N. W.; Allen, J. P. *Adv. Photosynth.* **1995**, *2*, 527.
[44] Tachibana, Y.; Vayssieres, L.; Durrant, J. R. *Nat. Photon.* **2012**, *6*, 511.
[45] Burnap, R. L. *Phys. Chem. Chem. Phys.* **2004**, *6*, 4803.
[46] Ananyev, G. M.; Zaltsman, L.; Vasko, C.; Dismukes, G. C. *BBA-Bioenergetics* **2001**, *1503*, 52.
[47] Takahashi, S.; Badger, M. R. *Trends Plant Sci.* **2011**, *16*, 53.
[48] Dau, H.; Grundmeier, A.; Loja, P.; Haumann, M. *Philos. Trans. R. Soc. B* **2008**, *363*, 1237.
[49] Siegbahn, P. E. M. *Chem. Eur. J.* **2008**, *14*, 8290.
[50] Siegbahn, P. E. M. *Acc. Chem. Res.* **2009**, *42*, 1871.
[51] Pal, R.; Negre, C. F. A.; Vogt, L.; Pokhrel, R.; Ertem, M. Z.; Brudvig, G. W.; Batista, V. S. *Biochemistry* **2013**, *52*, 7703.
[52] Kok, B.; Forbush, B.; McGloin, M. *Photochem. Photobiol.* **1970**, *11*, 457.
[53] Britt, R. D.; Oyala, P. H. *Science* **2014**, *345*, 736.
[54] Cox, N.; Pantazis, D. A.; Neese, F.; Lubitz, W. *Acc. Chem. Res.* **2013**, *46*, 1588.
[55] Cox, N.; Messinger, J. *BBA-Bioenergetics* **2013**, *1827*, 1020.
[56] Limburg, J.; A. Szalai, V.; W. Brudvig, G. *J. Chem. Soc., Dalton Trans.* **1999**, 1353.
[57] McEvoy, J. P.; Brudvig, G. W. *Chem. Rev.* **2006**, *106*, 4455.
[58] Siegbahn, P. E. M. *Chem. Eur. J.* **2006**, *12*, 9217.
[59] Siegbahn, P. E. M. *J. Photochem. Photobiol., B* **2011**, *104*, 94.
[60] Siegbahn, P. E. M. *BBA-Bioenergetics* **2013**, *1827*, 1003.
[61] Cox, N.; Retegan, M.; Neese, F.; Pantazis, D. A.; Boussac, A.; Lubitz, W. *Science* **2014**, *345*, 804.
[62] Yano, J.; Yachandra, V. *Chem. Rev.* **2014**, *114*, 4175.
[63] Pantazis, D. A.; Ames, W.; Cox, N.; Lubitz, W.; Neese, F. *Angew. Chem. Int. Ed.* **2012**, *51*, 9935.

[64] Haumann, M.; Liebisch, P.; Müller, C.; Barra, M.; Grabolle, M.; Dau, H. *Science* **2005**, *310*, 1019.
[65] Taguchi, T.; Gupta, R.; Lassalle-Kaiser, B.; Boyce, D. W.; Yachandra, V. K.; Tolman, W. B.; Yano, J.; Hendrich, M. P.; Borovik, A. S. *J. Am. Chem. Soc.* **2012**, *134*, 1996.
[66] Kern, J.; Alonso-Mori, R.; Tran, R.; Hattne, J.; Gildea, R. J.; Echols, N.; Glöckner, C.; Hellmich, J.; Laksmono, H.; Sierra, R. G.; Lassalle-Kaiser, B.; Koroidov, S.; Lampe, A.; Han, G.; Gul, S.; DiFiore, D.; Milathianaki, D.; Fry, A. R.; Miahnahri, A.; Schafer, D. W.; Messerschmidt, M.; Seibert, M. M.; Koglin, J. E.; Sokaras, D.; Weng, T.-C.; Sellberg, J.; Latimer, M. J.; Grosse-Kunstleve, R. W.; Zwart, P. H.; White, W. E.; Glatzel, P.; Adams, P. D.; Bogan, M. J.; Williams, G. J.; Boutet, S.; Messinger, J.; Zouni, A.; Sauter, N. K.; Yachandra, V. K.; Bergmann, U.; Yano, J. *Science* **2013**, *340*, 491.
[67] Kupitz, C.; Basu, S.; Grotjohann, I.; Fromme, R.; Zatsepin, N. A.; Rendek, K. N.; Hunter, M. S.; Shoeman, R. L.; White, T. A.; Wang, D.; James, D.; Yang, J.-H.; Cobb, D. E.; Reeder, B.; Sierra, R. G.; Liu, H.; Barty, A.; Aquila, A. L.; Deponte, D.; Kirian, R. A.; Bari, S.; Bergkamp, J. J.; Beyerlein, K. R.; Bogan, M. J.; Caleman, C.; Chao, T.-C.; Conrad, C. E.; Davis, K. M.; Fleckenstein, H.; Galli, L.; Hau-Riege, S. P.; Kassemeyer, S.; Laksmono, H.; Liang, M.; Lomb, L.; Marchesini, S.; Martin, A. V.; Messerschmidt, M.; Milathianaki, D.; Nass, K.; Ros, A.; Roy-Chowdhury, S.; Schmidt, K.; Seibert, M.; Steinbrener, J.; Stellato, F.; Yan, L.; Yoon, C.; Moore, T. A.; Moore, A. L.; Pushkar, Y.; Williams, G. J.; Boutet, S.; Doak, R. B.; Weierstall, U.; Frank, M.; Chapman, H. N.; Spence, J. C. H.; Fromme, P. *Nature* **2014**, *513*, 261.
[68] Kalyanasundaram, K. *Coord. Chem. Rev.* **1982**, *46*, 159.
[69] Moore, T. A.; Gust, D.; Mathis, P.; Mialocq, J.-C.; Chachaty, C.; Bensasson, R. V.; Land, E. J.; Doizi, D.; Liddell, P. A.; Lehman, W. R.; Nemeth, G. A.; Moore, A. L. *Nature* **1984**, *307*, 630.
[70] Wasielewski, M. R. *Chem. Rev.* **1992**, *92*, 435.
[71] Moore, G. F.; Konezny, S. J.; Song, H.-e.; Milot, R. L.; Blakemore, J. D.; Lee, M. L.; Batista, V. S.; Schmuttenmaer, C. A.; Crabtree, R. H.; Brudvig, G. W. *J. Phys. Chem. C* **2012**, *116*, 4892.
[72] White, H. S.; Becker, W. G.; Bard, A. J. *J. Phys. Chem.* **1984**, *88*, 1840.
[73] Milot, R. L.; Moore, G. F.; Crabtree, R. H.; Brudvig, G. W.; Schmuttenmaer, C. A. *J. Phys. Chem. C* **2013**, *117*, 21662.
[74] Frei, H. *CHIMIA* **2009**, *63*, 721.
[75] Bachmeier, A. *Diploma Thesis*, University of Erlangen-Nuremberg, 2010.
[76] Cuk, T.; Weare, W. W.; Frei, H. *J. Phys. Chem. C* **2010**, *114*, 9167.
[77] Han, H.; Frei, H. *J. Phys. Chem. C* **2008**, *112*, 16156.
[78] Nakamura, R.; Frei, H. *J. Am. Chem. Soc.* **2006**, *128*, 10668.
[79] Lin, W.; Frei, H. *J. Am. Chem. Soc.* **2005**, *127*, 1610.
[80] Macnaughtan, M. L.; Soo, H. S.; Frei, H. *J. Phys. Chem. C* **2014**, *118*, 7874.
[81] Kim, W.; Yuan, G.; McClure, B. A.; Frei, H. *J. Am. Chem. Soc.* **2014**, *136*, 11034.
[82] O'Regan, B.; Grätzel, M. *Nature* **1991**, *353*, 737.
[83] Bachmeier, A.; Siritanaratkul, B.; Armstrong, F. A. In *From Molecules to Materials-Pathways to Artificial Photosynthesis*; Rozhkova, E. A., Ariga, K., Eds.; Springer International Publishing: Switzerland, 2015, p 99.
[84] Chen, S.; Wang, L.-W. *Chem. Mater.* **2012**, *24*, 3659.
[85] Ye, H.; Park, H. S.; Bard, A. J. *J. Phys. Chem. C* **2011**, *115*, 12464.
[86] Park, Y.; McDonald, K. J.; Choi, K.-S. *Chem. Soc. Rev.* **2013**, *42*, 2321.
[87] Hong, S. J.; Lee, S.; Jang, J. S.; Lee, J. S. *Energy Environ. Sci.* **2011**, *4*, 1781.
[88] Shockley, W.; Queisser, H. J. *J. Appl. Phys.* **1961**, *32*, 510.

[89] Green, M. A. *Third Generation Photovoltaics: Advanced Solar Energy Conversion*; 2 ed.; Springer: Berlin, 2005.
[90] Conibeer, G. *Mater. Today* **2007**, *10*, 42.
[91] Brown, G. F.; Wu, J. *Laser Photon. Rev.* **2009**, *3*, 394.
[92] Sambur, J. B.; Novet, T.; Parkinson, B. A. *Science* **2010**, *330*, 63.
[93] Smith, M. B.; Michl, J. *Chem. Rev.* **2010**, *110*, 6891.
[94] Smith, M. B.; Michl, J. *Annu. Rev. Phys. Chem.* **2013**, *64*, 361.
[95] Park, N.-G. *Mater. Today* **2015**, *18*, 65.
[96] Jung, H. S.; Park, N.-G. *Small* **2015**, *11*, 10.
[97] Grätzel, M. *Nat. Mater.* **2014**, *13*, 838.
[98] Hodes, G. *Science* **2013**, *342*, 317.
[99] Kojima, A.; Teshima, K.; Shirai, Y.; Miyasaka, T. *J. Am. Chem. Soc.* **2009**, *131*, 6050.
[100] Lee, M. M.; Teuscher, J.; Miyasaka, T.; Murakami, T. N.; Snaith, H. J. *Science* **2012**, *338*, 643.
[101] Stranks, S. D.; Eperon, G. E.; Grancini, G.; Menelaou, C.; Alcocer, M. J. P.; Leijtens, T.; Herz, L. M.; Petrozza, A.; Snaith, H. J. *Science* **2013**, *342*, 341.
[102] Xing, G.; Mathews, N.; Sun, S.; Lim, S. S.; Lam, Y. M.; Grätzel, M.; Mhaisalkar, S.; Sum, T. C. *Science* **2013**, *342*, 344.
[103] Yella, A.; Lee, H.-W.; Tsao, H. N.; Yi, C.; Chandiran, A. K.; Nazeeruddin, M. K.; Diau, E. W.-G.; Yeh, C.-Y.; Zakeeruddin, S. M.; Grätzel, M. *Science* **2011**, *334*, 629.
[104] Liu, M.; Johnston, M. B.; Snaith, H. J. *Nature* **2013**, *501*, 395.
[105] Zhou, H.; Chen, Q.; Li, G.; Luo, S.; Song, T.-b.; Duan, H.-S.; Hong, Z.; You, J.; Liu, Y.; Yang, Y. *Science* **2014**, *345*, 542.
[106] Patwardhan, S.; Cao, D. H.; Hatch, S.; Farha, O. K.; Hupp, J. T.; Kanatzidis, M. G.; Schatz, G. C. *J. Phys. Chem. Lett.* **2015**, *6*, 251.
[107] Burschka, J.; Pellet, N.; Moon, S.-J.; Humphry-Baker, R.; Gao, P.; Nazeeruddin, M. K.; Grätzel, M. *Nature* **2013**, *499*, 316.
[108] Mei, A.; Li, X.; Liu, L.; Ku, Z.; Liu, T.; Rong, Y.; Xu, M.; Hu, M.; Chen, J.; Yang, Y.; Grätzel, M.; Han, H. *Science* **2014**, *345*, 295.
[109] Gersten, S. W.; Samuels, G. J.; Meyer, T. J. *J. Am. Chem. Soc.* **1982**, *104*, 4029.
[110] Concepcion, J. J.; Jurss, J. W.; Brennaman, M. K.; Hoertz, P. G.; Patrocinio, A. O. T.; Murakami Iha, N. Y.; Templeton, J. L.; Meyer, T. J. *Acc. Chem. Res.* **2009**, *42*, 1954.
[111] Hull, J. F.; Balcells, D.; Blakemore, J. D.; Incarvito, C. D.; Eisenstein, O.; Brudvig, G. W.; Crabtree, R. H. *J. Am. Chem. Soc.* **2009**, *131*, 8730.
[112] Blakemore, J. D.; Schley, N. D.; Balcells, D.; Hull, J. F.; Olack, G. W.; Incarvito, C. D.; Eisenstein, O.; Brudvig, G. W.; Crabtree, R. H. *J. Am. Chem. Soc.* **2010**, *132*, 16017.
[113] Schley, N. D.; Blakemore, J. D.; Subbaiyan, N. K.; Incarvito, C. D.; D'Souza, F.; Crabtree, R. H.; Brudvig, G. W. *J. Am. Chem. Soc.* **2011**, *133*, 10473.
[114] Duan, L.; Bozoglian, F.; Mandal, S.; Stewart, B.; Privalov, T.; Llobet, A.; Sun, L. *Nat. Chem.* **2012**, *4*, 418.
[115] Weller, M.; Overton, T.; Rourke, J.; Armstrong, F. *Inorganic Chemistry*; 6 ed.; Oxford University Press: Oxford, 2014.
[116] Kärkäs, M. D.; Verho, O.; Johnston, E. V.; Åkermark, B. *Chem. Rev.* **2014**, *114*, 11863.
[117] Berardi, S.; La Ganga, G.; Natali, M.; Bazzan, I.; Puntoriero, F.; Sartorel, A.; Scandola, F.; Campagna, S.; Bonchio, M. *J. Am. Chem. Soc.* **2012**, *134*, 11104.
[118] Kaveevivitchai, N.; Chitta, R.; Zong, R.; El Ojaimi, M.; Thummel, R. P. *J. Am. Chem. Soc.* **2012**, *134*, 10721.

[119] Al-Oweini, R.; Sartorel, A.; Bassil, B. S.; Natali, M.; Berardi, S.; Scandola, F.; Kortz, U.; Bonchio, M. *Angew. Chem. Int. Ed.* **2014**, *53*, 11182.
[120] Vagnini, M. T.; Smeigh, A. L.; Blakemore, J. D.; Eaton, S. W.; Schley, N. D.; D'Souza, F.; Crabtree, R. H.; Brudvig, G. W.; Co, D. T.; Wasielewski, M. R. *Proc. Natl. Acad. Sci. U. S. A.* **2012**, *109*, 15651.
[121] Brimblecombe, R.; Dismukes, G. C.; Swiegers, G. F.; Spiccia, L. *Dalton Trans.* **2009**, 9374.
[122] Young, K. J.; Martini, L. A.; Milot, R. L.; Snoeberger, R. C.; Batista, V. S.; Schmuttenmaer, C. A.; Crabtree, R. H.; Brudvig, G. W. *Coord. Chem. Rev.* **2012**, *256*, 2503.
[123] Swierk, J. R.; Mallouk, T. E. *Chem. Soc. Rev.* **2013**, *42*, 2357.
[124] Sartorel, A.; Bonchio, M.; Campagna, S.; Scandola, F. *Chem. Soc. Rev.* **2013**, *42*, 2262.
[125] Ashford, D. L.; Lapides, A. M.; Vannucci, A. K.; Hanson, K.; Torelli, D. A.; Harrison, D. P.; Templeton, J. L.; Meyer, T. J. *J. Am. Chem. Soc.* **2014**, *136*, 6578.
[126] Klepser, B. M.; Bartlett, B. M. *J. Am. Chem. Soc.* **2014**, *136*, 1694.
[127] Jeon, T. H.; Choi, W.; Park, H. *Phys. Chem. Chem. Phys.* **2011**, *13*, 21392.
[128] McCrory, C. C. L.; Jung, S.; Peters, J. C.; Jaramillo, T. F. *J. Am. Chem. Soc.* **2013**, *135*, 16977.
[129] Hara, M.; Waraksa, C. C.; Lean, J. T.; Lewis, B. A.; Mallouk, T. E. *J. Phys. Chem. A* **2000**, *104*, 5275.
[130] Tilley, S. D.; Cornuz, M.; Sivula, K.; Grätzel, M. *Angew. Chem. Int. Ed.* **2010**, *49*, 6405.
[131] Youngblood, W. J.; Lee, S.-H. A.; Kobayashi, Y.; Hernandez-Pagan, E. A.; Hoertz, P. G.; Moore, T. A.; Moore, A. L.; Gust, D.; Mallouk, T. E. *J. Am. Chem. Soc.* **2009**, *131*, 926.
[132] Bledowski, M.; Wang, L.; Neubert, S.; Mitoraj, D.; Beranek, R. *J. Phys. Chem. C* **2014**, *118*, 18951.
[133] Greenwood, N. N.; Earnshaw, A. *Chemistry of the Elements*; 2 ed.; Butterworth-Heinemann Ltd: Oxford, 1997.
[134] Kanan, M. W.; Nocera, D. G. *Science* **2008**, *321*, 1072.
[135] Dincă, M.; Surendranath, Y.; Nocera, D. G. *Proc. Natl. Acad. Sci. U. S. A.* **2010**, *107*, 10337.
[136] Risch, M.; Khare, V.; Zaharieva, I.; Gerencser, L.; Chernev, P.; Dau, H. *J. Am. Chem. Soc.* **2009**, *131*, 6936.
[137] Kanan, M. W.; Yano, J.; Surendranath, Y.; Dincă, M.; Yachandra, V. K.; Nocera, D. G. *J. Am. Chem. Soc.* **2010**, *132*, 13692.
[138] Steinmiller, E. M. P.; Choi, K.-S. *Proc. Natl. Acad. Sci. U. S. A.* **2009**, *106*, 20633.
[139] Pijpers, J. J. H.; Winkler, M. T.; Surendranath, Y.; Buonassisi, T.; Nocera, D. G. *Proc. Natl. Acad. Sci. U. S. A.* **2011**, *108*, 10056.
[140] Yang, J.; Walczak, K.; Anzenberg, E.; Toma, F. M.; Yuan, G.; Beeman, J.; Schwartzberg, A.; Lin, Y.; Hettick, M.; Javey, A.; Ager, J. W.; Yano, J.; Frei, H.; Sharp, I. D. *J. Am. Chem. Soc.* **2014**, *136*, 6191.
[141] Bledowski, M.; Wang, L.; Ramakrishnan, A.; Bétard, A.; Khavryuchenko, O. V.; Beranek, R. *ChemPhysChem* **2012**, *13*, 3018.
[142] Zhong, D. K.; Gamelin, D. R. *J. Am. Chem. Soc.* **2010**, *132*, 4202.
[143] Zhong, D. K.; Cornuz, M.; Sivula, K.; Gratzel, M.; Gamelin, D. R. *Energy Environ. Sci.* **2011**, *4*, 1759.
[144] Seabold, J. A.; Choi, K.-S. *Chem. Mater.* **2011**, *23*, 1105.
[145] Pilli, S. K.; Furtak, T. E.; Brown, L. D.; Deutsch, T. G.; Turner, J. A.; Herring, A. M. *Energy Environ. Sci.* **2011**, *4*, 5028.
[146] Zhong, D. K.; Choi, S.; Gamelin, D. R. *J. Am. Chem. Soc.* **2011**, *133*, 18370.

[147] Zhou, M.; Bao, J.; Bi, W.; Zeng, Y.; Zhu, R.; Tao, M.; Xie, Y. *ChemSusChem* **2012**, *5*, 1420.
[148] Abdi, F. F.; Firet, N.; van de Krol, R. *ChemCatChem* **2013**, *5*, 490.
[149] Moniz, S. J. A.; Zhu, J.; Tang, J. *Adv. Energy Mater.* **2014**, *4*, n/a.
[150] Trotochaud, L.; Ranney, J. K.; Williams, K. N.; Boettcher, S. W. *J. Am. Chem. Soc.* **2012**, *134*, 17253.
[151] Louie, M. W.; Bell, A. T. *J. Am. Chem. Soc.* **2013**, *135*, 12329.
[152] Lin, F.; Boettcher, S. W. *Nat. Mater.* **2014**, *13*, 81.
[153] Seabold, J. A.; Choi, K.-S. *J. Am. Chem. Soc.* **2012**, *134*, 2186.
[154] McDonald, K. J.; Choi, K.-S. *Energy Environ. Sci.* **2012**, *5*, 8553.
[155] Kim, T. W.; Choi, K.-S. *Science* **2014**, *343*, 990.
[156] Blakemore, J. D.; Gray, H. B.; Winkler, J. R.; Müller, A. M. *ACS Catal.* **2013**, *3*, 2497.
[157] Hunter, B. M.; Blakemore, J. D.; Deimund, M.; Gray, H. B.; Winkler, J. R.; Müller, A. M. *J. Am. Chem. Soc.* **2014**, *136*, 13118.
[158] Smith, R. D. L.; Prévot, M. S.; Fagan, R. D.; Zhang, Z.; Sedach, P. A.; Siu, M. K. J.; Trudel, S.; Berlinguette, C. P. *Science* **2013**, *340*, 60.
[159] Gregoire, J. M.; Xiang, C.; Mitrovic, S.; Liu, X.; Marcin, M.; Cornell, E. W.; Fan, J.; Jin, J. *J. Electrochem. Soc.* **2013**, *160*, F337.
[160] Xiang, C.; Suram, S. K.; Haber, J. A.; Guevarra, D. W.; Soedarmadji, E.; Jin, J.; Gregoire, J. M. *ACS Comb. Sci.* **2013**, *16*, 47.
[161] Haber, J. A.; Xiang, C.; Guevarra, D.; Jung, S.; Jin, J.; Gregoire, J. M. *ChemElectroChem* **2014**, *1*, 524.
[162] Haber, J. A.; Cai, Y.; Jung, S.; Xiang, C.; Mitrovic, S.; Jin, J.; Bell, A. T.; Gregoire, J. M. *Energy Environ. Sci.* **2014**, *7*, 682.
[163] Jacques, P.-A.; Artero, V.; Pécaut, J.; Fontecave, M. *Proc. Natl. Acad. Sci. U. S. A.* **2009**, *106*, 20627.
[164] Artero, V.; Chavarot-Kerlidou, M.; Fontecave, M. *Angew. Chem. Int. Ed.* **2011**, *50*, 7238.
[165] McCrory, C. C. L.; Uyeda, C.; Peters, J. C. *J. Am. Chem. Soc.* **2012**, *134*, 3164.
[166] Tran, P. D.; Barber, J. *Phys. Chem. Chem. Phys.* **2012**, *14*, 13772.
[167] Thoi, V. S.; Sun, Y.; Long, J. R.; Chang, C. J. *Chem. Soc. Rev.* **2013**, *42*, 2388.
[168] Connolly, P.; Espenson, J. H. *Inorg. Chem.* **1986**, *25*, 2684.
[169] Dempsey, J. L.; Brunschwig, B. S.; Winkler, J. R.; Gray, H. B. *Acc. Chem. Res.* **2009**, *42*, 1995.
[170] Schrauzer, G. N. *Acc. Chem. Res.* **1968**, *1*, 97.
[171] Dempsey, J. L.; Winkler, J. R.; Gray, H. B. *J. Am. Chem. Soc.* **2010**, *132*, 16774.
[172] Solis, B. H.; Hammes-Schiffer, S. *Inorg. Chem.* **2011**, *50*, 11252.
[173] Helm, M. L.; Stewart, M. P.; Bullock, R. M.; DuBois, M. R.; DuBois, D. L. *Science* **2011**, *333*, 863.
[174] Rakowski Dubois, M.; DuBois, D. L. *Acc. Chem. Res.* **2009**, *42*, 1974.
[175] Rakowski DuBois, M.; DuBois, D. L. *Chem. Soc. Rev.* **2009**, *38*, 62.
[176] Shaw, W. J.; Helm, M. L.; DuBois, D. L. *BBA-Bioenergetics* **2013**, *1827*, 1123.
[177] Wiese, S.; Kilgore, U. J.; Ho, M.-H.; Raugei, S.; DuBois, D. L.; Bullock, R. M.; Helm, M. L. *ACS Catal.* **2013**, *3*, 2527.
[178] Dutta, A.; DuBois, D. L.; Roberts, J. A. S.; Shaw, W. J. *Proc. Natl. Acad. Sci. U. S. A.* **2014**, *111*, 16286.
[179] Goff, A. L.; Artero, V.; Jousselme, B.; Tran, P.; Guillet, N. *Science* **2009**, *326*, 1384.
[180] Tran, P. D.; Le Goff, A.; Heidkamp, J.; Jousselme, B.; Guillet, N.; Palacin, S.; Dau, H.; Fontecave, M.; Artero, V. *Angew. Chem. Int. Ed.* **2011**, *50*, 1371.

[181] Andreiadis, E. S.; Jacques, P.-A.; Tran, P. D.; Leyris, A.; Chavarot-Kerlidou, M.; Jousselme, B.; Matheron, M.; Pécaut, J.; Palacin, S.; Fontecave, M.; Artero, V. *Nat. Chem.* **2013**, *5*, 48.
[182] Lakadamyali, F.; Reynal, A.; Kato, M.; Durrant, J. R.; Reisner, E. *Chem. Eur. J.* **2012**, *18*, 15464.
[183] Reynal, A.; Lakadamyali, F.; Gross, M. A.; Reisner, E.; Durrant, J. R. *Energy Environ. Sci.* **2013**, *6*, 3291.
[184] Gross, M. A.; Reynal, A.; Durrant, J. R.; Reisner, E. *J. Am. Chem. Soc.* **2014**, *136*, 356.
[185] Reynal, A.; Willkomm, J.; Muresan, N. M.; Lakadamyali, F.; Planells, M.; Reisner, E.; Durrant, J. R. *Chem. Commun.* **2014**, *50*, 12768.
[186] Huang, J.; Mulfort, K. L.; Du, P.; Chen, L. X. *J. Am. Chem. Soc.* **2012**, *134*, 16472.
[187] Moore, G. F.; Sharp, I. D. *J. Phys. Chem. Lett.* **2013**, *4*, 568.
[188] Li, L.; Duan, L.; Wen, F.; Li, C.; Wang, M.; Hagfeldt, A.; Sun, L. *Chem. Commun.* **2012**, *48*, 988.
[189] Krawicz, A.; Yang, J.; Anzenberg, E.; Yano, J.; Sharp, I. D.; Moore, G. F. *J. Am. Chem. Soc.* **2013**, *135*, 11861.
[190] Weingarten, A. S.; Kazantsev, R. V.; Palmer, L. C.; McClendon, M.; Koltonow, A. R.; SamuelAmanda, P. S.; Kiebala, D. J.; Wasielewski, M. R.; Stupp, S. I. *Nat. Chem.* **2014**, *6*, 964.
[191] Tran, P. D.; Wong, L. H.; Barber, J.; Loo, J. S. C. *Energy Environ. Sci.* **2012**, *5*, 5902.
[192] McCrory, C. C. L.; Jung, S.; Ferrer, I. M.; Chatman, S.; Peters, J. C.; Jaramillo, T. F. *J. Am. Chem. Soc.* **2015**.
[193] Vesborg, P. C. K.; Seger, B.; Chorkendorff, I. *J. Phys. Chem. Lett.* **2015**, 951.
[194] Merki, D.; Fierro, S.; Vrubel, H.; Hu, X. *Chem. Sci.* **2011**, *2*, 1262.
[195] Laursen, A. B.; Kegnaes, S.; Dahl, S.; Chorkendorff, I. *Energy Environ. Sci.* **2012**, *5*, 5577.
[196] Morales-Guio, C. G.; Hu, X. *Acc. Chem. Res.* **2014**, *47*, 2671.
[197] Morales-Guio, C. G.; Stern, L.-A.; Hu, X. *Chem. Soc. Rev.* **2014**, *43*, 6555.
[198] Lassalle-Kaiser, B.; Merki, D.; Vrubel, H.; Gul, S.; Yachandra, V. K.; Hu, X.; Yano, J. *J. Am. Chem. Soc.* **2015**, *137*, 314.
[199] Morales-Guio, C. G.; Liardet, L.; Mayer, M. T.; Tilley, S. D.; Grätzel, M.; Hu, X. *Angew. Chem. Int. Ed.* **2015**, *54*, 664.
[200] Seger, B.; Laursen, A. B.; Vesborg, P. C. K.; Pedersen, T.; Hansen, O.; Dahl, S.; Chorkendorff, I. *Angew. Chem. Int. Ed.* **2012**, *51*, 9128.
[201] Laursen, A. B.; Pedersen, T.; Malacrida, P.; Seger, B.; Hansen, O.; Vesborg, P. C. K.; Chorkendorff, I. *Phys. Chem. Chem. Phys.* **2013**, *15*, 20000.
[202] Tran, P. D.; Pramana, S. S.; Kale, V. S.; Nguyen, M.; Chiam, S. Y.; Batabyal, S. K.; Wong, L. H.; Barber, J.; Loo, J. *Chem. Eur. J.* **2012**, *18*, 13994.
[203] Bourgeteau, T.; Tondelier, D.; Geffroy, B.; Brisse, R.; Laberty-Robert, C.; Campidelli, S.; de Bettignies, R.; Artero, V.; Palacin, S.; Jousselme, B. *Energy Environ. Sci.* **2013**, *6*, 2706.
[204] Tang, M. L.; Grauer, D. C.; Lassalle-Kaiser, B.; Yachandra, V. K.; Amirav, L.; Long, J. R.; Yano, J.; Alivisatos, A. P. *Angew. Chem. Int. Ed.* **2011**, *50*, 10203.
[205] Popczun, E. J.; Read, C. G.; Roske, C. W.; Lewis, N. S.; Schaak, R. E. *Angew. Chem. Int. Ed.* **2014**, *53*, 5427.
[206] Popczun, E. J.; McKone, J. R.; Read, C. G.; Biacchi, A. J.; Wiltrout, A. M.; Lewis, N. S.; Schaak, R. E. *J. Am. Chem. Soc.* **2013**, *135*, 9267.
[207] Laursen, A. B.; Patraju, K. R.; Whitaker, M. J.; Retuerto, M.; Sarkar, T.; Yao, N.; Ramanujachary, K. V.; Greenblatt, M.; Dismukes, G. C. *Energy Environ. Sci.* **2015**, *8*, 1027.

[208] Liu, P.; Rodriguez, J. A. *J. Am. Chem. Soc.* **2005**, *127*, 14871.
[209] Callejas, J. F.; McEnaney, J. M.; Read, C. G.; Crompton, J. C.; Biacchi, A. J.; Popczun, E. J.; Gordon, T. R.; Lewis, N. S.; Schaak, R. E. *ACS Nano* **2014**, *8*, 11101.
[210] Lubitz, W.; Ogata, H.; Rüdiger, O.; Reijerse, E. *Chem. Rev.* **2014**, *114*, 4081.
[211] Jones, A. K.; Sillery, E.; Albracht, S. P. J.; Armstrong, F. A. *Chem. Commun.* **2002**, 866.
[212] Woolerton, T. W.; Vincent, K. A. *Electrochim. Acta* **2009**, *54*, 5011.
[213] Hexter, S. V.; Grey, F.; Happe, T.; Climent, V.; Armstrong, F. A. *Proc. Natl. Acad. Sci. U. S. A.* **2012**, *109*, 11516.
[214] Caputo, C. A.; Gross, M. A.; Lau, V. W.; Cavazza, C.; Lotsch, B. V.; Reisner, E. *Angew. Chem. Int. Ed.* **2014**, *53*, 11538.
[215] Parkin, A.; Goldet, G.; Cavazza, C.; Fontecilla-Camps, J. C.; Armstrong, F. A. *J. Am. Chem. Soc.* **2008**, *130*, 13410.
[216] Chang, C. D. *Cat. Rev. - Sci. Eng.* **1983**, *25*, 1.
[217] Koppenol, W. H.; Rush, J. D. *J. Phys. Chem.* **1987**, *91*, 4429.
[218] Benson, E. E.; Kubiak, C. P.; Sathrum, A. J.; Smieja, J. M. *Chem. Soc. Rev.* **2009**, *38*, 89.
[219] Kumar, B.; Llorente, M.; Froehlich, J.; Dang, T.; Sathrum, A.; Kubiak, C. P. *Annu. Rev. Phys. Chem.* **2012**, *63*, 541.
[220] Fenwick, A. Q.; Gregoire, J. M.; Luca, O. R. *J. Photochem. Photobiol., B* **2015**, *152*, 47.
[221] Appel, A. M.; Bercaw, J. E.; Bocarsly, A. B.; Dobbek, H.; DuBois, D. L.; Dupuis, M.; Ferry, J. G.; Fujita, E.; Hille, R.; Kenis, P. J. A.; Kerfeld, C. A.; Morris, R. H.; Peden, C. H. F.; Portis, A. R.; Ragsdale, S. W.; Rauchfuss, T. B.; Reek, J. N. H.; Seefeldt, L. C.; Thauer, R. K.; Waldrop, G. L. *Chem. Rev.* **2013**, *113*, 6621.
[222] Kim, D.; Sakimoto, K. K.; Hong, D.; Yang, P. *Angew. Chem. Int. Ed.* **2015**, *54*, 3259.
[223] Elschenbroich, C.; Salzer, A. *Organometallics, A Concise Introduction*; 2 ed.; Wiley VCH: Weinheim, 1991.
[224] Wenzhen, L. In *Advances in CO_2 Conversion and Utilization*; American Chemical Society: 2010; Vol. 1056, p 55.
[225] Jhong, H.-R. M.; Ma, S.; Kenis, P. J. A. *Curr. Opin. Chem. Eng.* **2013**, *2*, 191.
[226] Hori, Y. In *Modern Aspects of Electrochemistry*; Vayenas, C., White, R., Gamboa-Aldeco, M., Eds.; Springer New York: 2008; Vol. 42, p 89.
[227] Hori, Y.; Kikuchi, K.; Suzuki, S. *Chem. Lett.* **1985**, *14*, 1695.
[228] Gattrell, M.; Gupta, N.; Co, A. *J. Electroanal. Chem.* **2006**, *594*, 1.
[229] Li, C. W.; Kanan, M. W. *J. Am. Chem. Soc.* **2012**, *134*, 7231.
[230] Tang, W.; Peterson, A. A.; Varela, A. S.; Jovanov, Z. P.; Bech, L.; Durand, W. J.; Dahl, S.; Norskov, J. K.; Chorkendorff, I. *Phys. Chem. Chem. Phys.* **2012**, *14*, 76.
[231] Reske, R.; Mistry, H.; Behafarid, F.; Roldan Cuenya, B.; Strasser, P. *J. Am. Chem. Soc.* **2014**, *136*, 6978.
[232] Kuhl, K. P.; Cave, E. R.; Abram, D. N.; Jaramillo, T. F. *Energy Environ. Sci.* **2012**, *5*, 7050.
[233] Lu, Q.; Rosen, J.; Jiao, F. *ChemCatChem* **2015**, *7*, 38.
[234] Chen, Y.; Li, C. W.; Kanan, M. W. *J. Am. Chem. Soc.* **2012**, *134*, 19969.
[235] Zhu, W.; Michalsky, R.; Metin, Ö.; Lv, H.; Guo, S.; Wright, C. J.; Sun, X.; Peterson, A. A.; Sun, S. *J. Am. Chem. Soc.* **2013**, *135*, 16833.
[236] Hansen, H. A.; Varley, J. B.; Peterson, A. A.; Nørskov, J. K. *J. Phys. Chem. Lett.* **2013**, *4*, 388.
[237] Rosen, B. A.; Salehi-Khojin, A.; Thorson, M. R.; Zhu, W.; Whipple, D. T.; Kenis, P. J. A.; Masel, R. I. *Science* **2011**, *334*, 643.

[238] Salehi-Khojin, A.; Jhong, H.-R. M.; Rosen, B. A.; Zhu, W.; Ma, S.; Kenis, P. J. A.; Masel, R. I. *J. Phys. Chem. C* **2013**, *117*, 1627.
[239] Lu, Q.; Rosen, J.; Zhou, Y.; Hutchings, G. S.; Kimmel, Y. C.; Chen, J. G.; Jiao, F. *Nat. Commun.* **2014**, *5*, 3242.
[240] Chen, Y.; Kanan, M. W. *J. Am. Chem. Soc.* **2012**, *134*, 1986.
[241] Zhang, S.; Kang, P.; Meyer, T. J. *J. Am. Chem. Soc.* **2014**, *136*, 1734.
[242] Kortlever, R.; Balemans, C.; Kwon, Y.; Koper, M. T. M. *Catal. Today* **2015**, *244*, 58.
[243] LaTempa, T. J.; Rani, S.; Bao, N.; Grimes, C. A. *Nanoscale* **2012**, *4*, 2245.
[244] Neaţu, Ş.; Maciá-Agulló, J. A.; Concepción, P.; Garcia, H. *J. Am. Chem. Soc.* **2014**, *136*, 15969.
[245] Shown, I.; Hsu, H.-C.; Chang, Y.-C.; Lin, C.-H.; Roy, P. K.; Ganguly, A.; Wang, C.-H.; Chang, J.-K.; Wu, C.-I.; Chen, L.-C.; Chen, K.-H. *Nano Lett.* **2014**, *14*, 6097.
[246] Habisreutinger, S. N.; Schmidt-Mende, L.; Stolarczyk, J. K. *Angew. Chem. Int. Ed.* **2013**, *52*, 7372.
[247] Mao, J.; Li, K.; Peng, T. *Catal. Sci. Tech.* **2013**, *3*, 2481.
[248] Kondratenko, E. V.; Mul, G.; Baltrusaitis, J.; Larrazabal, G. O.; Perez-Ramirez, J. *Energy Environ. Sci.* **2013**, *6*, 3112.
[249] Beley, M.; Collin, J.-P.; Ruppert, R.; Sauvage, J.-P. *J. Chem. Soc., Chem. Commun.* **1984**, 1315.
[250] Hawecker, J.; Lehn, J.-M.; Ziessel, R. *J. Chem. Soc., Chem. Commun.* **1983**, 536.
[251] Hawecker, J.; Lehn, J.-M.; Ziessel, R. *Helv. Chim. Acta* **1986**, *69*, 1990.
[252] Bourrez, M.; Molton, F.; Chardon-Noblat, S.; Deronzier, A. *Angew. Chem. Int. Ed.* **2011**, *50*, 9903.
[253] Neri, G.; Walsh, J. J.; Wilson, C.; Reynal, A.; Lim, J. Y. C.; Li, X.; White, A. J. P.; Long, N. J.; Durrant, J. R.; Cowan, A. J. *Phys. Chem. Chem. Phys.* **2015**, *17*, 1562.
[254] Kou, Y.; Nabetani, Y.; Masui, D.; Shimada, T.; Takagi, S.; Tachibana, H.; Inoue, H. *J. Am. Chem. Soc.* **2014**, *136*, 6021.
[255] Kou, Y.; Nakatani, S.; Sunagawa, G.; Tachikawa, Y.; Masui, D.; Shimada, T.; Takagi, S.; Tryk, D. A.; Nabetani, Y.; Tachibana, H.; Inoue, H. *J. Catal.* **2014**, *310*, 57.
[256] Kobayashi, K.; Kikuchi, T.; Kitagawa, S.; Tanaka, K. *Angew. Chem. Int. Ed.* **2014**, *53*, 11813.
[257] Costentin, C.; Drouet, S.; Robert, M.; Savéant, J.-M. *Science* **2012**, *338*, 90.
[258] Bonin, J.; Robert, M.; Routier, M. *J. Am. Chem. Soc.* **2014**, *136*, 16768.
[259] Seshadri, G.; Lin, C.; Bocarsly, A. B. *J. Electroanal. Chem.* **1994**, *372*, 145.
[260] Barton, E. E.; Rampulla, D. M.; Bocarsly, A. B. *J. Am. Chem. Soc.* **2008**, *130*, 6342.
[261] Barton Cole, E.; Lakkaraju, P. S.; Rampulla, D. M.; Morris, A. J.; Abelev, E.; Bocarsly, A. B. *J. Am. Chem. Soc.* **2010**, *132*, 11539.
[262] Morris, A. J.; McGibbon, R. T.; Bocarsly, A. B. *ChemSusChem* **2011**, *4*, 191.
[263] Costentin, C.; Canales, J. C.; Haddou, B.; Savéant, J.-M. *J. Am. Chem. Soc.* **2013**, *135*, 17671.
[264] Morris, A. J.; Meyer, G. J.; Fujita, E. *Acc. Chem. Res.* **2009**, *42*, 1983.
[265] Windle, C. D.; Perutz, R. N. *Coord. Chem. Rev.* **2012**, *256*, 2562.
[266] Parkinson, B. A.; Weaver, P. F. *Nature* **1984**, *309*, 148.
[267] Reda, T.; Plugge, C. M.; Abram, N. J.; Hirst, J. *Proc. Natl. Acad. Sci. U. S. A.* **2008**, *105*, 10654.
[268] Bassegoda, A.; Madden, C.; Wakerley, D. W.; Reisner, E.; Hirst, J. *J. Am. Chem. Soc.* **2014**, *136*, 15473.
[269] Can, M.; Armstrong, F. A.; Ragsdale, S. W. *Chem. Rev.* **2014**, *114*, 4149.

[270] Wang, V. C.-C.; Ragsdale, S. W.; Armstrong, F. A. In *The Metal-Driven Biogeochemistry of Gaseous Compounds in the Environment*; Kroneck, P. M. H., Torres, M. E. S., Eds.; Springer Netherlands: 2014; Vol. 14, p 71.
[271] McKone, J. R.; Lewis, N. S.; Gray, H. B. *Chem. Mater.* **2013**, *26*, 407.
[272] Döscher, H.; Geisz, J. F.; Deutsch, T. G.; Turner, J. A. *Energy Environ. Sci.* **2014**, *7*, 2951.
[273] Newman, J.; Hoertz, P. G.; Bonino, C. A.; Trainham, J. A. *J. Electrochem. Soc.* **2012**, *159*, A1722.
[274] Pinaud, B. A.; Benck, J. D.; Seitz, L. C.; Forman, A. J.; Chen, Z.; Deutsch, T. G.; James, B. D.; Baum, K. N.; Baum, G. N.; Ardo, S.; Wang, H.; Miller, E.; Jaramillo, T. F. *Energy Environ. Sci.* **2013**, *6*, 1983.
[275] Herron, J. A.; Kim, J.; Upadhye, A. A.; Huber, G. W.; Maravelias, C. T. *Energy Environ. Sci.* **2015**, *8*, 126.
[276] Linsebigler, A. L.; Lu, G.; Yates, J. T. *Chem. Rev.* **1995**, *95*, 735.
[277] Walter, M. G.; Warren, E. L.; McKone, J. R.; Boettcher, S. W.; Mi, Q.; Santori, E. A.; Lewis, N. S. *Chem. Rev.* **2010**, *110*, 6446.
[278] Newman, J. *J. Electrochem. Soc.* **2013**, *160*, F309.
[279] Grätzel, M. *Nature* **2001**, *414*, 338.
[280] Minggu, L. J.; Wan Daud, W. R.; Kassim, M. B. *Int. J. Hydrogen Energy* **2010**, *35*, 5233.
[281] Li, Z.; Luo, W.; Zhang, M.; Feng, J.; Zou, Z. *Energy Environ. Sci.* **2013**, *6*, 347.
[282] Prévot, M. S.; Sivula, K. *J. Phys. Chem. C* **2013**, *117*, 17879.
[283] Yang, X.; Liu, R.; He, Y.; Thorne, J.; Zheng, Z.; Wang, D. *Nano Res.* **2015**, *8*, 56.
[284] Li, J.; Wu, N. *Catal. Sci. Tech.* **2015**, *5*, 1360.
[285] Kelly, N. A.; Gibson, T. L. *Int. J. Hydrogen Energy* **2006**, *31*, 1658.
[286] Park, J. H.; Bard, A. J. *Electrochem. Solid-State Lett.* **2006**, *9*, E5.
[287] Yamane, S.; Kato, N.; Kojima, S.; Imanishi, A.; Ogawa, S.; Yoshida, N.; Nonomura, S.; Nakato, Y. *J. Phys. Chem. C* **2009**, *113*, 14575.
[288] Li, L.; Duan, L.; Xu, Y.; Gorlov, M.; Hagfeldt, A.; Sun, L. *Chem. Commun.* **2010**, *46*, 7307.
[289] Brillet, J.; Cornuz, M.; Formal, F. L.; Yum, J.-H.; Grätzel, M.; Sivula, K. *J. Mater. Res.* **2010**, *25*, 17.
[290] Brillet, J.; Yum, J.-H.; Cornuz, M.; Hisatomi, T.; Solarska, R.; Augustynski, J.; Graetzel, M.; Sivula, K. *Nat. Photon.* **2012**, *6*, 824.
[291] Tong, L.; Iwase, A.; Nattestad, A.; Bach, U.; Weidelener, M.; Gotz, G.; Mishra, A.; Bauerle, P.; Amal, R.; Wallace, G. G.; Mozer, A. J. *Energy Environ. Sci.* **2012**, *5*, 9472.
[292] Zhao, Y.; Swierk, J. R.; Megiatto, J. D.; Sherman, B.; Youngblood, W. J.; Qin, D.; Lentz, D. M.; Moore, A. L.; Moore, T. A.; Gust, D.; Mallouk, T. E. *Proc. Natl. Acad. Sci. U. S. A.* **2012**, *109*, 15612.
[293] Lin, C.-Y.; Lai, Y.-H.; Mersch, D.; Reisner, E. *Chem. Sci.* **2012**, *3*, 3482.
[294] Alibabaei, L.; Brennaman, M. K.; Norris, M. R.; Kalanyan, B.; Song, W.; Losego, M. D.; Concepcion, J. J.; Binstead, R. A.; Parsons, G. N.; Meyer, T. J. *Proc. Natl. Acad. Sci. U. S. A.* **2013**, *110*, 20008.
[295] Abdi, F. F.; Han, L.; Smets, A. H. M.; Zeman, M.; Dam, B.; van de Krol, R. *Nat. Commun.* **2013**, *4*, 2195.
[296] Han, L.; Abdi, F. F.; van de Krol, R.; Liu, R.; Huang, Z.; Lewerenz, H.-J.; Dam, B.; Zeman, M.; Smets, A. H. M. *ChemSusChem* **2014**, *7*, 2832.
[297] Modestino, M. A.; Walczak, K. A.; Berger, A.; Evans, C. M.; Haussener, S.; Koval, C.; Newman, J. S.; Ager, J. W.; Segalman, R. A. *Energy Environ. Sci.* **2014**, *7*, 297.

[298] Bornoz, P.; Abdi, F. F.; Tilley, S. D.; Dam, B.; van de Krol, R.; Grätzel, M.; Sivula, K. *J. Phys. Chem. C* **2014**, *118*, 16959.
[299] Ding, C.; Qin, W.; Wang, N.; Liu, G.; Wang, Z.; Yan, P.; Shi, J.; Li, C. *Phys. Chem. Chem. Phys.* **2014**, *16*, 15608.
[300] Chen, Y.-S.; Manser, J. S.; Kamat, P. V. *J. Am. Chem. Soc.* **2015**, *137*, 974.
[301] Nozik, A. J. *Appl. Phys. Lett.* **1977**, *30*, 567.
[302] Haussener, S.; Xiang, C.; Spurgeon, J. M.; Ardo, S.; Lewis, N. S.; Weber, A. Z. *Energy Environ. Sci.* **2012**, *5*, 9922.
[303] Haussener, S.; Hu, S.; Xiang, C.; Weber, A. Z.; Lewis, N. S. *Energy Environ. Sci.* **2013**, *6*, 3605.
[304] Seger, B.; Castelli, I. E.; Vesborg, P. C. K.; Jacobsen, K. W.; Hansen, O.; Chorkendorff, I. *Energy Environ. Sci.* **2014**, *7*, 2397.
[305] Singh, M. R.; Stevens, J. C.; Weber, A. Z. *J. Electrochem. Soc.* **2014**, *161*, E3283.
[306] Reece, S. Y.; Hamel, J. A.; Sung, K.; Jarvi, T. D.; Esswein, A. J.; Pijpers, J. J. H.; Nocera, D. G. *Science* **2011**, *334*, 645.
[307] Liu, C.; Tang, J.; Chen, H. M.; Liu, B.; Yang, P. *Nano Lett.* **2013**, *13*, 2989.
[308] Liu, B.; Wu, C.-H.; Miao, J.; Yang, P. *ACS Nano* **2014**, *8*, 11739.
[309] Walczak, K.; Chen, Y.; Karp, C.; Beeman, J. W.; Shaner, M.; Spurgeon, J.; Sharp, I. D.; Amashukeli, X.; West, W.; Jin, J.; Lewis, N. S.; Xiang, C. *ChemSusChem* **2015**, *8*, 544.
[310] Wilker, M. B.; Shinopoulos, K. E.; Brown, K. A.; Mulder, D. W.; King, P. W.; Dukovic, G. *J. Am. Chem. Soc.* **2014**, *136*, 4316.
[311] Yin, Y.; Alivisatos, A. P. *Nature* **2005**, *437*, 664.
[312] Burda, C.; Chen, X.; Narayanan, R.; El-Sayed, M. A. *Chem. Rev.* **2005**, *105*, 1025.
[313] Bawendi, M. G.; Steigerwald, M. L.; Brus, L. E. *Annu. Rev. Phys. Chem.* **1990**, *41*, 477.
[314] Cozzoli, P. D.; Pellegrino, T.; Manna, L. *Chem. Soc. Rev.* **2006**, *35*, 1195.
[315] Brus, L. *J. Phys. Chem.* **1986**, *90*, 2555.
[316] Talapin, D. V.; Lee, J.-S.; Kovalenko, M. V.; Shevchenko, E. V. *Chem. Rev.* **2009**, *110*, 389.
[317] Wilker, M. B.; Schnitzenbaumer, K. J.; Dukovic, G. *Isr. J. Chem.* **2012**, *52*, 1002.
[318] Maeda, K.; Teramura, K.; Lu, D.; Takata, T.; Saito, N.; Inoue, Y.; Domen, K. *Nature* **2006**, *440*, 295.
[319] Osterloh, F. E. *Chem. Mater.* **2008**, *20*, 35.
[320] Kudo, A.; Miseki, Y. *Chem. Soc. Rev.* **2009**, *38*, 253.
[321] Maeda, K.; Domen, K. *J. Phys. Chem. Lett.* **2010**, *1*, 2655.
[322] Maeda, K.; Xiong, A.; Yoshinaga, T.; Ikeda, T.; Sakamoto, N.; Hisatomi, T.; Takashima, M.; Lu, D.; Kanehara, M.; Setoyama, T.; Teranishi, T.; Domen, K. *Angew. Chem. Int. Ed.* **2010**, *49*, 4096.
[323] Maeda, K.; Abe, R.; Domen, K. *J. Phys. Chem. C* **2011**, *115*, 3057.
[324] Maeda, K.; Domen, K. *MRS Bull.* **2011**, *36*, 25.
[325] Sato, S.; Arai, T.; Morikawa, T.; Uemura, K.; Suzuki, T. M.; Tanaka, H.; Kajino, T. *J. Am. Chem. Soc.* **2011**, *133*, 15240.
[326] Sasaki, Y.; Kato, H.; Kudo, A. *J. Am. Chem. Soc.* **2013**, *135*, 5441.
[327] Moriya, Y.; Takata, T.; Domen, K. *Coord. Chem. Rev.* **2013**, *257*, 1957.
[328] Sekizawa, K.; Maeda, K.; Domen, K.; Koike, K.; Ishitani, O. *J. Am. Chem. Soc.* **2013**, *135*, 4596.
[329] Abe, R.; Shinmei, K.; Koumura, N.; Hara, K.; Ohtani, B. *J. Am. Chem. Soc.* **2013**, *135*, 16872.
[330] Wang, D.; Hisatomi, T.; Takata, T.; Pan, C.; Katayama, M.; Kubota, J.; Domen, K. *Angew. Chem. Int. Ed.* **2013**, *52*, 11252.

[331] Martin, D. J.; Reardon, P. J. T.; Moniz, S. J. A.; Tang, J. *J. Am. Chem. Soc.* **2014**, *136*, 12568.
[332] Yang, M.-Q.; Zhang, N.; Pagliaro, M.; Xu, Y.-J. *Chem. Soc. Rev.* **2014**, *43*, 8240.
[333] Yang, L.; Zhou, H.; Fan, T.; Zhang, D. *Phys. Chem. Chem. Phys.* **2014**, *16*, 6810.
[334] Li, R.; Han, H.; Zhang, F.; Wang, D.; Li, C. *Energy Environ. Sci.* **2014**, *7*, 1369.
[335] Wang, Q.; Hisatomi, T.; Ma, S. S. K.; Li, Y.; Domen, K. *Chem. Mater.* **2014**, *26*, 4144.
[336] Li, P.; Zhou, Y.; Li, H.; Xu, Q.; Meng, X.; Wang, X.; Xiao, M.; Zou, Z. *Chem. Commun.* **2015**, *51*, 800.
[337] Iwashina, K.; Iwase, A.; Ng, Y. H.; Amal, R.; Kudo, A. *J. Am. Chem. Soc.* **2015**, *137*, 604.
[338] Tachibana, Y.; Moser, J. E.; Grätzel, M.; Klug, D. R.; Durrant, J. R. *J. Phys. Chem.* **1996**, *100*, 20056.
[339] Tseng, H.-W.; Wilker, M. B.; Damrauer, N. H.; Dukovic, G. *J. Am. Chem. Soc.* **2013**, *135*, 3383.
[340] Bott, A. *Curr. Sep.* **1998**, *3*, 87.
[341] Beranek, R. *Adv. Phys. Chem.* **2011**, 786759.
[342] Scanlon, D. O.; Dunnill, C. W.; Buckeridge, J.; Shevlin, S. A.; Logsdail, A. J.; Woodley, S. M.; Catlow, C. R. A.; Powell, M. J.; Palgrave, R. G.; Parkin, I. P.; Watson, G. W.; Keal, T. W.; Sherwood, P.; Walsh, A.; Sokol, A. A. *Nat. Mater.* **2013**, *12*, 798.
[343] Woolerton, T. W.; Sheard, S.; Chaudhary, Y. S.; Armstrong, F. A. *Energy Environ. Sci.* **2012**, *5*, 7470.
[344] Chu, S. In *University of Oxford Romanes Lecture* Oxford, 2014.
[345] Hu, S.; Shaner, M. R.; Beardslee, J. A.; Lichterman, M.; Brunschwig, B. S.; Lewis, N. S. *Science* **2014**, *344*, 1005.
[346] Shaner, M. R.; Hu, S.; Sun, K.; Lewis, N. S. *Energy Environ. Sci.* **2015**, *8*, 203.
[347] Lichterman, M. F.; Carim, A. I.; McDowell, M. T.; Hu, S.; Gray, H. B.; Brunschwig, B. S.; Lewis, N. S. *Energy Environ. Sci.* **2014**, *7*, 3334.
[348] Sun, K.; Saadi, F. H.; Lichterman, M. F.; Hale, W. G.; Wang, H.-P.; Zhou, X.; Plymale, N. T.; Omelchenko, S. T.; He, J.-H.; Papadantonakis, K. M.; Brunschwig, B. S.; Lewis, N. S. *Proc. Natl. Acad. Sci. U. S. A.* **2015**, *112*, 3612.
[349] Hamann, T. *Science* **2014**, *345*, 1566.
[350] Armstrong, F. A.; Hirst, J. *Proc. Natl. Acad. Sci. U. S. A.* **2011**, *108*, 14049.
[351] Kato, M.; Zhang, J. Z.; Paul, N.; Reisner, E. *Chem. Soc. Rev.* **2014**, *43*, 6485.
[352] Kato, M.; Cardona, T.; Rutherford, A. W.; Reisner, E. *J. Am. Chem. Soc.* **2012**, *134*, 8332.
[353] Kato, M.; Cardona, T.; Rutherford, A. W.; Reisner, E. *J. Am. Chem. Soc.* **2013**, *135*, 10610.
[354] Noji, T.; Suzuki, H.; Gotoh, T.; Iwai, M.; Ikeuchi, M.; Tomo, T.; Noguchi, T. *J. Phys. Chem. Lett.* **2011**, *2*, 2448.
[355] Badura, A.; Kothe, T.; Schuhmann, W.; Rögner, M. *Energy Environ. Sci.* **2011**, *4*, 3263.
[356] Wang, F.; Liu, X.; Willner, I. *Adv. Mater.* **2013**, *25*, 349.
[357] Yehezkeli, O.; Tel-Vered, R.; Michaeli, D.; Willner, I.; Nechushtai, R. *Photosynth. Res.* **2014**, *120*, 71.
[358] Yehezkeli, O.; Tel-Vered, R.; Wasserman, J.; Trifonov, A.; Michaeli, D.; Nechushtai, R.; Willner, I. *Nat. Commun.* **2012**, *3*, 742.
[359] Cuendet, P.; Grätzel, M.; Pelaprat, M. L. *J. Electroanal. Chem.* **1984**, *181*, 173.
[360] Yadav, R. K.; Baeg, J.-O.; Oh, G. H.; Park, N.-J.; Kong, K.-j.; Kim, J.; Hwang, D. W.; Biswas, S. K. *J. Am. Chem. Soc.* **2012**, *134*, 11455.

[361] Yadav, R. K.; Baeg, J.-O.; Kumar, A.; Kong, K.-j.; Oh, G. H.; Park, N.-J. *J. Mater. Chem. A* **2014**, *2*, 5068.
[362] Liu, J.; Cazelles, R.; Chen, Z. P.; Zhou, H.; Galarneau, A.; Antonietti, M. *Phys. Chem. Chem. Phys.* **2014**, *16*, 14699.
[363] Bachmeier, A.; Armstrong, F. *Curr. Opin. Chem. Biol.* **2015**, *25*, 141.
[364] Zadvornyy, O. A.; Lucon, J. E.; Gerlach, R.; Zorin, N. A.; Douglas, T.; Elgren, T. E.; Peters, J. W. *J. Inorg. Biochem.* **2012**, *106*, 151.
[365] Sakai, T.; Mersch, D.; Reisner, E. *Angew. Chem. Int. Ed.* **2013**, *52*, 12313.
[366] Roth, L. E.; Nguyen, J. C.; Tezcan, F. A. *J. Am. Chem. Soc.* **2010**, *132*, 13672.
[367] Krassen, H.; Schwarze, A.; Friedrich, B.; Ataka, K.; Lenz, O.; Heberle, J. *ACS Nano* **2009**, *3*, 4055.
[368] Lubner, C. E.; Applegate, A. M.; Knörzer, P.; Ganago, A.; Bryant, D. A.; Happe, T.; Golbeck, J. H. *Proc. Natl. Acad. Sci. U. S. A.* **2011**, *108*, 20988.
[369] Samuel, A. P. S.; Co, D. T.; Stern, C. L.; Wasielewski, M. R. *J. Am. Chem. Soc.* **2010**, *132*, 8813.
[370] King, P. W. *BBA-Bioenergetics* **2013**, *1827*, 949.
[371] Brown, K. A.; Wilker, M. B.; Boehm, M.; Dukovic, G.; King, P. W. *J. Am. Chem. Soc.* **2012**, *134*, 5627.
[372] McDonald, T. J.; Svedruzic, D.; Kim, Y.-H.; Blackburn, J. L.; Zhang, S. B.; King, P. W.; Heben, M. J. *Nano Lett.* **2007**, *7*, 3528.
[373] Svedružić, D.; Blackburn, J. L.; Tenent, R. C.; Rocha, J.-D. R.; Vinzant, T. B.; Heben, M. J.; King, P. W. *J. Am. Chem. Soc.* **2011**, *133*, 4299.
[374] Krishnan, S.; Armstrong, F. A. *Chem. Sci.* **2012**, *3*, 1015.
[375] Blakemore, J. D.; Gupta, A.; Warren, J. J.; Brunschwig, B. S.; Gray, H. B. *J. Am. Chem. Soc.* **2013**, *135*, 18288.
[376] Adamska, A.; Silakov, A.; Lambertz, C.; Rüdiger, O.; Happe, T.; Reijerse, E.; Lubitz, W. *Angew. Chem. Int. Ed.* **2012**, *51*, 11458
[377] Reisner, E.; Fontecilla-Camps, J. C.; Armstrong, F. A. *Chem. Commun.* **2009**, 550.
[378] Reisner, E.; Powell, D. J.; Cavazza, C.; Fontecilla-Camps, J. C.; Armstrong, F. A. *J. Am. Chem. Soc.* **2009**, *131*, 18457.
[379] Woolerton, T. W.; Sheard, S.; Reisner, E.; Pierce, E.; Ragsdale, S. W.; Armstrong, F. A. *J. Am. Chem. Soc.* **2010**, *132*, 2132.
[380] Woolerton, T. W.; Sheard, S.; Pierce, E.; Ragsdale, S. W.; Armstrong, F. A. *Energy Environ. Sci.* **2011**, *4*, 2393.
[381] Chaudhary, Y. S.; Woolerton, T. W.; Allen, C. S.; Warner, J. H.; Pierce, E.; Ragsdale, S. W.; Armstrong, F. A. *Chem. Commun.* **2012**, *48*, 58.
[382] Brown, K. A.; Dayal, S.; Ai, X.; Rumbles, G.; King, P. W. *J. Am. Chem. Soc.* **2010**, *132*, 9672.
[383] Qin, P.; Zhu, H.; Edvinsson, T.; Boschloo, G.; Hagfeldt, A.; Sun, L. *J. Am. Chem. Soc.* **2008**, *130*, 8570.
[384] Gardner, J. M.; Beyler, M.; Karnahl, M.; Tschierlei, S.; Ott, S.; Hammarström, L. *J. Am. Chem. Soc.* **2012**, *134*, 19322.
[385] Ji, Z.; He, M.; Huang, Z.; Ozkan, U.; Wu, Y. *J. Am. Chem. Soc.* **2013**, *135*, 11696.
[386] Mulder, D. W.; Boyd, E. S.; Sarma, R.; Lange, R. K.; Endrizzi, J. A.; Broderick, J. B.; Peters, J. W. *Nature* **2010**, *465*, 248.
[387] Nicolet, Y.; Piras, C.; Legrand, P.; Hatchikian, E. C.; Fontecilla-Camps, J. C. *Structure* **1999**, *7*, 13.
[388] Peters, J. W.; Lanzilotta, W. N.; Lemon, B. J.; Seefeldt, L. C. *Science* **1998**, *282*, 1853.
[389] Page, C. C.; Moser, C. C.; Chen, X.; Dutton, P. L. *Nature* **1999**, *402*, 47.

[390] Moser, C. C.; Keske, J. M.; Warncke, K.; Farid, R. S.; Dutton, P. L. *Nature* **1992**, *355*, 796.
[391] Topoglidis, E.; Discher, B. M.; Moser, C. C.; Dutton, P. L.; Durrant, J. R. *ChemBioChem* **2003**, *4*, 1332.
[392] Hong, G.; Pachter, R. *ACS Chem. Biol.* **2012**, *7*, 1268.
[393] Cohen, J.; Kim, K.; King, P.; Seibert, M.; Schulten, K. *Structure* **2005**, *13*, 1321.
[394] Hong, G.; Cornish, A. J.; Hegg, E. L.; Pachter, R. *BBA-Bioenergetics* **2011**, *1807*, 510.
[395] Long, H.; King, P. W.; Chang, C. H. *J. Phys. Chem. B* **2014**, *118*, 890.
[396] Cornish, A. J.; Gärtner, K.; Yang, H.; Peters, J. W.; Hegg, E. L. *J. Biol. Chem.* **2011**, *286*, 38341.
[397] Ginovska-Pangovska, B.; Ho, M.-H.; Linehan, J. C.; Cheng, Y.; Dupuis, M.; Raugei, S.; Shaw, W. J. *BBA-Bioenergetics* **2014**, *1837*, 131.
[398] Myers, W. K.; Stich, T. A.; Suess, D. L. M.; Kuchenreuther, J. M.; Swartz, J. R.; Britt, R. D. *J. Am. Chem. Soc.* **2014**, *136*, 12237.
[399] Mulder, D. W.; Ratzloff, M. W.; Shepard, E. M.; Byer, A. S.; Noone, S. M.; Peters, J. W.; Broderick, J. B.; King, P. W. *J. Am. Chem. Soc.* **2013**, *135*, 6921.
[400] Foster, C. E.; Krämer, T.; Wait, A. F.; Parkin, A.; Jennings, D. P.; Happe, T.; McGrady, J. E.; Armstrong, F. A. *J. Am. Chem. Soc.* **2012**, *134*, 7553.
[401] Lemon, B. J.; Peters, J. W. *Biochemistry* **1999**, *38*, 12969.
[402] Goldet, G.; Brandmayr, C.; Stripp, S. T.; Happe, T.; Cavazza, C.; Fontecilla-Camps, J. C.; Armstrong, F. A. *J. Am. Chem. Soc.* **2009**, *131*, 14979.
[403] Baffert, C.; Bertini, L.; Lautier, T.; Greco, C.; Sybirna, K.; Ezanno, P.; Etienne, E.; Soucaille, P.; Bertrand, P.; Bottin, H.; Meynial-Salles, I.; De Gioia, L.; Léger, C. *J. Am. Chem. Soc.* **2011**, *133*, 2096.
[404] Stripp, S. T.; Goldet, G.; Brandmayr, C.; Sanganas, O.; Vincent, K. A.; Haumann, M.; Armstrong, F. A.; Happe, T. *Proc. Natl. Acad. Sci. U. S. A.* **2009**, *106*, 17331.
[405] Swanson, K. D.; Ratzloff, M. W.; Mulder, D. W.; Artz, J. H.; Ghose, S.; Hoffman, A.; White, S.; Zadvornyy, O. A.; Broderick, J. B.; Bothner, B.; King, P. W.; Peters, J. W. *J. Am. Chem. Soc.* **2015**, *137*, 1809.
[406] Berggren, G.; Adamska, A.; Lambertz, C.; Simmons, T. R.; Esselborn, J.; Atta, M.; Gambarelli, S.; Mouesca, J. M.; Reijerse, E.; Lubitz, W.; Happe, T.; Artero, V.; Fontecave, M. *Nature* **2013**, *499*, 66.
[407] Esselborn, J.; Lambertz, C.; Adamska-Venkatesh, A.; Simmons, T.; Berggren, G.; Noth, J.; Siebel, J.; Hemschemeier, A.; Artero, V.; Reijerse, E.; Fontecave, M.; Lubitz, W.; Happe, T. *Nat. Chem. Biol.* **2013**, *9*, 607.
[408] Hexter, S. V. *D. Phil. Thesis*, University of Oxford, 2014.
[409] Camara, J. M.; Rauchfuss, T. B. *Nat. Chem.* **2012**, *4*, 26.
[410] Finkelmann, A. R.; Stiebritz, M. T.; Reiher, M. *Chem. Sci.* **2014**, *5*, 215.
[411] Lambertz, C.; Chernev, P.; Klingan, K.; Leidel, N.; Sigfridsson, K. G. V.; Happe, T.; Haumann, M. *Chem. Sci.* **2014**, *5*, 1187.
[412] Bruschi, M.; Greco, C.; Kaukonen, M.; Fantucci, P.; Ryde, U.; De Gioia, L. *Angew. Chem. Int. Ed.* **2009**, *48*, 3503.
[413] von Abendroth, G.; Stripp, S. T.; Silakov, A.; Croux, C.; Soucaille, P.; Girbal, L.; Happe, T. *Int. J. Hydrogen Energy* **2008**, *33*, 6076.
[414] Gorwa, M. F.; Croux, C.; Soucaille, P. *J. Bacteriol.* **1996**, *178*, 2668.
[415] Garcin, E.; Vernede, X.; Hatchikian, E. C.; Volbeda, A.; Frey, M.; Fontecilla-Camps, J. C. *Structure* **1999**, *7*, 557.
[416] Montet, Y.; Amara, P.; Volbeda, A.; Vernede, X.; Hatchikian, E. C.; Field, M. J.; Frey, M.; Fontecilla-Camps, J. C. *Nat. Struct. Mol. Biol.* **1997**, *4*, 523.

[417] Baltazar, C. A.; Teixeira, V.; Soares, C. *J. Biol. Inorg. Chem.* **2012**, *17*, 543.
[418] Buhrke, T.; Lenz, O.; Krauss, N.; Friedrich, B. *J. Biol. Chem.* **2005**, *280*, 23791.
[419] Lauterbach, L.; Lenz, O. *J. Am. Chem. Soc.* **2013**, *135*, 17897.
[420] Wulff, P.; Day, C. C.; Sargent, F.; Armstrong, F. A. *Proc. Natl. Acad. Sci. U. S. A.* **2014**, *111*, 6606.
[421] Fritsch, J.; Lenz, O.; Friedrich, B. *Nat. Rev. Micro.* **2013**, *11*, 106.
[422] Szőri-Dorogházi, E.; Maróti, G.; Szőri, M.; Nyilasi, A.; Rákhely, G.; Kovács, K. L. *PLoS ONE* **2012**, *7*, e34666.
[423] Ogata, H.; Nishikawa, K.; Lubitz, W. *Nature* **2015**, *520*, 571.
[424] Dementin, S.; Burlat, B.; De Lacey, A. L.; Pardo, A.; Adryanczyk-Perrier, G.; Guigliarelli, B.; Fernandez, V. M.; Rousset, M. *J. Biol. Chem.* **2004**, *279*, 10508.
[425] Ogata, H.; Hirota, S.; Nakahara, A.; Komori, H.; Shibata, N.; Kato, T.; Kano, K.; Higuchi, Y. *Structure* **2005**, *13*, 1635.
[426] Volbeda, A.; Martin, L.; Cavazza, C.; Matho, M.; Faber, B.; Roseboom, W.; Albracht, S. J.; Garcin, E.; Rousset, M.; Fontecilla-Camps, J. *J. Biol. Inorg. Chem.* **2005**, *10*, 239.
[427] van Gastel, M.; Stein, M.; Brecht, M.; Schröder, O.; Lendzian, F.; Bittl, R.; Ogata, H.; Higuchi, Y.; Lubitz, W. *J. Biol. Inorg. Chem.* **2006**, *11*, 41.
[428] Bleijlevens, B.; van Broekhuizen, F.; De Lacey, A.; Roseboom, W.; Fernandez, V.; Albracht, S. J. *J. Biol. Inorg. Chem.* **2004**, *9*, 743.
[429] Hidalgo, R.; Ash, P. A.; Healy, A. J.; Vincent, K. A. *Angew. Chem. Int. Ed.* **2015**, *54*, 7110.
[430] Murphy, B. J.; Hidalgo, R.; Roessler, M. M.; Evans, R. M.; Ash, P. A.; Myers, W. K.; Vincent, K. A.; Armstrong, F. A. *J. Am. Chem. Soc.* **2015**, *137*, 8484.
[431] Evans, R. M., Mechanism of Hydrogen Activation by [NiFe]-hydrogenases, personal communication, 2015.
[432] Goris, T.; Wait, A. F.; Saggu, M.; Fritsch, J.; Heidary, N.; Stein, M.; Zebger, I.; Lendzian, F.; Armstrong, F. A.; Friedrich, B.; Lenz, O. *Nat. Chem. Biol.* **2011**, *7*, 310.
[433] Pandelia, M.-E.; Nitschke, W.; Infossi, P.; Giudici-Orticoni, M.-T.; Bill, E.; Lubitz, W. *Proc. Natl. Acad. Sci. U. S. A.* **2011**, *108*, 6097.
[434] Parkin, A.; Sargent, F. *Curr. Opin. Chem. Biol.* **2012**, *16*, 26.
[435] Evans, R. M.; Parkin, A.; Roessler, M. M.; Murphy, B. J.; Adamson, H.; Lukey, M. J.; Sargent, F.; Volbeda, A.; Fontecilla-Camps, J. C.; Armstrong, F. A. *J. Am. Chem. Soc.* **2013**, *135*, 2694.
[436] Riethausen, J.; Rüdiger, O.; Gärtner, W.; Lubitz, W.; Shafaat, H. S. *ChemBioChem* **2013**, *14*, 1714.
[437] Volbeda, A.; Amara, P.; Iannello, M.; De Lacey, A. L.; Cavazza, C.; Fontecilla-Camps, J. C. *Chem. Commun.* **2013**, *49*, 7061.
[438] Marques, M. C.; Coelho, R.; De Lacey, A. L.; Pereira, I. A. C.; Matias, P. M. *J. Mol. Biol.* **2010**, *396*, 893.
[439] Medina, M.; Claude Hatchikian, E.; Cammack, R. *BBA-Bioenergetics* **1996**, *1275*, 227.
[440] Darensbourg, M. Y.; Weigand, W. *Eur. J. Inorg. Chem.* **2011**, *2011*, 994.
[441] Dobbek, H.; Gremer, L.; Kiefersauer, R.; Huber, R.; Meyer, O. *Proc. Natl. Acad. Sci. U. S. A.* **2002**, *99*, 15971.
[442] Ragsdale, S. *Crit. Rev. Biochem. Mol. Biol.* **2004**, *39*, 165.
[443] Jeoung, J.-H.; Fesseler, J.; Goetzl, S.; Dobbek, H. In *The Metal-Driven Biogeochemistry of Gaseous Compounds in the Environment*; Kroneck, P. M. H., Torres, M. E. S., Eds.; Springer Netherlands: 2014; Vol. 14, p 37.
[444] Wang, V. C.-C.; Ragsdale, S. W.; Armstrong, F. A. *ChemBioChem* **2013**, *14*, 1845.

[445] Svetlitchnyi, V.; Dobbek, H.; Meyer-Klaucke, W.; Meins, T.; Thiele, B.; Römer, P.; Huber, R.; Meyer, O. *Proc. Natl. Acad. Sci. U. S. A.* **2004**, *101*, 446.
[446] Dobbek, H.; Svetlitchnyi, V.; Gremer, L.; Huber, R.; Meyer, O. *Science* **2001**, *293*, 1281.
[447] Craft, J. L.; Ludden, P. W.; Brunold, T. C. *Biochemistry* **2002**, *41*, 1681.
[448] Gray, H. B.; Winkler, J. R. *Proc. Natl. Acad. Sci. U. S. A.* **2005**, *102*, 3534.
[449] Wu, M.; Ren, Q.; Durkin, A. S.; Daugherty, S. C.; Brinkac, L. M.; Dodson, R. J.; Madupu, R.; Sullivan, S. A.; Kolonay, J. F.; Nelson, W. C.; Tallon, L. J.; Jones, K. M.; Ulrich, L. E.; Gonzalez, J. M.; Zhulin, I. B.; Robb, F. T.; Eisen, J. A. *PLoS Genet* **2005**, *1*, e65.
[450] Jeoung, J.-H.; Dobbek, H. *J. Biol. Inorg. Chem.* **2012**, *17*, 167.
[451] Wang, P.-h.; Bruschi, M.; De Gioia, L.; Blumberger, J. *J. Am. Chem. Soc.* **2013**, *135*, 9493.
[452] Lindahl, P. A. *Biochemistry* **2002**, *41*, 2097.
[453] Lindahl, P. A. *Angew. Chem. Int. Ed.* **2008**, *47*, 4054.
[454] Feng, J.; Lindahl, P. A. *Biochemistry* **2004**, *43*, 1552.
[455] Jeoung, J.-H.; Dobbek, H. *Science* **2007**, *318*, 1461.
[456] Amara, P.; Mouesca, J.-M.; Volbeda, A.; Fontecilla-Camps, J. C. *Inorg. Chem.* **2011**, *50*, 1868.
[457] Lindahl, P. A. *J. Inorg. Biochem.* **2012**, *106*, 172.
[458] Tan, G. O.; Ensign, S. A.; Ciurli, S.; Scott, M. J.; Hedman, B.; Holm, R. H.; Ludden, P. W.; Korszun, Z. R.; Stephens, P. J.; Hodgson, K. O. *Proc. Natl. Acad. Sci. U. S. A.* **1992**, *89*, 4427.
[459] Ralston, C. Y.; Wang, H.; Ragsdale, S. W.; Kumar, M.; Spangler, N. J.; Ludden, P. W.; Gu, W.; Jones, R. M.; Patil, D. S.; Cramer, S. P. *J. Am. Chem. Soc.* **2000**, *122*, 10553.
[460] Gu, W.; Seravalli, J.; Ragsdale, S. W.; Cramer, S. P. *Biochemistry* **2004**, *43*, 9029.
[461] Kumar, M.; Lu, W. P.; Liu, L.; Ragsdale, S. W. *J. Am. Chem. Soc.* **1993**, *115*, 11646.
[462] Seravalli, J.; Ragsdale, S. W. *Biochemistry* **2008**, *47*, 6770.
[463] Svetlitchnyi, V.; Peschel, C.; Acker, G.; Meyer, O. *J. Bacteriol.* **2001**, *183*, 5134.
[464] Chen, Z.; Dinh, H. N.; Miller, E. *Photoelectrochemical Water Splitting: Standards, Experimental Methods, and Protocols*; Springer, 2013.
[465] Armstrong, F. A.; Belsey, N. A.; Cracknell, J. A.; Goldet, G.; Parkin, A.; Reisner, E.; Vincent, K. A.; Wait, A. F. *Chem. Soc. Rev.* **2009**, *38*, 36.
[466] Blanford, C. F. *Chem. Commun.* **2013**, *49*, 11130.
[467] Vincent, K. A.; Parkin, A.; Armstrong, F. A. *Chem. Rev.* **2007**, *107*, 4366.
[468] Léger, C. In *Practical Approaches to Biological Inorganic Chemistry*; Louro, R. R. C. O., Ed.; Elsevier: Oxford, 2013, p 179.
[469] Bard, A. J.; Faulkner, L. R. *Electrochemical Methods: Fundamentals and Applications*; 2nd ed.; John Wiley & Sons Inc.: New York, 2001.
[470] Fisher, A. C. *Electrode Dynamics*; Oxford University Press: Oxford, 1996.
[471] Wedler, G. *Lehrbuch der Physikalischen Chemie*; 5 ed.; WILEY-VCH: Weinheim, 2004.
[472] Atkins, P.; Paula, J. d. *Atkins' Physical Chemistry*; 9 ed.; Oxford University Press: Oxford, 2010.
[473] Léger, C.; Jones, A. K.; Albracht, S. P. J.; Armstrong, F. A. *J. Phys. Chem. B* **2002**, *106*, 13058.
[474] Ludwig, M.; Cracknell, J. A.; Vincent, K. A.; Armstrong, F. A.; Lenz, O. *J. Biol. Chem.* **2009**, *284*, 465.
[475] Brattain, W. H.; Garrett, C. G. B. *Bell Syst. Tech. J.* **1955**, *34*, 129.

[476] Bockris, J. O. M.; Khan, S. U. M. *Surface Electrochemistry: A Molecular Level Approach*; Plenum Press: New York, 1993.
[477] Myamlin, V. A.; Pleskov, Y. V. *Electrochemistry of Semiconductors*; Plenum Press: New York, 1967.
[478] Rajeshwar, K. In *Semiconductor Electrodes and Photoelectrochemistry*; Licht, S., Ed.; WILEY-VCH Weinheim, 2002, p 1.
[479] Finklea, H. O. In *Semiconductor Electrodes*; Finklea, H. O., Ed.; Elsevier Science Publishers: Amsterdam, 1988, p 1.
[480] Irebo, T.; Zhang, M.-T.; Markle, T. F.; Scott, A. M.; Hammarström, L. *J. Am. Chem. Soc.* **2012**.
[481] Tan, M. X.; Laibinis, P. E.; Nguyen, S. T.; Kesselman, J. M.; Stanton, C. E.; Lewis, N. S. In *Prog. Inorg. Chem.*; John Wiley & Sons, Inc.: 1994, p 21.
[482] Gelderman, K.; Lee, L.; Donne, S. W. *J. Chem. Educ.* **2007**, *84*, 685.
[483] Berger, T.; Anta, J. A.; Morales-Flórez, V. *J. Phys. Chem. C* **2012**, *116*, 11444.
[484] Kavan, L.; Kratochvilová, K.; Grätzel, M. *J. Electroanal. Chem.* **1995**, *394*, 93.
[485] Wang, H.; He, J.; Boschloo, G.; Lindström, H.; Hagfeldt, A.; Lindquist, S.-E. *J. Phys. Chem. B* **2001**, *105*, 2529.
[486] Zhang, Q.; Celorrio, V.; Bradley, K.; Eisner, F.; Cherns, D.; Yan, W.; Fermín, D. J. *J. Phys. Chem. C* **2014**, *118*, 18207.
[487] Boschloo, G.; Fitzmaurice, D. *J. Phys. Chem. B* **1999**, *103*, 2228.
[488] He, J.; Lindström, H.; Hagfeldt, A.; Lindquist, S.-E. *Sol. Energy Mater. Sol. Cells* **2000**, *62*, 265.
[489] Odobel, F.; Pellegrin, Y.; Gibson, E. A.; Hagfeldt, A.; Smeigh, A. L.; Hammarström, L. *Coord. Chem. Rev.* **2012**, *256*, 2414.
[490] Zhu, H.; Hagfeldt, A.; Boschloo, G. *J. Phys. Chem. C* **2007**, *111*, 17455.
[491] Gärtner, W. W. *Phys. Rev.* **1959**, *116*, 84.
[492] Sprunken, H. R.; Schumacher, R.; Schindler, R. N. *Farad. Discuss.* **1980**, *70*, 55.
[493] Randles, J. E. B. *Farad. Discuss.* **1947**, *1*, 11.
[494] Brett, C. M. A.; Oliveira Brett, A. M. *Electrochemistry: Principles, Methods, and Applications*; Oxford University Press: Oxford, 1993.
[495] Marcus, R. A. *Angew. Chem. Int. Ed.* **1993**, *32*, 1111.
[496] Levich, V.; Dogonadze, R. *Dokl. Akad. Nauk SSSR* **1959**, *124*, 123.
[497] Hush, N. S. *Electrochim. Acta* **1968**, *13*, 1005.
[498] Marcus, R. A.; Sutin, N. *BBA-Bioenergetics* **1985**, *811*, 265.
[499] Sutin, N.; Creutz, C. *J. Chem. Educ.* **1983**, *60*, 809.
[500] Sutin, N. *Acc. Chem. Res.* **1982**, *15*, 275.
[501] Marcus, R. A. *J. Phys. Chem.* **1956**, *24*, 966.
[502] Marcus, R. A. *Farad. Discuss.* **1960**, *29*, 21.
[503] Marcus, R. A. *J. Phys. Chem.* **1963**, *67*, 853.
[504] Marcus, R. A. *J. Phys. Chem.* **1965**, *43*, 679.
[505] Murov, S. L.; Carmichael, I.; Hug, G. L. *Handbook of Photochemistry*; 2 ed.; Marcel Dekker, Inc.: New York, 1993.
[506] Léger, C.; Bertrand, P. *Chem. Rev.* **2008**, *108*, 2379.
[507] Compton, R. G.; Banks, C. E. *Understanding Voltammetry*; 2 ed.; Imperial College Press: London, 2011.
[508] Miller, J. R.; Calcaterra, L. T.; Closs, G. L. *J. Am. Chem. Soc.* **1984**, *106*, 3047.
[509] Atkins, P. W.; de Paula, J.; Friedman, R. *Physical Chemistry: Quanta, Matter, and Change*; 2 ed.; Oxford University Press: Oxford, 2014.
[510] Oevering, H.; Paddon-Row, M. N.; Heppener, M.; Oliver, A. M.; Cotsaris, E.; Verhoeven, J. W.; Hush, N. S. *J. Am. Chem. Soc.* **1987**, *109*, 3258.

[511] Johnson, M. D.; Miller, J. R.; Green, N. S.; Closs, G. L. *J. Phys. Chem.* **1989**, *93*, 1173.
[512] Winkler, J. R.; Gray, H. B. *Chem. Rev.* **1992**, *92*, 369.
[513] Gray, H. B.; Winkler, J. R. *Chem. Phys. Lett.* **2009**, *483*, 1.
[514] Davis, W. B.; Svec, W. A.; Ratner, M. A.; Wasielewski, M. R. *Nature* **1998**, *396*, 60.
[515] Wielopolski, M. *Testing Molecular Wires: A Photophysical and Quantum Chemical Assay*; Springer-Verlag: Berlin Heidelberg, 2010.
[516] Shih, C.; Museth, A. K.; Abrahamsson, M.; Blanco-Rodriguez, A. M.; Di Bilio, A. J.; Sudhamsu, J.; Crane, B. R.; Ronayne, K. L.; Towrie, M.; Vlček, A.; Richards, J. H.; Winkler, J. R.; Gray, H. B. *Science* **2008**, *320*, 1760.
[517] Winkler, J. R.; Gray, H. B. *J. Am. Chem. Soc.* **2014**, *136*, 2930.
[518] Winkler, J. R.; Gray, H. B. *Chem. Rev.* **2014**, *114*, 3369.
[519] Sazanov, L. A.; Hinchliffe, P. *Science* **2006**, *311*, 1430.
[520] Hagen, W. R. *Dalton Trans.* **2006**, 4415.
[521] Drago, R. S. *Physical Methods for Chemists*; 2 ed.; Surfside Scientific Publishers: Gainesville, 1992.
[522] Hagen, W. R. *Biomolecular EPR Spectroscopy*; CRC Press: Boca Raton, 2008.
[523] Chasteen, N. D.; Snetsinger, P. A. In *Physical Methods in Bioinorganic Chemistry: Spectroscopy and Magnetism*; Lawrence Que, J., Ed.; University Science Books: Sausalito, 2000, p 187.
[524] Roessler, M. M. *D. Phil. Thesis*, University of Oxford, 2012.
[525] Wait, A. F.; Brandmayr, C.; Stripp, S. T.; Cavazza, C.; Fontecilla-Camps, J. C.; Happe, T.; Armstrong, F. A. *J. Am. Chem. Soc.* **2011**, *133*, 1282.
[526] Greco, C.; Bruschi, M.; De Gioia, L.; Ryde, U. *Inorg. Chem.* **2007**, *46*, 5911.
[527] Greco, C.; Bruschi, M.; Fantucci, P.; Ryde, U.; De Gioia, L. *ChemPhysChem* **2011**, *12*, 3376.
[528] Foster, C. E. *D. Phil. Thesis*, University of Oxford, 2012.
[529] Chernev, P.; Lambertz, C.; Brünje, A.; Leidel, N.; Sigfridsson, K. G. V.; Kositzki, R.; Hsieh, C.-H.; Yao, S.; Schiwon, R.; Driess, M.; Limberg, C.; Happe, T.; Haumann, M. *Inorg. Chem.* **2014**, *53*, 12164.
[530] Brown, K. L.; Clark, G. R.; Headford, C. E. L.; Marsden, K.; Roper, W. R. *J. Am. Chem. Soc.* **1979**, *101*, 503.
[531] Green, M. L. H.; Parkin, G.; Moynihan, K. J.; Prout, K. *J. Chem. Soc., Chem. Commun.* **1984**, 1540.
[532] Gambarotta, S.; Floriani, C.; Chiesi-Villa, A.; Guastini, C. *Organometallics* **1986**, *5*, 2425.
[533] Berke, H.; Bankhardt, W.; Huttner, G.; v. Seyerl, J.; Zsolnai, L. *Chem. Ber.* **1981**, *114*, 2754.
[534] Bell, R. P. In *Adv. Phys. Org. Chem.*; Gold, V., Ed.; Academic Press: 1966; Vol. Volume 4, p 1.
[535] Hilal, S. H.; Bornander, L. L.; Carreira, L. A. *QSAR & Combinatorial Science* **2005**, *24*, 631.
[536] Guthrie, J. P. *Can. J. Chem.* **1975**, *53*, 898.
[537] Wait, A. F. *D. Phil. Thesis*, University of Oxford, 2011.
[538] Guigliarelli, B.; Bertrand, P. In *Adv. Inorg. Chem.*; Sykes, A. G., Ed.; Academic Press: 1999; Vol. Volume 47, p 421.
[539] Bachmeier, A.; Esselborn, J.; Hexter, S. V.; Krämer, T.; Klein, K.; Happe, T.; McGrady, J. E.; Myers, W. K.; Armstrong, F. A. *J. Am. Chem. Soc.* **2015**, *137*, 5381.
[540] Pollock, R. C.; Lee, H.-I.; Cameron, L. M.; DeRose, V. J.; Hales, B. J.; Orme-Johnson, W. H.; Hoffman, B. M. *J. Am. Chem. Soc.* **1995**, *117*, 8686.

[541] Hoffman, B. M.; DeRose, V. J.; Doan, P. E.; Gurbiel, R. J.; Houseman, A. L. P.; Telser, J. *Biol. Magn. Reson.* **1993**, *13*, 151.
[542] Siebel, J. F.; Adamska-Venkatesh, A.; Weber, K.; Rumpel, S.; Reijerse, E.; Lubitz, W. *Biochemistry* **2015**, *54*, 1474.
[543] Soo, H. S.; Agiral, A.; Bachmeier, A.; Frei, H. *J. Am. Chem. Soc.* **2012**, *134*, 17104.
[544] Topoglidis, E.; Campbell, C.; Cass, A. G.; Durrant, J. R. *Langmuir* **2001**, *17*, 7899.
[545] Topoglidis, E.; Lutz, T.; Durrant, J. R.; Palomares, E. *Bioelectrochemistry* **2008**, *74*, 142.
[546] Frey, M. *ChemBioChem* **2002**, *3*, 153.
[547] Parkin, A.; Seravalli, J.; Vincent, K. A.; Ragsdale, S. W.; Armstrong, F. A. *J. Am. Chem. Soc.* **2007**, *129*, 10328.
[548] Armstrong, F. A.; Heering, H. A.; Hirst, J. *Chem. Soc. Rev.* **1997**, *26*, 169.
[549] Armstrong, F. A. In *Bioinorganic Chemistry*; Springer Berlin Heidelberg: 1990; Vol. 72, p 137.
[550] Morra, S.; Valetti, F.; Sadeghi, S. J.; King, P. W.; Meyer, T.; Gilardi, G. *Chem. Commun.* **2011**, *47*, 10566.
[551] Woolerton, T. W. *D. Phil. Thesis*, University of Oxford, 2012.
[552] Bacsa, R. R.; Kiwi, J. *Appl. Catal., B* **1998**, *16*, 19.
[553] Park, S. W.; Huang, C. P. *J. Colloid Interface Sci.* **1987**, *117*, 431.
[554] Wang, V. C.-C.; Can, M.; Pierce, E.; Ragsdale, S. W.; Armstrong, F. A. *J. Am. Chem. Soc.* **2013**, *135*, 2198.
[555] Murphy, B. J.; Sargent, F.; Armstrong, F. A. *Energy Environ. Sci.* **2014**, *7*, 1426.
[556] Hexter, S. V.; Esterle, T. F.; Armstrong, F. A. *Phys. Chem. Chem. Phys.* **2014**, *16*, 11822.
[557] Kavan, L.; Grätzel, M.; Rathouský, J.; Zukalb, A. *J. Electrochem. Soc.* **1996**, *143*, 394.
[558] Fabregat-Santiago, F.; Mora-Seró, I.; Garcia-Belmonte, G.; Bisquert, J. *J. Phys. Chem. B* **2003**, *107*, 758.
[559] Meissner, D.; Memming, R.; Kastening, B. *J. Phys. Chem.* **1988**, *92*, 3476.
[560] Lee, M. S.; Cheon, I. C.; Kim, Y. I. *Bull. Korean Chem. Soc.* **2003**, *24*, 1155.
[561] Boschloo, G.; Fitzmaurice, D. *J. Electrochem. Soc.* **2000**, *147*, 1117.
[562] Kavan, L.; Grätzel, M.; Gilbert, S. E.; Klemenz, C.; Scheel, H. J. *J. Am. Chem. Soc.* **1996**, *118*, 6716.
[563] Spadavecchia, F.; Cappelletti, G.; Ardizzone, S.; Ceotto, M.; Falciola, L. *J. Phys. Chem. C* **2011**, *115*, 6381.
[564] Barbé, C. J.; Arendse, F.; Comte, P.; Jirousek, M.; Lenzmann, F.; Shklover, V.; Grätzel, M. *J. Am. Ceram. Soc.* **1997**, *80*, 3157.
[565] Odobel, F.; Pellegrin, Y. *J. Phys. Chem. Lett.* **2013**, *4*, 2551.
[566] Odobel, F.; Le Pleux, L.; Pellegrin, Y.; Blart, E. *Acc. Chem. Res.* **2010**, *43*, 1063.
[567] Boschloo, G.; Hagfeldt, A. *J. Phys. Chem. B* **2001**, *105*, 3039.
[568] Qin, P.; Wiberg, J.; Gibson, E. A.; Linder, M.; Li, L.; Brinck, T.; Hagfeldt, A.; Albinsson, B.; Sun, L. *J. Phys. Chem. C* **2010**, *114*, 4738.
[569] Mahmood, T.; Saddique, M. T.; Naeem, A.; Westerhoff, P.; Mustafa, S.; Alum, A. *Ind. Eng. Chem. Res.* **2011**, *50*, 10017.
[570] Bachmeier, A.; Wang, V. C.-C.; Woolerton, T. W.; Bell, S.; Fontecilla-Camps, J. C.; Can, M.; Ragsdale, S. W.; Chaudhary, Y. S.; Armstrong, F. A. *J. Am. Chem. Soc.* **2013**, *135*, 15026.
[571] Renaud, A.; Chavillon, B.; Cario, L.; Pleux, L. L.; Szuwarski, N.; Pellegrin, Y.; Blart, E.; Gautron, E.; Odobel, F.; Jobic, S. *J. Phys. Chem. C* **2013**, *117*, 22478.

[572] Gonzalez-Elipe, A. R.; Holgado, J. P.; Alvarez, R.; Munuera, G. *J. Phys. Chem.* **1992**, *96*, 3080.
[573] Powar, S.; Wu, Q.; Weidelener, M.; Nattestad, A.; Hu, Z.; Mishra, A.; Bauerle, P.; Spiccia, L.; Cheng, Y.-B.; Bach, U. *Energy Environ. Sci.* **2012**, *5*, 8896.
[574] Kuciauskas, D.; Freund, M. S.; Gray, H. B.; Winkler, J. R.; Lewis, N. S. *J. Phys. Chem. B* **2001**, *105*, 392.
[575] Smeigh, A. L.; Pleux, L. L.; Fortage, J.; Pellegrin, Y.; Blart, E.; Odobel, F.; Hammarstrom, L. *Chem. Commun.* **2012**, *48*, 678.
[576] Morris, C. J.; Black, A. C.; Pealing, S. L.; Manson, F. D.; Chapman, S. K.; Reid, G. A.; Gibson, D. M.; Ward, F. B. *Biochem. J.* **1994**, *302*, 587.
[577] Cuendet, P.; Grätzel, M. *Photochem. Photobiol.* **1984**, *39*, 609.
[578] Kim, Y.; Ikebukuro, K.; Muguruma, H.; Karube, I. *J. Biotechnol.* **1998**, *59*, 213.
[579] Jiang, Z.; Lü, C.; Wu, H. *Ind. Eng. Chem. Res.* **2005**, *44*, 4165.
[580] Lu, J.; Li, H.; Cui, D.; Zhang, Y.; Liu, S. *Anal. Chem.* **2014**, *86*, 8003.
[581] Song, W.; Vannucci, A. K.; Farnum, B. H.; Lapides, A. M.; Brennaman, M. K.; Kalanyan, B.; Alibabaei, L.; Concepcion, J. J.; Losego, M. D.; Parsons, G. N.; Meyer, T. J. *J. Am. Chem. Soc.* **2014**, *136*, 9773.
[582] Taylor, P.; Pealing, S. L.; Reid, G. A.; Chapman, S. K.; Walkinshaw, M. D. *Nat. Struct. Mol. Biol.* **1999**, *6*, 1108.
[583] Hoertz, P. G.; Chen, Z.; Kent, C. A.; Meyer, T. J. *Inorg. Chem.* **2010**, *49*, 8179.
[584] Turner, K. L.; Doherty, M. K.; Heering, H. A.; Armstrong, F. A.; Reid, G. A.; Chapman, S. K. *Biochemistry* **1999**, *38*, 3302.
[585] Bachmeier, A.; Hall, S.; Ragsdale, S. W.; Armstrong, F. A. *J. Am. Chem. Soc.* **2014**, *136*, 13518.
[586] Lemon, B. I.; Liu, F.; Hupp, J. T. *Coord. Chem. Rev.* **2004**, *248*, 1225.
[587] Park, H.; Bae, E.; Lee, J.-J.; Park, J.; Choi, W. *J. Phys. Chem. B* **2006**, *110*, 8740.
[588] Liang, Y.; Tsubota, T.; Mooij, L. P. A.; van de Krol, R. *J. Phys. Chem. C* **2011**, *115*, 17594.
[589] Abdi, F. F.; van de Krol, R. *J. Phys. Chem. C* **2012**, *116*, 9398.
[590] Pendlebury, S. R. In *ISF-1 Young* Uppsala, 2015.
[591] Barroso, M.; Mesa, C. A.; Pendlebury, S. R.; Cowan, A. J.; Hisatomi, T.; Sivula, K.; Grätzel, M.; Klug, D. R.; Durrant, J. R. *Proc. Natl. Acad. Sci. U. S. A.* **2012**, *109*, 15640.
[592] Iwase, A.; Kudo, A. *J. Mater. Chem.* **2010**, *20*, 7536.
[593] Gordon, E. J. *J. Am. Chem. Soc.* **2014**, *136*, 13469.
[594] Adams, M. W.; Mortenson, L. E. *J. Biol. Chem.* **1984**, *259*, 7045.
[595] Kim, J. H.; Nam, D. H.; Park, C. B. *Curr. Opin. Biotechnol.* **2014**, *28*, 1.
[596] Choudhury, S.; Baeg, J.-O.; Park, N.-J.; Yadav, R. K. *Angew. Chem. Int. Ed.* **2012**, *51*, 11624.
[597] Mifsud, M.; Gargiulo, S.; Iborra, S.; Arends, I. W. C. E.; Hollmann, F.; Corma, A. *Nat. Commun.* **2014**, *5*.
[598] Sucheta, A.; Cammack, R.; Weiner, J.; Armstrong, F. A. *Biochemistry* **1993**, *32*, 5455.
[599] Girbal, L.; von Abendroth, G.; Winkler, M.; Benton, P. M. C.; Meynial-Salles, I.; Croux, C.; Peters, J. W.; Happe, T.; Soucaille, P. *Appl. Environ. Microbiol.* **2005**, *71*, 2777.
[600] Happe, T.; Naber, J. D. *Eur. J. Biochem.* **1993**, *214*, 475.
[601] Kuchenreuther, J. M.; Grady-Smith, C. S.; Bingham, A. S.; George, S. J.; Cramer, S. P.; Swartz, J. R. *PLoS ONE* **2010**, *5*.
[602] Akhtar, M. K.; Jones, P. R. *Appl. Microbiol. Biotechnol.* **2008**, *78*, 853.
[603] Bradford, M. M. *Anal. Biochem.* **1976**, *72*, 248.
[604] Hemschemeier, A.; Melis, A.; Happe, T. *Photosynth. Res.* **2009**, *102*, 523.

[605] Roseboom, W.; De Lacey, A. L.; Fernández, V. M.; Hatchikian, E. C.; Albracht, S. *J. Biol. Inorg. Chem.* **2006**, *11*, 102.
[606] Albracht, S. J.; Roseboom, W.; Hatchikian, E. C. *J. Biol. Inorg. Chem.* **2006**, *11*, 88.
[607] Stoll, S.; Schweiger, A. *J. Magn. Reson.* **2006**, *178*, 42.
[608] Becke, A. D. *Phys. Rev. A* **1988**, *38*, 3098.
[609] Perdew, J. *Phys. Rev. B.* **1986**, *33*, 8822.
[610] Schäfer, A.; Huber, C.; Ahlrichs, R. *J. Phys. Chem.* **1994**, *100*, 5829.
[611] Becke, A. D. *J. Phys. Chem.* **1993**, *98*, 5648.
[612] Frisch, M. J. T., G. W.; Schlegel, H. B.; Scuseria, G. E.; Robb, M. A.; Cheeseman, J. R.; Scalmani, G.; Barone, V.; Mennucci, B.; Petersson, G. A.; Nakatsuji, H.; Caricato, M.; Li, X.; Hratchian, H. P.; Izmaylov, A. F.; Bloino, J.; Zheng, G.; Sonnenberg, J. L.; Hada, M.; Ehara, M.; Toyota, K.; Fukuda, R.; Hasegawa, J.; Ishida, M.; Nakajima, T.; Honda, Y.; Kitao, O.; Nakai, H.; Vreven, T.; Montgomery, J. A., Jr.; Peralta, J. E.; Ogliaro, F.; Bearpark, M.; Heyd, J. J.; Brothers, E.; Kudin, K. N.; Staroverov, V. N.; Kobayashi, R.; Normand, J.; Raghavachari, K.; Rendell, A.; Burant, J. C.; Iyengar, S. S.; Tomasi, J.; Cossi, M.; Rega, N.; Millam, M. J.; Klene, M.; Knox, J. E.; Cross, J. B.; Bakken, V.; Adamo, C.; Jaramillo, J.; Gomperts, R.; Stratmann, R. E.; Yazyev, O.; Austin, A. J.; Cammi, R.; Pomelli, C.; Ochterski, J. W.; Martin, R. L.; Morokuma, K.; Zakrzewski, V. G.; Voth, G. A.; Salvador, P.; Dannenberg, J. J.; Dapprich, S.; Daniels, A. D.; Farkas, Ö.; Foresman, J. B.; Ortiz, J. V.; Cioslowski, J.; Fox, D. J. **2009**, *Gaussian 09, Revision A. 02, Gaussian, Inc., Wallingford CT*.
[613] Kaur, I.; Pandya, D. K.; Chopra, K. L. *J. Electrochem. Soc.* **1980**, *127*, 943.
[614] Hatchikian, E. C.; Bruschi, M.; Le Gall, J. *Biochem. Biophys. Res. Commun.* **1978**, *82*, 451.
[615] Trammell, S. A.; Moss, J. A.; Yang, J. C.; Nakhle, B. M.; Slate, C. A.; Odobel, F.; Sykora, M.; Erickson, B. W.; Meyer, T. J. *Inorg. Chem.* **1999**, *38*, 3665.
[616] Pealing, S. L.; Cheesman, M. R.; Reid, G. A.; Thomson, A. J.; Ward, F. B.; Chapman, S. K. *Biochemistry* **1995**, *34*, 6153.
[617] Compton, R. G.; Sanders, G. H. W. *Electrode Potentials*; Oxford University Press: Oxford, 1996.

Appendices

Appendix A

Derivation of the Nernst equation

Consider the general reaction [507,617]

$$\nu_{\mathrm{A}}\mathrm{A} + \nu_{\mathrm{B}}\mathrm{B} + \cdots + e^{-}(\mathrm{metal}) \rightleftharpoons \nu_{\mathrm{C}}\mathrm{C} + \nu_{\mathrm{D}}\mathrm{D} + \cdots, \tag{A:1}$$

where ν_{i} are the stoichiometric coefficients of the individual components *i*. With the *electrochemical potential* $\tilde{\mu}_{\mathrm{i}}$ of component *i* being related to its chemical potential μ_{i} by

$$\tilde{\mu}_{\mathrm{i}} = \mu_{\mathrm{i}} + z_{\mathrm{i}}F\phi, \tag{A:2}$$

where $z_{\mathrm{i}}F\phi$ is the electrical energy of species *i* (z_{i} is the charge carried by *i*, F is Faraday's constant, and ϕ is the potential of the particular phase (electrode or solution) in which *i* resides), the electrochemical potentials of the reactants and products in the equilibrium described by eq. (A:1) can be expressed as

$$\nu_{\mathrm{A}}\tilde{\mu}_{\mathrm{A}} + \nu_{\mathrm{B}}\tilde{\mu}_{\mathrm{B}} + \cdots + \tilde{\mu}_{\mathrm{e}^-} = \nu_{\mathrm{C}}\tilde{\mu}_{\mathrm{C}} + \nu_{\mathrm{D}}\tilde{\mu}_{\mathrm{D}} + \cdots. \tag{A:3}$$

The different $\tilde{\mu}_i$ can be substituted according to eq. (A:2):

$$\begin{aligned}\nu_{\mathrm{A}}(\mu_{\mathrm{A}} + z_{\mathrm{A}}F\phi_{\mathrm{s}}) + \nu_{\mathrm{B}}(\mu_{\mathrm{B}} + z_{\mathrm{B}}F\phi_{\mathrm{s}}) + \cdots + (\mu_{\mathrm{e}^-} - F\phi_{\mathrm{m}}) \\ = \nu_{\mathrm{C}}(\mu_{\mathrm{C}} + z_{\mathrm{C}}F\phi_{\mathrm{s}}) + \nu_{\mathrm{D}}(\mu_{\mathrm{D}} + z_{\mathrm{D}}F\phi_{\mathrm{s}}) + \cdots.\end{aligned} \tag{A:4}$$

Conservation of electrical charge requires that

$$\nu_{\mathrm{A}}z_{\mathrm{A}} + \nu_{\mathrm{B}}z_{\mathrm{B}} + \cdots - 1 = \nu_{\mathrm{C}}z_{\mathrm{C}} + \nu_{\mathrm{D}}z_{\mathrm{D}} + \cdots. \tag{A:5}$$

Rearrangement of eq. (A:4), substitution into eq. (A:5), and solving for $F(\phi_{\mathrm{m}} - \phi_{\mathrm{s}})$ leads to

$$F(\phi_{\mathrm{m}} - \phi_{\mathrm{s}}) = \nu_{\mathrm{A}}\mu_{\mathrm{A}} + \nu_{\mathrm{B}}\mu_{\mathrm{B}} + \cdots + \mu_{\mathrm{e}^-} - \nu_{\mathrm{C}}\mu_{\mathrm{C}} - \nu_{\mathrm{D}}\mu_{\mathrm{D}}. \tag{A:6}$$

With

$$\mu_{\mathrm{i}} = \mu_{\mathrm{i}}^{0} + RT\ln a_{\mathrm{i}}. \tag{A:7}$$

follows

$$F(\phi_{\mathrm{m}} - \phi_{\mathrm{s}}) = \nu_{\mathrm{A}}(\mu_{\mathrm{A}}^{0} + RT\ln a_{\mathrm{A}}) + \nu_{\mathrm{B}}(\mu_{\mathrm{B}}^{0} + RT\ln a_{\mathrm{B}}) + \cdots + \mu_{\mathrm{e}^-} - \nu_{\mathrm{C}}(\mu_{\mathrm{C}}^{0} + RT\ln a_{\mathrm{C}}) - \nu_{\mathrm{D}}(\mu_{\mathrm{D}}^{0} + RT\ln a_{\mathrm{D}}). \quad \text{(A:8)}$$

Substitution of the term

$$F\Delta\phi^{0} = (\nu_{\mathrm{A}}\mu_{\mathrm{A}}^{0} + \nu_{\mathrm{B}}\mu_{\mathrm{B}}^{0} + \cdots) - (\nu_{\mathrm{C}}\mu_{\mathrm{C}}^{0} + \nu_{\mathrm{D}}\mu_{\mathrm{D}}^{0} + \cdots) + \mu_{\mathrm{e}^-}, \quad \text{(A:9)}$$

which is constant at a fixed temperature and pressure, into eq. (A:8), and rearrangement lead to a general statement of the Nernst equation:

$$\phi_{\mathrm{m}} - \phi_{\mathrm{s}} = \Delta\phi^{0} + \frac{RT}{F}\ln\left\{\frac{a_{\mathrm{A}}^{\nu_{\mathrm{A}}} a_{\mathrm{B}}^{\nu_{\mathrm{B}}} \cdots}{a_{\mathrm{C}}^{\nu_{\mathrm{C}}} a_{\mathrm{D}}^{\nu_{\mathrm{D}}} \cdots}\right\}. \quad \text{(A:10)}$$

For 'ideally' behaving solutions activities can be approximated to concentrations. With $E = \phi_{\mathrm{m}} - \phi_{\mathrm{s}}$ and $E^{0} = \Delta\phi^{0}$, and by introducing z for the number of electrons transferred in the process (as a means of generalisation to account for processes with $z > 1$), eq. (A:9) can be rewritten as

$$E = E^{0} + \frac{RT}{zF}\ln\frac{[\mathrm{Ox}]}{[\mathrm{Red}]}, \quad \text{(A:11)}$$

which, when at equilibrium ($E = E_{\mathrm{eq}}$), equates eq. (2:7) in section 2.2.4.

With the change in free energy ΔG being defined as the sum of the products of the stoichiometric coefficients ν_{i} and the chemical potentials μ_{i} of the individual components i

$$\Delta G = \sum \nu_i \mu_i, \quad \text{(A:12)}$$

the relationship between the Nernst equation and ΔG becomes apparent:

$$\Delta G = \sum \nu_{\mathrm{i}} \mu_{\mathrm{i}}^{0} + RT \sum \nu_{\mathrm{i}} \ln a_{\mathrm{i}} \quad \text{(A:13)}$$

or, rearranged:

$$\Delta G = \Delta G^{0} + RT\ln\prod_{\mathrm{i}}[a_{\mathrm{i}}]^{\nu_{\mathrm{i}}}. \quad \text{(A:14)}$$

Hence,

$$\Delta G = -zFE. \qquad \text{(A:15)}$$

Appendix B

Derivation of the Mott-Schottky equation

Consider an *n*-type semiconductor under depletion [482]. The density of electrons and holes at the surface, n_s and p_s, respectively, is related to their constant bulk values by

$$n(x) = n_b e^{\frac{e_0 \Delta\phi}{k_B T}} \qquad \text{and} \qquad p(x) = p_b e^{-\frac{e_0 \Delta\phi}{k_B T}}, \tag{B:1}$$

where $\Delta\phi = \phi_x - \phi_b$ represents the surface-bulk potential difference, *i.e.* the band-bending, and n_b and p_b are the electron and hole concentrations in the bulk of the semiconductor. The potential, the charge density (ρ), and the number of carriers (n and p) all depend on the distance (x) away from interface into the semiconductor bulk. The charge density in an *n*-type semiconductor can be expressed as [476]

$$\rho(x) = e_0(-n(x) + p(x) - N_A + N_D) \tag{B:2}$$

and $n >> p$, $N_D >> N_A$. Further, the density of electrons in the bulk principally equals the donor density, *i.e.* $n_b \approx N_D$. Using these simplifications, eq. (B:2) can be rewritten as follows:

$$\rho(x) = e_0 N_D \left(1 - e^{\frac{e_0 \Delta\phi}{k_B T}}\right). \tag{B:3}$$

The charge density is related to the potential by the Poisson equation [494]:

$$\frac{d^2\phi(x)}{dx^2} = \frac{-\rho(x)}{\varepsilon_r \varepsilon_0}. \tag{B:4}$$

Using the substitution

$$v = -\Delta\phi = -(\phi_x - \phi_b) \tag{B:5}$$

eq. (B:4) can be expressed as

$$-\frac{d^2 v}{dx^2} = -\frac{\rho(x)}{\varepsilon_r \varepsilon_0} \tag{B:6}$$

and substituted in eq. (B:3):

$$\frac{\mathrm{d}^2 v}{\mathrm{d}x^2} = \frac{e_0 N_\mathrm{D}}{\varepsilon_\mathrm{r}\varepsilon_0}\left(1 - e^{\frac{-e_0 v}{k_\mathrm{B}T}}\right). \tag{B:7}$$

With the property of derivatives [494]

$$\frac{\mathrm{d}^2 v}{\mathrm{d}x^2} = \frac{1}{2}\frac{\mathrm{d}}{\mathrm{d}v}\left(\frac{\mathrm{d}v}{\mathrm{d}x}\right)^2 \tag{B:8}$$

eq. (B:7) transforms into

$$\mathrm{d}\left(\frac{\mathrm{d}v}{\mathrm{d}x}\right)^2 = \frac{2e_0 N_\mathrm{D}}{\varepsilon_\mathrm{r}\varepsilon_0}\left(1 - e^{\frac{-e_0 v}{k_\mathrm{B}T}}\right)\mathrm{d}v. \tag{B:9}$$

Integration gives

$$\left(\frac{\mathrm{d}v}{\mathrm{d}x}\right)^2 = \frac{2e_0 N_\mathrm{D}}{\varepsilon_\mathrm{r}\varepsilon_0}\left(v + \frac{k_\mathrm{B}T}{e_0}e^{\frac{-e_0 v}{k_\mathrm{B}T}}\right) + \mathrm{const.} \tag{B:10}$$

Taking into account that in the bulk of the semiconductor ($x \to \infty$) $\phi_\mathrm{x} = \phi_\mathrm{b}$, *i.e.* there is no potential difference between two points ($v = 0$) and $\frac{\mathrm{d}v}{\mathrm{d}x} = 0$,

$$\left(\frac{\mathrm{d}v}{\mathrm{d}x}\right)^2 = \frac{2e_0 N_\mathrm{D}}{\varepsilon_\mathrm{r}\varepsilon_0}\left(v - \frac{k_\mathrm{B}T}{e_0}\left(1 - e^{\frac{-e_0 v}{k_\mathrm{B}T}}\right)\right). \tag{B:11}$$

At the surface with $x = 0$; $v = v_\mathrm{s}$, the following approximation can be used for the depletion layer of the semiconductor:

$$v_\mathrm{s} \gg \frac{k_\mathrm{B}T}{e_0}. \tag{B:12}$$

Then, eq. (B:11) simplifies to

$$\left(\frac{\mathrm{d}v}{\mathrm{d}x}\right)_{x=0} = \left(\frac{2e_0 N_\mathrm{D}}{\varepsilon_\mathrm{r}\varepsilon_0}\left(v_\mathrm{s} - \frac{k_\mathrm{B}T}{e_0}\right)\right)^{1/2}. \tag{B:13}$$

Using Gauss' law to express the total charge Q [476] as

$$Q = \varepsilon_\mathrm{r}\varepsilon_0\left(\frac{\mathrm{d}v}{\mathrm{d}x}\right), \tag{B:14}$$

and combining eqs. (B:13) and (B:14), eq. (B:15) is obtained:

$$Q = \left(2\varepsilon_r\varepsilon_0 e_0 N_D \left(v_s - \frac{k_B T}{e_0}\right)\right)^{1/2}. \quad \text{(B:15)}$$

The interfacial capacitance of the space-charge layer C_{sc} is given as

$$C_{sc} = \frac{dQ}{dv_s}. \quad \text{(B:16)}$$

Substitution of eq. (B:15) into eq. (B:16) and differentiation yields

$$C_{sc} = \frac{\varepsilon_r\varepsilon_0 e_0 N_D}{\sqrt{2}\sqrt{\varepsilon_r\varepsilon_0 e_0 N_D (v_s - \frac{k_B T}{e_0})}} = \left(\frac{2}{\varepsilon_r\varepsilon_0 e_0 N_D}\left(v_s - \frac{k_B T}{e_0}\right)\right)^{-1/2}. \quad \text{(B:17)}$$

With $v_s = 0$ at $E = E_{fb}$

$$v_s = E - E_{fb}, \quad \text{(B:18)}$$

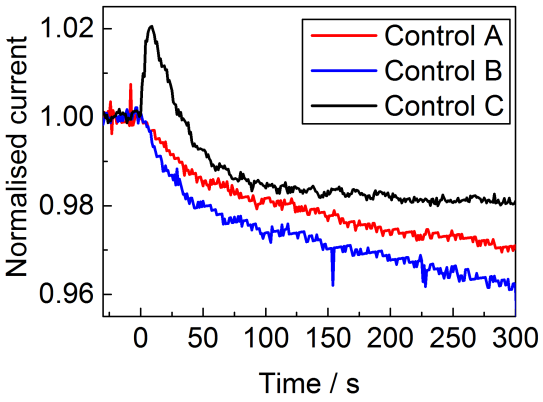
and eq. (B:17) transforms into the Mott-Schottky equation eq. (2:40) [482]:

$$C_{sc}^{-2} = \frac{2}{\varepsilon_r\varepsilon_0 e_0 N_D}\left(E - E_{fb} - \frac{k_B T}{e_0}\right). \quad \text{(B:19)}$$

Appendix C

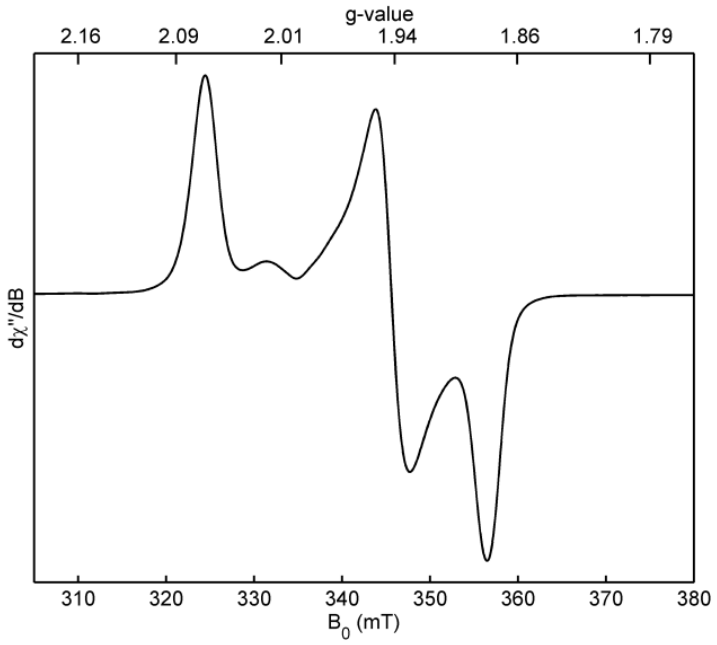
The effect of H_2 consumption by *Ca*HydA at high potential

The effect of H_2 consumption by *Ca*HydA at oxidising potentials was determined by chronoamperometry, since in inhibition studies using acetaldehyde (described in section 3.2.3) the gas flow had to be interrupted simultaneously to aldehyde injection, because of the high volatility of MeCHO (bp 20 ºC). The figure below depicts three control experiments carried out analogously to the inhibition studies described in section 3.2.3, apart from buffer solution being injected into the electrochemical cell at $t = 0$ instead of acetaldehyde (H_2 flow was turned off simultaneously to buffer injection; the electrode was poised at 0.0 V *vs*. SHE; $\omega = 3000$ rpm; pH 6.0 phosphate buffer; dark). In all three cases, less than 5% activity is lost during 5 min, the typical time-course of an actual inhibition experiment.



Appendix D

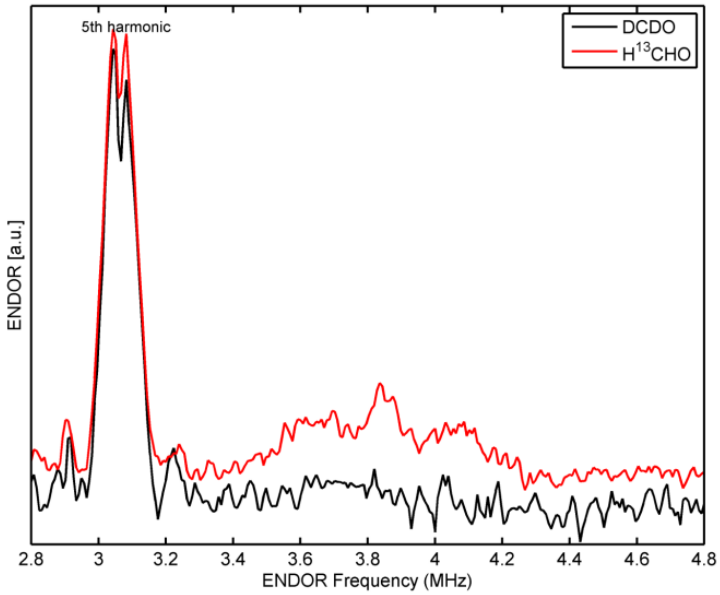
Continuous-wave EPR spectrum of formaldehyde-inhibited CrHydA1



X-band EPR spectrum of formaldehyde-inhibited *Cr*HydA1 collected at 11 K, 9.3902 GHz, with a total spin concentration of 830 μM. Non-saturating conditions were employed, *i.e.* microwave power of 1 mW, modulation amplitude of 1 Gauss, and digital smoothing of 10 points of 1 point per Gauss in a sweep of 1500 G in 10 s. The minor signal at 330 mT ($g = 2.025$) most likely corresponds to a decay product following HCHO inhibition of *Cr*HydA1.

Appendix E

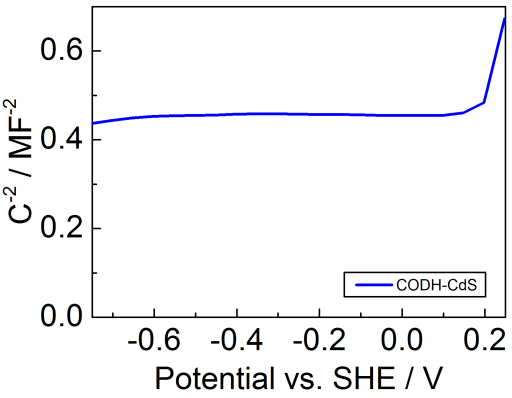
X-band ENDOR natural abundance carbon control



X-band ENDOR spectrum of a ^{2}H control, DCDO, with natural abundance carbon (*i.e.* approximately 99% ^{12}C), compared to formaldehyde isotopically labelled with ^{13}C. The two spectra are scaled to the 5th harmonic of the ^{1}H-ENDOR signal (as indicated in the figure). Data was collected at g = 1.944, under the same conditions as in Figure 3:18.

Appendix F

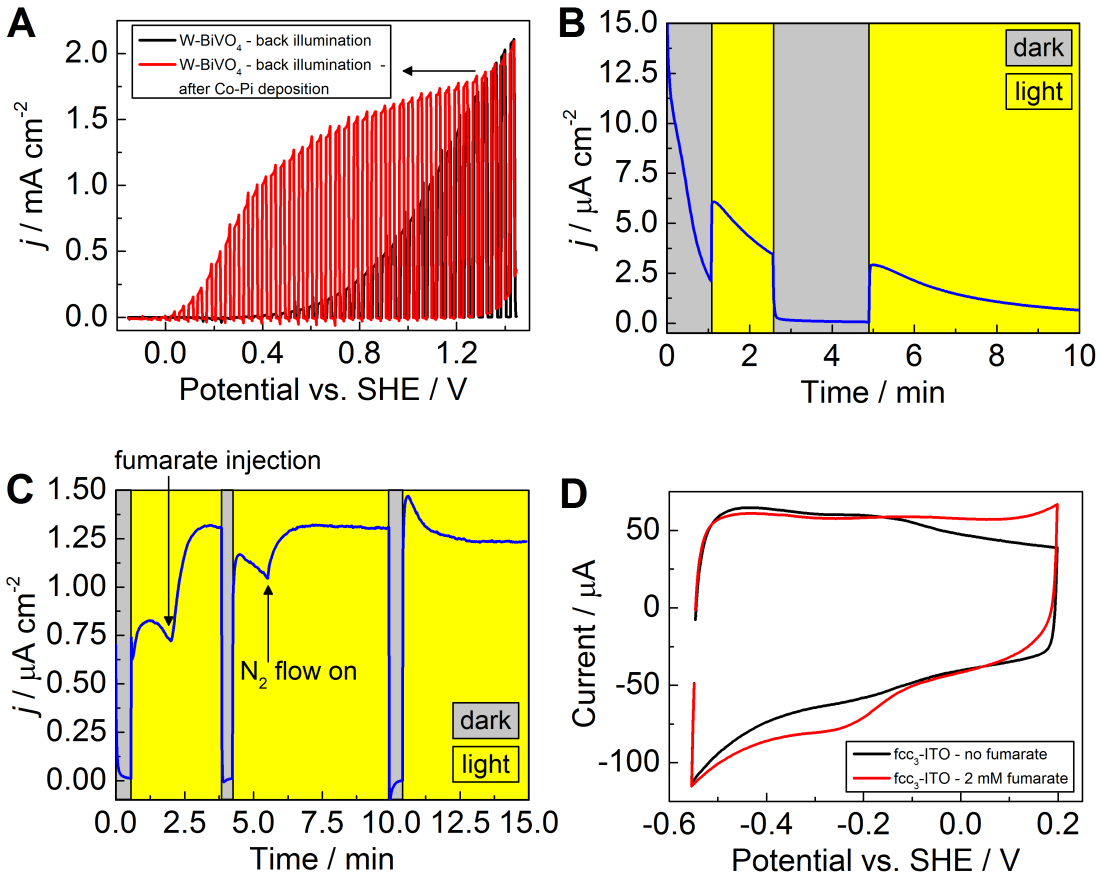
Mott-Schottky experiment on CODH-CdS



Mott-Schottky plot ($1/C^2$ *vs. E*) recorded at 20 °C, 1 kHz for CODH-CdS under 100% N_2 in a 0.2 M MES (pH 6.0) cell buffer solution.

Appendix G

Photoelectrocatalytic fumarate reduction under inverse connections



Photoelectrocatalysis experiment carried out with reversed connections, *i.e.* Co-Pi-W–$BiVO_4$ as the working electrode and fcc_3–ITO as counter. (A) Linear sweep voltammograms recorded before and after Co-Pi deposition on W–$BiVO_4$; 10 mV s^{-1}, chopped illumination (0.5 Hz, back illumination), 25 °C, 0.1 M KPi buffer (pH 7.0). (B) Current *vs.* time trace of the Co-Pi-W–$BiVO_4$ WE connected to the bare *meso*–ITO electrode (CE) in a two-compartment photoelectrochemical cell at zero external bias. Conditions: no gas flow, 25 °C,

0.1 M KPi buffer (pH 7.0). (C) Chronoamperometry experiment depicting photocurrent densities corresponding to visible-light-driven fumarate reduction; 25 °C, 0.1 M KPi buffer (pH 7.0). The reduction compartment was sparged with N_2 to allow efficient substrate transport to the electrode, gas flow was turned off during injection of fumarate (final concentration 2 mM) into the reduction compartment at $t = 2.0$ min. (D) Cyclic voltammogram of fcc_3–ITO recorded after chronoamperometry experiments depicted in (C); 30 mV s^{-1}, 25 °C, 0.1 M KPi buffer (pH 7.0), N_2 flow. The red trace, recorded after introducing fumarate (final concentration 2 mM) into the solution, shows that the enzyme is still catalytically active towards fumarate reduction.